UNIVERSITÀ DELLA CALABRIA

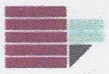

UNIVERSITÀ DELLA CALABRIA

Dipartimento di Fisica

Dottorato di ricerca in
SCIENZE E TECNOLOGIE FISICHE, CHIMICHE E DEI MATERIALI

XXX Ciclo

Measurement of isolated-photon plus jet production in pp collisions at $\sqrt{s} = 13$ TeV with the ATLAS detector at the LHC

Dottorando:
Giuseppe Callea

Coordinatore:
Prof. Vincenzo Carbone

Supervisore:
Prof. Enrico Tassi

Co-supervisori:
Prof.ssa Claudia Glasman

Prof. Juan Terrón

Settore Scientifico Disciplinare: FIS/01

"Whatever Works"
Boris Yellnikoff

Abstract

The study of the production of prompt photons in association with hadronic jets provides a test of perturbative Quantum Chromodynamics and gives information on the proton parton distribution functions. The colorless prompt photon represents a clean probe of the hard partonic interaction since the photon is produced in the hard scattering and does not undergo hadronization. The measurement of the angular correlations between the photon and the hadronic jets is a test of perturbative Quantum Chromodynamics at large hard scattering scales and over a large range of proton momentum fraction. In this thesis, the dynamics of isolated-photon production in association with a jet in proton-proton collisions at a centre-of-mass energy of 13 TeV are studied with the ATLAS detector at the Large Hadron Collider using a dataset with an integrated luminosity of 3.2 fb^{-1}. Photons are required to have transverse energies above 125 GeV. Jets are identified using the anti-k_t algorithm with radius parameter $R = 0.4$ and are required to have transverse momenta above 100 GeV. Measurements of isolated-photon plus jet cross sections are presented as functions of the leading-photon transverse energy, the leading-jet transverse momentum, the azimuthal angular separation between the photon and the jet, the photon-jet invariant mass and the scattering angle in the photon-jet centre-of-mass system. Tree-level plus parton-shower predictions from Sherpa and Pythia as well as next-to-leading-order QCD predictions from Jetphox and Sherpa are compared to the measurements.

Abstract in italiano

Lo studio dei fotoni prompt in associazione a getti adronici fornisce un test per la Cromodinamica Quantistica perturbativa. I fotoni, in quanto privi di carica di colore, possono essere efficacemente usati come sonde per lo studio delle funzioni di distribuzione dei partoni all'interno del protone, poichè vengono prodotti durante lo scattering duro, ma non sono soggetti ad adronizzazione. In particolare, la misura della sezione d'urto del processo di produzione di fotoni prompt, può essere usata per studiare la densità dei gluoni all'interno del protone. In questa tesi, la dinamica della produzione di fotoni isolati in associazione a getti adronici in collisioni protone-protone viene studiata utilizzando il campione di dati raccolto dal rivelatore ATLAS, situato presso il Large Hadron Collider, corrispondente ad una luminosità integrata di 3.2 fb^{-1} ad una energia nel centro di massa di 13 TeV. I fotoni con energia trasversa maggiore di 125 GeV vengono selezionati. I getti vengono identificati tramite l'algoritmo anti-k_t, con raggio R = 0.4 e selezionati se il loro momento trasverso è maggiore di 100 GeV. Le sezioni d'urto misurate, vengono presentate in funzione dell'energia trasversa del fotone, del momento trasverso del getto, della separazione azimutale tra il fotone e il getto, della massa invariante del sistema fotone-getto e del loro angolo di scattering nel sistema del centro di massa. Le misure di sezioni d'urto singolo-differenziali sono state controntate con le predizioni dei Monte Carlo al leadind-order di Pythia e Sherpa e con i calcoli al next-to-leading order di Jetphox e Sherpa.

Contents

Introduction

The production of prompt photons in association with hadronic jets in proton-proton collisions, $pp \to \gamma + \text{jet} + X$, provides a testing ground for perturbative Quantum Chromodynamics (pQCD) in a cleaner eviroment than in jet production, since the colorless photon originates directly from the hard interaction. The measurement of the angular correlations between the photon and the jet can be used to probe the dynamics of the hard-scattering process. Since the dominant production mechanism in pp collisions is through the $qg \to q\gamma$ process, which dominates at Leading Order (LO), measurements of prompt photon plus jet production have been used to contrain the gluon density in the proton [1, 2, 3], to tune the Monte Carlo models and to test the t-channel quark exchange. In addition, the study of prompt photon production is important because this process constitutes one of the main backgrounds in the identification of the Higgs boson decaying into a photon pairs. The $pp \to \gamma + \text{jet} + X$ process, could proceeds through two different mechanisms:

- direct photon (mostly quark-gluon Compton scattering, $qg \to \gamma g$, or quark-antiquark annihilation, $q\bar{q} \to \gamma g$), originated during the hard process;
- fragmentation photon, produced in the fragmentation of a parton with high p_{T}.

The measurements of prompt photon production require the applicaton of an isolation condition on the photons, based on the amount of transverse energy inside a cone of radius R, centred around the photon direction in the pseudorapidity and azimuthal angle plane. As a consequence of this isolation cut, the relative contribution to the total cross section from fragmentation photons decreases. These requirements are thought to avoid the contribution coming from neutral hadrons decays into photons, such as π^0 and η mesons inside jets.
The production of isolated prompt photons in association with jets in pp collisions at $\sqrt{s} = 7$ and 8 TeV was already studied by the ATLAS [4, 5, 6] and

CMS [7, 8, 9] collaborations. The increase in the centre-of-mass energy of pp collisions at the LHC to 13 TeV allows the exploration of the dynamics of photon plus jet production in a new regime with the goals of extending the test on pQCD predictions at higher energy transfers than achieved before, as well as investigating the description of the data by the predictions of different Monte Carlo generators. This thesis presents studies on the production of inclusive isolated-photons plus jet, in pp collisions at $\sqrt{s} = 13$ TeV with the ATLAS detector using an integrated luminosity of 3.2 fb^{-1}. The goal of this analysis is to study the kinematics and dynamics of the photon plus jet events, through the measurement of the differential cross sections as function of the main variables of the photon and jet system. The measured differential cross sections have been compared to the predictions of the LO Pythia and Sherpa Monte Carlo event generator and the next-to-leading Order (NLO) QCD predictions of Jetphox and NLO Sherpa.
This thesis is structured as follows:
Chapter 1 provides the theoretical framework for the prompt photon production and a short description of the applied jet algorithm. Chapter 2 contains a description of the ATLAS detector. In Chapter 3, the main features of the Pythia and Sherpa event generators are discussed. Chapter 4 is devoted to the photon and jets reconstruction procedure used by ATLAS. In Chapter 5 the event selection and the background subtraction method are discussed and the detector level results are shown. Chapter 6 reports the studies on the reconstruction quality and the selection efficiency and purity. In Chapter 7 the cross section measurement procedure is explained. Chapter 8 lists the various sources of systematic uncertainties that affect the measurement. Chapter 9 is dedicated to the NLO QCD calculations of Jetphox and NLO Sherpa and the associated theoretical uncertainties. In Chapters 10, the results of the measurement and the conclusions of the thesis are reported.

Chapter 1

Theoretical framework

1.1 The Standard Model

The Standard Model (SM) [10, 11, 12] of the elementary particles physics is an established theory which provides a fundamental description of all elementary particles and their interactions. It is a non-abelian gauge theory based on three symmetry groups: $SU(3)_C \otimes SU(2)_L \otimes U(1)_Y$. The local $SU(2)_L \otimes U(1)_Y$ symmetry corresponds to the electroweak interaction, described by the Glashow-Salam-Weinberg model, which combines the electromagnetic and the weak interactions. While $SU(3)_C$ reflects the symmetry of the strong interaction, described by Quantum Chromodynamics (QCD). Particles of half-integer spin, called fermions, form the basic constituents of matter while, the interactions between them are described by the exchange of force-mediating bosons of integer spin. Figure 1.1 lists the particles that are included in the SM and their most important properties. It includes three generation of quarks, three generations of leptons and their respective neutrinos and the gauge bosons, which mediate three fundamental forces: weak, electromagnetic and strong forces. For each particle exists in nature an anti-particle with the same mass but opposite intrinsic quantum numbers. The particles of the Lagrangian density of the Standard Model are massless in principle, unlike the ones observed in nature. Thus, a theoretical mechanism must be introduced to explain the presence of the massive particles. In the SM, the Higgs scalar field introduces a spontaneous breaking of the symmetry when it acquires a non-vanishing vacuum expectation value and provides the mass to the fermions through the Yukawa interactions. It is common to refere to this mechanism as the "Brout-Englert-Higgs mechanism" [13] [14]. The Higgs boson, whose existence was postulated in the Brout-Englert-Higgs mechanism, was experimentally discovered by the ATLAS and CMS exper-

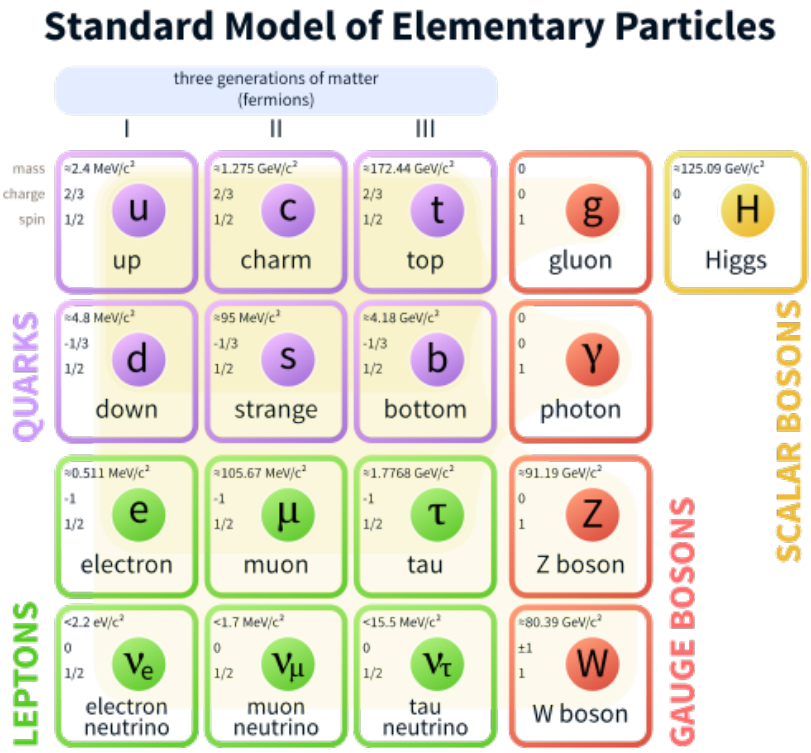

Figure 1.1: Table of particles

timents at the Large Hadron Collider (LHC), with a mass around 125 GeV [15, 16, 17, 18]. After its discovery, Francois Englert and Peter Higgs were awarded of the Nobel prize for physics in 2013 [19].

1.2 Quantum Chromodynamics

As already mentioned in the previous section, QCD [20] is the theory of the strong interactions based on the group SU(3) with a non-abelian gauge invariance. Quarks and antiquarks are particles with spin 1/2 and they strongly interact throught the exchange of gauge bosons called gluons, which can interact between themeselves, unlike the photons in Quantum Electrodynamics, since they are carriers of the color charge. For this reason, gluon dynamics is the mainly responsible of the asymptotic freedom property of the QCD theory. The idea of quarks came from the need to have the manifestation of the SU(3) group of flavour, observed in the spectra of low mass hadrons. In the quark model, baryons are made of three valence quarks (or antiquarks)

and mesons by valence quark-antiquark pairs. In a naive picture, the proton is made of three valence quarks, two up and one down quark of respective electric charge 2/3 and -1/3. However, the proton structure is more complex. Due to the quark interactions, gluons are radiated by the valence quarks and split into quark-antiquark pairs, known as sea-quarks, which make possible to find other quark flavor inside the proton. The proton structure can be described by the parton distribution functions which takes into account gluons, valence and sea-quarks.

1.3 The factorization theorem

The interaction between two hadrons can be calculated in perturbative QCD (pQCD) only in the precence of an hard scale, which characterizes the partonic cross section. The reason of this constraint is due to the behaviour of the strong coupling costant α_s [21, 22]. As a result of the renormalization of the theory, α_s depends on the renormalization scale, typically set to equal to an high energy scale or a transferred momentum Q, which characterizes the given processes. Figure 1.2 shows that the strong coupling constant decreases as the transferred momentum increases and, in the high energy limit, the coupling vanishes showing the asymptotic freedom of QCD. Instead, at low values of Q, α_s behaviour has a steep increase, so it is not possible to use a perturbative approach to describe soft processes in QCD. When it is

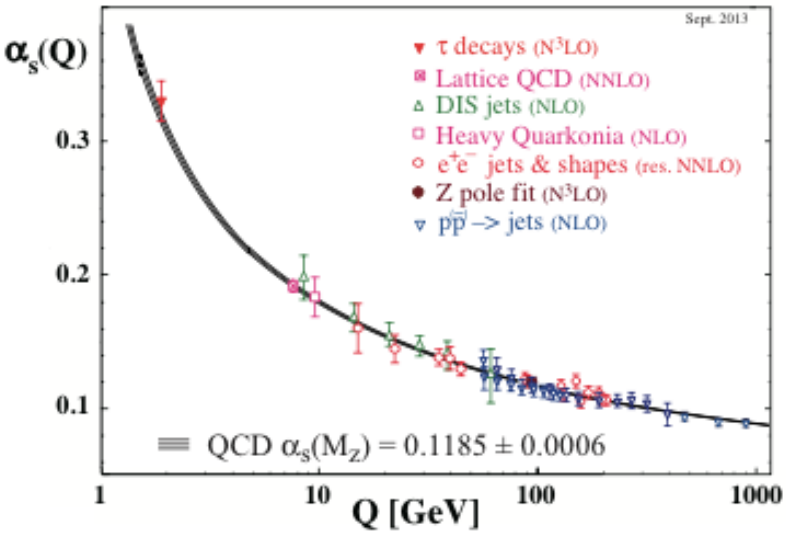

Figure 1.2: Evolution of α_s as function of Q.

possible to apply pQCD, the factorization theorem [23] states that the cross section of any QCD process can be written as the convolution of the parton distribution functions (PDFs) with the partonic cross section, as shown in Eq. 1.1:

$$\sigma(P_1, P_2) = \sum_{q_1,q_2} \int dx_1 f_{q_1/p}(x_1, \mu_f^2) \int dx_2 f_{q_2/p}(x_2, \mu_f^2) \hat{\sigma}(x_1, x_2, \alpha_s(\mu_R^2), \mu_F^2, \mu_R^2), \tag{1.1}$$

where P_1 and P_2 are the momenta of the incoming hadrons, q_1 and q_2 are the partons inside the two colliding hadrons involved in the hard subprocess of cross section $\hat{\sigma}$. $f_{q/p}$ (x,μ_f^2) represents the PDF of the parton q, carrying a fraction x of the P hadron momentum.

1.4 Partonic cross sections

The partonic cross section can be calculated using pQCD and Feynmann diagrams techniques and can be expressed as:

$$\hat{\sigma} = \hat{\sigma}^{(0)} + \alpha_s \cdot \hat{\sigma}^{(1)} + O(\alpha_s^2) \tag{1.2}$$

where $\hat{\sigma}^{(0)}$ represents the contribution at leading order, $\hat{\sigma}^{(1)}$ is the contribution at next-to-leading order. When calculating high-order terms of the perturbative expansion, two kinds of divergences appear:

- Ultraviolet divergences (UV), which come from the integration over loop momenta but they can be removed after the renormalization of the theory. In actual calculations, the most often used renormalisation schemes are:
  - Minimal Subtraction (MS) scheme;
  - Modified Minimal Subtraction ($\overline{MS}$) scheme;
  - On-Shell scheme.

  The renormalization of the theory implies the introduction of a scale parameter μ_{R}, called renormalization scale. The μ_{R} dependence of the strong coupling constant is described by the Callan-Symanzik equation [24].

- Infrared and collinear divergences appear in the calculation of the real and virtual corrections in the limit of vanishing energy of an emitted

parton or when two partons become collinear. In analogy to the renormalization procedure, a factorization scale μ_F is introduced to remove the infrared and collinear divergences. After this procedure, both PDFs and partonic cross sections acquire a dependence on the factorization scale.

1.5 PDFs

The PDFs parametrize the hadron constituents in the non-perturbative regime. Once they are determined for a given process, it is possible to use them for other perturbative hadronic processes. The PDFs depend on the fraction x of the hadron momentum, carried by a parton at a given factorization scale. They cannot be determined in pQCD calculations but knowing their x depen-

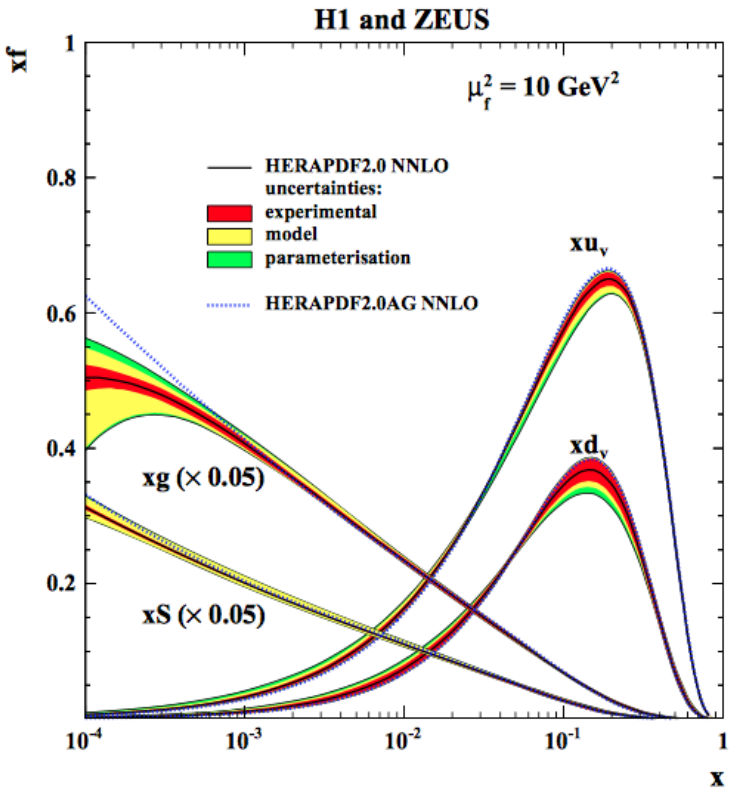

Figure 1.3: The proton's parton distribution functions as determined by the H1 and ZEUS collaborations at HERA (HERAPDF2.0).

dence at a fixed scale (called as an example Q_0^2), it is possible to determine

them at any higher scale Q^2, see Figure 1.3. The evolution of the PDFs with respect to the factorization scale is determined in pQCD by the DGLAP (Dokshitzer, Gribov, Lipatov, Altarelli, Parisi) equations [25, 26, 27, 28]:

$$\frac{d}{d\ln\mu_F} f_{a/h}(x,\mu_F^2) = \sum_b \int_0^1 \frac{dz}{z} P_{ab}(z,\alpha_s(\mu_F^2)) f_{b/h}(\frac{x}{z},\mu_F^2), \tag{1.3}$$

where P_{ab} is the splitting function, which coincides with the probability of emission of a parton a from a parton b. $f_{a/h}$ and $f_{b/h}$ are respectively the PDFs af partons a and b inside an hadron. The splitting functions can also be computed as a power expansion in the strong coupling constant as well as the partonic cross section:

$$P_{ab}(x,\alpha_s(\mu_F)) = P_{ab}^{(1)}(x)(\frac{\alpha_s(\mu_F^2)}{\pi}) + P_{ab}^{(2)}(x)(\frac{\alpha_s(\mu_F^2)}{\pi})^2 + O((\alpha_s(\mu_F^2)/\pi)^3) \tag{1.4}$$

where $P_{ab}^{(1)}$ and $P_{ab}^{(2)}$ are respectively the spliting functions at LO and NLO.

1.6 Theory of prompt photon production

As already mentioned in the introduction, the measurements of prompt photons in association with hadronic jets provide a direct test of pQCD predictions. "Prompt" means that the photons are not produced in hadron or massive gauge bosons decays. Moreover, one of the main motivations for these measurements is their potential to constraint the gluon PDF in the proton, since the dominant contribution to the cross section comes from the gluon-quark interactions [29]. The study of the prompt photon production has some advantages respect to the study of the inclusive jets. The energy resolution is generally better in the electromagnetic calorimeter than in the hadronic calorimeter and the photon energy scale systematic uncertainty is usually smaller than the jet energy scale systematic uncertainty. Since the photons do not fragment, their directions and energies are straightforwardly measured in the electromagnetic calorimeter, without the need of a jet algorithm for the reconstruction. To investigate the dynamic of the photon plus jet production, the variable θ^* is introduced:

$$\cos\theta^* = \frac{\Delta y}{2} \tag{1.5}$$

where Δy is the difference in rapidity between the photon and the jet in the final state. θ^* coincides with the scattering angle in the centre-of-mass frame and its distribution is sensitive to the spin of the exchanged particle.

In proton-proton collisions, a prompt photon with high E_{T}, can be produced via two mechanisms, as shown in Figure 1.4:

- Direct photon, where the photon originates from an hard subprocess and its well separated from any hadronic activity;
- Fragmentation photon, where the photon is the result of the collinear fragmentation of a parton and its accompanied by hadron activity.

At LO, the contribution for the direct photon production is given by the processed $qg \to \gamma q$ (also called QCD Compton process) and $q\bar{q} \to \gamma g$ (annihilation process). The contribution for the fragmentation photon appears when a collinear singularity occurs in the calculation of the subprocess $qg \to q\gamma g$. Depending on the nature of the colliding hadrons and on the $\sqrt{s}$ and E_{T} values, either of these processes can dominate. In proton-proton or proton-nucleus collisions the Compton process dominates over the entire E_{T} range, while in proton-antiproton collisions the Compton process dominates at low E_{T} and the annihilation process becomes dominant for high E_{T}. At LO in pQCD, the direct photon contribution is expected to follow the angular distribution $(1 - |\cos\theta^*|)^{-1}$ when $|\cos\theta^*| \to 1$, while the fragmentation photon contribution is expected to have a $(1 - |\cos\theta^*|)^{-2}$ distribution when $|\cos\theta^*| \to 1$. According to the factorization theorem, the fragmentation singularities are factorized to all orders in α_{s} and absorbed into quark and gluon fragmentation functions of the photon, $D_q^{\gamma}(z, \mu_f)$ and $D_g^{\gamma}(z, \mu_f)$, where z is the relative fraction of the fragmenting parton momentum taken by the photon. The fragmentation functions are defined in a factorization scheme with a chosen value of μ_{F}, to have the same order of the hard scale of the process. When μ_{F} is larger than O(1) GeV, the fragmentation functions behave as $\alpha/\alpha_s(\mu_f)$ and, as a result, the fragmentation photon contribution is of the same order ($\mathrm{O}(\alpha\alpha_{\mathrm{s}})$) as the Born level terms in the direct mechanism. At leading order, the final state for direct and fragmentation photon productions is characterized by a γ and an high-p_{T} parton, which is the topology of the $\gamma + jet$ production from an experimental point of view. When the direct process occurs, the photon is generally well separated from the hadronic activity, while when a fragmentation photon comes out, the γ will be probably accompanied by hadrons, except when it carries with itself most of the momentum of the fragmenting parton. But most of these fragmentation processes are suppressed by an isolation criterium which will be introduced in the following chapters. The LO hadron differential cross section, denoted by $d\sigma^{LO}/dP_T^{\gamma}$ for the process $pp \to \gamma + jet + X$, is given by the sum of the

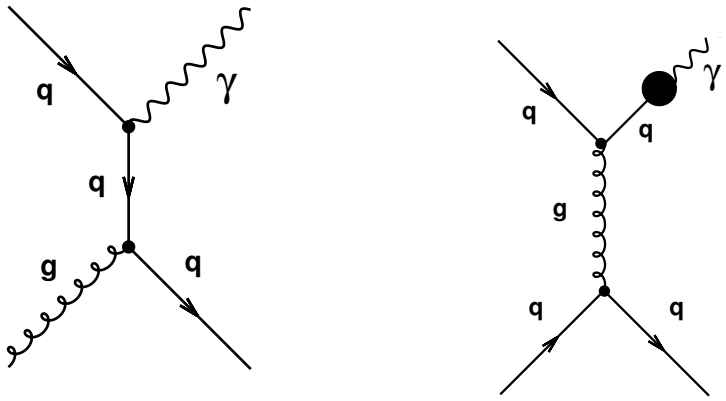

Figure 1.4: Feynman diagrams for prompt photon production at LO

fragmentation and direct contributions, and can be written as:

$$\frac{d\sigma^{LO}}{dp_T^\gamma} = \frac{d\hat{\sigma}^{L0,\gamma}}{dp_T^\gamma}(p_T^\gamma, \mu_F) + \sum_a \int_0^1 \frac{dz}{z} \frac{d\hat{\sigma}^{LO,a}}{dp_T}(\frac{p_T^\gamma}{z}, \mu_F, \mu_f) D_a^{LO,\gamma}(z, \mu_f) \quad (1.6)$$

where $d\hat{\sigma}^{LO,a}/dp_T$ and $d\hat{\sigma}^{L0,\gamma}/dp_T^\gamma$ are the partonic cross sections already convoluted with the partonic distribution functions. $d\hat{\sigma}^{L0,a}/dp_T^\gamma$ is the production differential cross section of a parton in the hard collision; $D_a^{LO,\gamma}(z, \mu_f)$ is the fragmentation function of the parton into a photon and μ_F is the factorization scale for partons in the initial state. In Eq. 1.6 the dynamics is contained in the partonic cross section, while the no-perturbative contributions are factorized into the parton density of the proton and the fragmentation functions of the photon. In Figure 1.5 (left) there is a collinear singularity

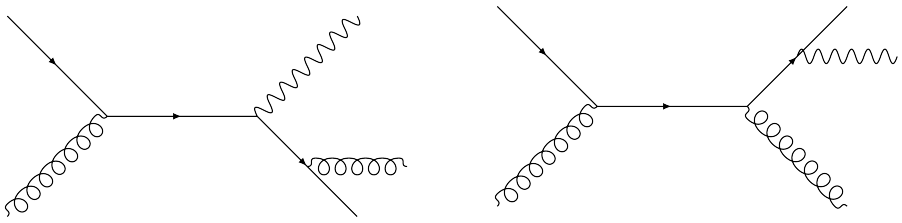

Figure 1.5: Two Feynman diagrams showing two kinds of singularities.

when the momenta of the final state quark and gluon are parallel, but the divergence cancels when real and virtual gluon contributions are summed. The contribution coming from Figure 1.5 (right) is more interesting. The singularity (when the photon and the quark are parallel), does not cancel, but it has to be absorbed into the photon fragmentation function $D_q^\gamma(z, \mu)$

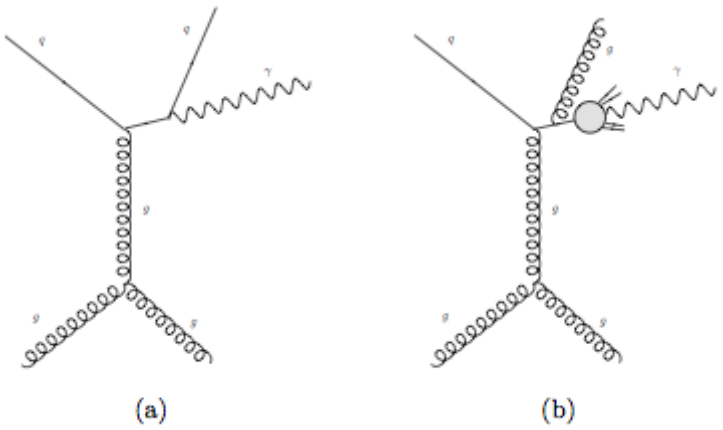

Figure 1.6: NLO Feynman diagrams for the prompt photon production

representing the probability of finding a photon carrying longitudinal momentum fraction z in a quark jet at scale $\mu_{\rm f}$. $D_q^\gamma(z,\mu_f)$ is not calculable in perturbation theory, but follows DGLAP evolution equations similar to the ones associated to the proton PDFs.

1.6.1 NLO calculation

The distinction between the direct and the fragmentation photon production has no physical meaning beyond LO. From a theoretical point of view, the distinction is defined by an arbitrary choice, which follows from the necessity of factorizing the final state collinear singularities and absorbing them into the fragmentation functions. This factorization requires the introduction of an arbitrary fragmentation scale $\mu_{\rm f}$, which relies on the arbitrary choice of the factorization scheme and defines the finite part of the high-order corrections, absorbed in the fragmentation functions together with the singularities. An example of the Feynman diagrams for prompt photon production at NLO are shown in Figure 1.6. The remaining finite part is then included in the high order contribution to the partonic cross sections. In general, taking into account high-order calculations, Eq. 1.6, can be written as

$$\frac{d\sigma}{dP_T^\gamma} = \frac{d\hat{\sigma}^\gamma}{dP_T^\gamma}(P_T^\gamma,\mu_F,\mu_R,\mu_f) + \sum_a \int_0^1 \frac{dz}{z}\frac{d\hat{\sigma}^a}{dP_T^\gamma}(P_T^\gamma/z,\mu_F,\mu_R,\mu_f)D_a^\gamma(z,\mu_f). \tag{1.7}$$

The cross sections $d\hat{\sigma}^{\gamma}/dP_T^{\gamma}$ and $d\hat{\sigma}^{a}/dP_T^{\gamma}$ are known up to NLO in α_s,

$$\frac{d\hat{\sigma}^{\gamma}}{dP_T^{\gamma}} = (\frac{\alpha_s(\mu_R)}{\pi})\frac{d\hat{\sigma}^{\gamma}_{born}}{dP_T^{\gamma}}(P_T^{\gamma},\mu_F) + (\frac{\alpha_s(\mu_R)}{\pi})^2\frac{d\hat{\sigma}^{\gamma}_{HO}}{dP_T^{\gamma}}(P_T^{\gamma},\mu_F,\mu_R,\mu_f) \quad (1.8)$$

$$\frac{d\hat{\sigma}^{a}}{dP_T^{\gamma}} = (\frac{\alpha_s(\mu_R)}{\pi})^2\frac{d\hat{\sigma}^{a}_{born}}{dP_T^{\gamma}}(P_T^{\gamma},\mu_F) + (\frac{\alpha_s(\mu_R)}{\pi})^3\frac{d\hat{\sigma}^{a}_{HO}}{dP_T^{\gamma}}(P_T^{\gamma},\mu_F,\mu_R,\mu_f) \quad (1.9)$$

The expressions of $d\hat{\sigma}_{born}/dP_T^{\gamma}$ and $d\hat{\sigma}^{a}_{HO}/dP_T^{\gamma}$ for the direct and fragmentation contributions can be found in [30]. A detailed description of the NLO computations of the photon plus jet production can be find in Chapter 9.

1.7 Jet algorithms

Jet reconstruction algorithms are useful tools designed to combine the calorimeter energy deposits into jets, where the reconstructed jet shoud best reproduce the properties of the initial partons. There isn't a general jet algorithm to reconstruct the final state partons, it depends on the case which is object of study. From an experimental point of view, jet algorithms must not depend on the presence of soft particles or hadron decay products. While, for the theoretical point of view, there are some guidelines that the jet algorithms have to follow:

- Infrared safety: The presence of any additional soft particles between two particles belonging to the same jet, should not interfere with the recombination of these two particles into a jet and its reconstruction. In other words, if a soft particle is present, it should not affect the number of reconstructed jets;
- Collinear safety: The jet should be reconstructed independently of the fact that an amount of transverse momentum is carried by only one particle or two splitted collinear ones;
- Input-object independence: the jet topology should be reconstructed independently at detector, parton or particle level.

There are two methods to reconstruct the jets starting from the final state particles:

- Cluster algorithms;
- Cone type algorithms.

Algorithms like the k_{t} or the anti-k_{t} [31], belong to the family of the cluster algorithms and they are based on a sequential recombination of particles. Cone type algorithms, like the SISCone, are based instead on the maximization of the energy density inside a cone of fixed size, with a special condition to avoid overlapping of stable cones. Jets are generally defined from the transverse energy flow in the rapidity-azimuthal angle plane, which guarantees the Lorentz invariance under longitudinal boosts, with respect to the colliding particles. Within the class of the recombination algorithms, the distance between a pair of object (d_{ij}) is defined as:

$$d_{ij} = min(E^2_{T,i}, E^2_{T,j})\frac{\Delta^2_{ij}}{R^2} \tag{1.10}$$

where $E^2_{T,i}$ and $E^2_{T,j}$ are the transverse energies of the i and j objects, R is the radius parameter and Δ_{ij}, defined as $\Delta^2_{ij} = (y_i - y_j)^2 + (\phi_i - \phi_j)^2$, represents the distance in the rapidity-azimutham angle plane between i and j. Following the previous equation, the clustering proceeds identifying the shortest distance between the objects and looking if it is a d_{ij}, recombining i and j, or if it is the distance between a jet i and the beam B (d_{iB}), and removing it from the list of entities. This procedure is repeated until there are no entities left. There is an extended definition for the distances expressed in the k_{t} and in the Cambridge/Aachen algorithms:

$$d_{ij} = min(E^{2p}_{T,i}, E^{2p}_{T,j})\frac{\Delta^2_{ij}}{R^2} \tag{1.11}$$

where $d_{iB} = E^{2p}_{T,i}$. If $p = 1$, the inclusive k_{t} algorithm is defined, while $p = 0$ corresponds to the Cambridge/Aachen algorithm. Negative values of p lead to a different behaviour of the jet algorithms, making them flexible to soft radiation. The case of $p = -1$ corresponds to the anti-k_{t} jet-cluster algorithm, which is the one used in this analysis (with $R = 0.4$) for the jet reconstruction.

1.7.1 The anti-k_{t} algorithm

Consider an event with well separated hard particles with transverse energies $E_{\mathrm{T,i}}$ and a lot of soft particles. The distance

$$d_{ij} = min(\frac{1}{E^2_{T,i}}, \frac{1}{E^2_{T,j}})\frac{\Delta^2_{ij}}{R^2} \tag{1.12}$$

between an hard particle i and a soft particle j is determined only by the transverse energy of i and the separation Δ_{ij} between the two particles,

because soft particles tend to accumulate close to the hard particles instead of clustering between themselves, so d_{ij} for similary separated soft particles will be much larger. If an hard particle does not have an hard neighbour within a distance of $2R$, it will accumulate all the soft particles within a circle with a radius R, resulting as a perfect conical jet. If another hard particle is present and $R < \Delta_{12} < 2R$, there will be two jets, but is not possible that they both are perfectly conical. A schematic view of the anti-k_{t} algorithm reconstruction procedure is shown in Figure 1.7.

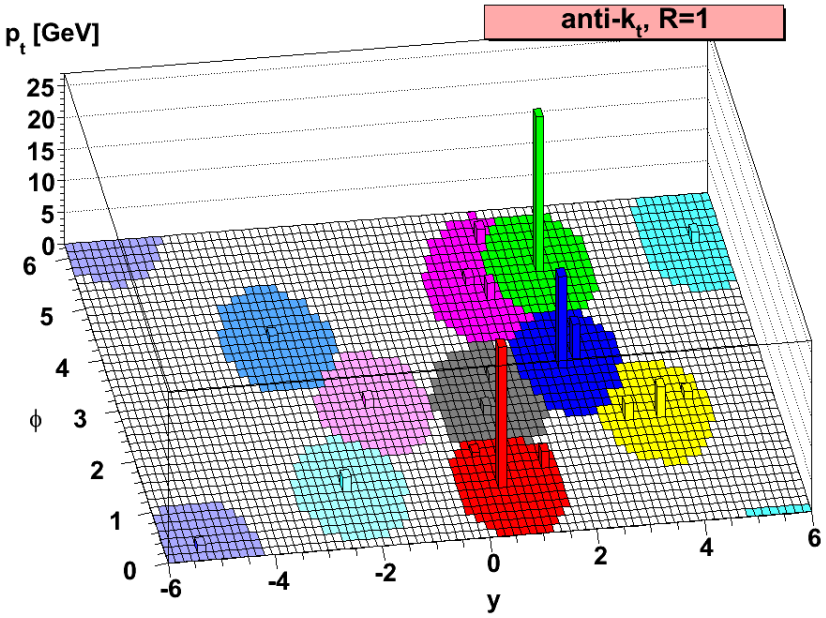

Figure 1.7: Jet reconstruction with the anti-k_{t} algorithm: the colored areas around each jet are the regions in which soft particles are merged into a given jet.

1.7.2 Recombination schemes

The jet that has a higher E_{T} is going to have a perfect cone shape, while the jet with lower E_{T} is going to have a partly conical shape, due to the overlapping part with the first jet. If they have both the same transverse energy, neither jet is going to be conical and the overlapping part will be divided by a line between the two. If $\Delta_{12} < R$, these particles cluster into a single jet, and if $E_{\mathrm{T1}} > E_{\mathrm{T2}}$, the new jet will be conical and centered on E_{T1}. For $E_{\mathrm{T1}} \approx E_{\mathrm{T2}}$, the shape will be a union of both cones (radius $< R$)

around both hard particles, plus a cone of radius R centered on the final jet. Combining particles into jets, there are some schemes that can be followed to combine momenta:

- E-scheme
- p_{T} scheme;
- p_{T}^2 scheme;
- E_{T} scheme;
- E_{T}^2 scheme.

The E-scheme is used in this analysis for the recombination procedure and simply sums the four-vectors of the involved particles. The other schemes incorporate an initial stage in which the initial momenta are made massless, rescaling the energy (3-momentum) to be equal to the 3-momentum (energy) for the p_{T} and p_{T}^2 (E_{T} and E_{T}^2) schemes.

Chapter 2

The LHC and the ATLAS detector

The Large Hadron Collider (LHC) [32] is a superconducting hadron collider built in a 27 km underground tunnel, constructed beneath the French-Swiss border close to Geneva (see Figure 2.1). The main goal of the LHC is to

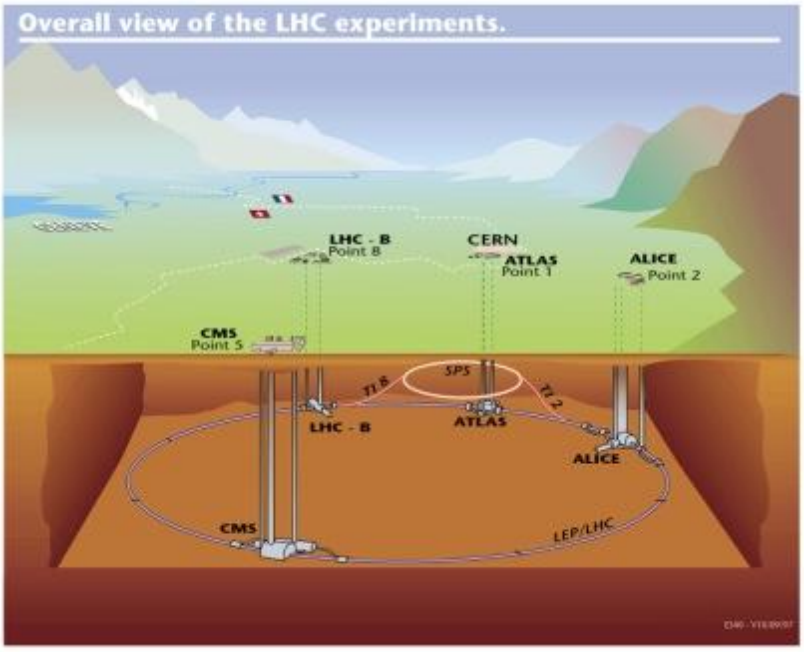

Figure 2.1: Overall view of the LHC experiments

reveal physics beyond the Standard Model. The number of events per second generated in collisions is given by the expression:

$$N_{events} = \mathcal{L} \cdot \sigma, \tag{2.1}$$

where $\mathcal{L}$ is the machine instantaneous luminosity and σ is the cross section of the process that we are studying. There are four main experiments which study the results of proton-proton collisions provided at the LHC: ATLAS [33], CMS [34], LHCb [35] and ALICE [36]. ATLAS and CMS are two high luminosity multi-purpose experiments, LHCb is a low luminosity experiment designed to study b-quark physics, while ALICE is an heavy ion experiment. Luminosity at the LHC is not constant during physics runs, but decays because of the degradation of the intensities and the emittance of the two circulating beams, due to collisions.
ATLAS searches for new phenomena and performs tests of the Standard Model. The main components of the ATLAS detector (see Figure 2.2) are the inner detector, the calorimeter systems and the muon spectrometer. The resolution and rapidity coverage of the ATLAS main components are reported in Figure 2.3. Because of the large collisions rate, the detector requires fast electronics and sensor elements. An high granularity is also required to reduce the influence of overlapping events. A large acceptance in pseudorapidity is also needed, with full coverage in azimuthal angle. The inner detector plays an important role in the track and vertex reconstruction, thanks to its very high resolution and granularity. The electromagnetic calorimeter is essential to identify electrons, positrons and photons, and to study their associate kinematic variables. Meanwhile the hadronic calorimeter is used to measure jet transverse and missing energies. Good muon identification is also required, with high momentum resolution. To reject background events, high-efficient triggers are required to get an adequate trigger rate for the processes, which are object of study. The ATLAS dimensions are 25 m height and 44 m in length. Its weight is about 7000 tons. It is symmetric around the interaction point, covering the whole solid angle. There is a superconducting solenoid surrounding the inner-detector cavity, and there are three superconducting toroids (a barrel and two endcaps) set with an eight-fold azimuthal symmetry around the calorimeters.

2.1 Inner Detector

The Inner Detector (ID) (as shown in Figure 2.4), is permeated by a solenoidal field of 2 T generated by a central solenoid. The ID has length of 5.3 m and diameter of 2.5 m and it consists of 3 complementary sub-detectors. It is possible to get pattern recognition, momentum, vertex measurements and particle identification. This is the result of a combination of high resolution semiconductor pixel and strip detectors in the inner part of the tracking volume, and straw-tube tracking detector, which has the capability of detect

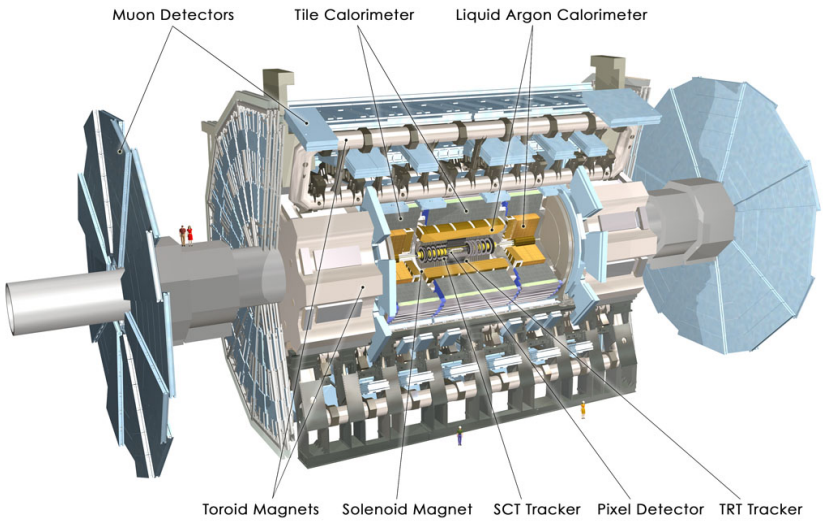

Figure 2.2: The ATLAS Detector

Detector component	Required resolution	η coverage
Tracking	σ_{p_T}/p_T =0.05% $\oplus$ 1%	±2.5
EM calorimetry	σ_E/E =10%/$\sqrt{E}$ $\oplus$ 0.7%	±3.2
Hadronic calorimeters (jets)		
barrel and end-cap	σ_E/E =50%/$\sqrt{E}$ $\oplus$ 3%	±3.2
forward	σ_E/E =100%/$\sqrt{E}$ $\oplus$ 10%	3.1< $\|\eta\|$ <4.9
Muon spectrometer	σ_{p_T}/p_T =10% at p_T = 1 TeV	±2.7

Figure 2.3: Resolutions and η coverage of the main ATLAS detector components

transition radiations in its outer part. The highest granularity is achieved around the vertex region using semiconductor pixel detectors followed by a silicon microstrip detector. At larger radii typically 36 tracking points are provided by the straw tube tracker. In the barrel region the high-precision detectors are arranged in concentric cylinders around the beam axis, while the end-cap detectors are mounted on disks perpendicular to the beam axis. The barrel of the Transition Radiation Tracker (TRT) straws are parallel to the beam direction. All endcap tracking elements are located in planes perpendicular to the beam direction.

Item		Radial extension (mm)	Length (mm)
Overall ID envelope		$0 < R < 1150$	$0 < \|z\| < 3512$
Beam-pipe		$29 < R < 36$	
Pixel	Overall envelope	$45.5 < R < 242$	$0 < \|z\| < 3092$
3 cylindrical layers	Sensitive barrel	$50.5 < R < 122.5$	$0 < \|z\| < 400.5$
2×3 disks	Sensitive end-cap	$88.8 < R < 149.6$	$495 < \|z\| < 650$
SCT	Overall envelope	$255 < R < 549$ (barrel)	$0 < \|z\| < 805$
		$251 < R < 610$ (end-cap)	$810 < \|z\| < 2797$
4 cylindrical layers	Sensitive barrel	$299 < R < 514$	$0 < \|z\| < 749$
2×9 disks	Sensitive end-cap	$275 < R < 560$	$839 < \|z\| < 2735$
TRT	Overall envelope	$554 < R < 1082$ (barrel)	$0 < \|z\| < 780$
		$617 < R < 1106$ (end-cap)	$827 < \|z\| < 2744$
73 straw planes	Sensitive barrel	$563 < R < 1066$	$0 < \|z\| < 712$
160 straw planes	Sensitive end-cap	$644 < R < 1004$	$848 < \|z\| < 2710$

Figure 2.4: Run-1 Inner detector layout.

2.1.1 TRT

The ID provides tracking measurements in a range matched by the precision measurements of the electromagnetic calorimeter [37]. The electron identification capabilities are provided by the detection of transition radiation photons. The TRT is made of various straw- tubes filled with a Xenon gas mixture, with a diameter of 4 mm and long up to 150 cm. In 2012 a gradually increasing number of Xe leaks were detected in the TRT. Because of the high cost of Xenon gas, some TRT modules were filled with a significantly less expensive Argon-based gas mixture. It gives a continuous tracking, 36 hits per track, with a good pattern recognition, given by the 4 mm diameter gas mixture tubes. TRT provides only $R - \Phi$ information, with an accuracy of 130 μm per straw. In the barrel, straws are 144 cm long and they are parallel to the beam axis, while in the endcap region, they are 37 cm long and are arranged radially in wheels. Transition radiation photons are absorbed by the Xe and Ar atoms, depositing additional energy in the gas and leading to significantly higher readout signals with an amplitude that can exceed the 6 keV high threshold. This functionality provides substantial discriminating power between electrons and pions over the energy range between 1 and 200 GeV and represents a key component of the electron identification selection criteria. The TRT readout channels are 351000.

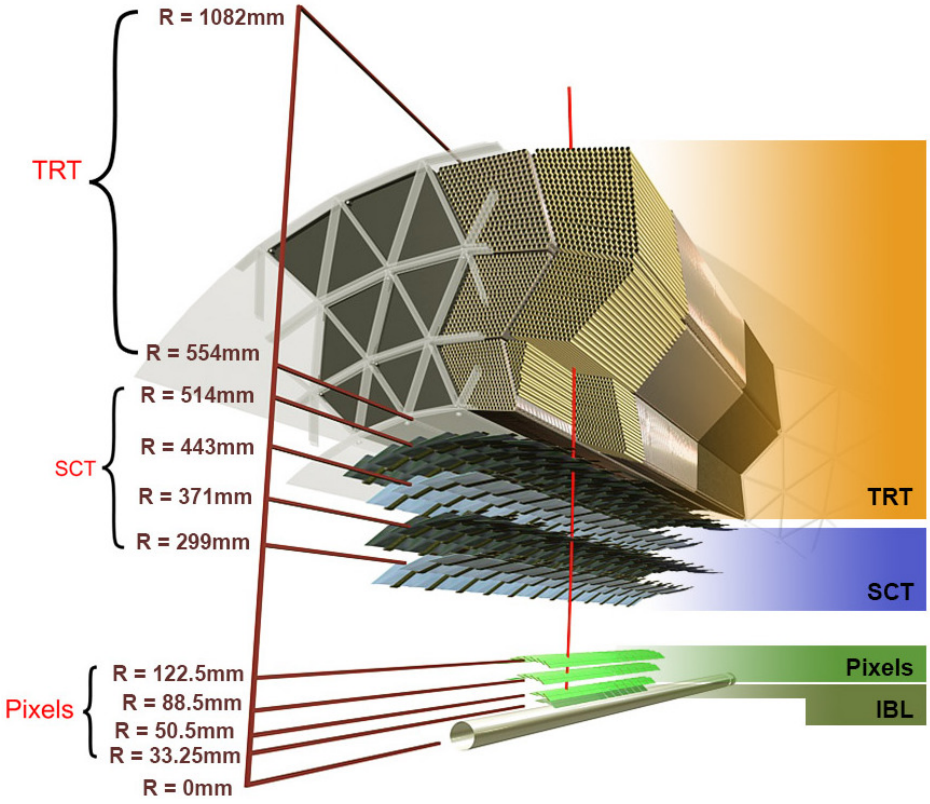

Figure 2.5: Inner detector perspective layout

2.1.2 Pixel Detector

The Run-1 Pixel Detector is the innermost part of the detector and contains three concentric layers and three disks on each end-cap, usually crossed by each track, with a total of 1744 modules with 46080 read-out pixels each [38]. Using silicon pixel detectors, the highest granularity is found around the vertex region. The pixel sensors are all the same, with a minimum pixel size in $(R - \Phi) \times z$ of 50×400 μm^2. The detecting material is silicon 250 μm thick. Each module contains 16 readout chips and other electronic components. The smallest unit that can be read out is a pixel (50 by 400 μm); there are roughly 47,000 pixels per module. The minute pixel size is designed for extremely precise tracking very close to the interaction point. In total, the Pixel Detector has over 80 million read-out channels, which is about 50 % of the total readout channels of the whole experiment. Having such a large count created a considerable design and engineering challenge. Another challenge was the radiation to which the Pixel Detector is exposed because of its proximity to the interaction point, requiring that all components be

radiation hard in order to continue operating after significant exposures. A fourth barrel layer, named "Insertable B-Layer (IBL)" [39], has been installed as part of a detector upgrade during the first Long Shutdown (LS1) in 2013-2014. It represents the innermost layer and it is designed to improve tracking performances and provide better vertexing resolution near the interaction point. The IBL is installed at a radius of $r = 33.5$ mm and it covers the pseudorapidity region of $|\eta| < 3.03$. It consists of 14 staves with ~ 12 million 50×250 μm^2 pixel sensors. The IBL staves are placed between the inner positioning tube (IPT) at $r = 29.0$ mm and the inner support tube (IST) at $r = 42.5$ mm. The IPT and IST are made of carbon fibre and resin. The thickness of the IPT goes from 0.325 mm for $|z| < 311$ mm, to 0.455 mm at the farthest edge.

2.1.3 SCT

The Semi-Conductor Tracker (SCT) is the middle component of the inner detector. It is similar in concept and function to the Pixel Detector but with long, narrow strips rather than small pixels, making coverage of a larger area practical. For the SCT, eight strip layers are crossed by each track. It uses small angle strips to measure both coordinates ($(R - \Phi)$ and Z). Each strip measures 80 μm by 12 cm. The SCT is the most critical part of the inner detector for basic tracking in the plane perpendicular to the beam, since it measures particles over a much larger area than the Pixel Detector, with more sampled points and roughly equal (albeit one-dimensional) accuracy. It is composed of four double layers of silicon strips, and has 6.3 million readout channels and a total area of 61 square meters. The semiconductor trackers also allow impact parameter measurements and vertexing for heavy-flavour and τ-lepton tagging.

2.2 Calorimeters

The ATLAS calorimeter system [40] (see Figure 2.6 and 2.7) is located between the ID and the Muon Spectrometer. It consists of many sampling detectors with a fully Φ symmetry and coverage around the beam axis, covering the pseudo-rapidity range of $|\eta| < 4.9$, ideally suited for precise measurements of the particle energies and positions. Its granularity is set to satisfy the requirements for jet reconstruction and measurements of the missing transverse energy E_{T}^{miss}. The main components of the ATLAS calorimeter system, are shown in Figure 2.6.

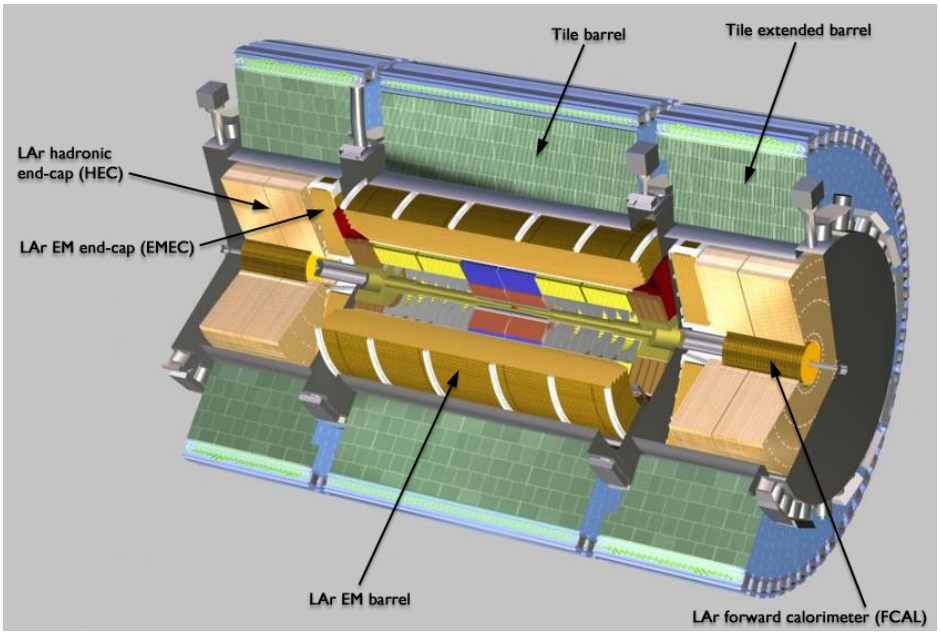

Figure 2.6: View of calorimeters

2.2.1 Electromagnetic Calorimeter

The Liquid Argon (LArg) electromagnetic calorimeter (EM) [41], which covers a range of $|\eta| < 3.2$, provides great performances in terms of energy and position resolution, thanks to its high granularity. It is divided into a central barrel that covers the beam pipe until $|\eta| < 1.475$ and two endcaps with $1.375 < |\eta| < 3.2$ coverage. The LArg is segmented in 3 longitudinal layers in the region $0< |\eta| <2.5$, and two in the higher-η region ($2.5< |\eta| <3.2$). An additional layer called pre-sampler, is placed in front of the calorimeter in the region up to $|\eta| <1.8$, and measures the energy deposits from the electromagnetic showers produced before the calorimeter.

2.2.2 Hadronic Calorimeters

The Hadronic Calorimeter in ATLAS [42] covers a pseudo-rapidity range of $|\eta| < 3.9$. Its central part is a sampling calorimeter, called TileCal, which uses steel as passive material and scintillating tiles to measure the deposited energies. The end-cap regions of the hadronic calorimeter (HEC) are samplings calorimeters that use LArg as active material and copper as absorber. The tile calorimeter, with a range of $|\eta| < 1.7$, has scintillator-tile detectors, divided into a big barrel and two small barrel cylinders, it is placed just outside the LArg electromagnetic calorimeter. The barrel covers a region of

$|\eta| < 1$, while the two extended barrels cover a range of $0.8 < |\eta| < 1.7$, both are segmented into three layers with different interaction lengths. To read the scintillating tiles, wavelength shifting fibers into two different photon multiplier tubes are used. The orientation of the scintillating tiles, radially and normal to the beam line, allows a full projective azimuthal coverage while the grouping of readout fibres imply a "pseudo-projective" geometry in η.

2.2.3 Hadronic endcap calorimeter

The HEC is composed by two indipendent wheels per endcap, located just behind the electromagnetic calorimeter end caps. Each wheel was built with 32 identical modules and is divided in two segments (4 segments per end cap). The inner wheel are made of 25 copper plates, with a radius of 0.475 m, while the outer wheel are built from 50 mm copper plates with a radius of 2.03 m. These copper plates are interleaved with LAr gaps, providing the active medium.

2.2.4 LAr forward calorimeter

The FCal (Forward Calorimeter) provides both electromagnetic and hadronic measurements, and extends the calorimeter pseudo-rapidity coverage from $|\eta| < 3.1$ to $|\eta| < 4.9$. The modules are made of copper (the first) and tungsten to measure respectively electromagnetic particles and the energy of hadronic interactions. Every single module consists of a matrix with longitudinal channels cointaining an electrode structure with concentric rods and tubes (parallel to the beam axis). In the gap between the rods and the tube, LArg is the active medium. Although the FCal is not used for precision measurements, it provides valuable informations for missing transverse momentum determination and reconstruction of very forward jets.

2.3 Magnet system

The ATLAS detector uses two large superconducting magnet systems [43] to bend charged particles so that their momenta can be measured. This bending is due to the Lorentz force, which is proportional to velocity.

2.3.1 Solenoid magnet

The central ATLAS solenoid [44] has a length of 5.3 m with a core of 2.4 m. The conductor is a composite that consists of a flat superconducting cable

	Barrel		End-cap	
EM calorimeter				
Number of layers and $\|\eta\|$ coverage				
Presampler	1	$\|\eta\| < 1.52$	1	$1.5 < \|\eta\| < 1.8$
Calorimeter	3	$\|\eta\| < 1.35$	2	$1.375 < \|\eta\| < 1.5$
	2	$1.35 < \|\eta\| < 1.475$	3	$1.5 < \|\eta\| < 2.5$
			2	$2.5 < \|\eta\| < 3.2$
Granularity $\Delta\eta \times \Delta\phi$ versus $\|\eta\|$				
Presampler	0.025×0.1	$\|\eta\| < 1.52$	0.025×0.1	$1.5 < \|\eta\| < 1.8$
Calorimeter 1st layer	$0.025/8 \times 0.1$	$\|\eta\| < 1.40$	0.050×0.1	$1.375 < \|\eta\| < 1.425$
	0.025×0.025	$1.40 < \|\eta\| < 1.475$	0.025×0.1	$1.425 < \|\eta\| < 1.5$
			$0.025/8 \times 0.1$	$1.5 < \|\eta\| < 1.8$
			$0.025/6 \times 0.1$	$1.8 < \|\eta\| < 2.0$
			$0.025/4 \times 0.1$	$2.0 < \|\eta\| < 2.4$
			0.025×0.1	$2.4 < \|\eta\| < 2.5$
			0.1×0.1	$2.5 < \|\eta\| < 3.2$
Calorimeter 2nd layer	0.025×0.025	$\|\eta\| < 1.40$	0.050×0.025	$1.375 < \|\eta\| < 1.425$
	0.075×0.025	$1.40 < \|\eta\| < 1.475$	0.025×0.025	$1.425 < \|\eta\| < 2.5$
			0.1×0.1	$2.5 < \|\eta\| < 3.2$
Calorimeter 3rd layer	0.050×0.025	$\|\eta\| < 1.35$	0.050×0.025	$1.5 < \|\eta\| < 2.5$
Number of readout channels				
Presampler	7808		1536 (both sides)	
Calorimeter	101760		62208 (both sides)	
LAr hadronic end-cap				
$\|\eta\|$ coverage			$1.5 < \|\eta\| < 3.2$	
Number of layers			4	
Granularity $\Delta\eta \times \Delta\phi$			0.1×0.1	$1.5 < \|\eta\| < 2.5$
			0.2×0.2	$2.5 < \|\eta\| < 3.2$
Readout channels			5632 (both sides)	
LAr forward calorimeter				
$\|\eta\|$ coverage			$3.1 < \|\eta\| < 4.9$	
Number of layers			3	
Granularity $\Delta x \times \Delta y$ (cm)			FCal1: 3.0×2.6	$3.15 < \|\eta\| < 4.30$
			FCal1: ~ four times finer	$3.10 < \|\eta\| < 3.15$, $4.30 < \|\eta\| < 4.83$
			FCal2: 3.3×4.2	$3.24 < \|\eta\| < 4.50$
			FCal2: ~ four times finer	$3.20 < \|\eta\| < 3.24$, $4.50 < \|\eta\| < 4.81$
			FCal3: 5.4×4.7	$3.32 < \|\eta\| < 4.60$
			FCal3: ~ four times finer	$3.29 < \|\eta\| < 3.32$, $4.60 < \|\eta\| < 4.75$
Readout channels			3524 (both sides)	
Scintillator tile calorimeter				
	Barrel		Extended barrel	
$\|\eta\|$ coverage	$\|\eta\| < 1.0$		$0.8 < \|\eta\| < 1.7$	
Number of layers	3		3	
Granularity $\Delta\eta \times \Delta\phi$	0.1×0.1		0.1×0.1	
Last layer	0.2×0.1		0.2×0.1	
Readout channels	5760		4092 (both sides)	

Figure 2.7: Main parameters of the ATLAS calorimeter system [40]

located in the center of an aluminum stabiliser with rectangular cross-section. It is designed to provide a field of 2 T with a peak magnetic field of 2.6 T. The total assembly weight is 5.7 tons.

2.3.2 Toroidal magnets

The outer toroidal magnetic field [45] is produced by eight very large air-core superconducting barrel loops and two end-caps air toroidal magnets (see Figure 2.8), all situated outside the calorimeters and within the muon system. The endcap coils systems are rotated by 22.5 degrees with respect to the Barrel Toroids in order to provide radial overlap and to optimise the bending power in the interface regions of both coil systems. This magnetic field extends over an area 26 m long and 20 m in diameter, and it stores 1.6

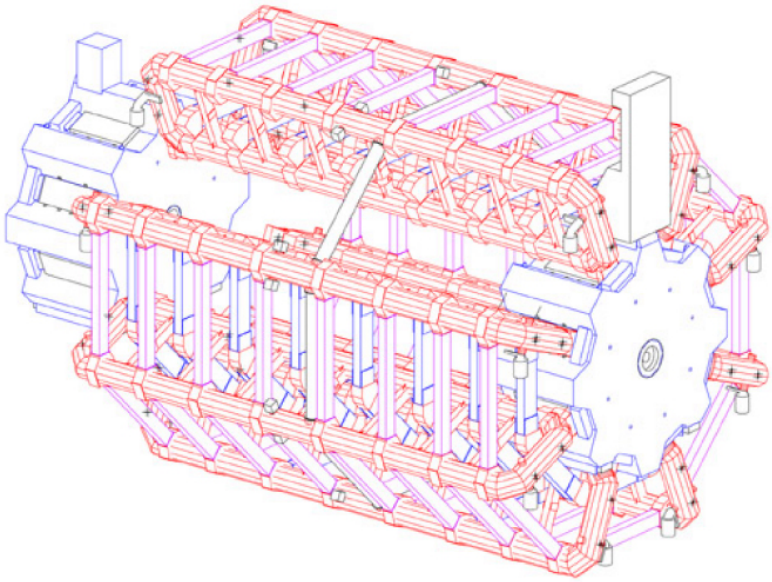

Figure 2.8: The toroidal magnets layout

GJ of energy. Its magnetic field is not uniform, because a solenoid magnet of sufficient size would be prohibitively expensive to build. The integrated magnetic field varies between 2 and 8 T m.

2.4 Muon Spectrometer

Since muons are the only detectable particles that pass the calorimeter system with minimal interaction, a tracking system is needed. The muon spectrometer [46], is the outer part of the ATLAS detector, it surrounds the hadronic calorimeter with a long barrel and two end-caps magnets, providing an excellent muon momentum resolution and minimum multiple scattering effects, in the range of $|\eta| < 2.7$ with three layers of high precision tracking chambers. A cross sectional and a longitudinal view of the muon spectrometer are presented, respectivelly, in Fig.2.9 and 2.10.

Its purpose is to measure with high precision the muon momentum, using the magnetic field generated by external toroid magnets. Over the range $|\eta|$ <1.4, magnetic bending is provided by the large barrel toroid, for 1.6 $< |\eta| < 2.7$, muon tracks are bent by two smaller end-cap magnets inserted into both ends of the barrel toroid, and in the region $1.4 < |\eta| < 1.6$, the bending is provided by a combination of the barrel and end-cap fields. Precise momentum measurement is performed by determining the track coordinates

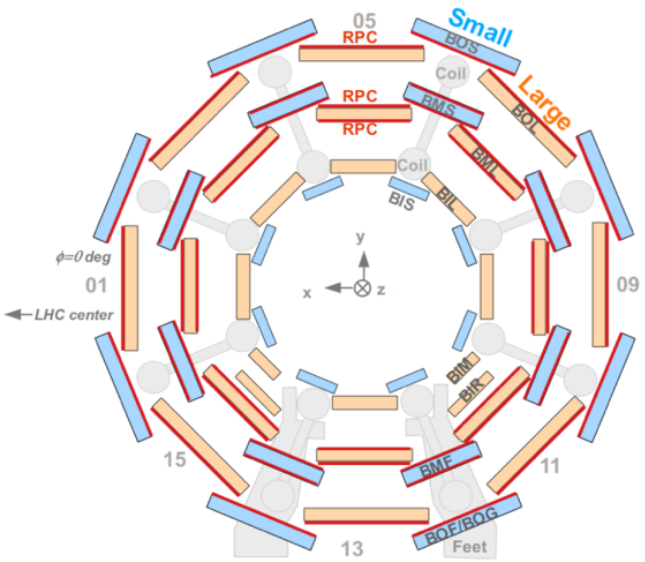

Figure 2.9: Cross sectional view of the barrel muon spectrometer

in the bending plane. Monitored Drift Tubes (MDTs) are used for this task for their high measurement accuracy predictability. In the forward region ($2 < |\eta| < 2.7$), the innermost layer uses radiation hard Catode Strip Chambers (CSCs) to handle the expected particle fluxes with their higher rate capability and time resolution. Fast triggering and second coordinate determination is provided by Resistive Plate Chambers (RPCs) in the barrel and Thin Gap Chambers (TGCs) in the end-caps. More details about these subsystems are given in the following.

2.4.1 Monitored Drift Tubes

The Monitored Drift Tubes chambers cover the rapidity region $|\eta| < 2$ of the muon spectrometer. The basic elements of these chambers are tubes with a diameter of 29.97 mm filled with Ar/CO_2 gas mixture at the pressure of 3 bar. When a muon crosses the tube, the electrons generated in the ionization of the gas are collected at the central tungsten-rhenium wire that has a diameter of 50 μm and is maintained at a potential of 3080 V in order to work in the avalanche regime; at this working point, the maximum drift time is around 700 ns. The tubes are arranged in 2×4 monolayers for the inner stations and 2×3 for the outer stations to form a station that can be rectangular in the barrel and trapezoidal in the endcaps. The two multi-layers of each

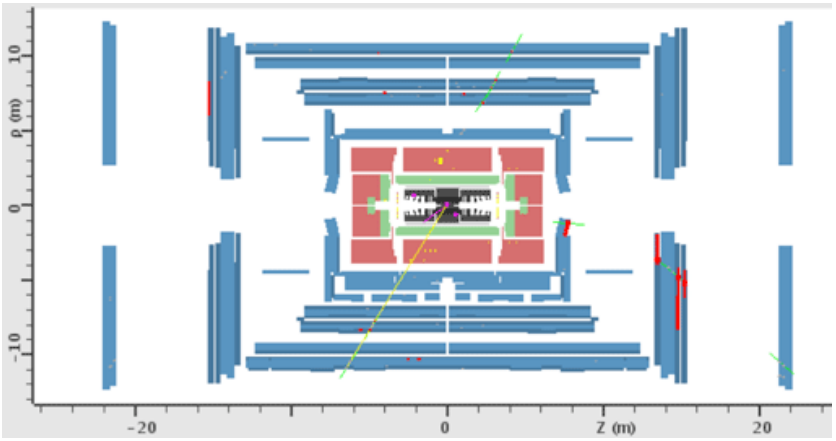

Figure 2.10: Longitudinal view of the ATLAS detector

station are placed on either side of a special support structure (spacer), that ensure the accurate positioning of the tubes with respect to each other. In the case of non vertical chambers, the support structure also slightly bends the tubes of the chambers in order to compensate the gravitational sag of the wires which are not in a vertical position. Moreover deformation are expected to occur and may change with time (due to thermal gradients) and they are monitored by an in-plane optical system that have its component mounted on the spacers.

2.4.2 Catode Strip Chambers

The Cathode Strip Chambers are multi-wire proportional chambers with the wires oriented in the radial direction. They use a gas mixture of Ar/CO_2 and work at an operating voltage of 1900 V combining high spatial, time and double track resolution with high-rate capability and low neutron sensitivity. CSCs are used to substitute the MDT in the innermost layer of the endcap region in the pseudo-rapidity range of $2.0 \leq |\eta| \leq 2.7$ where rates higher than the MDT rate capability (safe operation up to 150 Hz/cm^2) are reached. The whole CSC system consists of two disks with eight chambers each (eight small and eight large). The cathodes are segmented, one with the strips perpendicular and the other parallel to the wires. The cathode-anode spacing is equal to the anode wire pitch (2.54 mm) and the position of the track is then obtained by interpolation between the charges induced on neighbouring cathode strips. The read out pitch of 5.31 mm and 5.56 mm for the large and small chambers respectively in the bending direction allows to reach a 60 μm resolution for each CSC plane. In the non-bending direction the resolution

is 5 mm.

2.4.3 Resistive Plate Chambers

The Resistive Plate Chambers are gaseous detectors made of two resistive plates of phenoli-melaminic plastic laminate with a volume resistivity of 1010 Ω cm that are kept at an inter-distance of 2 mm by insulating spacers and with the outside surface coated with a thin layer of graphite paint to assure the HV and the ground connection of the resistive electrodes. In order to have a formation of an avalanche along the ionising track, an electric field of 4.9 kV /mm is applied. The signal produced is read out thanks to the capacitive coupling to copper strips that are mounted on the outer faces of the resistive plates. The RPCs are used in the barrel region $|\eta| \leq 1.05$ to provide the muon trigger and to measure the second coordinate in the non bending direction and they are arranged in three concentric cylindrical layers around the beam axis. The inter-distance between the middle and outer layers permits the trigger to select tracks with 9 GeV $< p_{\mathrm{T}} <$ 35 GeV while the two middle chambers provide the low-p_{T} trigger (6 GeV $< p_{\mathrm{T}} <$ 9 GeV). An RPC chamber is composed by two rectangular detector units that are contiguous to each other; each unit is then composed by two independent detector layers identical for all the RPCs.

2.4.4 Thin Gap Chambers

The Thin Gap Chambers are mounted in two concentric rings located in the endcap regions and covers the rapidity range between $1.05 \leq |\eta| \leq 2.0$. This detector provides the muon trigger capability in the endcap regions and the determination of the second, azimuthal coordinate to complement the measurement of the MDT in the bending (radial) direction. TGCs have a structure very similar to the one of the multiwire proportional chamber, with the difference that the anode wire pitch (1.8 mm) is larger than the anode-cathode distance (1.4 mm). The cathodic strips are separated from the gas volumes with graphite layers and have a pitch that goes from 14.6 and 49.1 mm with an orientation that is orthogonal to the anodic wires. The voltage working point of the TGC is 2.9 kV .

2.5 Forward detectors

Three smaller detector systems cover the ATLAS forward region. The main function of the first two systems is to determine the luminosity delivered

to ATLAS. At 17 m from the interaction point lies LUCID (LUminosity measurement using Cherenkov Integrating Detector). It detects inelastic pp scattering in the forward direction, and is the main online relative-luminosity monitor for ATLAS. The second detector is ALFA (Absolute Luminosity For ATLAS), used during special physics runs. Located at 240 m, it consists of scintillating fibre trackers located inside Roman pots which are designed to approach as close as 1 mm to the beam. The third system is the Zero-Degree Calorimeter (ZDC), which plays a key role in determining the centrality of heavy-ion collisions, in those special runs. It is located at 140 m from the interaction point, just beyond the point where the common straight-section vacuum-pipe divides back into two independent beam-pipes. The ZDC modules consist of layers of alternating quartz rods and tungsten plates which will measure neutral particles at pseudorapidities $\eta \geq 8.2$.

2.6 Trigger System

At the high luminosity provided by the LHC, the ATLAS trigger system is an important component of the experiment. With a bunch spacing of 25 ns, the detector generates a data rate of 40 MHz ($\sim$ 40 GB/sec), the trigger system decides in real-time, whether to record or reject the data from a collision, decreasing the recording rate to $\sim$ 1 kHz. In Run-1, the ATLAS Trigger system was composed of three levels: the Level-1 trigger (L1) which is hardware-based, Level-2 (L2) and Event Filter (EF) which are implemented in software [47]. These software trigger levels were replaced for Run-2 by a single High-Level-Trigger (HLT) [48].

2.6.1 L1 trigger

L1 is built with fast custom electronics in order to get a latency of less than 2.5 μs after bunch crossing, reducing the rate to a maximum of 100 kHz. From the information of the calorimeters and muons tracks, L1 identifies physics objects and classifies them as: jet, electron/photon, muon and missing transverse energy (E_{T}^{miss}). Geometrical areas in the detector in which the presence or multiplicity of certain signals are flagged as Regions Of Interest (ROI) are processed in the next trigger level.

2.6.2 HLT

The HLT is a computing system connected by fast dedicated networks. Sophisticated selection algorithms are applied to the ROIs, or to the full-event

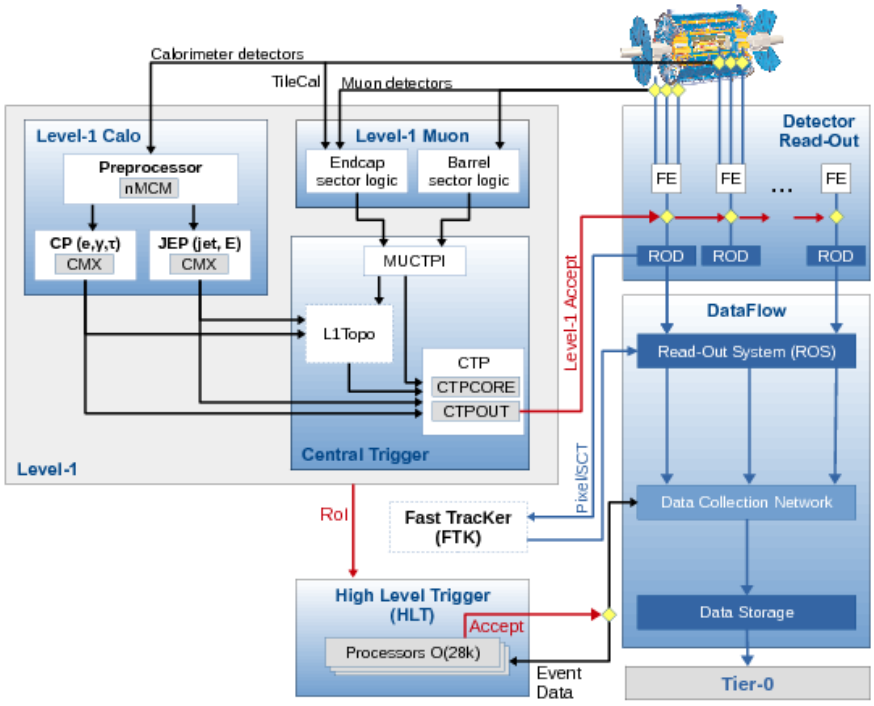

Figure 2.11: The ATLAS TDAQ system in Run 2.

information, within an average processing time of 200 ms. The output rate is reduced in the HLT from 100 kHz to an output rate of approximately 1 kHz. All events passing the HLT selection are written to disks.

2.7 Data acquisition system

The Trigger and Data Acquisition (TDAQ) system architecture is shown in Figure 2.11. The L1 trigger decision is formed by the Central Trigger Processor (CTP), which retrieves inputs from the L1 calorimeter (L1Calo) and L1 muon (L1Muon) triggers, as well as several other subsystems such as the Minimum Bias Trigger Scintillators (MBTS), LUCID and ZDC. The CTP limits the minimum time between two consecutive L1 accepts (simple dead-time) to avoid overlapping between readout windows, and restricts the number of L1 accepts allowed in a given number of bunch-crossing (complex dead-time) to avoid front-end buffers from overflowing. In the 2015 running period, the simple dead-time was set to 4 bunch-crossings (100 ns). After the L1 acceptance, the events are buffered in the Read-Out System (ROS) and processed by the HLT The HLT receives the ROI informations which can be

used for regional reconstruction in the trigger algorithms. After the events are accepted by the HLT, they are transferred to local storage at the experimental site and exported to the Tier-0 facility at CERN's computing centre for offline reconstruction. The DCS (Detector Control System) permits the coherent and safe operation of the ATLAS detector hardware, and serves as a homogeneous interface to all sub-detectors and to the technical infrastructure of the experiment. It controls, continuously monitors and archives the operational parameters, signals any abnormal behaviour to the operator, and allows automatic or manual corrective actions to be taken. Typical examples are high and low-voltage systems for detector and electronics, gas and cooling systems, magnetic field, temperatures, and humidity. The DCS enables bi-directional comunication with the data acquisition system in order to synchronise the state of the detector with the data-taking. It also handles the communication between the sub-detectors and other systems which are controlled independently, such as the LHC accelerator, the CERN technical services, the ATLAS magnets, and the detector safety system.

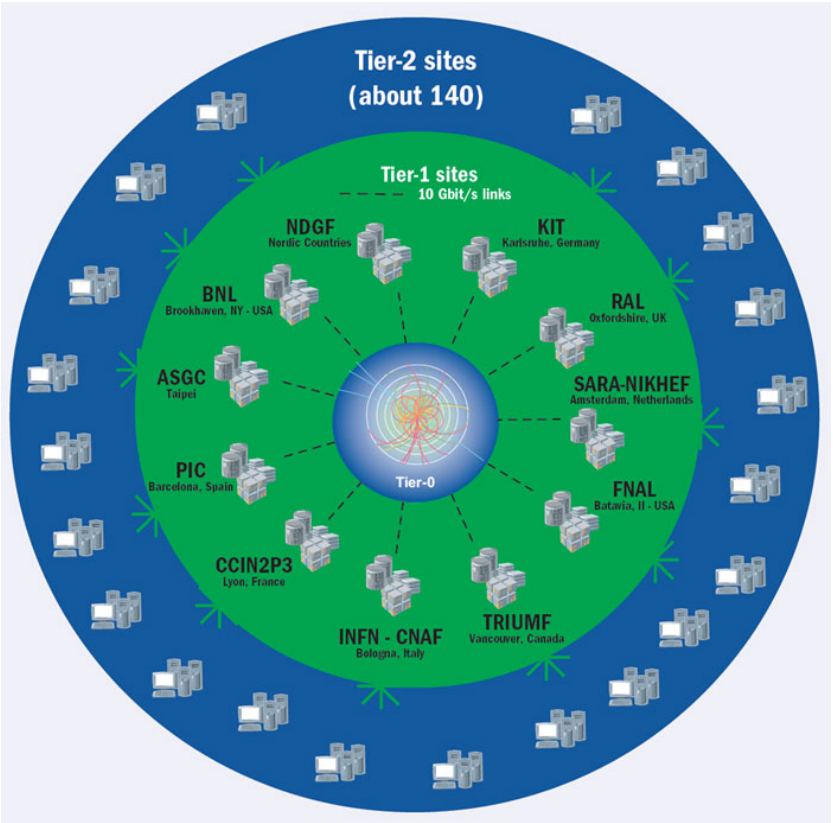

Figure 2.12: Structure of the ATLAS Tiers in 2014.

2.8 The ATLAS Computing Model

The ATLAS Computing Model [49] is based on the Grid [50] paradigm and on a high degree of decentralization and sharing of computing resources: off-site facilities are vital to the operation of ATLAS in a way that was not the case for previous CERN-based experiments. The CERN Tier-0 [51] facility is the place where the primary event processing occurs. The RAW data are archived at CERN and copied to the Tier-1 facilities around the world. The Tier-1 provides also the reprocessing capacity, the access to the data in various processed versions, and allows scheduled analysis of the processed data by physics analysis groups. Derived datasets produced by the physics groups are copied to the Tier-2 facilities for further analysis. The Tier-2 facilities also provide the simulation capacity for the experiment, with the simulated data housed at Tier-1s. In addition, Tier-2 centers will provide analysis facilities, and some will provide the capacity to produce calibration sets based on raw data processing. Additional computing resources will be available for data processing and analysis at Tier-3 centers and other computing facilities to which ATLAS may have access. The structure of the ATLAS Tiers is shown in Figure 2.12. A CERN Analysis Facility provides an additional analysis capacity, with an important role in the calibration and algorithmic development work.

Chapter 3

Monte Carlo simulations

The following aspects of Monte Carlo event generators are discussed in this chapter:

- elementary hard subprocess generation;
- initial and final state parton shower;
- electromagnetic final-state radiation;
- multiple scattering;
- hadronisation.

The simulation of direct and fragmentation prompt photon processes are also discussed.

3.1 Monte Carlo event generators

The interaction between the fundamental objects (quarks, leptons and gauge bosons) has a more complicated structure than expected. In fact one needs to introduce three main correction types:

- bremsstrahlung-type corrections;
- higher order corrections;
- quark and gluon confinement.

A Monte Carlo (MC) event generator simulates events aleatory weighted with a statistical distribution derived from the cross section of the simulated process. The goal is to generate events as detailed as could be observed

in a perfect detector. To handle the complex structure of the process, the simulation is not done in one step, but by a "factorization" of the entire process in a number of components, each one with a particular accuracy. The output of the simulation should be in the form of an event, with the same average behavior and the same fluctuations as the data. In data, fluctuations arise from the quantum mechanics character of the underlying theory, while MC techniques are used to select all the relevant variables according to the desired probability distributions. Some loss of information is inevitable, but this happens just for rare cases. The main differences between the various Monte Carlo generators are in the modelling of the initial and final state radiation, hadronisation and underlying event. MC simulation are extremelly useful for developing new analysis methods in absence of real data and to understand the feasibility of the proposed measurements. They are also useful to study the detector imperfections and to correct data and theoretical calculations to allow a comparison between them and the data. A proton-proton collision can be simulated following some general steps:

- PDF sets are used to simulate the incoming partons distributions from the proton beams. The PDFs are modelled according to the experimental data and input to the MC program;
- an incoming parton from the colliding protons enters the hard-scattering process. The hard-scattering is generated according to the matrix elements (ME);
- short lived particles produced in the hard scattering decay. The simulation of the decays is achieved by using experimental measurements of the width of these particles or on theoretical calculations;
- initial and final state radiation is calculated by branching the incoming and outgoing partons and included in the process;
- at this level, the event is made of partons and it is also called parton-level of the MC simulation. From the final state partons, the hadronisation process starts. This involves soft interactions that cannot be described by a perturbative approach and it needs a modellization;
- the interactions of the spectator partons from the incoming protons is calculated and included; also the remnant may have an internal structure and a net colour charge that is connected to the rest of the initial state. The resulting particles form what is known as the underlying event;

- additional interactions of pairs of protons in the crossing are taken into account. These interactions are generally soft but can generate extra hard events. This is also known as pileup. Pileup events are simulated using different pp collisions and then merged only at detector level to take out-of-time pileup into account;

- the short-lived particles decay into more stable particles. This stage is also knows as the hadron level or particle level of the simulation. Particle level usually does not include pileup events;

- the set of stable particles is provided as input to the detector simulation, including the modelling of the interaction of the particles with a magnetic field, with the detector matter and the response of each subdetector.

After this last step, a set of observables similar to those obtained in real collisions are produced and can be used in the analysis.

3.2 Comparison between different MC generators

The implementation of each step described in the previous section can be made in different ways for each MC generator. Sometimes multiple programs are combined to generate events, each taking care of some part of the simulation.

3.2.1 Hard scattering

Theoretical calculations of the hard scattering lie at the start of any MC generator. Once the interacting parton has been chosen from the PDF, the characteristic of the hard scattering needs to be generated. This includes the calculation of the matrix element and provides the initial configuration of the final state partons that will be used to generate the full simulation.

- in Pythia [52], only $2 \to 2$ or $2 \to 1$ processes are simulated. The ME are only LO;

- in Sherpa [53], $2 \to$ n matrix elements at tree levels are calculated. This means that Sherpa is capable of include additional partons to the final state directly in the matrix element calculation. Sherpa can also compute NLO matrix elements.

3.2.2 Initial and final state radiation

From the initial and final state particles obtained in the previous step, additional QCD and QED radiation is obtained by using the parton shower (PS) approach. In this approach, additional radiation is interpreted as a series of independent splitting processes such as: $q \to qg$ or $g \to gg$. The evolution of the PS is governed by the DGLAP equations, deciding when and how each splitting takes place. The evolution of the parton shower is characterized by a virtuality scale Q^2, which gives an approximate sense of time ordering to the cascade. Final state showers are time-like ($m^2 = E^2 - p^2 \geq 0$). Starting from some maximum scale Q^2_{max}, an original parton is evolved downwards in Q^2 until a branching occurs, distributing its energy among its daughters. The process of successive branchings is cut-off at some lower scale Q_0, typically arounf 1 GeV for QCD branchings. Initial state shower are space-like, which means that in the sequence of branchings that bring from the shower initiator to the hard interaction, particles have $m^2 = E^2 - p^2 < 0$. It is handled within the backwards evolution scheme which starts from the two incoming partons at the hard interaction, where showers are traced in descending values of Q^2. In this approach, the choice of of the hard scattering is based on the use of evolved parton distributions, which means that the inclusive effects of initial state radiation are already included. The implementation of the PS in the MC generators differ mainly on the choice of the evolution scale Q^2:

- in PYTHIA the evolution scale is defined as $Q^2 = p_{\mathrm{T}}^2 = z(1-z^2)m^2$ for final state radiation, where z describes the fraction of the original energy taken by one of the daughters. This gives rise to p_{T} ordered branchings. In QCD showers, corrections to the leading-log picture, called coherence effects, lead to an ordering of subsequent emissions in terms of increasing angles. The p_{T} ordered shower automatically leads to the correct angular ordering;

- in SHERPA, the evolution scale is defined as $Q^2 = p^2 - m^2$. Color coherence during evolution is taken into account by an explicit angular veto, which means that a branching is rejected if the opening angle of the emission is larger than the one of the previous branching.

3.2.3 Matching between matrix element and parton shower

Using ME and PS at the same time is necessary to avoid the double counting. This may arise if a specific configuration has been generated first in the matrix element and then in the parton shower approach. A matching scheme defines, on an event-by-event basis, which of the two paths should be followed

according to the kinematics. Althought they are implemented in different ways, all matching schemes of LO MC programs follow a common strategy:

- a jet observable is defined and all relevant cross sections for the processes to be generated with additional n-jets in the final state are evaluated;
- hard parton samples are produced with a probability proportional to the respective cross section, in a corresponding kinematic configuration following the matrix element;
- the individual configurations are accepted or rejected with a dynamical, kinematics-dependent probability. In case the event is rejected, the previous step is repeated, possibly with a new number of jets;
- the PS is invoked with suitable initial conditions. In all cases, the parton shower is constrained not to produce any extra jets, so the configurations that would fall into the realm of matrix elements with higher jet multiplicity are vetoed in the parton shower step.

3.2.4 Hadronisation

The hadronisation, in which colourless hadrons are constructed from the coloured final state particles exiting from the parton shower, is based on the Lund string model [54] in the case of PYTHIA and on the cluster model [55] in the case of SHERPA:

- Lund model: it is a model based on the idea that the long distance QCD interaction can be described by colour strings. These strings connect the partons and lead the exchange of momenta between them. They also can be fragmented and gain energy as the parton gets separated. This fragmentation is the source of new partons that at the end of the process couple with the primary ones to create hadrons. The four-momentum of the hadrons is calculated using information both from the final parton and the connecting strings.
- Cluster model: This model is based on the preconfinement property of QCD. After the perturbative parton showering, all outgoing gluons are split non-perturbatively into light quark-antiquark or diquark-antidiquark pairs. At this point the event consists of a set of outgoing quarks and antiquarks. In the limit of a large number of colours, each final state colour line can be followed from a quark/antidiquark to an antiquark/diquark with which it can form a colour singlet cluster. By

virtue of pre-confinement, these clusters have a distribution of mass and spatial size that peaks at low values, falls rapidly for large cluster masses and sizes, and is asymptotically independent of the hard subprocess type and scale. The clusters thus formed are fragmented into hadrons: if a cluster is too light to decay into two hadrons, it is taken to represent the lightest single hadron of its flavour and its mass is shifted to the appropriate value by an exchange of 4-momentum between the neighbouring clusters.

3.2.5 Underlying event

The underlying event is modelled by the introduction of Multiple Parton Interactions (MPI). Additional interactions are considered between the spectator partons of the hard process. The basic idea of such model is to postulate the probability distribution of multiple scatterings.

3.3 MC samples for photon + jet production

The MC programs Pythia 8.186 [56] and Sherpa 2.1.1 [53] were used to generate the simulated events to study the characteristics of the $\gamma + jet$ production. These samples were also used to determine the correction factors necessary to obtain the particle-level cross sections and to estimate hadronisation corrections to the NLO QCD calculations. In both generators, the partonic processes are simulated using LO matrix elements, with the inclusion of initial and final state parton showers. Fragmentation into hadrons was performed using the Lund string model in the case of Pythia and a modified version of the cluster model for Sherpa. The LO NNPDF2.3 [57] (for Pythia) and the NLO CT10 [58] (for Sherpa) parton distribution functions were used to parametrize the proton structure. Both samples include a simulation of the underlying event. The event generator parameters were set according to the "A14" tune for Pythia and the "CT10" tune for Sherpa. All the samples of generated events were passed through the Geant-4 based [59] ATLAS detector and trigger simulation programs [60]. They were reconstructed and analyzed by the same program chain as the data. The Pythia simulation of the signal includes LO photon plus jet events from both direct processes (called the hard component) and photon bremsstrahlung in QCD dijet events (called the brem component). The Sherpa samples were generated with tree level matrix elements for photon plus jet final states with up to four additional partons, supplemented with the parton showers. The brem component is simulated differently in Pythia and Sherpa. In

PYTHIA, photons can be radiated in the PS without any restrinction on the opening angle with respect to the parent parton ans, as a result, the photon can be emitted very close to the parton direction. In SHERPA, photons are not emitted in the parton shower and the brem component is simulated through matrix elements of $2 \to N$ processes, with $N \geq 3$. In this way the collinear singularities are avoided by restricting the emission through an implementation of the Frixione's criterium [61]. This criterium requires the total transverse energy inside a cone of radius υ around the generated final-state photon, excluding the photon itself, to be below a certain threshold, $E_{\mathrm{T}}^{\mathrm{max}}(\upsilon) = \epsilon E_{\mathrm{T}}^{\gamma}((1-\cos\upsilon)/(1-\cos R))^{n}$, for all $\upsilon < R$. The parameters for the threshold were chosen to be $R = 0.3$, n=2 and $\epsilon = 0.025$. As a result, photons are not emitted close to the parent parton, This requirement on the photon isolation at ME level for $\upsilon = R = 0.3$ results in $E_{\mathrm{T}}^{max}(0.3) = 0.025{\cdot}E_{\mathrm{T}}^{\gamma}$. The measured distributions are unfolded to a phase-space region in which the photon is required to be $E_{\mathrm{T,part}}^{\mathrm{iso}} < 4.2 \cdot 10^{-3} \cdot E_{\mathrm{T}}^{\gamma} + 10$ GeV. The Frixione's requirement is tighter than the isolation cut at particle level. Since the MC samples of events generated with PYTHIA include the contribution radiated off quarks without any restriction on the opening angle, those samples are used as the nominal ones. The generated samples were filtered before the full detector simulation was applied: the presence of a prompt photon with transverse energy in a given range was required at the particle level in order to have sufficient statistics over the entire spectrum in E_{T}^{γ}. The PYTHIA and SHERPA samples are listed in Figure 3.1. To combine these samples, one would weight the events by a factor A, different for each sample and defined as:

$$A = \frac{\sigma \times \epsilon^{\mathrm{eff}}}{N^{\mathrm{events}}} \tag{3.1}$$

where σ represents the sample cross section, ϵ^{eff} its filter efficiency and N^{events} is the total number of generated events for each sample.

Generator	Number of events	Cross section [nb]	E_{T}^{γ} range [GeV]	Filter (effic.)
PYTHIA	2885800	1.0621e+05	70 – 140	(3.9049e-05)
	996400	6.7046e+03	140 – 280	(4.8927e-05)
	967199	3.4426e+02	280 – 500	(5.6152e-05)
	994200	2.3729e+01	500 – 800	(5.2447e-05)
	92000	2.2869e+00	800 – 1000	(3.4994e-05)
	99500	7.0203e-01	1000 – 1500	(3.6900e-05)
	98300	3.9345e-02	1500 – 2000	(3.6688e-05)
	94700	3.3277e-03	2000 – 2500	(3.3896e-05)
	98300	3.2495e-04	2500 – 3000	(2.9921e-05)
SHERPA	1999200	3.129e+00	70 – 140	CVetoBVeto (0.3996)
	1997400	3.1329e+00	70 – 140	CFilterBVeto (0.48199)
	499400	3.1352e+00	70 – 140	BFilter (0.11728)
	9974800	2.4741e-01	140 – 280	CVetoBVeto (0.41049)
	1993200	2.4739e-01	140 – 280	CFilterBVeto (0.50284)
	997600	2.4937e-01	140 – 280	BFilter (0.12874)
	997200	1.3648e-02	280 – 500	CVetoBVeto (0.41834)
	500000	1.3617e-02	280 – 500	CFilterBVeto (0.47349)
	99800	1.3874e-02	280 – 500	BFilter (0.14069)
	200000	9.2334e-04	500 – 1000	CVetoBVeto (0.38226)
	100000	9.2185e-04	500 – 1000	CFilterBVeto (0.47148)
	20000	9.3819e-04	500 – 1000	BFilter (0.14811)
	100000	1.8432e-05	1000 – 2000	CVetoBVeto (0.37036)
	50000	1.8388e-05	1000 – 2000	CFilterBVeto (0.46691)
	10000	1.9046e-05	1000 – 2000	BFilter (0.15751)
	101000	7.9682e-08	2000 – 4000	CVetoBVeto (0.36729)
	50500	8.0331e-08	2000 – 4000	CFilterBVeto (0.46642)
	10600	8.2035e-08	2000 – 4000	BFilter (0.1692)
	1000	2.4843e-12	4000 – inf	CVetoBVeto (0.40351)
	800	2.5134e-12	4000 – inf	CFilterBVeto (0.41614)
	1000	2.5431e-12	4000 – inf	BFilter (0.14831)

Figure 3.1: PYTHIA and SHERPA signal MC samples. In the case of SHERPA, the following filters were applied: BFilter, which requires a B hadron, CFilterBVeto, which requires a C hadron and removes the overlap with the BFilter sample, and CVetoBVeto, which rejects events with a B or C hadron. These samples are non-overlapping.

Chapter 4

Photon and jet reconstruction and identification

4.1 Photons in ATLAS

The electromagnetic calorimeter has been designed so that the energy of the electrons and photons is deposited in its cells (depicted in Figure 4.1). In fact both electrons and photons, when entering the calorimeter, produce electromagnetic showers that form electromagnetic clusters. When electrons pass through the inner detector, they leave a track, bent by the magnetic field of the solenoid magnet. On the other hand, photons do not interact in the tracker, but when they traverse the Inner Detector material, there is a certain probability for them to convert into an electron-positron pair. The conversion may happen anywhere before the calorimeter and a conversion vertex may be or not reconstructed. The photon reconstruction combines the informations coming from the calorimeter layers (including the presampler) and the inner detector, in order to distinguish between electrons, converted and unconverted photons. The method used to reconstruct, identify and calibrate the photons is summarized in the following subsections.

4.1.1 Photon reconstruction

The electromagnetic shower, originating from an energetic interaction of a photon with the electromagnetic calorimeter, deposits a significant amount of energy in a small number of neighbouring calorimeter cells. As photons and electrons have very similar signatures in the calorimeter, their reconstruction proceeds in parallel. A full description of the photon reconstruction can be found in [62]. The reconstruction of unconverted and converted photons proceeds in the following way:

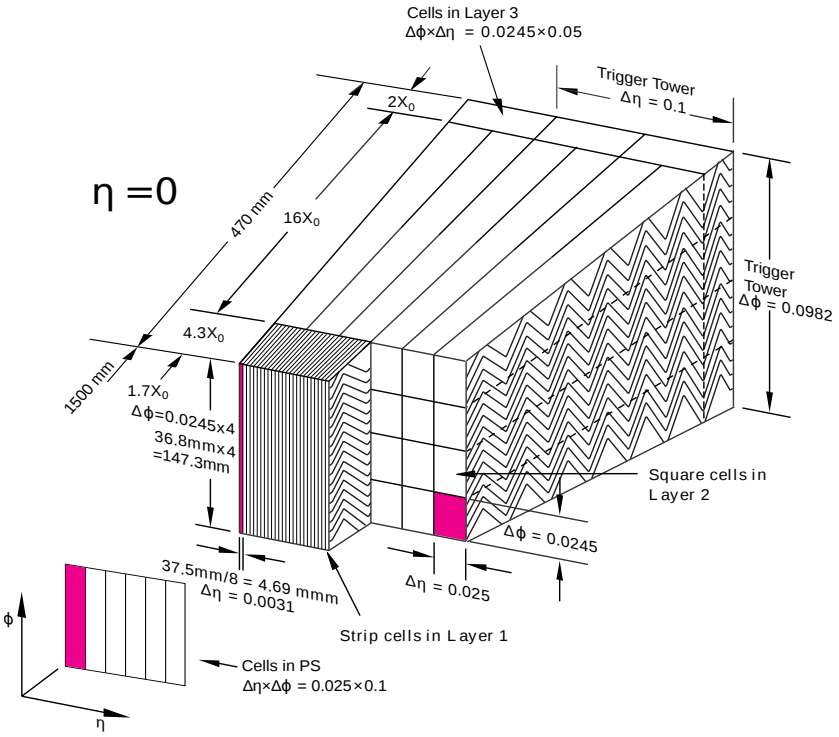

Figure 4.1: A view of a barrel module (at $\eta = 0$) af the ATLAS electromagnetic calorimeter

- Search for seed cluster of EM cells;
- Reconstruct tracks in the ID which are loosely matched to the seed clusters;
- Use those tracks, consistent with originating from a photon conversion, to create conversion vertex candidates;
- Match the conversion vertex candidates to the seed clusters;
- Identify the seed cluster as electron, converted or unconverted photon candidates.

In the following, each reconstruction step is described in detail.

Seed cluster reconstruction: The reconstruction of a photon candidate, in the rapidity region $|\eta^{\gamma}| < 2.5$, begins with the creation of a preliminary set of seed clusters of electromagnetic calorimeter cells. A sliding-window algorithm [63] scans the calorimeter looking for seed clusters with transverse

momentum larger than 2.5 GeV, measured in projective towers with the size of $\Delta\eta \times \Delta\phi = 0.075 \times 0.123$. After an energy comparison, duplicated clusters of lower energy are removed from nearby seed clusters. From MC simulations, the efficiency of the initial cluster reconstruction is estimated to be 95% at $E_{\mathrm{T}} = 7$ GeV to more than 99% above $E_{\mathrm{T}} = 15$ GeV.

Track reconstruction: Once the seed clusters are reconstructed, inner detector tracks that are loosely matched to the clusters are searched [64], with the purpose of identify and reconstruct electron and photons that may come from conversion. Track reconstruction has two sub-steps: pattern recognition and track fit. The pattern recognition uses the pion hypothesis for energy loss due to interactions with the detector material, complemented with a modified pattern recognition algorithm that takes into account energy loss for possible bremsstrahlung. If a track seed, consisting of three hits in different layers of the silicon detectors (Pixel and SCT), with a transverse momentum larger than 1 GeV can not be successfully extended to a full track and it falls within one of the EM cluster RoI, a second attempt is performed using another pattern recognition with the electron hypothesis that allows for larger energy loss. Track candidates are then fitted using the ATLAS Global χ^2 Track Fitter [65, 66] either with the pion hypothesis or the electron hypothesis.

Track conversion: The selected tracks that may come from a photon conversion, are used to create the conversion vertex candidates. In case of "double track", conversion vertex candidates are reconstructed from pairs of opposite charged tracks in the ID that are likely to be electrons. The likelihood to be an electron for each track, is required to be at least 10 % (80 %) for tracks with (without) hits in the silicon detectors. Since the tracks of a photon conversion are parallel at the conversion vertex, some geometric requirements are used to constraint the track pairs. Three categories of track pairs are selected, whether both tracks (Si-Si), none (TRT-TRT) or only one of them (Si-TRT) have hits in the silicon detectors. The conversion vertex is found after the use of a constrained fit with three degrees of freedom. The fit is performed using the five measured helix parameters of each of the two involved tracks with the constraint that they are parallel at the vertex. In the case of "single track conversion", tracks without hits in the b-layer that either have an electron likelihood greater than 95 %, or have no hits in the TRT, are considered as single-track' conversion vertex candidates. Since it is not possible to perform the fit this time, the conversion vertex is defined to be the location of the first measurement of the track. Those tracks which pass

through an inactive region of the b-layer are not considered as single-tack conversion, unless they are missing a hit in the second pixel layer.

Track-cluster matching: The matching of the conversion vertex candidated to the clusters relies on an extrapolation of the conversion candidates to the second sampling layer of the calorimeter, and the comparison of the extrapolated coordinates to those of the cluster center (ΔR). The extrapolation method depends on the type of the conversion vertex candidates. In the case of double-track conversion vertex candidates for which the track transverse momenta differ by less than a factor of four from each other, each track is extrapolated to the second sampling layer of the calorimeter and is required to be matched to the cluster. If the difference in p_{T} is more than a factor four, the photon direction is reconstructed from the electron and positron directions determined by the conversion vertex fit. For single-track conversion vertex candidates, the track is extrapolated from its last measurement. Conversion vertex candidates built from tracks with hits in the silicon detectors are considered matched to a cluster if the angular distance between the extrapolated tracks and the cluster center is smaller than 0.05 in both η and ϕ. If the extrapolation is performed for single-track conversions, the window in ϕ is increased to 0.1 in the direction of the bending. In case of tracks without hits in the silicon detectors, the matching requirements are tighter regarding distance in ϕ (0.02/0.03), but looser in η (0.2/0.35) since the TRT does not provide a measurement of the pseudorapidity. In case of multiple conversion vertex candidates matched to the same cluster, the preference is given to double-track candidates over single-track candidates. Furthermore preference is given to the candidate with more tracks with hits in the silicon detectors and with smaller ΔR between the cluster and the track.

Cluster identification: The final arbitration between the electron, converted and unconverted photon hypotesis for the reconstructed EM clusters is performed as in Reference [70], however the procedure was slightly changed in Run-2:

- The candidate is flagged as a photon if no track with at least 4 silicon detector hits is matched to the cluster or a conversion vertex is found in the silicon detector and the electron track is part of the vertex and has no pixel detector hits;
- The candidate is flagged as an electron if no conversion vertex or a track with an innermost pixel detector hit are matched (or at least 2 pixel detector hits if the innermost layer is not expected) to the cluster and no conversion vertex in the silicon detector is found;

- The candidate is considered ambiguous otherwise and also if E(cluster)/P(track) $>$ 10 GeV or track-$p_{\mathrm{T}} < 2$ GeV or if the matched track has no pixel hits.

Studies on MC simulations on Run-1 showed that 96 % of true photons with $E_{\mathrm{T}} > 25$ GeV are expected to be reconstructed as photon candidates, while the remaining 4% are incorrectly reconstructed as electrons but not as photons. The efficiency to reconstruct photon conversions decreases at high E_{T}, where it becomes more difficult to separate the two tracks from the conversions. Such conversions with very close-by tracks are often not recovered as single-track conversion because of the tighter selections, including the transition radiation requirement, applied to single-track conversion candidates. After the changes introduced in Run-2 the performance has slightly improved; contamination between electrons and photons is reduced and converted/unconverted photons separation is slightly better. The final photon energy measurement is performed using information from the calorimeter, with a cluster size that depends on the photon classification. In the barrel, a cluster of size $\Delta\eta \times \Delta\phi = 0.075 \times 0.172$ is used for both converted and unconverted photon candidates. In the end-cap, a cluster size $\Delta\eta \times \Delta\phi = 0.125 \times 0.123$ is used for all the candidates.

4.1.2 Photon calibration

The calibration of the measured energy of electrons and photons is fundamental for many physics measurements [67]. A multivariate (MVA) regression algorithm, based on simulations, calibrates the energy of electromagnetic particles, correcting for the deposited energy in front of the calorimeter, the longitudinal and lateral leakage and for other local effects. Furthermore, in order to account for any residual disagreement between data and simulation, the energy scale of electrons is extracted using $Z \to ee$ events through an in-situ procedure. A fundamental rule for the whole calibration chain is that the detector geometry and the model of particle interaction with matter are accurately handled by the simulation. The whole procedure is described in the following sections.

Detector non-uniformity corrections

Data are corrected for the measured time-dependent defects in specific detector regions. These corrections typically take into account non-nominal high-voltage regions or geometric effects not perfectly simulated. These cor-

rections are needed because in a few sectors of the EM calorimeter, the high-voltage is set to a non-nominal value due to short circuits present in specific LAr electrods. Another correction is associated with the different gains of calorimeter cells readout (high, medium and low), since in the $Z \to ee$ events used to calculate the in-situ correction electrons have mostly cells in high gain. For more energetic objects with calorimeter cells in medium or low gain, an additional correction is applied.

Layer intercalibration

Further corrections are needed in data to adjust residual effects not perfectly accounted by the simulations. The intercalibration of the first and second calorimeter layers (E_1/E_2) uses muons from $Z \to \mu\mu$ decays as probes, since muon energy deposits in the calorimeter are insensitive to the amount of passive material upstream of the EM calorimeter and constitue a direct probe of the energy response. Denoting $< E_{1/2} >$ the ratio of the deposited energies in L1 and L2, the intercalibration result is defined as $\alpha_{1/2} =< E_{1/2} >^{data} / < E_{1/2} >^{MC}$. The L1/L2 calibration bias $\alpha_{1/2}$ is removed by applying an $|\eta|$-dependent correction to data to the energy measured in L2 ($E_2^{corr} = E_2 \times \alpha_{1/2}$). These coefficients are verified by a study of the electron energy response with $Z \to ee$ events. The determination of the pre-sampler (PS) energy scale exploits the PS energy distributions of electrons in data and simulation. This is done after taking into account the possible mis-modeling of the upstream passive material calculated with a set of detector material variations in the simulation. It is estimated using electrons from W and Z decays. This is addressed by exploiting the expected correlation between $E_{1/2}$ and the PS energy (E_0) for electrons, at a given η value, under variations of the passive material upstream of the PS. A second correction to the PS energy scale, that takes into account the mis-modeling of the material between the PS and L1, is evaluated using converted photons. No dedicated intercalibration of the third EM longitudinal layer is carried out, as its contribution should be negligible in the energy range covered by the present calibration.

MVA calibration

The core of the procedure is based on the optimizaton of the energy calibration using multivariate techniques on large samples of single particle Monte Carlo simulation. The exploited regression MVA technique is based on a boosted decision tree with gradient boosting. With this procedure the EM clusters are calibrated to the original electron and photon energy in the sim-

ulated MC samples. The calibration coefficients are calculated separately for electrons, converted and unconverted photons. The quantities used in this process are the total energy measured (E_{acc}), the ratio of the pre-sampler layer energy to the calorimeter energy (E_0/E_{acc}), the energy measured in the first two layers of the calorimeter (E_1/E_2), the cluster barycenter pseudorapidity in the ATLAS coordinate system (η_{cluster}) and the cluster barycenter in η and ϕ within the $\eta \times \phi$ cells. The variable η_{cluster} is included since it is correlated with the passive-material variations in front of the calorimeter. The inclusion of the barycenter location in the $\eta \times \phi$ is important to accurately correct particles that hit the cell close to the edge. For converted photons, the radius of conversion R_{conv} is used as an additional input to the MVA only if the p_{T} is above 3 GeV. For conversions with both tracks containing at least one hit in one of the silicon detectors, further quantities are considered: the ratio of the transverse momenta of the converted tracks to E_{calo} and the fraction of the conversion momentum carried by the highest-p_{T} track, $p_{\text{T}}^{\text{max}}/p_{\text{T}}^{\text{conv}}$. The MVA algorithm is optimized in different regions of the phase space, the sample is divided into bins of η_{cluster}, $E_{\text{T}}^{\text{acc}}$ and according to the particle type. The binning is chosen to follow the known detector geometry variations. The calibration covers the rapidity region up to 2.5, including the transition region between the barrel and the end-cap (crack) of the electromagnetic calorimeter. In the crack region, the amount of material traversed before reaching the first active layer of the calorimeter is quite high and the resolution is very degraded.

In-situ corrections

After the application of the corrections for the non-uniformity of the detector response and of the simulation-based calibration, a residual disagreement in the energy scale and resolution may appear between data and simulation. In order to correct this residual mismatch, a correction evaluated with an in-situ procedure is applied. The energy miscalibration is defined as the difference in response between data and simulation, and is parametrized as:

$$E_i^{data} = E_i^{MC}(1 + \alpha_i) \tag{4.1}$$

where E_i^{data} and E_i^{MC} are the electron energies in data and simulation respectively, and α_i represents the deviation from optimal calibration, in the rapidity region i. The difference in energy resolution between data and simulation, which does not depend on the energy (at first order), can be modelled by an additional effective constant term ($c_i^{'}$) for a given pseudorapidity region:

$$\left(\frac{\sigma(E)}{E}\right)_i^{data} = \left(\frac{\sigma(E)}{E}\right)_i^{MC} \oplus c_i^{'} \tag{4.2}$$

Using $Z \rightarrow ee$ events selected in the 2015 data sample, the energy scale corrections (α_i) and additional constant terms for the energy resolution ($c_i^{'}$) have been estimated. The measured values are reported in Figure 4.2, along with the total systematic uncertainty of the in-situ calibration procedure. These corrections are applied both to electrons and photons.

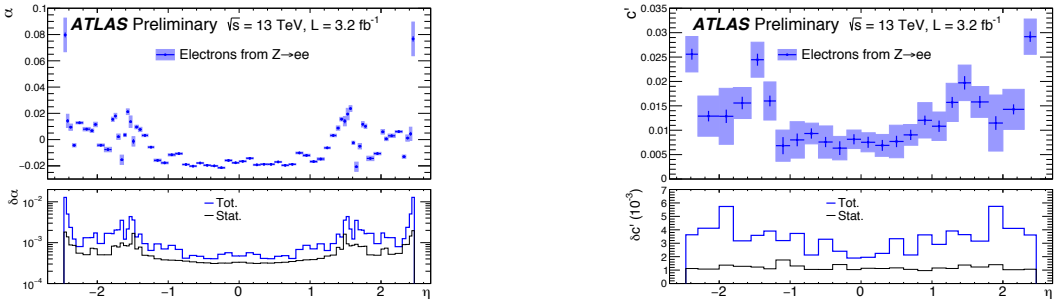

Figure 4.2: (Left) Energy scale factor α and (Right) additional constant term $c^{'}$ for energy resolution from $Z \rightarrow ee$ events as a function of η. The uncertainty bands on the top plots represent the total uncertainties on these quantities, while the thin black (resp. thick blue) lines at the bottom represent the statistical (resp. total) uncertainties.

$Z \rightarrow ee$ calibration applied to high energy electrons and photons

The corrections explained in the previous section are expected to be valid for electrons coming from the Z decay, then one can assume that the scale is the same for the photons. The universality of the corrections is tested using photons from radiative Z decays in the electron and muon channels. Residual miscalibrations between data and simulation are parametrized as $E_i^{data} = (1 + \delta\alpha_i) \cdot E_i^{MC}$ following a similar procedure to the one applied to the electrons from Z decays, described in the in-situ corrections section.

Systematic uncertainties on the e/γ calibration

This section resumes the sources of systematic uncertainty for e/γ calibration.

- **Presampler**: uncertainty on the energy scale of the thin PS layer;
- **Layer intercalibration**: uncertainty on the scale factors $\alpha_{1/2}$, used to intercalibrate the first two layers of the electromagnetic calorimeter as a function of η. The values of $\alpha_{1/2}$ have been checked using the 2015 dataset, and found to be in good agreement with the measurement

using the Run-1 dataset. An additional systematic uncertainty equal to the maximum observed discrepancy ($\sim 1.5\%$) has been included in the uncertainty model. A further uncertainty, relative to the muon to electron extrapolation, is taken into account;

- **Layer 2 gain**: the dependence of the energy response from the gain used in the readout chain and its relative uncertainty is taken into account;

- **Material**: the uncertainties relative to the description of the material before the calorimeter for $|\eta| < 2.5$. This is evaluated using distorted material geometry samples;

- **In-situ calibration**: the uncertainty on the scale and additional constant term due to the selection criteria for the candidate electrons and on the strategies for the extraction of α_i and $ci^{'}$ parameters, are evaluated;

- **Pedestal**: small baseline shifts were observed in data and an effect coming from the pedestal determination in electronics calibration. Data is corrected as a function of the bunch train position, given the high luminosity in Run-2 this systematic uncertainty is estimated to be $\pm$ 20 MeV;

- **Pileup and temperature**: the in-situ calibration procedure accounts for possible differences in pileup and temperature conditions between data and simulation for 2015 data;

- **Tile scintillators**: 4 independent sources of uncertainty on the response of the scintillators in the crack region have been considered: data-simulation difference evaluated as the difference in the mean of the energy in the scintillators in $Z \to ee$ events (between 1% and 4.3%, depending on η). Uncertainty on the electromagnetic scale calibration factor that converts the Tile Calorimeter signals to the energy deposited by electrons (spread of 2.4%). Initial intercalibration using the Minimum Bias (MB) system3: 1%. Uncertainty of the calibration using laser over the whole year: 4%.

The main sources of uncertainty on the energy scale and the ones that have been updated in Run-2 are reported in [68] for $|\eta| < 0.6$ and 5 GeV$< E_{\mathrm{T}} <$ 1 TeV for electrons, unconverted and converted photons. It can be seen that the systematics are low in the region near $m_Z \sim 91$ GeV (where the scale is measured from $Z \to ee$) and increase at lower and higher energies. The

values of most of the systematic uncertainties have been taken from Run-1 results.

4.1.3 Photon isolation

The isolation of a reconstructed object describes the amount of activity in the area around the object that does not come from the object itself. In the photon case, it can be used as a discriminating variable to reject the jet background. The isolation is computed both in the calorimeter, using the deposited energy in its cells, and in the inner detector, reconstructing the tranverse momentum of each track. Additional corrections are applied to this variable in order to correct for energy leakage of the object in the isolation cone and for pileup. Both track and calorimeter isolations are computed into a cone of radius $R = 0.X$, with X equal to 2, 3, and 4. Smaller cones are usually chosen to reduce the dependence of the pileup and to reduce inefficiencies in busy environments such as those occurring from $t\bar{t}H$ production. While larger cones (0.4) are optimized for tight and high pt photons. The evaluation of different kinds of isolation and the relative corrections is discussed in the following.

Track isolation

The track isolation is computed by summing the tranverse momenta of the ID reconstructed tracks which fall into a cone centred around the lepton/photon direction. A first track selection is applied before summing the p_{T} of the tracks, as shown in Table 4.1. The first five lines correspond to the "Loose" track selection, while the last two cuts are introduced to maximise the fake lepton background (p_{T} cut) and to minimize the pileup dependence of the track isolation ($|z_0 \sin\theta|$ cut). This variable is quite pileup robust for electrons due to the impact parameter cuts, which constrain the tracks to come from the same vertex associated to the electron. The subtraction of the electron/photon energy from the track isolation is performed removing the e/γ associated tracks. However, since electrons can emit bremsstrahlung radiation and photons can convert into secondary electrons, their energy deposit should be considered for the first isolation count. To this purpose, the tracks are extrapolated to the middle layer of the calorimeter, and all those that fall into a $\Delta\eta \times \Delta\phi = 0.005 \times 0.1$ window around the electron cluster position, are considered as part of the electron/photon.

Criterium	Cut value
$\|\eta\|$	< 2.5
N_{Si}	≥ 7
$N_{\mathrm{mod}}^{\mathrm{sh}}$	≤ 1
$N_{\mathrm{Si}}^{\mathrm{hole}}$	≤ 2
$N_{\mathrm{Pix}}^{\mathrm{hole}}$	≤ 1
p_{T}	> 1 GeV
$z_0 \sin\theta$	< 3 mm

Table 4.1: Selection for the track isolation. N_{Si} is the number of hits in the silicon detectors; $N_{\mathrm{mod}}^{\mathrm{sh}}$ is the number of shared modules (the sum of the pixel and SCT shared hits); $N_{\mathrm{Si}}^{\mathrm{hole}}$ is the number of silicon holes (missing hits in the silicon detectors); $N_{\mathrm{Pix}}^{\mathrm{hole}}$ is the number of pixel holes; z_0 is the difference of longitudinal impact parameter of the track, and the position of a given vertex.

Calorimetric isolation

The TopoCluster based isolation, called **TopoEtCone**, is computed as the sum of topological cluster transverse energies within a cone. The electron and photon directions are given by the position of the associated rectangular calorimeter cluster used to reconstruct the electron/photon energy. TopoClusters are seeded by cells with an energy more than four time above the noise threshold of that cell. The clusters are then expanded by adding neighboring cells that have an energy more than two times above the noise level. Neighboring cells are considered in the three spacial directions and across all calorimeter layers, excluding the cells from the Tile gap scintillators. All clusters within the cone are summed but only positive energy topoclusters are used. Those used in the isolation computation are not further re-calibrated, but they are simply calibrated at the electromagnetic scale. All positive energy topological clusters whose barycenter falls within a cone centered around the electron/photon direction are summed into what is called the raw TopoEtCone isolation $E_{\mathrm{T,raw}}^{\mathrm{iso}}$. The isolation energy defined as the sum of all the topo clusters still includes the electron/photon energy called the core energy ($E_{\mathrm{T,core}}$). This quantity needs to be substracted from the raw isolation in order to get the real isolation variable. For electrons and photons the 5×7 core subtraction method is used. In this technique, adopted since Run-1, the cells included in a 5×7 rectangle around the electron/photon direction are simply removed from the isolation variable. The advantage of this simple method is to have a stable subtraction for real or fakes objects

for any transverse momentum and pileup. On the other hand, the technique does not completely remove the e/γ energy, so an additional leakage correction is needed. This leakage is evaluated using Monte Carlo samples of single electrons and photons without pileup and derived in 10 η bins, chosen to follow the material distribution in the EM calorimeter. Separate corrections are used for electrons, converted and unconverted photons. The isolation energy is fitted for each $|\eta|$ slice with a Crystal Ball (CB) function. The mean of the CB function corresponds to the energy leakage effect in the isolation cone and it is used as correction. Also a pileup and underlying event correction is needed to evaluate the value of $E_{\mathrm{T}}^{\mathrm{iso}}$. It is estimated using the ambient energy density technique, evaluated from the mean of the energy deposited in the calorimeter by non-hard events, following these steps:

- Positive energy topological clusters are reconstructed in the whole calorimeter acceptance using the $\mathrm{k_t}$ jet finding algorithm of radius 0.5, with no p_{T} threshold;
- The area A_i of each jet in the event is estimated from a Voronoi [69] tessellation algorithm;
- The energy density of each jet is computed as $\rho_i = p_{T,i}/A_i$;
- The median of the distribution of all the energy densities in the event, ρ_{median}, is used as an estimator of the energy density of the event.

The pileup correction is then evaluated as:

$$E_{\mathrm{T,pileup}}(\eta) = \rho_{median}(\eta) \times (\pi R^2 - A_{\mathrm{core}}) \tag{4.3}$$

where R is the radius of the isolation cone and A_{core} is the area of the 5×7 core that was subtracted. The fully corrected isolation is computed as the sum of the topoclusters, subtracking the central core of the object, the leakage and the pileup corrections.

$$E_{\mathrm{T,corr}}^{\mathrm{iso}} = E_{\mathrm{T,raw}}^{\mathrm{iso}} - E_{\mathrm{T,core}} - E_{\mathrm{T,leakage}} - E_{\mathrm{T,pileup}} \tag{4.4}$$

4.1.4 Photon identification

After the reconstruction, not all of the candidates are real prompt photons, but some fake photons may come from hadronic decays or to hadrons wrongly identified as photons. In order to separate the real from the fakes, a careful photon candidates identification is necessary. Real photons typically produce narrow energy deposits in the electromagnetic calorimeter and a minimal

leakage in the hadronic calorimeter, while fake photons are accompanied by a sizable surrounding of hadronic activity. In addition, the decays of neutral mesons into a photon pair, such as $\pi^0 \to \gamma\gamma$, are often misidentified due to the small separation between the photon pair. Photon identification (γ_{ID}) in ATLAS is based on a set of cuts on several discriminating variables (DVs). Such variables describe lateral and longitudinal shower shapes in the EM calorimeter and the shower leakage fraction in the hadronic calorimeter. Through those discriminating variables it is possible to define two levels of γ_{ID}, "*loose*" and "*tight*". The *loose* identification level exploits the DVs only in the hadronic calorimeter and the second sampling layer of the electromagnetic calorimeter, providing an highly efficient selection with fair fake rejection and it is typically used for trigger level analysis and for background studies. The *tight* identification level exploits the full granularity of the electromagnetic calorimeter, including the fine segmentation of the first sampling layer, and applies tighter requirements also on the DVs used by the loose requirement. The requirements on the discriminating variables are tuned separately for converted and unconverted photons, to account for calorimeter geometry and for different effects on the shower shapes from the material upstream of the calorimeter, which is non uniform as a function of $|\eta|$. A summary of the DVs used by the loose and tight photon identification criteria is given in Table 4.2. An alternative identification criterium, called "**loose'**", based on five of the discriminating variables described in Table 4.2, namely R_{had}, R_η, w_2, R_ϕ and w_{stot}. For systematic studies, the loose' definition is modified to include the variables R_{had}, R_η, w_2, R_ϕ, w_{stot}, ΔE and E_{ratio} (a tighter version of loose') and to include only R_{had}, R_η, w_2 and R_ϕ (a looser version of loose'), as explained in Table 4.3. In order to compensate the differences between the data and the simulation in the lateral shower shapes, some correction factors, known as "Fudge Factors", are applied to the MC samples. The precise measurement of the γ_{ID} efficiency is performed using three data-driven methods, as the description of the photon interaction with the material is not precise enough to accurately determine the efficiency from the simulation only. The used data-driven methods are described in the following:

- **Radiative Z boson decays**: based on a pure photon sample of selected radiative decays of the Z boson, $Z \to \ell^+\ell^-\gamma$ (where $\ell = e, \mu$) allows a precise measurent in the low photon tranverse energy region.

- **Electron extrapolation**: is based on the similarity between the electromagnetic showers induced by isolated electrons and photons in the EM calorimeter and the possibility to extrapolate the photon distributions of the DVs from an electron sample from $Z \to e^+e^-$. Due

Category	Description	Name	*loose*	*tight*
Acceptance	$\|\eta\| < 2.37$, with $1.37 < \|\eta\| < 1.52$ excluded	–	•	•
Hadronic leakage	Ratio of E_T in the first sampling layer of the hadronic calorimeter to E_T of the EM cluster (used over the range $\|\eta\| < 0.8$ or $\|\eta\| > 1.37$)	R_{had1}	•	•
	Ratio of E_T in the hadronic calorimeter to E_T of the EM cluster (used over the range $0.8 < \|\eta\| < 1.37$)	R_{had}	•	•
EM Middle layer	Ratio of 3×7 $\eta \times \phi$ to 7×7 cell energies	R_η	•	•
	Lateral width of the shower	w_{η_2}	•	•
	Ratio of 3×3 $\eta \times \phi$ to 3×7 cell energies	R_ϕ		•
EM Strip layer	Shower width calculated from three strips around the strip with maximum energy deposit	w_{s_3}		•
	Total lateral shower width	$w_{s_{tot}}$		•
	Energy outside the core of the three central strips but within seven strips divided by energy within the three central strips	F_{side}		•
	Difference between the energy associated with the second maximum in the strip layer and the energy reconstructed in the strip with the minimum value found between the first and second maxima	ΔE		•
	Ratio of the energy difference associated with the largest and second largest energy deposits to the sum of these energies	E_{ratio}		•

Table 4.2: Discriminating variables used for *loose* and *tight* photon identification.

Name	Cuts not applied w.r.t. **Tight**
Loose'2	F_{side}, w_{s3}
Loose'3	F_{side}, w_{s3}, ΔE
Loose'4	F_{side}, w_{s3}, ΔE, E_{ratio}
Loose'5	F_{side}, w_{s3}, ΔE, E_{ratio}, w_{stot}

Table 4.3: Various definitions of the loose' requirement with respect to the tight identidication criteria. loose'4, defined relaxing the F_{side}, w_{s3}, ΔE and E_{ratio} cuts, is choses as the nominal definition for the photon plus jet analisis. The alternative definitions are used to evaluate the systematic uncertainty on the background estimation.

to the Z decay kinematics, this method covers an intermediate photon transverse momentum range.

- **Matrix method**: exploits a technique to determine the amount of background in a sample of isolated photon candidates. The isolation of the reconstructed photons is used as a discriminating property, in order to extract the sample purity before and after the photon identification requirement. This method has the advantage of covering a large E_{T} range.

More details about the three data-driven methods can be found in Appendix A. The loose identification efficiency rises from 97% at $E_{\text{T}} = 20$ GeV to above 99% for $E_{\text{T}} > 40$ GeV for both converted and unconverted photons [70]. The efficiency of the tight identification increases from 53–64% (47-61%) for unconverted (converted) photons at $E_{\text{T}} \approx 10$ GeV to 88–92% (96–98%) for $E_{\text{T}} \geq 100$ GeV [71]. These results are shown in Figure 4.3 for unconverted and in Figure 4.4 for converted photons.

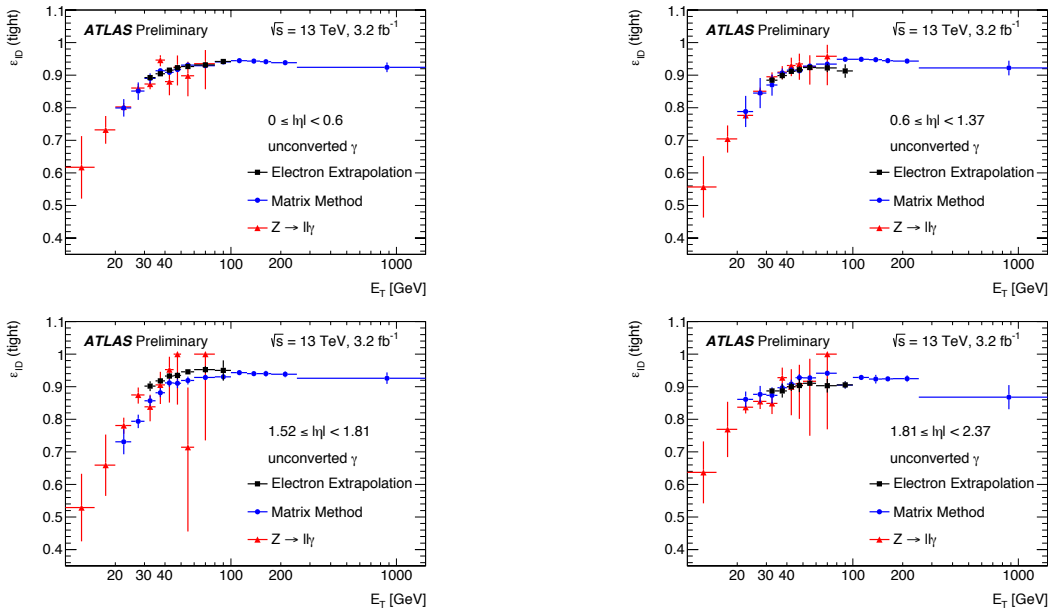

Figure 4.3: Comparison between the tight identification efficiencies for unconverted photons, obtained with the three data-driven methods, as a function of E_{T} in the region $20 \leq E_{\mathrm{T}} \leq 1500$ GeV, in four pseudo-rapidity intervals. The uncertainty bars represent the sum in quadrature of the statistical and systematic uncertainties, estimated for each method [71].

4.2 Jets in ATLAS

Hadronic jets used for ATLAS physics analysis are reconstruted by the anti-k_t algorithm, using as input positive-energy topological clusters of calorimeter cell energies (topoclusters). Topoclusters are built from neighbouring calorimeter cells containing a significant energy above a noise threshold, estimated from measurements of calorimeter electronic noise and simulated pileup noise. The calorimeter cells are measured at the EM scale, corresponding to a response proportional to the energy deposited by electromagnetically interacting particles. The jet four-momenta were computed from the sum of the jet-constituent four-momenta, treating each as a four-vector with zero mass. At this stage, the jet four-momenta are measured at the EM scale.

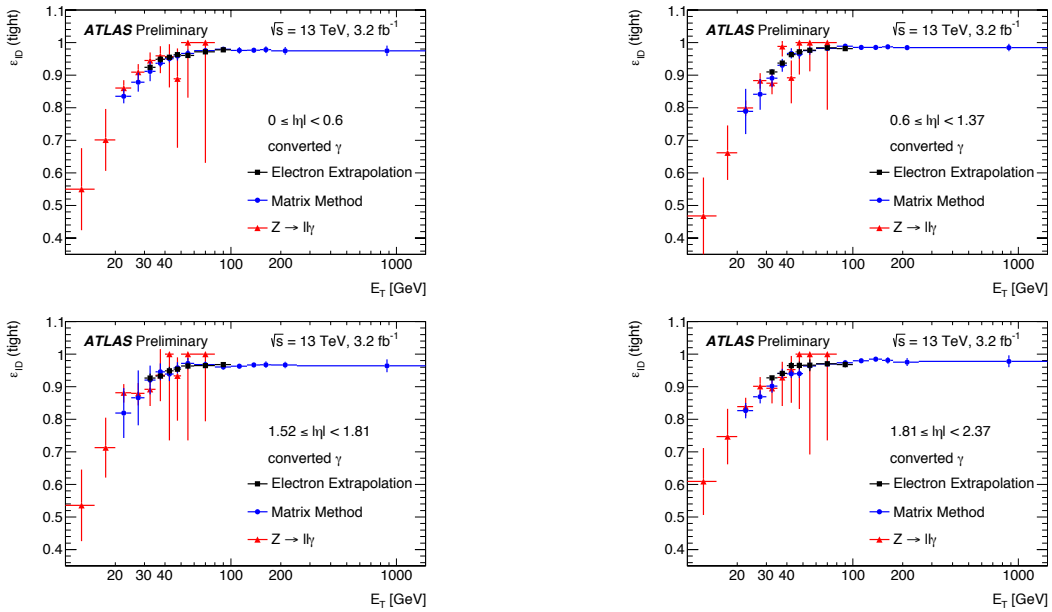

Figure 4.4: Comparison between the tight identification efficiencies for converted photons, obtained with the three data-driven methods, as a function of E_{T} in the region $20 \leq E_{\mathrm{T}} \leq 1500$ GeV, in four pseudo-rapidity intervals. The uncertainty bars represent the sum in quadrature of the statistical and systematic uncertainties, estimated for each method [71].

4.2.1 Jet calibration

Figure 4.5 presents an overview of the ATLAS calibration scheme for EM scale calorimeter jets. The calibration restores the jet energy scale to that of truth jets reconstructed at particle-level energy scale. Each stage of the calibration corrects the full four-momentum unless otherwise stated, scaling the jet p_{T}, energy and mass [72, 73]. The **origin correction** recalculates the jet four-momentum to point to the hard scattering primary vertex rather than the center of the detector, while keeping the jet energy constant. This correction improves the η resolution of jets, as measured from the difference between reconstructed jets and particle-level jets in MC simulations.
The **pileup correction** removes the energy contamination due to in-time and out-time-pileup. It consists of two components: an area-based p_{T} density subtraction [74], applied at per-event level, and a residual correction derived from the MC simulations. More details are given in the following. The area-based method subtracts the per-event pileup contribution to the p_{T} of each jet according to its area. The pileup contribution is calculated from the median p_{T} density (ρ) of jets in the $\eta - \phi$ plane. The calculation of ρ

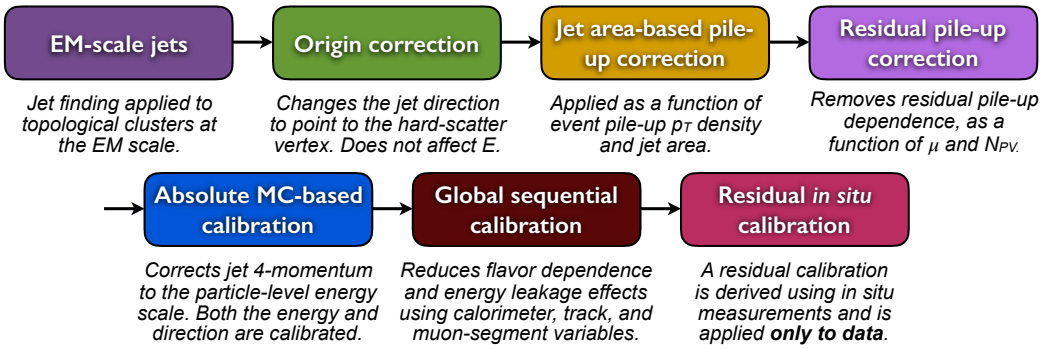

Figure 4.5: Calibration stages for EM scale jets.

uses only positive-energy topoclusters within $|\eta| < 2$ that are clustered using the k_t algorithm with a jet size of $R = 0.4$. The k_t algorithm is chosen for its sensitivity to soft radiation and is only used in the jet-area method. The central $|\eta|$ selection is necessitated by the higher calorimeter occupancy in the forward region. The p_T density of each jet is taken to be p_T/A, where the area A of a jet is calculated using ghost association. In this procedure, simulated ghost particles of infinitesimal momentum are added uniformly in solid angle to the event before the jet reconstruction. The area of a jet is measured from the relative number of ghost particles associated after clustering. The ratio between the ρ subtracted jet p_T and the uncorrected jet p_T is taken as a correction factor applied to the jet four-momentum, and does not affect the jet angular coordinates. The ρ calculation is derived from the central, lower-occupancy regions of the calorimeter, and does not fully describe the pileup sensitivity in the forward calorimeter region or in the higher-occupancy core of high-p_T jets. It is observed that after this correction some dependence of anti-k_t jet p_T on the amount of pileup remains, and an additional residual correction is derived. A dependence is seen on the number of primary vertex (N_{PV}), sensitive to in-time pileup, and the average interactions per bunch crossing (μ), sensitive to out-of.time pileup. The residual p_T dependence on $N_{PV}(\alpha)$ and $\mu(\beta)$ are observed to be fairly linear and independent of one another. Linear fits are used to derive the α and β coefficients separately in bins of p_T and η. The pileup corrected p_T^{corr}, after the area-based and residual corrections is given by:

$$p_T^{corr} = p_T^{reco} - \rho \times A - \alpha \times (N_{PV} - 1) - \beta \times \mu \tag{4.5}$$

where p_T^{reco} refers to the EM scale p_T of the reconstructed jet before any pileup correcation is applied. The dependence of the area-based and residual corrections on N_{PV} and μ are shown as a function of $|\eta|$ in Figure 4.6.

The absolute **jet energy scale and η calibration** corrects the recon-

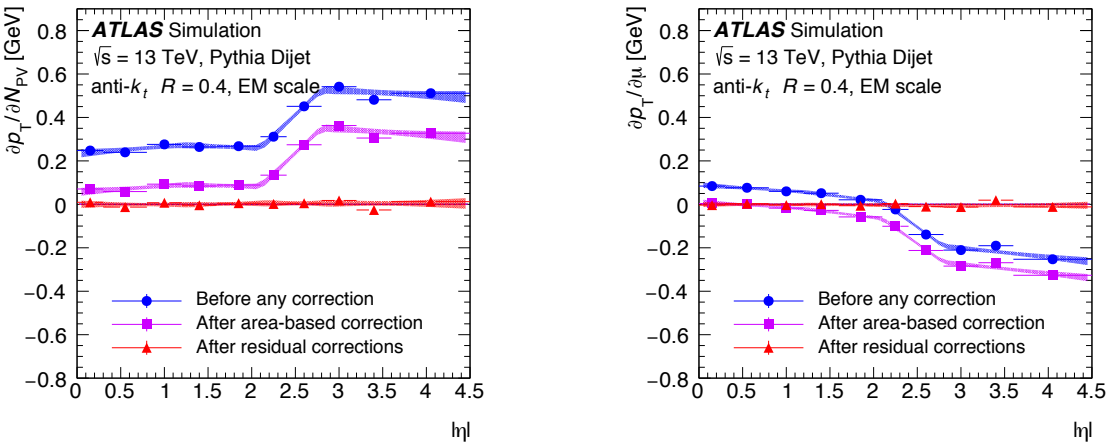

Figure 4.6: Dependence of EM-scale anti-k$_t$ jet p_{T} on (left) in-time pileup (N_{PV} averaged over μ) and (right) out-of-time pileup (μ averaged over N_{PV}). The dependence is shown in bins of $|\eta|$ before pileup corrections (blue circle), after the area-based correction (violet square), and after the residual correction (red triangle). The shaded bands represent the 68% confidence intervals of the linear fits in 4 regions of $|\eta|$. The values of the fitted dependence on in-time and out-of-time pileup after the area-based correction (purple shaded band) are taken as the residual correction factors α and β, respectevely [73].

structed jet four-momentum to the particle-level scale and accounts for biases in the jet η reconstruction. Such biases are primarly caused by the transition between different calorimeter technologies and the sudden change in calorimeter granularity. The calibration is derived from MC simulations using reconstructed jets after the application of the origin and pileup corrections. The jet energy scale (JES) calibration is derived first as a correction of the reconstructed jet energy to the particle-level jet energy. Reconstructed jets are matched geometrically to particle-level jets within ΔR <0.3. Only isolated jets are used to avoid any ambiguities in the matching of calorimeter jets to particle-level jets. An isolated calorimeter jet is required to have no other calorimeter jet of $p_{\mathrm{T}} > 5$ GeV within $\Delta R = 1$, and only one particle-level jet of $p_{\mathrm{T}}^{truth} > 7$ GeV within $\Delta R = 0.6$. The average energy response is defined as the mean of a Gaussian fit to the core of the $E^{\mathrm{reco}}/E^{\mathrm{truth}}$ distribution for jets, binned in E_T^{truth} and η_{det}. The response is derived as a function of η_{det}, the jet η pointing from the geometrical center of the detector, to remove any ambiguity as to which region of the detector is being measured. Gaps and transition between calorimeter subdetectors result in a lower energy re-

sponse due to absorbed or undetected particles, evident when parametrized by η_{det}. A numerical inversion procedure is used to derive corrections from E^{reco} to E^{truth}. The average response is parametrized as a function of E^{reco} and the jet calibration factor is taken as the inverse of the average energy response. Good closure of the JES calibration is seen across the entire η range. A bias is seen in the reconstructed jet η as a function of η_{det} which is larger in jet that encompass two calorimeter regions with different energy responses caused by changes in calorimeter geometry or technology. This artificially increases the energy of one side of the jet with respect to the other, altering the reconstructed four-momentum. The barrel-endcap ($|\eta_{det}| \approx 1.4$) and endcap-forward ($|\eta_{\text{det}}| \approx 3.1$) transition regions are the most affected by this effect. A second correction is therefore derived as the difference between the reconstructed η^{reco} and the particle-level η^{truth}, parametrized as a function of E^{truth} and $|\eta_{det}|$. Unlike the other calibration steps, the η calibration alters only the jet p_{T} and η, not the full four-momentum. Jets calibrated with the full energy scale and η calibration are considered to be at EM+JES.

Global sequential calibration: Following the previous calibrations, a residual dependence of the JES on longitudinal and transverse features of the jet is observed. Such differences may arise due to details of the detector interaction and of the particle composition of jets, with the response varying between quark- and gluon-initiated jets. Five observables are identified to improve the resolution of the jet energy through a global sequential calibration (GSC). For each observable, an independent jet four-momentum correction is derived by inverting the jet response in MC simulations. An overall constant is applied to each numerical inversion to ensure the average energy is unchanged at each stage. The effect of each correction is therefore to remove the dependence of the jet response to each observable while conserving the overall energy scale at the EM+JES. Corrections for each observable are applied independently and sequentially to the jet four momentum, neglecting correlations between observables. No improvement was found from including such correlations or altering the sequence of the correlations. The five stages of the GSC account for the dependence of the jet response on:

- f_{Tile0}, the fraction of jet energy measured in the first layer of the hadronic Tile calorimeter ($|\eta_{\text{det}}| < 1.7$);
- f_{Lar3}, the fraction of jet energy measured in the third layer of the electromagnetic LAr calorimeter ($|\eta_{\text{det}}| < 3.5$;
- $width_{\text{trk}}$, the average p_{T}-weighted transverse distance in the $\eta-\phi$ plane between the jet axis and all tracks of $p_{\text{T}} > 1$ GeV ghost associated to the jet ($|\eta_{\text{det}}| < 2.5$);

- n_{trk}, the number of tracks with $p_{\mathrm{T}} > 1$ GeV ghost associate to the jet ($|\eta_{\mathrm{det}}| < 2.5$);
- $N_{segments}$, the number of muon segments associated to the jet ($|\eta_{\mathrm{det}}| < 2.7$);

The N_{segments} correction reduces the tails of the response distribution caused by high-p_{T} jets that are not fully contained in the calorimeter, referred to as punch-through jets. The first four corrections are derived as a function of the jet p_{T}, while the punch-through correction is derived as a function of the jet energy, being better correlated with the energy escaping the calorimeter. The underlying distributions of these five observables are fairly well modelled by MC simulations. Slight differences with data have a negligible impact on the GSC as long as the dependence of the average jet response on the observables is well modelled in MC simulations. This average response dependence was tested using the dijet tag-and-probe method. The average p_{T} asymmetry between back-to-back jets was measured as a function of each observable and found to be compatible between data and MC, with small differences compared to the size of corrections.
The last step of the jet calibration accounts for differences in the jet response between data and MC simulations, which arise from limitations in the description of the detector response and material, as well as in the simulation of the hard scatter, underlying event, pileup, jet formation, and electromagnetic and hadronic interactions with the detector. Differences between data and MC simulation are quantified by balancing the p_{T} of a jet against other well-measured reference objects. The η-intercalibration corrects the response of forward jets to well-measured central jets using dijet events. Three other in situ calibrations correct for differences in the response of central jet with respect to well-measured reference objects, each focusing on a different p_{T} region using Z-boson, photon and multijet systems. For each in-situ calibration, a response $R_{\mathrm{in-situ}}$ is defined in data and MC as the average p_{T} ratio between a jet and a reference object in a given region of p_{T}^{ref} of the reference object. It is proportional to the jet response in the calorimeter at the EM+JES, but it is also sensitive to secondary effects such as gluon radiation and the loss of energy outside of the jet radius. Assuming that these secondary effects are well modelled in the MC simulation, the ratio $c = R^{\mathrm{data}}_{\mathrm{in-situ}}/R^{\mathrm{MC}}_{\mathrm{insitu}}$ is a useful estimation of the ratio between the JES in data and MC. Through numerical inversion a correction is derived to the jet four-momentum. Event selections are designed to reduce the impact of any secondary effects, and their mismodelling in simulation is covered by systematic uncertainties derived from the choice of MC generator. The correction is derived as a function of jet p_{T}, and also as a function of jet η in the η-intercalibration. The η-intercalibration

corrects the jet energy scale of forward jets ($0.8 < |\eta_{\text{det}}| < 4.5$) to that of cental jets ($|\eta_{\text{det}}| < 0.8$) in a dijet system. The boson balance analyses use a well-calibrated photon or Z-boson, the latter decaying into an electron or muon pair, to measure the p_{T} response of the recoiling jet in the central region up to a p_{T} of about 950 GeV. The multijet balance analysis calibrates central ($|\eta| < 1.2$), high-p_{T} jets ($300 < p_{\text{T}} < 2000$ GeV) recoiling against a collection of well-calibrated, lower-p_{T} jets. While the Z/γ and multijet balance calibrations are derived from central jets, their corrections are applicable for forward jets whose energy scale have been equalised by the η-intercalibration procedure. The calibration constants derived in each of these analyses are statistically combined into a final in situ calibration covering the region $20 < p_{\text{T}} < 2000$ GeV.

The final calibration includes a set of 76 JES systematic uncertainty terms

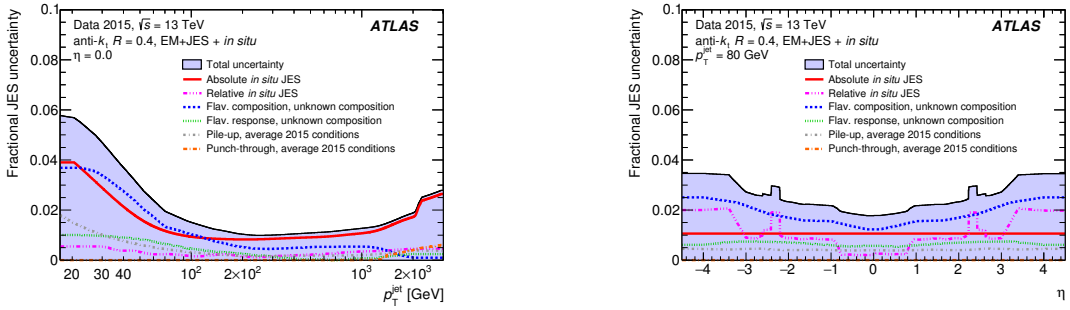

Figure 4.7: JES uncertainty as a function of P_T^{jet} and η^{jet} [73].

propagated from the individual calibrations and studies. The majority (65) of uncertainties come from the $Z/\gamma - jet$ and multijet balance in situ calibrations and account for assumptions made in the event topology, MC simulations, sample statistics, and propagated uncertainties on the electron, muon and photon energy scales. The remaining 11 uncertainties are derived from other sources. Four pileup uncertainties are included to account for potential mismodelling of N_{PV}, μ, ρ and the residual p_{T} dependence. Three η-intercalibration uncertainties account for potential physics mismodelling, statistical uncertainties, and the method non-closure in the region $2 < |\eta_{\text{det}}| < 2.6$. Two additional uncertainties account for differences in the jet response and simulated jet composition of light-quark and gluon-initiated jets. An uncertainty is also considered on the GSC punch-through correction, derived as the maximum difference in the jet response in data and MC as a function of the number of muon segments. An high-p_{T} uncertainty is derived from single-particle response studies and is applied to jets above 2 TeV, beyond the reach of the in situ methods. The full combination of all

the uncertainties is shown in Fig. 4.7 as a function of p_{T}^{jet} at $\eta^{\mathrm{jet}} = 0$ and as a function of η^{jet} at $p_{\mathrm{T}}^{jet} = 60$ GeV. Each uncertainty is generally treated independently of one another but fully correlated across $p_{\mathrm{T}}^{\mathrm{jet}}$ and η^{jet}. Exceptions are the correlated electron and photon energy scale measurements and the propagated multijet-balance uncertainties related to pileup, punch-through, η-intercalibration, and jet flavor. The uncertainty is largest at low $p_{\mathrm{T}}^{\mathrm{jet}}$, starting at 5.7% and decreasing to 1% at 200 GeV. It rises after 200 GeV due to the statistical uncertainties related to the insitu calibration and increases sharply after 2 TeV, where the multijet-balance measurements end and larger uncertainties are taken from the single-particle response. The uncertainty is fairly constant as a function of η^{jet} and reaches a maximum of 3.7% for the most forward jets. A sharp feature can be seen at $2 < |\eta^{\mathrm{jet}}| < 2.6$ due to the non-closure uncertainty of the η-intercalibration.

Chapter 5

Data selection

The data used in this analysis were collected with the ATLAS detector during the 25 ns proton-proton collision running period in 2015, when the LHC operated at a centre-of-mass energy of $\sqrt{s} = 13$ TeV. Only events collected in stable beams conditions and satisfying detector and data-quality requirements are considered. The total integrated luminosity of the collected sample amounts to 3.16 ± 0.07 fb^{-1}, as shown in Figure 5.1. Events were recorded using a single-photon high-level trigger with a nominal transverse energy threshold of 120 GeV (HLT_120_loose), seeded by a level-1 trigger with a nominal threshold equal to 22 GeV (L1_EM22VHI) [1]. The selection criteria applied by the trigger on the DVs are looser than the photon loose identification criteria applied in the offline analysis and allow a plateau of constant efficiency close to 100 % for the true prompt photons of $E_{\mathrm{T}}^{\gamma} > 125$ GeV and pseudorapidity $|\eta^{\gamma}| < 2.37$, as explained in Section 5.5. The HLT_120_loose was the lowest-threshold unprescaled photon trigger during the 2015 data-taking period. The trigger requirement was not applied on the MC samples since the trigger efficiency was estimated with a data-driven method and the data are corrected for that effect.

5.1 Event selection

The sample of isolated-photon + jet events was selected offline using the following selection criteria:

[1] In Run-2, the rate of electromagnetic triggers (EM) can be controlled by raising thresholds, adding hadronic core isolation (H), adding electromagnetic isolation (I) and varying thresholds with η to account for energy loss (V). However, for the range in E_{T}^{γ} considered in this analysis, no isolation requirement is applied

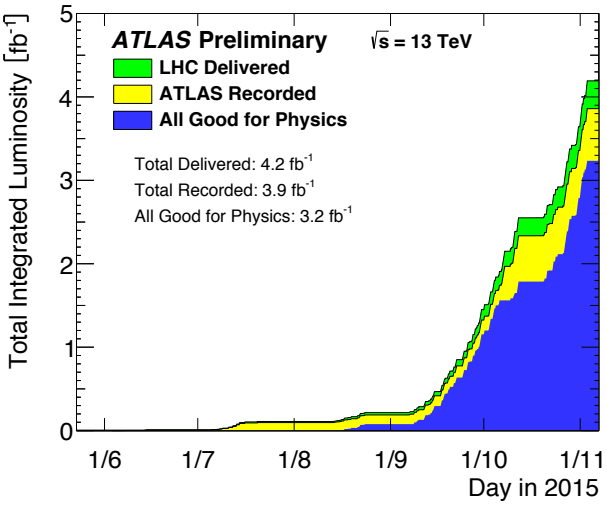

Figure 5.1: Total integrated luminosity delivered by the LHC (green), recorded by the ATLAS detector (yellow) and certified to be good quality data (blue) during stable beams for pp collisions at 13 TeV centre-of-mass energy in 2015.

- the events are required to have at least one reconstructed primary vertex, with at least two associated tracks of $p_{\mathrm{T}} > 400$ MeV, consistent with the average beam-spot position;
- events with problems associated to noise burst and data-integrity errors in the LAr calorimeter are rejected;
- if a part of the detector is missing in some events, the events are then removed from the sample;
- events are rejected if the Tile calorimeter output is corrupted;
- events with SCT problems are rejected.

The selection criteria applied to photons and jets are described in the following sections.

5.2 Photon selection

Both reconstructed and calibrated converted and unconverted photons are considered in this analysis. The applied photon-candidate selection criteria are listed below:

- events in which the photon has transverse energy $E_{\mathrm{T}}^{\gamma} > 125$ GeV and $|\eta^{\gamma}| < 2.37$ are selected. The event is excluded if the photon falls in the pseudo-rapidity region $1.37 < |\eta^{\gamma}| < 1.56$;

- an ambiguity resolver tool [70] is used to reject electrons faking photons. The resolver ensures that an event having a converted photon with a track reconstructed in a region where the first layer of the pixel is not working properly is eliminated. Such a requirement significantly reduces the number of misidentified electrons as converted photons and the background of electrons faking photons is expected to be negligible;

- in events with multiple candidates satisfying the previous requirements, only the loose-photon candidate with the highest transverse energy (leading photon) is retained for further studies;

- the candidates are required to pass the loose' identification criteria. This intermediate sample of events is used in the background subtraction method;

- the leading photon is required to pass the tight identification criteria;

- the isolation transverse energy, $E_{\mathrm{T}}^{\mathrm{iso}}$ (TopoEtCone40), of the leading photon is required to be lower than $4.2 \cdot 10^{-3} \cdot E_{\mathrm{T}}^{\gamma} + 4.8$ GeV, which amounts to a cut on E_{T}^{iso} of 5.3 (11.1) GeV for $E_{\mathrm{T}}^{\gamma} = 125$ (1500) GeV;

- additional corrections are applied to the simulated events to match the overall event conditions of the data sample and to account for known differences between data and simulations.

An E_{T}^{γ}-dependent isolation requirement is used to keep the signal to background ratio as high as possible as well as to achieve a constant reconstruction effiency throughout the whole E_{T}^{γ} range measured. Figure 5.2 show the efficiency of the E_{T}^{γ}-dependent cut on photon candidates in the MC at reconstruction level for PYTHIA and SHERPA, respectively. The probability of a photon passing the isolation requirement as a function of E_{T}^{γ} is shown for the E_{T}^{γ}-dependent requirement and several fixed cuts. The improved performance of the E_{T}^{γ} is clearly seen, especially at high E_{T}^{γ}, where all the fixed thresholds show a sizeable decrease in the probability. There are differences between the efficiencies evaluated with PYTHIA and SHERPA, which are due to the bias from tighter parton level cuts in the SHERPA samples; specifically, the photons in the brem component are less isolated than those in the direct component and so more events are rejected. Nevertheless, these differences in efficiencies do not propagate into the final results since the cross section

are measured for isolated photons.

To define the phase-space region that corresponds to the E_{T}^{γ}-dependent iso-

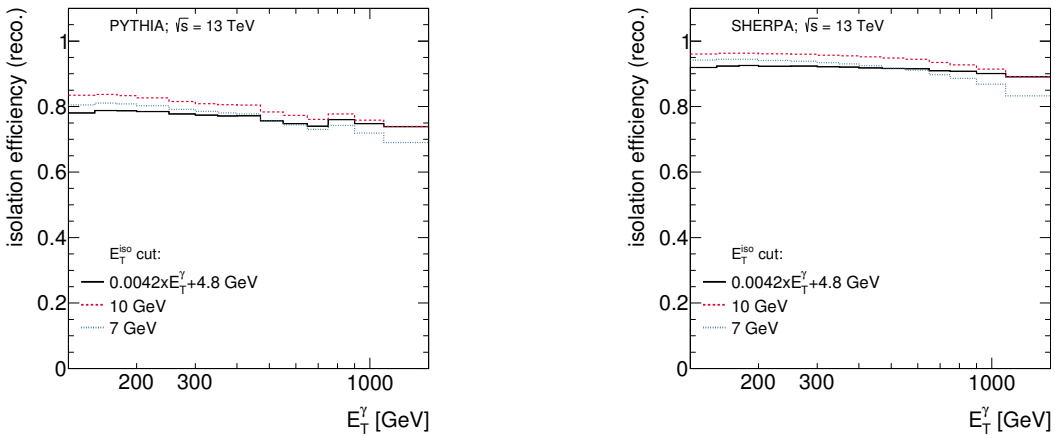

Figure 5.2: The measured $E_{\mathrm{T}}^{\mathrm{iso}}$ efficiency as a function of E_{T}^{γ} for PYTHIA (left) and SHERPA right.

lation requirement at reco level, the isolation at particle level is studied. The equivalent requirement at particle level is determined by studying the correlation between the reconstruction and particle level as a function of E_{T}^{iso}. The E_{T}^{iso} variable at particle level is computed using all the hadron in the final state (arising from the hard interaction as well as those arising from the underlying event simulation) and is also corrected using the jet-area method. To determine which requirement at particle level would provide the smallest extrapolation in the cross section, studies of the correlation between isolation energy at reconstruction and particle levels are performed and explained below. Figure 5.3 shows the correlation between the E_{T}^{iso} variable evaluated at the reconstructed and particle levels. In both PYTHIA and SHERPA there is a very good correlation in the signal region; in the tail of the distribution (in which the background dominates) the correlation is situated below the diagonal and presents a wide spread. The profiles of the correlations are also included in the same figure; they are used in the following discussion to make comparisons. The same dependence is observed splitting the correlation plots in different E_{T}^{γ} ranges. This trend is observed in the signal region for both MC samples and for the PYTHIA's hard and brem components and for SHERPA in each E_{T}^{γ} region.

The requirement on E_{T}^{iso} at particle level equivalent to the E_{T}^{γ}-dependent one, applied at reconstruction level, was determined by performing a linear fit to the profiles in the region $5 < E_{\mathrm{T}}^{iso} < 20$ GeV in each E_{T}^{γ} region. A χ^2 fit to the results shown gives 9.63 ± 0.11 (9.91 ± 0.11) GeV as threshold

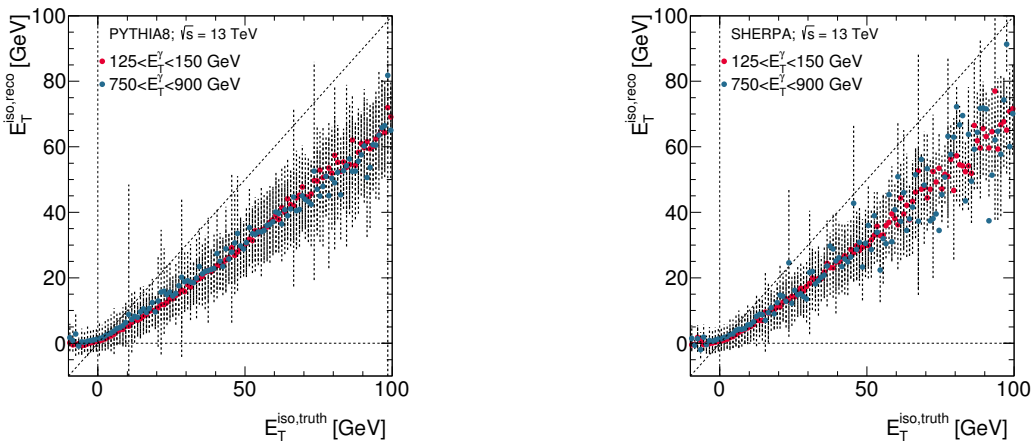

Figure 5.3: The profile of the $E_{\mathrm{T}}^{\mathrm{iso,reco}}$ vs. $E_{\mathrm{T}}^{\mathrm{iso,part}}$ correlation for PYTHIA (left) and SHERPA (right), in different E_{T}^{γ} regions. The error bars represent the width of the distribution in each $E_{\mathrm{T}}^{\mathrm{iso}}$ bin.

for PYTHIA (SHERPA) and 0.0039 ± 0.0004 (0.0043 ± 0.0004) as slope, as shown in Figure 5.4. Therefore, a requirement on E_{T}^{iso} of $4.2 \cdot 10^{-3} \cdot E_{\mathrm{T}}^{\gamma} + 10$ GeV was used at particle level.

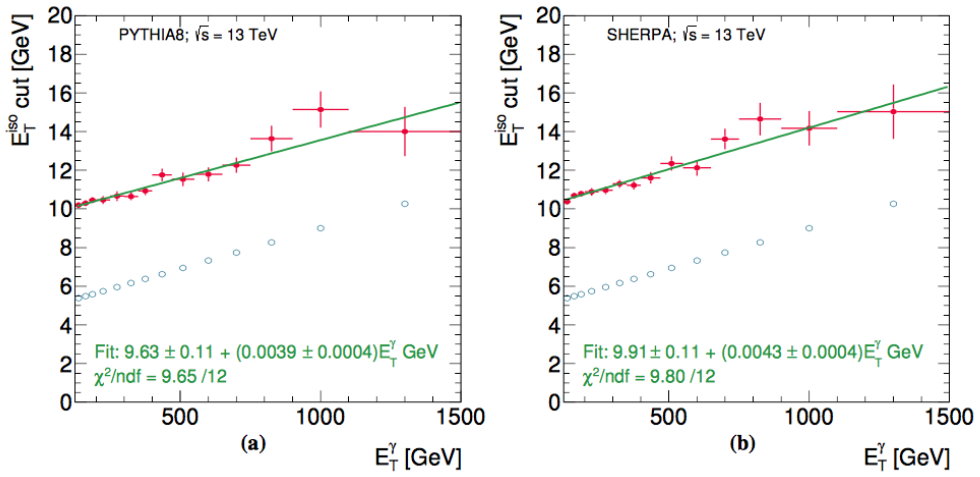

Figure 5.4: Summary of the values obtained for the requirement at particle level as a function of E_{T}^{γ} for (a) PYTHIA and (b) SHERPA (dots). The open circles represent the E_{T}^{γ}-dependent requirement used at reco level evaluated at the center of each bin. The solid line is the result of a straight-line fit to the values obtained for the requirement at particle level.

5.3 Jet selection

Jets reconstructed using the anti-k_t algorithm with a radius parameter $R = 0.4$ and calibrated following the procedure described in the prevous chapter, are retained for this analysis. The selection criteria involving the jets in an event are listed below:

- the event is rejected if there is at least one jet fulfilling the "LooseBad" cleaning condition [75];
- events with at least one jet candidate with rapidity $|y^{\text{jet}}| < 2.37$ are selected;
- the jets whose axis lays within a cone of radius $R = 0.8$ around the photon candidate, are discarted;
- the event is retained if the jet with highest transverse momentum (leading jet) has $p_{\text{T}}^{\text{jet}} > 100$ GeV.

5.4 Data samples

The number of data events selected by using the requirements listed in the previous sections amounts to 895746. After the isolation and identification requirements, the backgound of events with more than one photon or with an electron mis-identified as a photon is $\sim 0.1\%$. Figures 5.5 and 5.6 show the distributions as functions of the leading-photon transverse energy (E_{T}^{γ}), the absolute value of leading-photon pseudorapidity (η^{γ}) and the leading-photon azimuthal angle (ϕ^{γ}), as well as of the leading-jet transverse momentum ($p_{\text{T}}^{\text{jet-lead}}$), the absolute value of the leading-jet rapidity ($y^{\text{jet-lead}}$) and the leading-jet azimuthal angle ($\phi^{\text{jet-lead}}$) for the selected photon+jet sample. Figure 5.7 shows the distributions as functions of the absolute value of the difference in rapidity between the leading photon and the leading jet ($|\Delta\eta^{\gamma-\text{jetlead}}| \equiv |\eta^{\gamma} - y^{\text{jet-lead}}|$) and in the azimuthal angle beween the leading-photon and the leading-jet ($|\Delta\phi^{\gamma-\text{jetlead}}| \equiv |\phi^{\gamma} - \phi^{\text{jet-lead}}|$) for the selected photon+jet sample. For the measurements of the cross sections as functions of the invariant mass of the leading-photon and leading-jet system ($m^{\gamma-\text{jet}}$) and $|\cos\theta^*| \equiv |\tanh((\eta^{\gamma} - y^{\text{jet-lead}})/2)|$, additional requirements are imposed to remove the bias due to the rapidity and transverse-momentum cuts on the photon and the jet. To perform unbiased measurements for $m^{\gamma-\text{jet}}$ and $|\cos\theta^*|$, the additional requirements $|\eta^{\gamma} + y^{\text{jet-lead}}| < 2.37$, $|\cos\theta^*| < 0.83$ and $m^{\gamma-\text{jet}} > 450$ GeV are imposed. The first two requirements avoid the bias induced by cuts on η^{γ} and $y^{\text{jet-lead}}$, yielding slices of $\cos\theta^*$ with the same lenght

along the $\eta^{\gamma} + y^{\mathrm{jet-lead}}$ plane. The third requirement avoids the bias due to the $E_{\mathrm{T}}^{\gamma} > 125$ GeV cut, which can be seen in the $|\cos\theta^{*}| - m^{\gamma-\mathrm{jet}}$ plane. The unbiased kinematic regions are shown as hatched areas in Figure 5.8. The number of events in the data after these additional requirements is 137741. Figure 5.9 shows the $m^{\gamma-jet}$ and $|\cos\theta^{*}|$ distributions. The binning of each distribution has been chosen accordng the experimental resolution and the statistical population, expecially at high values of E_{T}^{γ}, $p_{\mathrm{T}}^{\mathrm{jet-lead}}$ and $m^{\gamma-\mathrm{jet}}$, where the statistics are poorer.

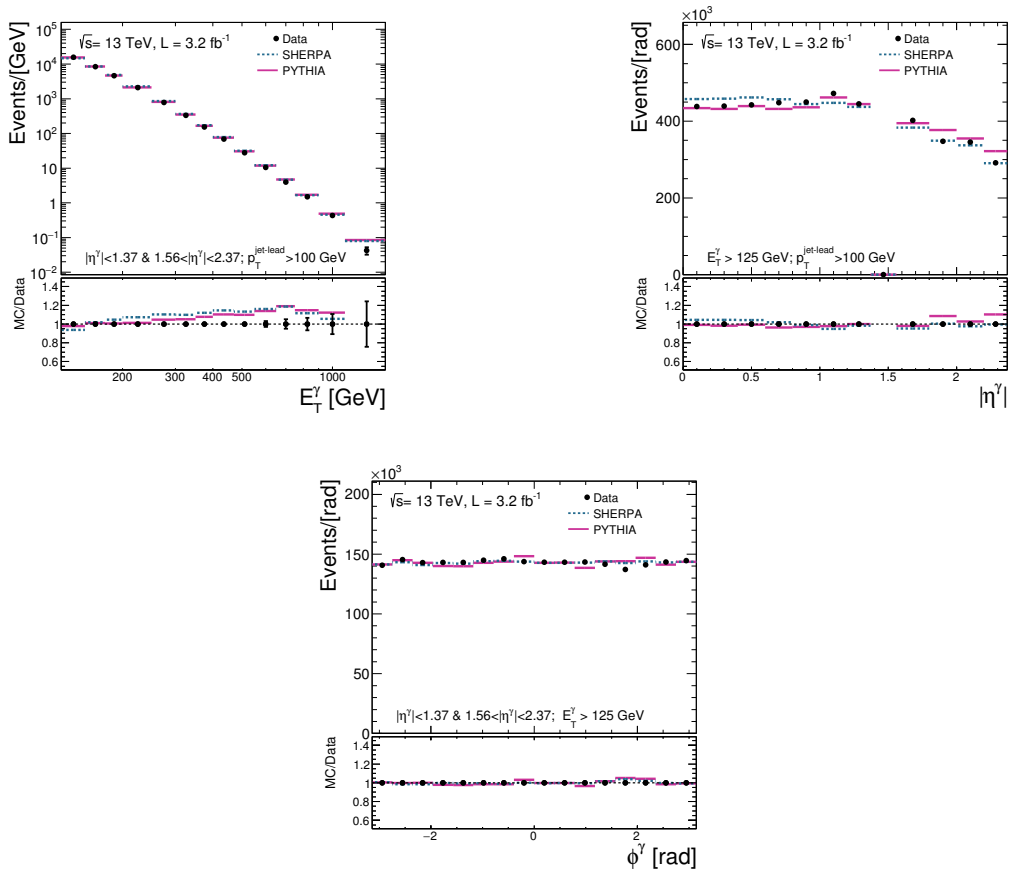

Figure 5.5: The measured E_{T}^{γ}, $|\eta^{\gamma}|$ and ϕ^{γ} distributions for the leading photon in the photon+jet sample. For comparison, the MC simulations of the signal from PYTHIA and SHERPA are also included. Both MC simulations are normalised to the data. The lower part of the figures shows the ratio of the MC to the data distribution.

Note that even after the application of the tight identification and isolation requirements, a small but non-negligible contribution of background still affects the selected sample. This background originates predominantly from multijet QCD processes, in which a jet is misidentified as a photon. This jet contains usually a light neutral meson, mostly π^0, that decays in two collimated photons, which carry most of the energy of the jet. This background is removed by using a data-driven technique. The average number of interaction per bunch crossing is $< \mu > \approx 13.5$ for the data collected with the HLT_g120_loose trigger. Differences in the pile-up conditions between data and MC simulations are corrected for.

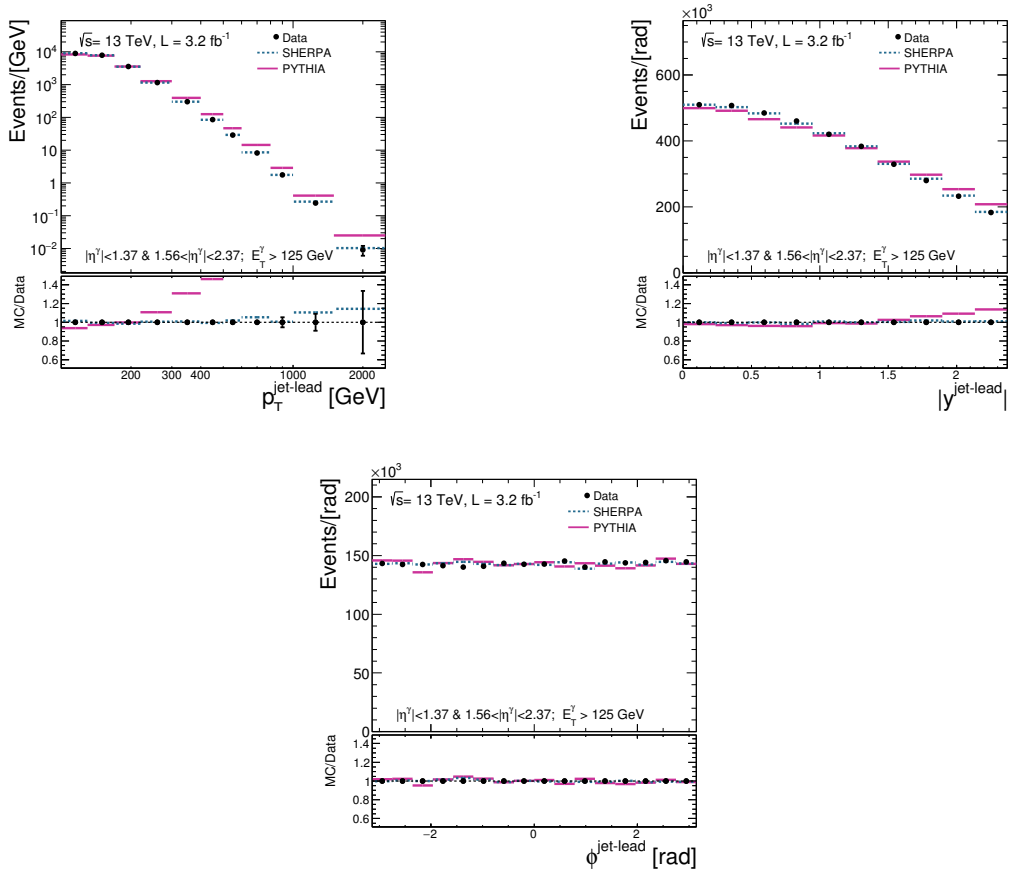

Figure 5.6: The measured $p_{\mathrm{T}}^{\mathrm{jet-lead}}$, $|y^{\mathrm{jet-lead}}|$ and $\phi^{\mathrm{jet-lead}}$ distributions for the leading jet in the photon+jet sample. For comparison, the MC simulations of the signal from PYTHIA and SHERPA are also included. Both MC simulations are normalised to the data. The lower part of the figures shows the ratio of the MC to the data distribution.

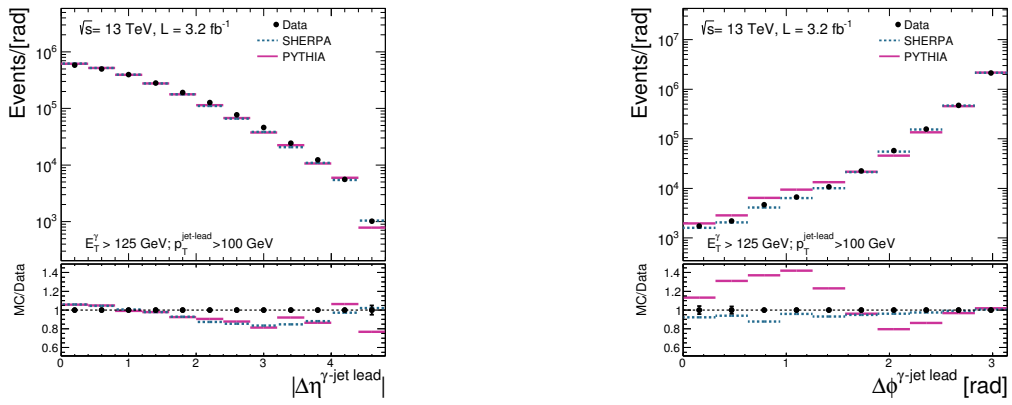

Figure 5.7: The measured $|\Delta\eta^{\gamma-\mathrm{jet}}|$, and $|\Delta\phi^{\gamma-\mathrm{jet}}|$ distributions in the photon+jet sample. For comparison, the MC simulations of the signal from PYTHIA and SHERPA are also included. Both MC simulations are normalised to the data. The lower part of the figures shows the ratio of the MC to the data distribution.

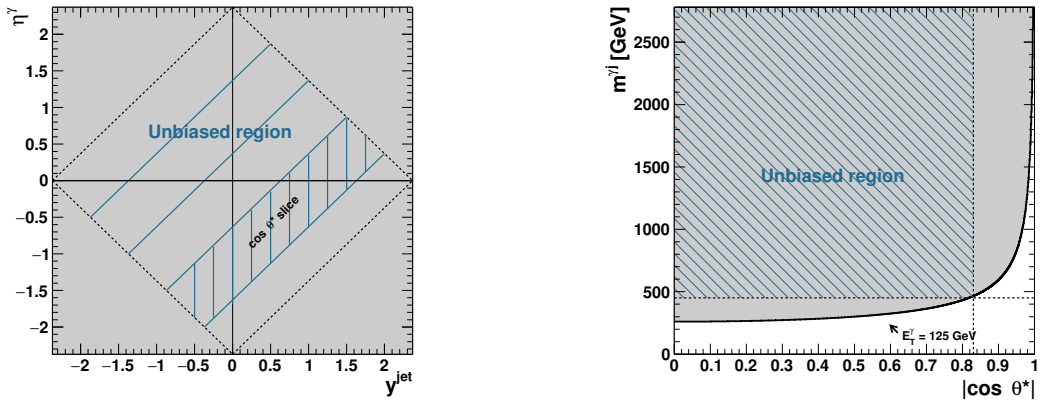

Figure 5.8: The selected regions in the η^{γ}-y^{jet} and $m^{\gamma-\mathrm{jet}}$-$|\cos\theta^*|$ planes. (Left) $\eta^{\gamma} + y^{\mathrm{jet}} = 2.37$ (first quadrant), $\eta^{\gamma} - y^{\mathrm{jet}} = 2.37$ (second quadrant), $\eta^{\gamma} + y^{\mathrm{jet}} =$ -2.37 (third quadrant) and $\eta^{\gamma} - y^{\mathrm{jet}} = 2.37$ (fourth quadrant). (Right) the horizontal (vertical) dashed line corresponds to $m^{\gamma-\mathrm{jet}} > 450$ GeV ($|\cos\theta^*| < 0.83$) and the solid line corresponds to $E_{\mathrm{T}}^{\gamma} = 125$ GeV.

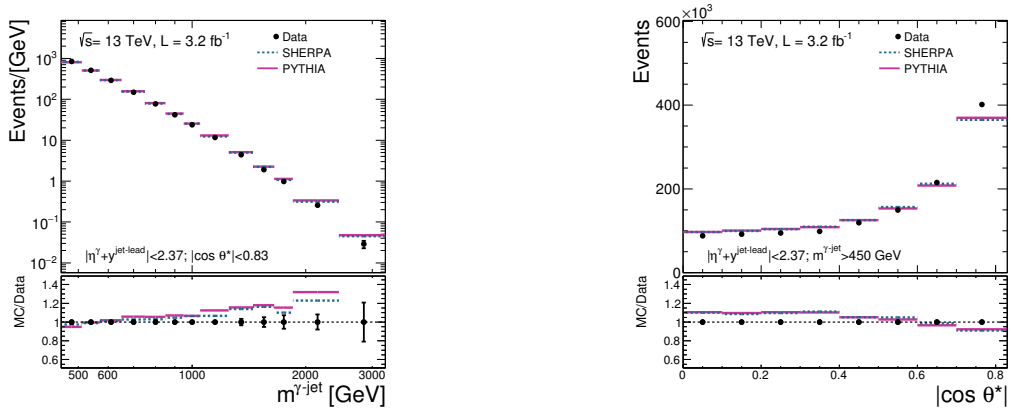

Figure 5.9: The measured $m^{\gamma-\text{jet}}$, and $|\cos\theta^*|$ distributions in the photon+jet sample. For comparison, the MC simulations of the signal from PYTHIA and SHERPA are also included. Both MC simulations are normalised to the data. The lower part of the figures shows the ratio of the MC to the data distribution.

5.5 Trigger efficiency

The efficiency of the trigger used in this analysis (HLT_g120_loose) was evaluated from the data using lower-threshold prescaled triggers. Specifically, the efficiency was evaluated using the HLT_g100_loose trigger (which has a threshold energy of 100 GeV) as:

$$\epsilon_{trigger} = \frac{N_{HLT\_g100\_loose \otimes HLT\_g120\_loose}}{N_{HLT\_g100\_loose}} \tag{5.1}$$

where $N_{HLT\_g100\_loose \otimes HLT\_g120\_loose}$ is the number of events that pass all the selection criteria listed in the previous sections and fullfill the conditions of the triggers HLT_g100_loose and HLT_g120_loose. $N_{HLT\_g100\_loose}$ is the number of events that pass all the selection criteria listed in the previous sections and fullfill the conditions of the trigger HLT_g100_loose. This procedure relies on the assumption that the HLT_g100_loose is 100 % efficient for photons [76] with $E_{\text{T}}^{\gamma} > 125$ GeV. The resulting efficiencies of the HLT_g120_loose trigger for the selected photon+jet sample are:

- tight and isolated selection: > 99.4 %;
- tight and non-isolated selection: > 98.4 %;
- non-tight and isolated selection: > 98.3 %;

- non-tight and non-isolated selection: > 97.5 %.

The above selected samples correspond to the regions A, B, C and D, respectively, of the data-driven background-subtraction method. Figures 5.10 to 5.13 show the trigger efficiency as a function of E_{T}^{γ}, $p_{\mathrm{T}}^{\mathrm{jet-lead}}$, $m^{\gamma-\mathrm{jet}}$, $|\cos\theta^{*}|$ and $\Delta\phi^{\gamma-\mathrm{jet}}$. The measurements of the differential cross sections are corrected for the trigger efficiency.

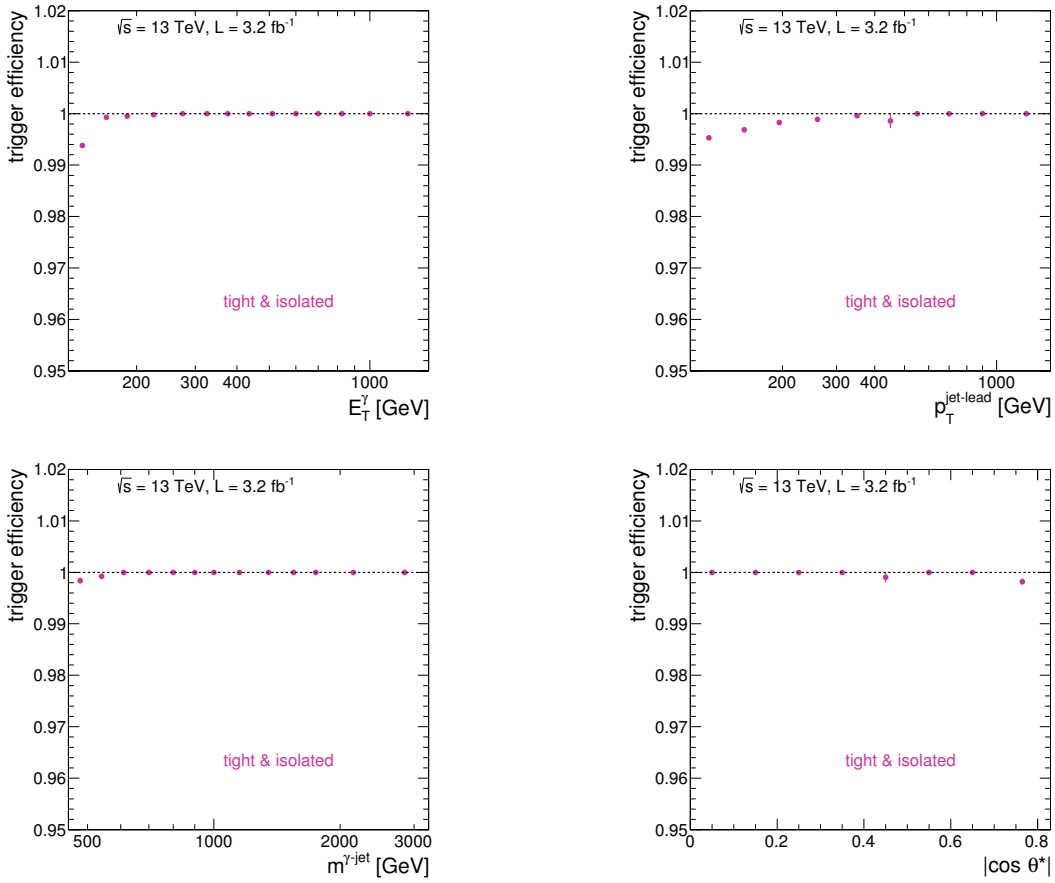

Figure 5.10: Trigger efficiency as a function of E_{T}^{γ}, $p_{\mathrm{T}}^{\mathrm{jet-lead}}$, $m^{\gamma-\mathrm{jet}}$ and $|\cos\theta^{*}|$ for the tight and isolated (signal) region.

5.5.1 Trigger efficiency uncertainty

The efficiency of the trigger used in this analysis (HLT_g120_loose) for each data sample together with its uncertainty is listed below:

- photon+jet: efficiency = 99.70 ± 0.02 (stat) ± 0.21 (syst) %;

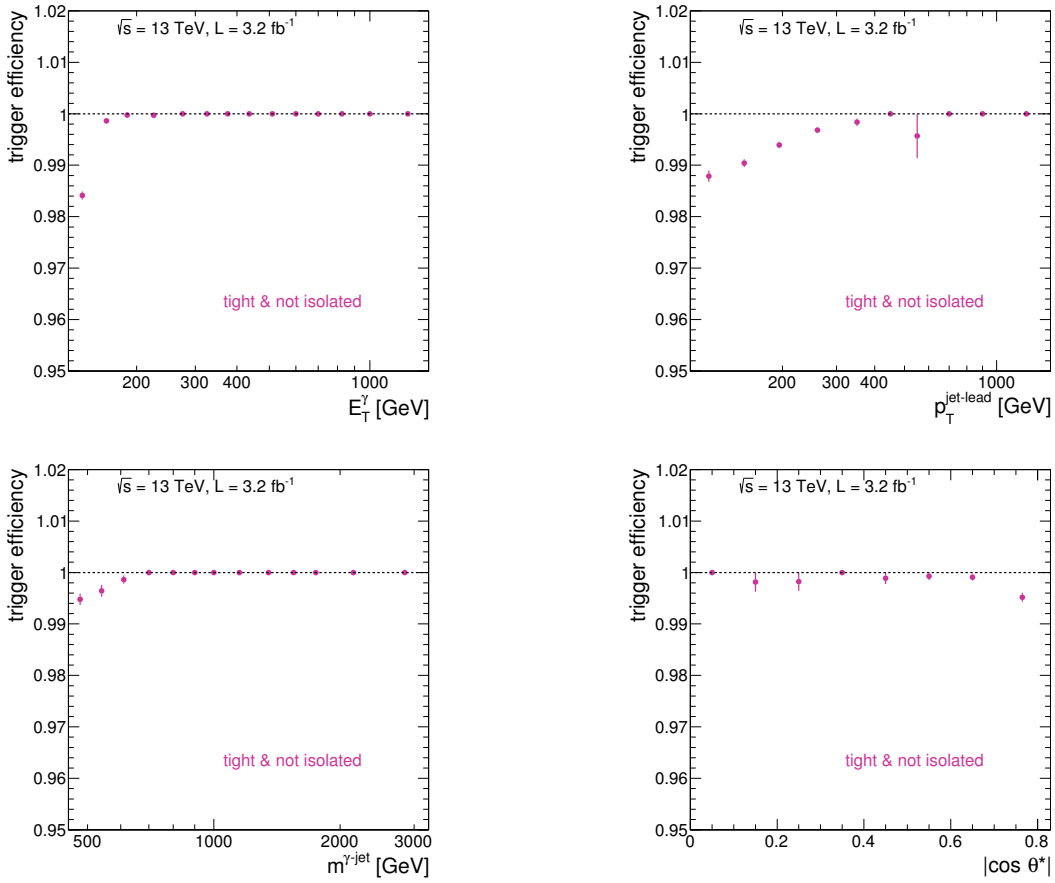

Figure 5.11: Trigger efficiency as a function of E_{T}^{γ}, $p_{\mathrm{T}}^{\mathrm{jet-lead}}$, $m^{\gamma-\mathrm{jet}}$ and $|\cos\theta^{*}|$ for the tight and not isolated region.

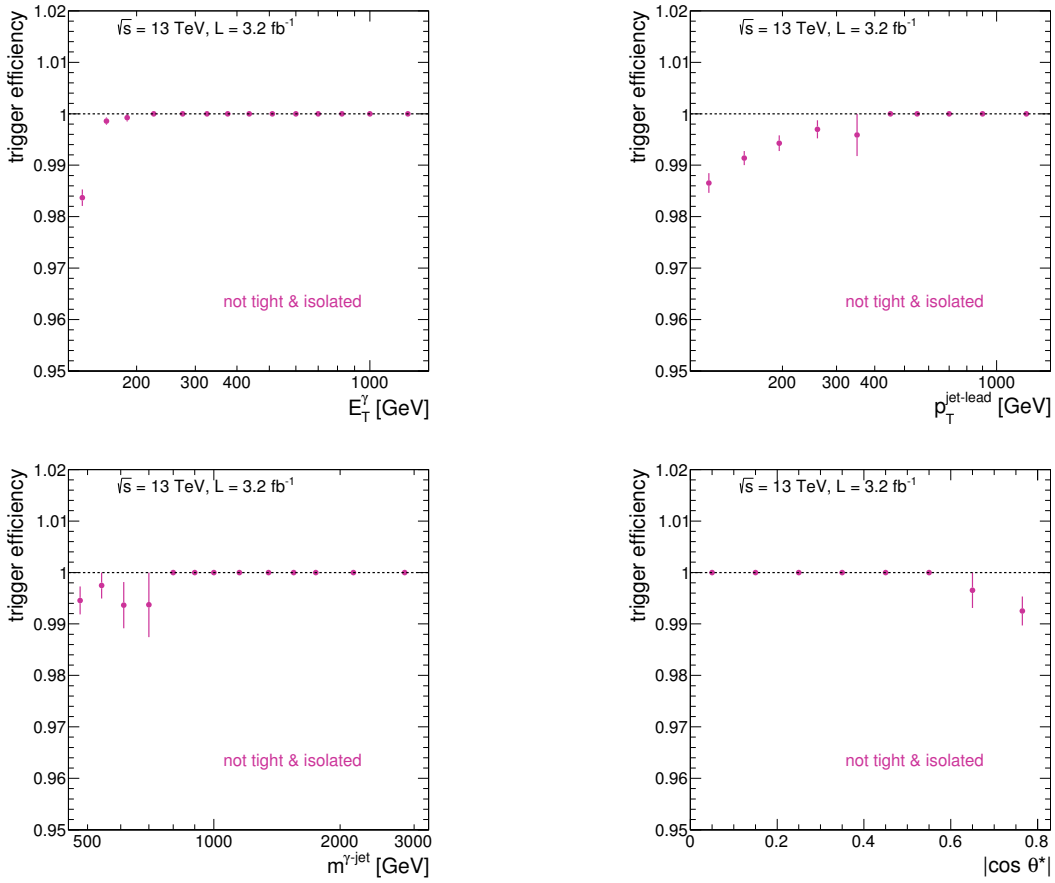

Figure 5.12: Trigger efficiency as a function of E_{T}^{γ}, $p_{\mathrm{T}}^{\mathrm{jet-lead}}$, $m^{\gamma-\mathrm{jet}}$ and $|\cos\theta^{*}|$ for the non tight and isolated region.

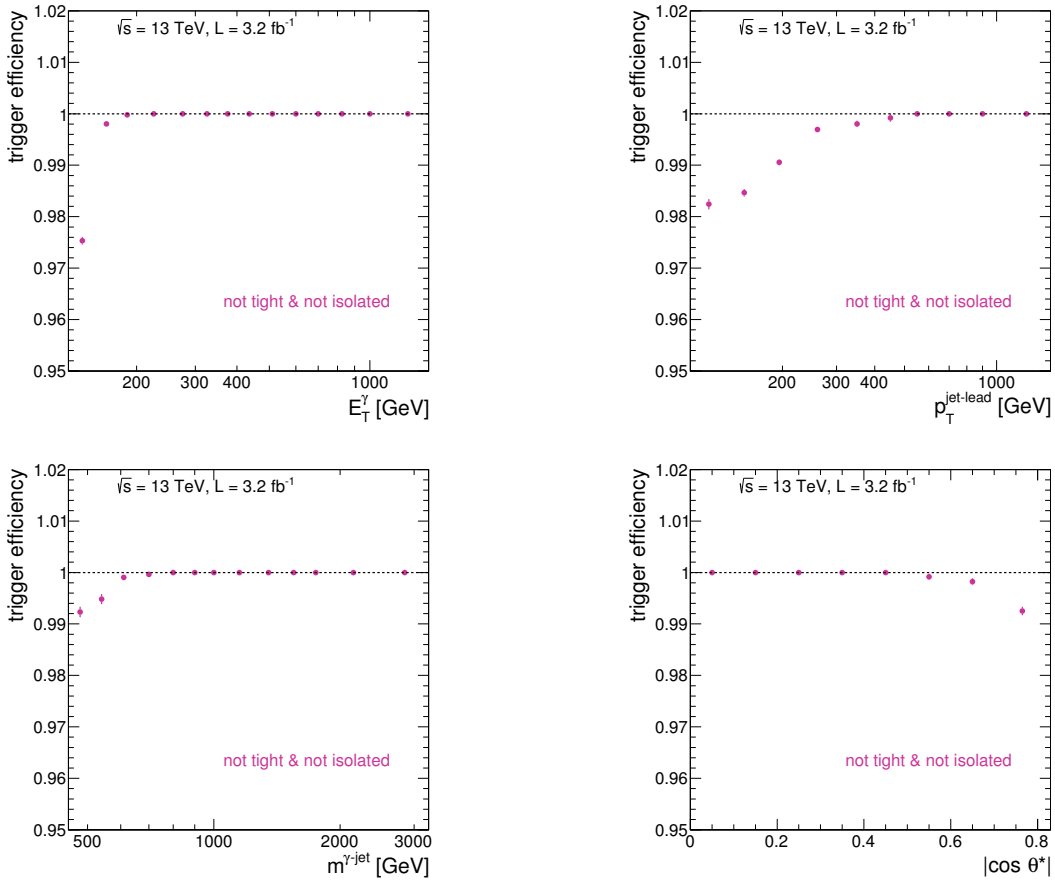

Figure 5.13: Trigger efficiency as a function of E_{T}^{γ}, $p_{\mathrm{T}}^{\mathrm{jet-lead}}$, $m^{\gamma-\mathrm{jet}}$ and $|\cos\theta^{*}|$ for the non tight and non isolated region.

- photon+jet with additional requirements for $m^{\gamma-jet}$ and $|\cos\theta^*|$ distributions: efficiency = 99.92 ± 0.03 (stat) ± 0.05 (syst) %;

The statistical uncertainty is computed using Bayesian confidence intervals and corresponds to the efficiency measured in data with a bootstrap method [79] over HLT_g100_loose. The systematic uncertainty is calculated as the standard deviation between the efficiency computed in data and MC. For this study, the trigger requirement is applied on the SHERPA MC since these are the baseline for unfolding the data. This comparison between MC and data is expected to contain the effect in the efficiency of the background in the data sample. This is a conservative approach since these differences also contain the inaccuracies of the detector description in MC, the uncertainty on the μ-reweighting plus any small difference in the kinematics of signal events.

5.6 Additional corrections to simulated events

Additional corrections were applied to the simulated events to match the overall event conditions of the data sample and to account for known differences between data and simulation. These corrections are:

- pileup corrections: to match the in-time and out-of-time pileup conditions in the data, the distribution of $< \mu >$ in simulated events is reweighted to that of the data. Figure 5.14 shows the distribution of $< \mu >$ for data, after applying a general scale factor of 1/1.16, to achieve a better agreement between data and MC for the distribution of the number of primary vertices, before and after the application of such corrections. The reweighting factors for PYTHIA and SHERPA are very similar. These corrections are then propagated through the whole analysis. Figure 5.15 shows the distribution in the number of primary vertices for data and MC, before and after the application of these factors;

- photon identification corrections: fudge factors are applied to the photon shower-shape variables in the signal MC simulated events to correct for the differences observed between data and MC simulation in the photon-cluster discriminating variables;

- photon isolation corrections: since the MC simulations of the $E_{\mathrm{T}}^{\mathrm{iso}}$ do not describe the position of the peak in the data, data-driven corrections to the simulated simulated $E_{\mathrm{T}}^{\mathrm{iso}}$ variable are applied as a shift of the isolation distribution for each photon in each event;

- photon-energy smearing corrections to account for the differences in energy resolution between data and simulations.

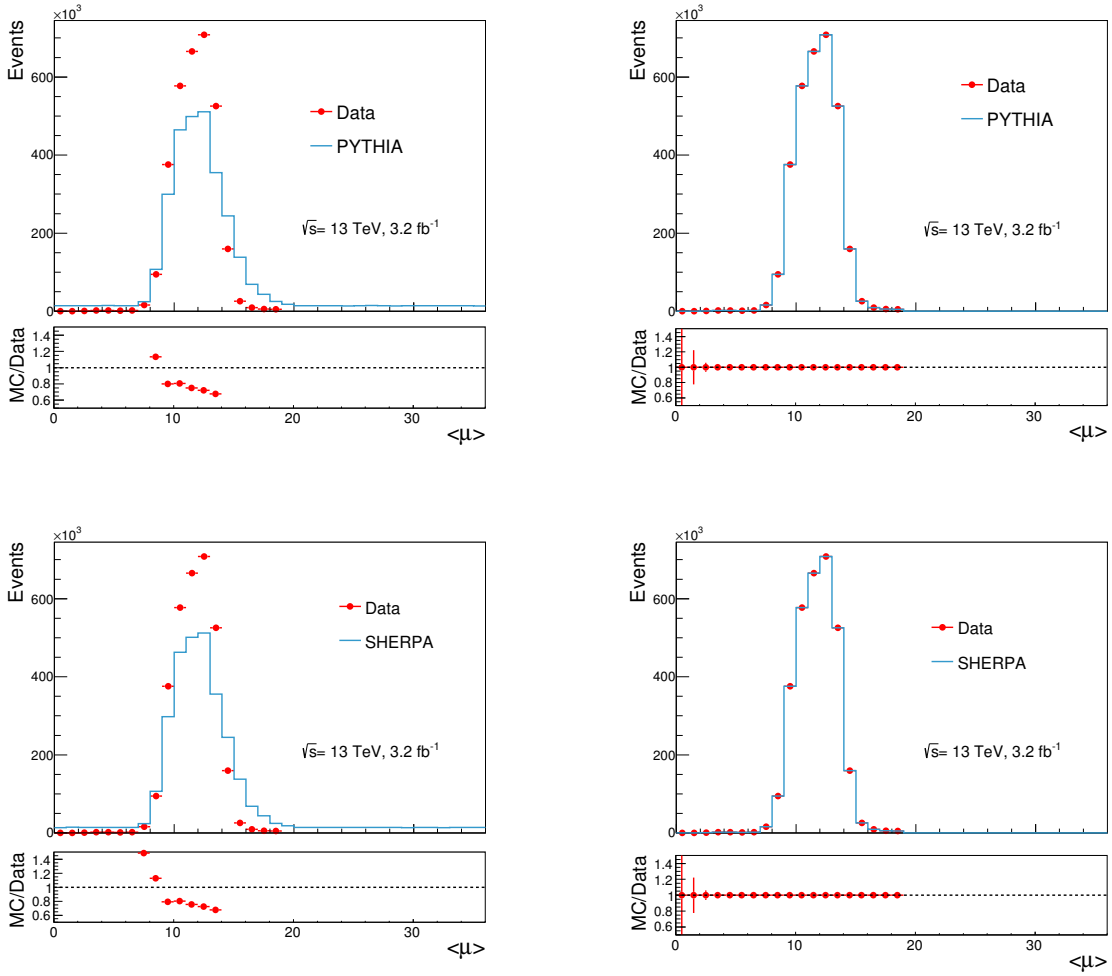

Figure 5.14: Distribution of the average number of interactions per bunch crossing for the sample of loose' photons in data (dots) and PYTHIA or SHERPA (histograms) before (left) and after (right) reweighting.

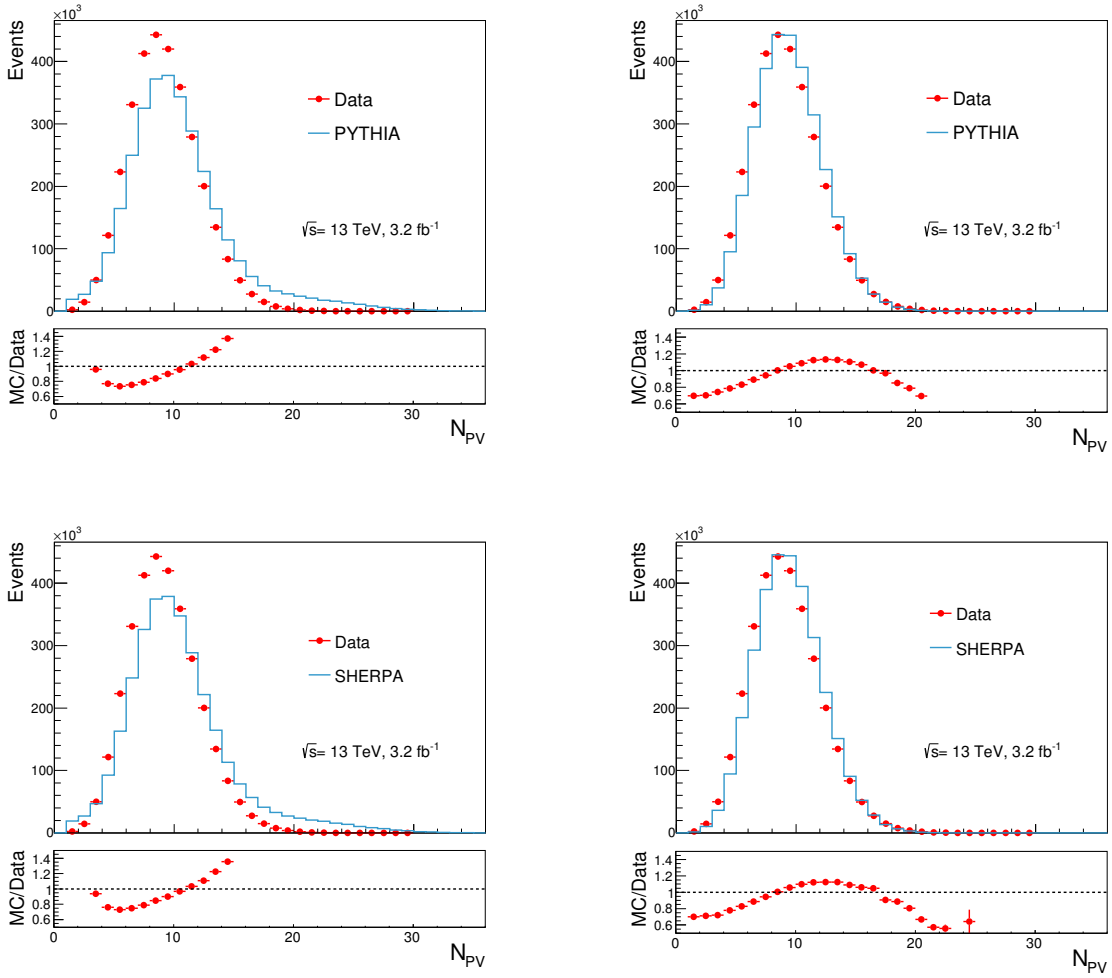

Figure 5.15: Distribution of the number of primary vertices for the sample of loose' photons in data (dots) and PYTHIA or SHERPA (histograms) before (left) and after (right) reweighting.

5.7 Background estimation and subtraction

A non-negligible contribution of background remains in the selected sample, even after the application of the tight identification and isolation requirements. This background originates predominantly from multi-jet processes, in which a jet is misidentified as a photon. This jet usually contains a light neutral meson, predominantly, a π^0 that decays into two collimated photons, which carry most of the energy of the jet. The subtraction of the small remaining background is performed using a data-driven technique based on the ABCD method. Before performing the background subtraction, it is important to study first the distributions in $E_{\mathrm{T}}^{\mathrm{iso}}$ for data and MC. A comparison of the distributions in $E_{\mathrm{T}}^{\mathrm{iso}}$ for tight and non-tight photon candidates in data in the background control regions is needed to support the adequacy of these regions in the ABCD method. In addition, the adequacy of the description of the $E_{\mathrm{T}}^{\mathrm{iso}}$ distribution in data by the MC simulatons for the signal needs to be addressed in view of the requirement on $E_{\mathrm{T}}^{\mathrm{iso}}$ as well as of the use of the MC simulations to estimate the signal leakage fractions. The isolation profile of a signal-enriched sample was extracted from the data. For this study, a sample was obtained by applying all the selection criteria described in the previous section, except for the tight and isolation requirements. Two sub-samples were selected by applying the tight identification criteria: the sub-sample of candidates that fulfill the selection requirements (tight subsample) and the sub-sample of candidates that pass the loose' criteria but fail the tight requirements (non-tight sample). The non-tight subsample is expected to be enriched in background candidates. The $E_{\mathrm{T}}^{\mathrm{iso}}$ distribution for these samples are shown in Figure 5.16. The $E_{\mathrm{T}}^{\mathrm{iso}}$ distribution of the non-tight candidates was scaled so that the integral for $E_{\mathrm{T}}^{\mathrm{iso}} > 10$ GeV, where the contribution from the signal is exprected to be small, is the same as the integral of the tight candidates for $E_{\mathrm{T}}^{\mathrm{iso}} > 10$ GeV. The rescaled background distribution is subtracted from that of the tight photon candidates to extract the isolation profile of signal-like candidates, as shown in Figure 5.16. It is observed that the MC simulations exhibit a peak which reproduces that in the data; this is the result of applying the data-driven corrections on $E_{\mathrm{T}}^{\mathrm{iso}}$ in the MC simulations, otherwise the peak is somewhat shifted towards lower values of $E_{\mathrm{T}}^{\mathrm{iso}}$ with respect to the data. The estimation of the background from the MC samples is not reliable. Therefore, a background-subtraction method, which does not rely on MC samples of background, is devised using signal-suppressed control regions to obtain a purer photon signal sample. The method is briefly summarized below [77] [78]. The background contamination is estimated and then subtracted by using a counting technique based

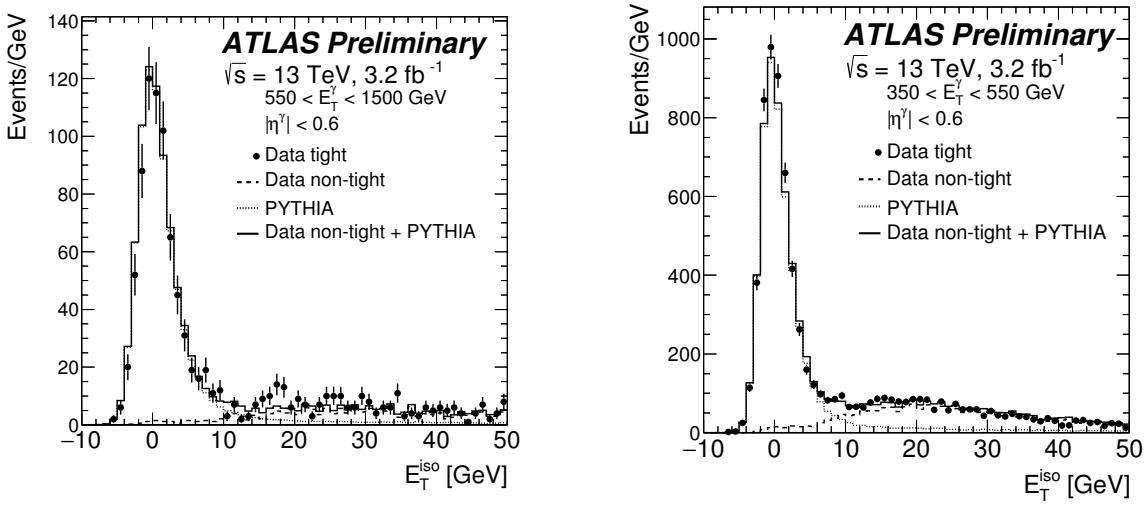

Figure 5.16: (Left) the measured $E_{\mathrm{T}}^{\mathrm{iso}}$ before applying the isolation requirement, for the events that pass (black dots) and fail (dashed line) the tight identification criteria. For comparison, the MC simulations of PYTHIA and SHERPA are also included. (Right) the measured $E_{\mathrm{T}}^{\mathrm{iso}}$ before applying the isolation requirement, after subtracking the non-tight to the tight events (black dots).

on the observed number of events in control regions of a two-dimentional plane. This subtraction is performed in each bin of each observable. The plane is defined by using the photon identification variable γ_{ID} and the $E_{\mathrm{T}}^{\mathrm{iso}}$ variable, as shown in Figure 5.17. These two variables are chosen because they are expected to be uncorrelated for the backgroung events. Four regions are defined in this plane:

- "A" is the signal region, which contains tight and isolated ($E_{\mathrm{T}}^{\mathrm{iso}} < 4.2 \cdot 10^{-3} \cdot E_{\mathrm{T}}^{\gamma} + 4.8$ GeV) photon candidates;
- "B" is the control region, which contains tight and non-isolated ($E_{\mathrm{T}}^{\mathrm{iso}} > 4.2 \cdot 10^{-3} \cdot E_{\mathrm{T}}^{\gamma} + (4.8 + 2)$ GeV) photon candidates. An upper cut on $E_{\mathrm{T}}^{\mathrm{iso}}$ of 50 GeV is also imposed;
- "C" is the control region, which contains non-tight and isolated ($E_{\mathrm{T}}^{\mathrm{iso}} < 4.2 \cdot 10^{-3} \cdot E_{\mathrm{T}}^{\gamma} + 4.8$ GeV) photon candidates;
- "D" is the background control region, which contains non-tight and non-isolated ($E_{\mathrm{T}}^{iso} > 4.2 \cdot 10^{-3} \cdot E_{\mathrm{T}}^{\gamma} + (4.8 + 2)$ GeV) photon candidates. An upper cut on $E_{\mathrm{T}}^{\mathrm{iso}}$ of 50 GeV is also imposed;

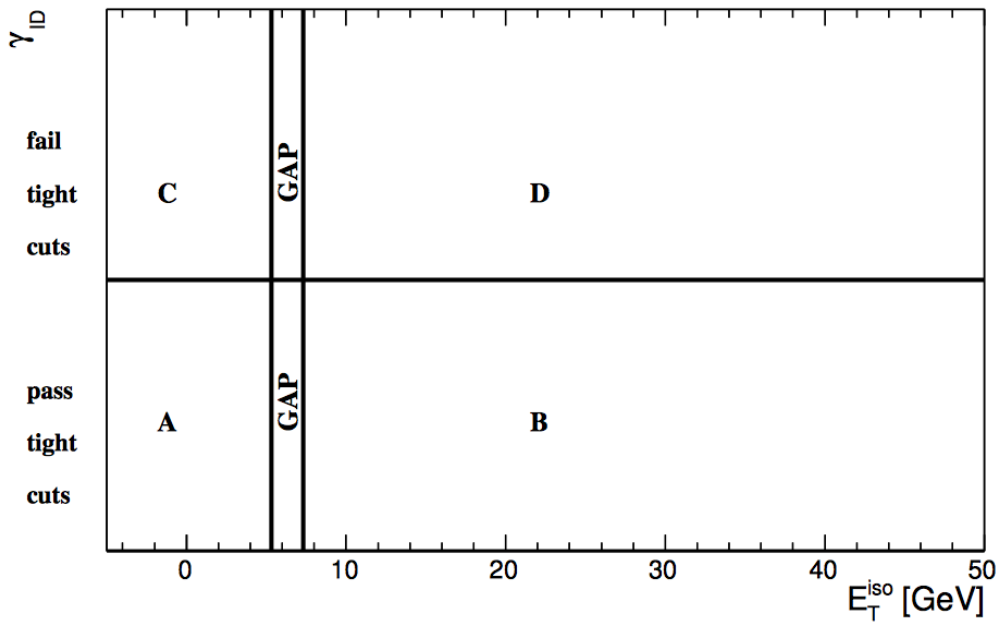

Figure 5.17: Illustration of the two-dimensional plane of the photon identification variables vs. the transverse isolation energy used to estimate the background yield in the signal region A, from the observed yields in the three control regions, B, C and D. The vertical lines correspond to the requirements on $E_{\mathrm{T}}^{\mathrm{iso}}$ for $E_{\mathrm{T}}^{\gamma} = 125$ GeV

Therefore, the number of signal events in the signal region A is given by

$$N_{\mathrm{A}}^{sig} = N_{\mathrm{A}} - R_{\mathrm{bckg}} \cdot (N_{\mathrm{B}} - \epsilon_{\mathrm{B}} \cdot N_{\mathrm{A}}^{sig}) \cdot \frac{(N_{\mathrm{C}} - \epsilon_{\mathrm{C}} \cdot N_{\mathrm{A}}^{\mathrm{sig}})}{(N_{\mathrm{D}} - \epsilon_{\mathrm{D}} \cdot N_{\mathrm{A}}^{\mathrm{sig}})} \tag{5.2}$$

where $N_{\mathrm{A}}^{\mathrm{sig}}$ is the expected number of signal events, N_{k}, with k = A, B, C, D is the number of observed events in each region and

$$R_{\mathrm{bckg}} = \frac{N_{\mathrm{A}}^{\mathrm{bckg}} \cdot N_{\mathrm{D}}^{\mathrm{bckg}}}{N_{\mathrm{B}}^{\mathrm{bckg}} \cdot N_{\mathrm{C}}^{\mathrm{bckg}}} \tag{5.3}$$

is taken as $R_{\mathrm{bckg}} = 1$ for the nominal results; $N_{\mathrm{k}}^{\mathrm{bckg}}$, with k = A, B, C, D is the number of background events in each region. R_{bckg} is a measure of the correlation between γ_{ID} and $E_{\mathrm{T}}^{\mathrm{iso}}$ in background events. Deviations with respect to $R_{\mathrm{bckg}} = 1$ are taken into account as systematic uncertainties. Eq. 5.3 takes into account the expected number of signal events in the three background control regions via the signal leakage fractions, $\epsilon_{\mathrm{k}} = N_{\mathrm{k}}^{\mathrm{sig}}/N_{\mathrm{A}}^{\mathrm{sig}}$

with k= B, C, D. The signal leakage fractions are extracted from the MC simulations of the signal and are shown in Figures 5.18 and 5.19 for PYTHIA and SHERPA, respectively and then compared together 5.20. The fraction $\epsilon_{\rm C}$, which represents the signal leaking into the non-tight and isolated control region, is approximately constant for all variables and very similar for PYTHIA and SHERPA. The fraction $\epsilon_{\rm B}$, signal leakage into the tight and non-isolated control region, is smaller for SHERPA than PYTHIA; this is due to the different treatment of the brem component in the two MC simulations. The fraction $\epsilon_{\rm D}$, the signal leakage into the non-tight and non-isolated control region, is very different between PYTHIA and SHERPA; this is the region most affected by the different treatment of the brem component in both models. The fractions $\epsilon_{\rm B}$ and $\epsilon_{\rm C}$ increases as functions of some variables, for example in $p_{\rm T}^{\rm jet-lead}$, due to the increasing fraction of the brem component as $p_{\rm T}^{\rm jet-lead}$ increases. The signal purity, computed as $P = N_{\rm A}^{\rm sig}/N_{\rm A}$, is shown in Figure 5.21 for the PYTHIA and SHERPA MC samples. For some of the points at high $E_{\rm T}^{\gamma}$, $p_{\rm T}^{jet-lead}$ and $m^{\gamma-{\rm jet}}$ in which the purity is above the unity or consistent with the unity but with a large statistical uncertainty, the purity was set to 1. The purity is in general above 90 % for the estimation using either PYTHIA or SHERPA to compute the signal leakage fractions. The error bars in the figures account for statistical uncertainties in the data for the signal region A as well as for the control regions B, C and D.

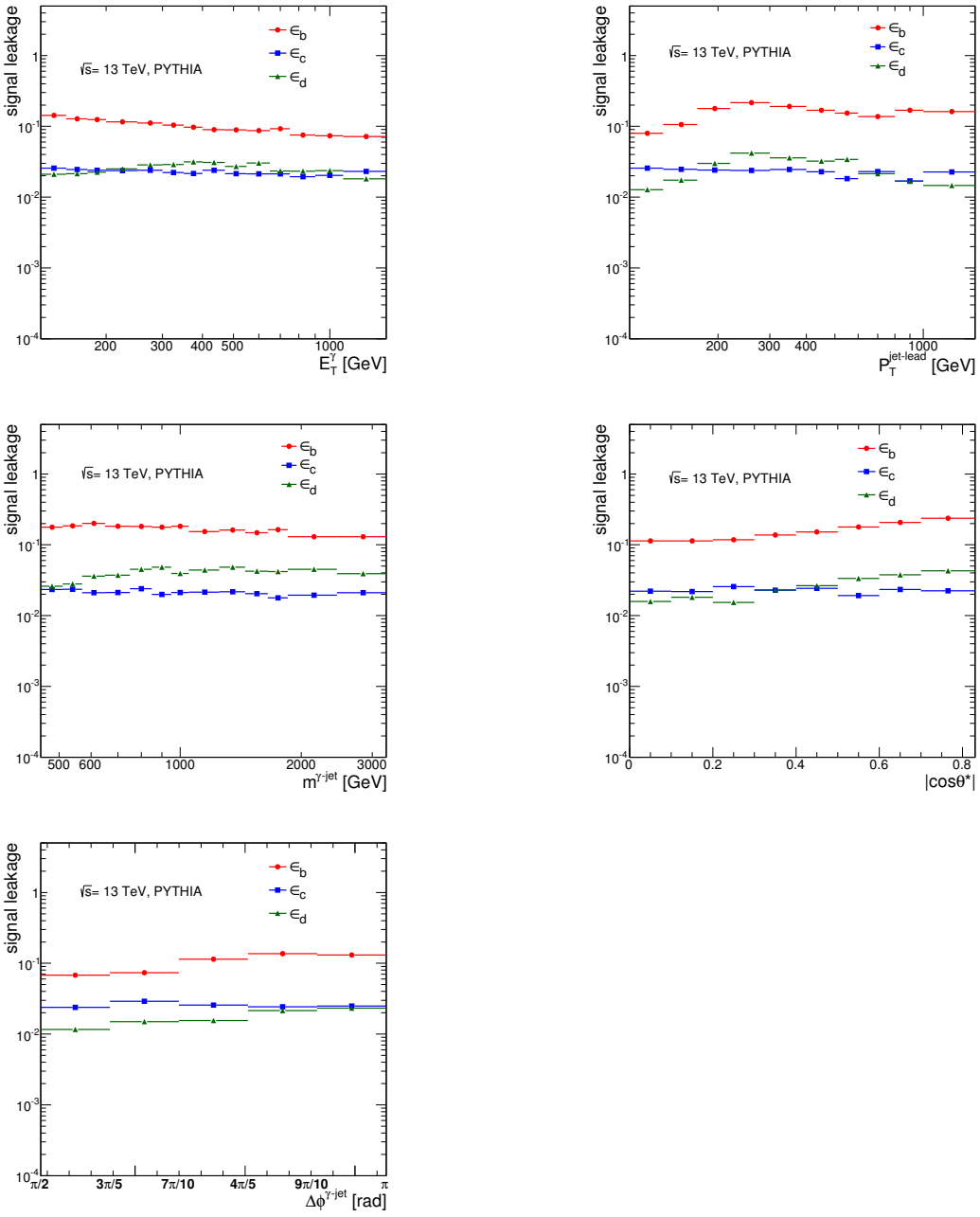

Figure 5.18: Signal leakage fractions from PYTHIA for B (dots), C (squares) and D (triangles) control regions as functions of the studied variables.

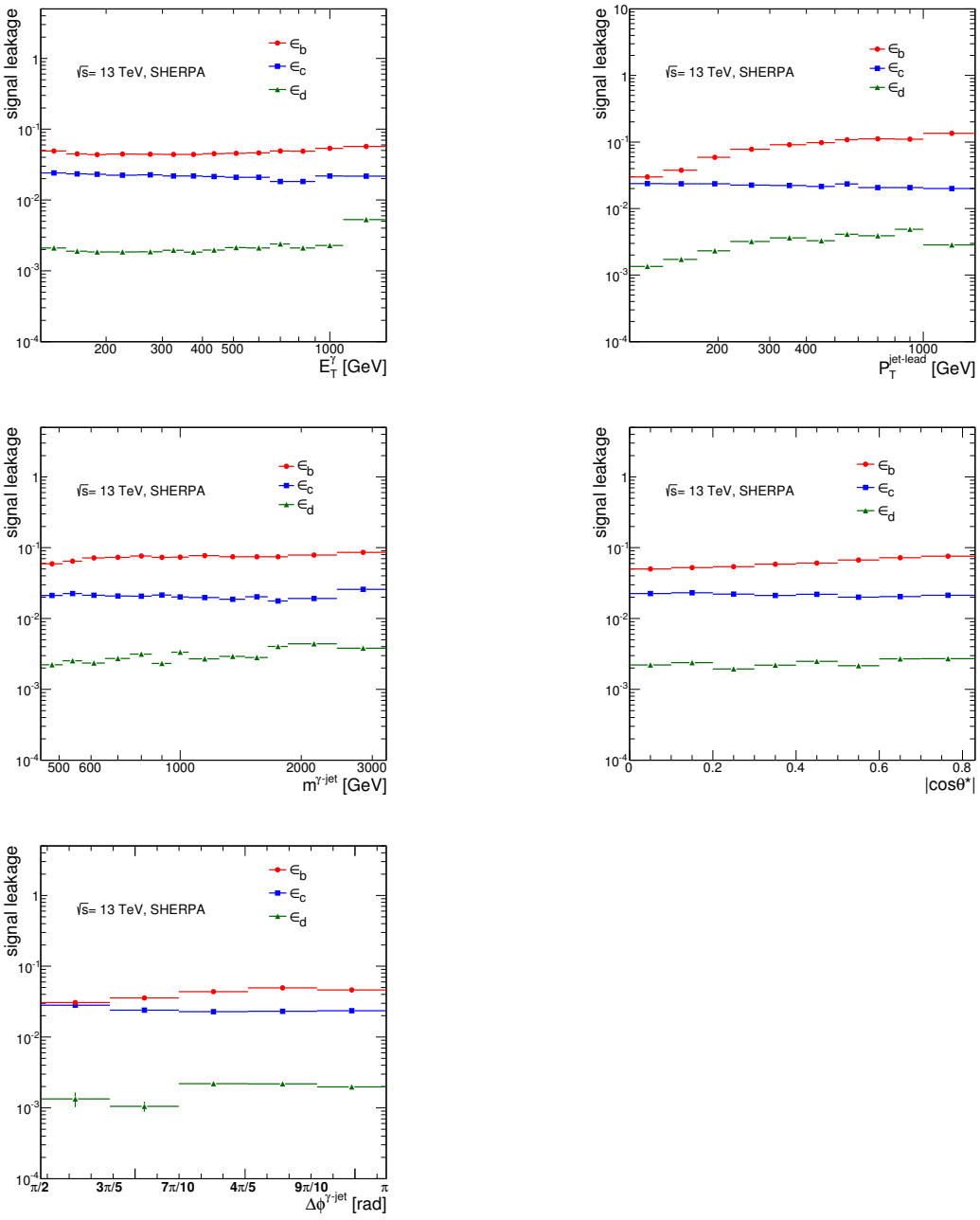

Figure 5.19: Signal leakage fractions from SHERPA for B (dots), C (squares) and D (triangles) control regions as functions of the studied variables.

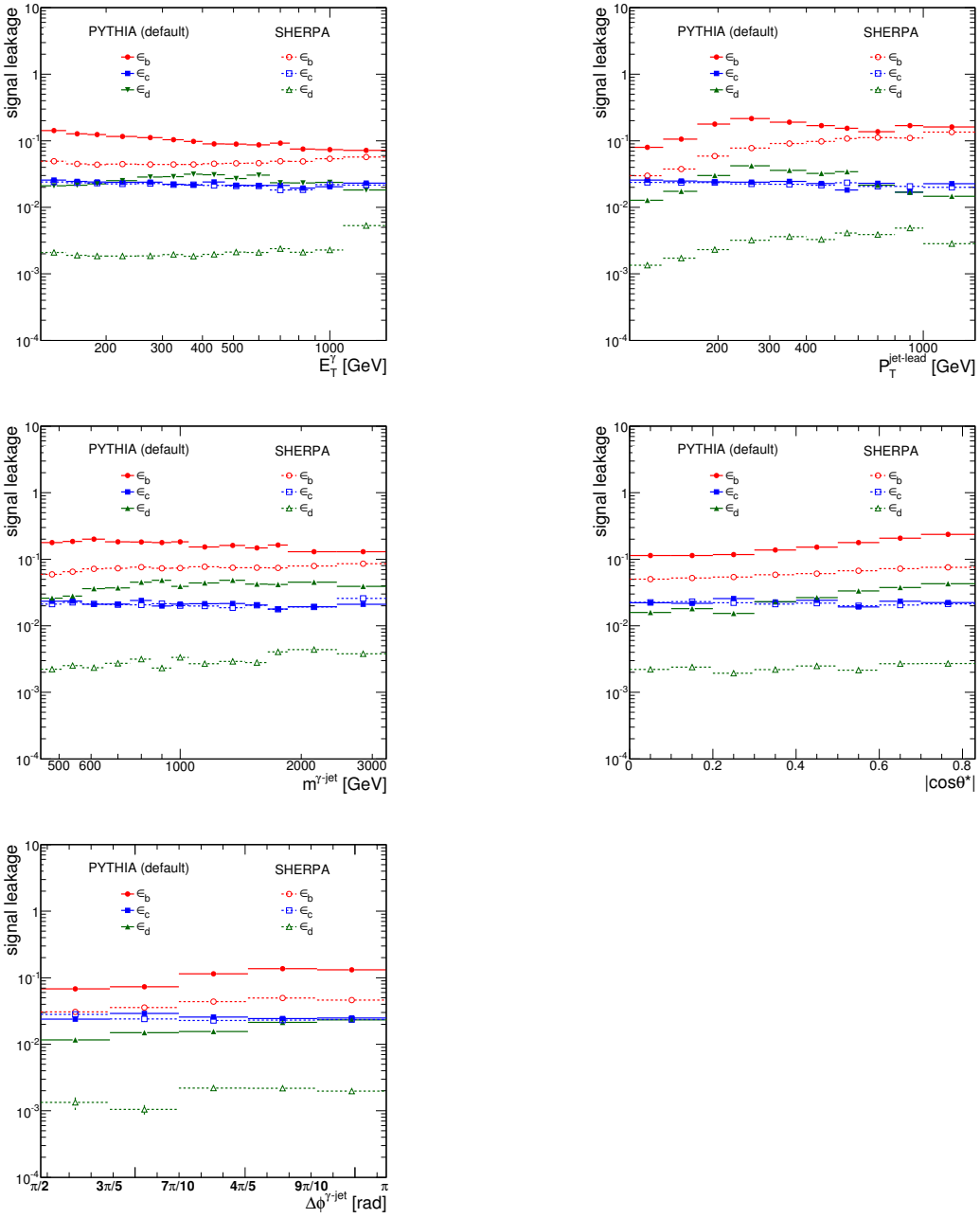

Figure 5.20: Signal leakage fractions from PYTHIA and SHERPA for B (dots), C (squares) and D (triangles) control regions as functions of the studied variables.

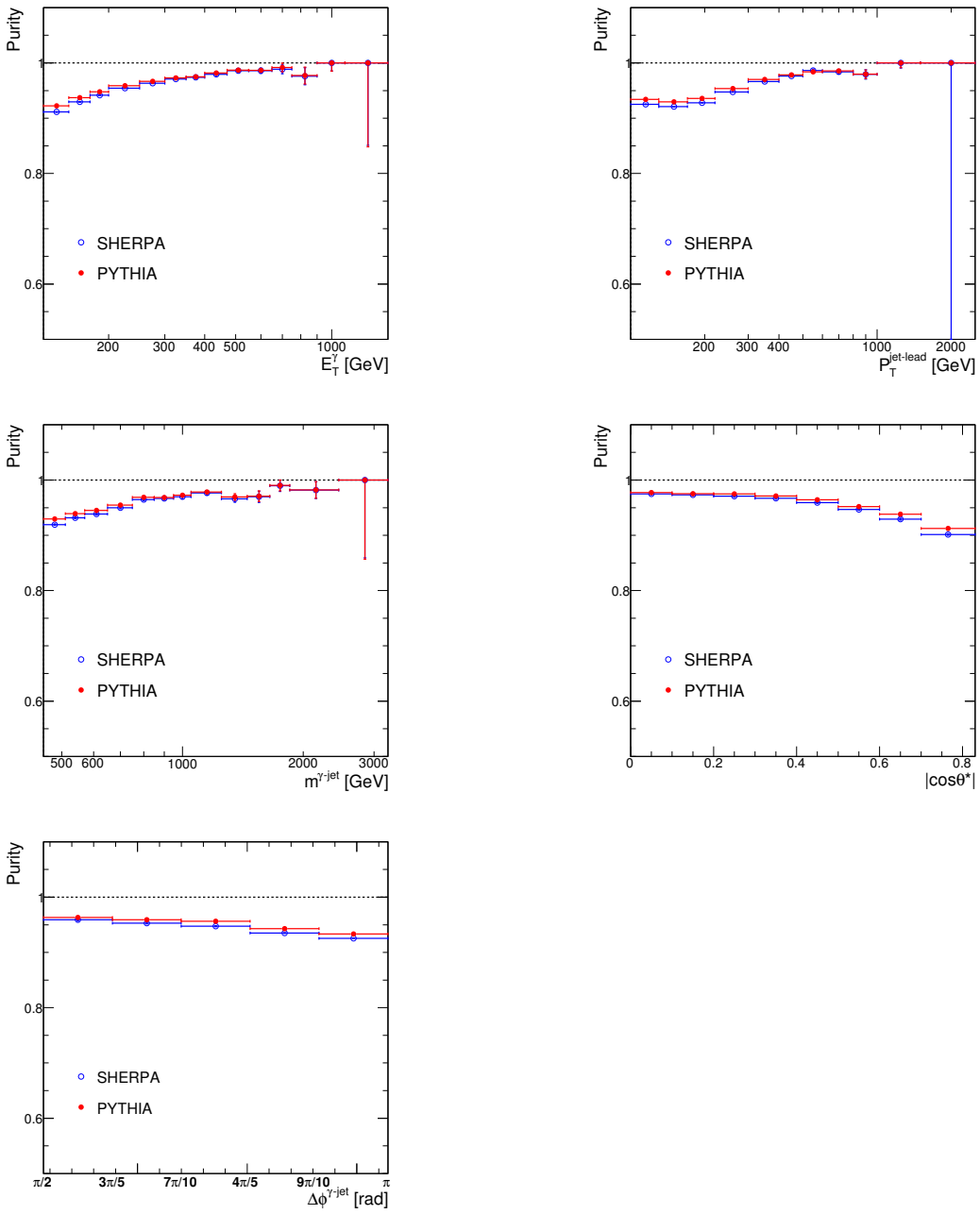

Figure 5.21: Estimated signal purities in data using PYTHIA (dots) and SHERPA (open circles) as a function of E_{T}^{γ}, $p_{\mathrm{T}}^{\mathrm{jet-lead}}$, $\Delta\phi^{\gamma-\mathrm{jet}}$,$m^{\gamma-\mathrm{jet}}$ and $|\cos\theta^*|$.

5.7.1 Background from electrons faking photons

The background from electrons faking photons is investigated using SHERPA 2.2 MC samples for W/Z + jet. The fraction of W + jets background to photon+jet production as a function of the different variables is shown in Figure 5.22. The fraction of Z + jets background to photon+jet production as a function of the different variables is shown in Figure 5.23. As expected, the background from electrons faking photons is negligible. The use of the MC samples for the estimation of this source of background is supported by the data-driven studies performed in [80].

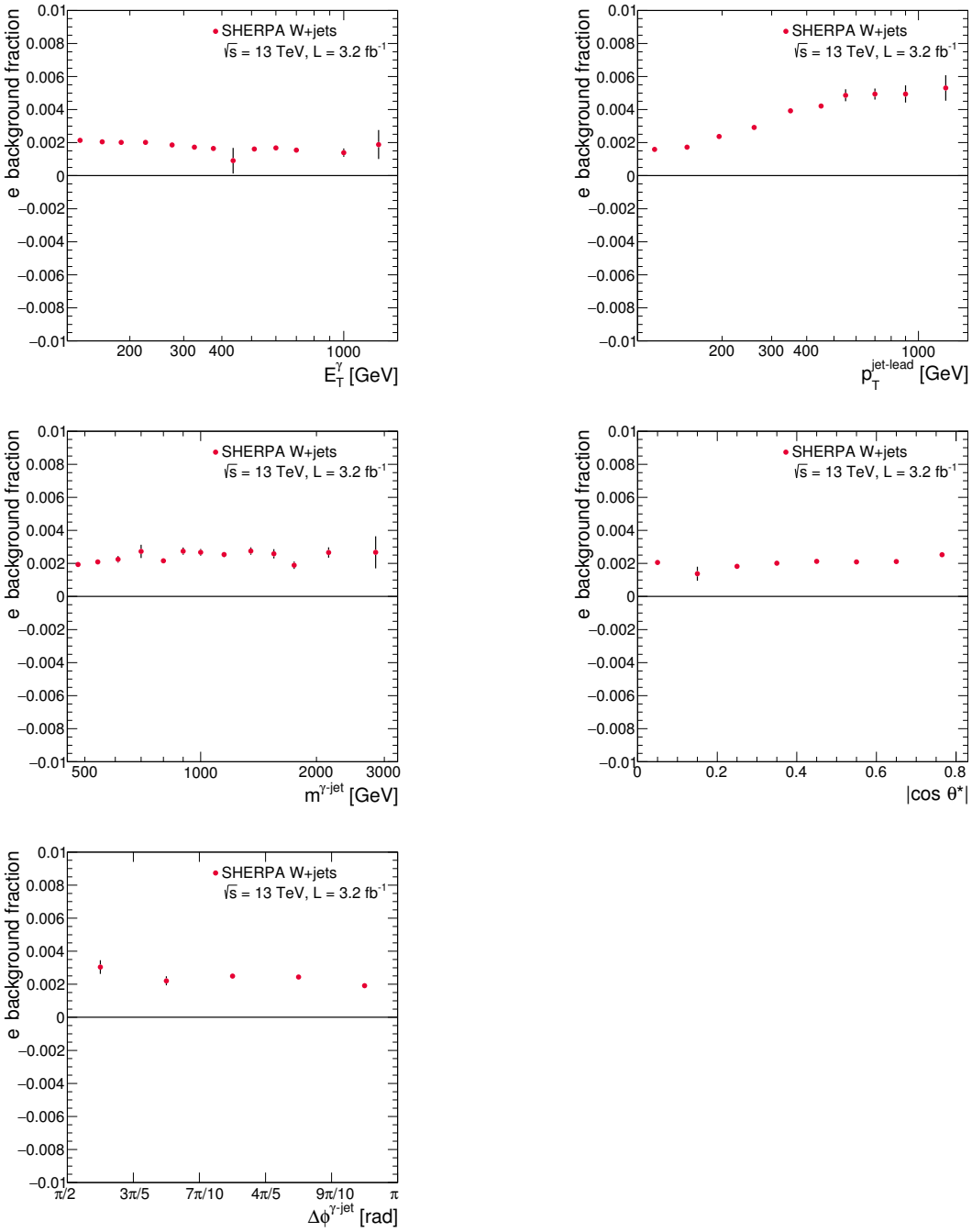

Figure 5.22: Fraction of W+jet background to photon+jet production as a function of E_{T}^{γ}, $p_{\mathrm{T}}^{\mathrm{jet-lead}}$, $m^{\gamma-\mathrm{jet}}$ and $|\cos\theta^{*}|$ using the MC samples of SHERPA 2.2. Truth matching to $e^{\pm}$ is applied with $\Delta R < 0.2$. The error bars represent the statistical uncertainty of the MC samples.

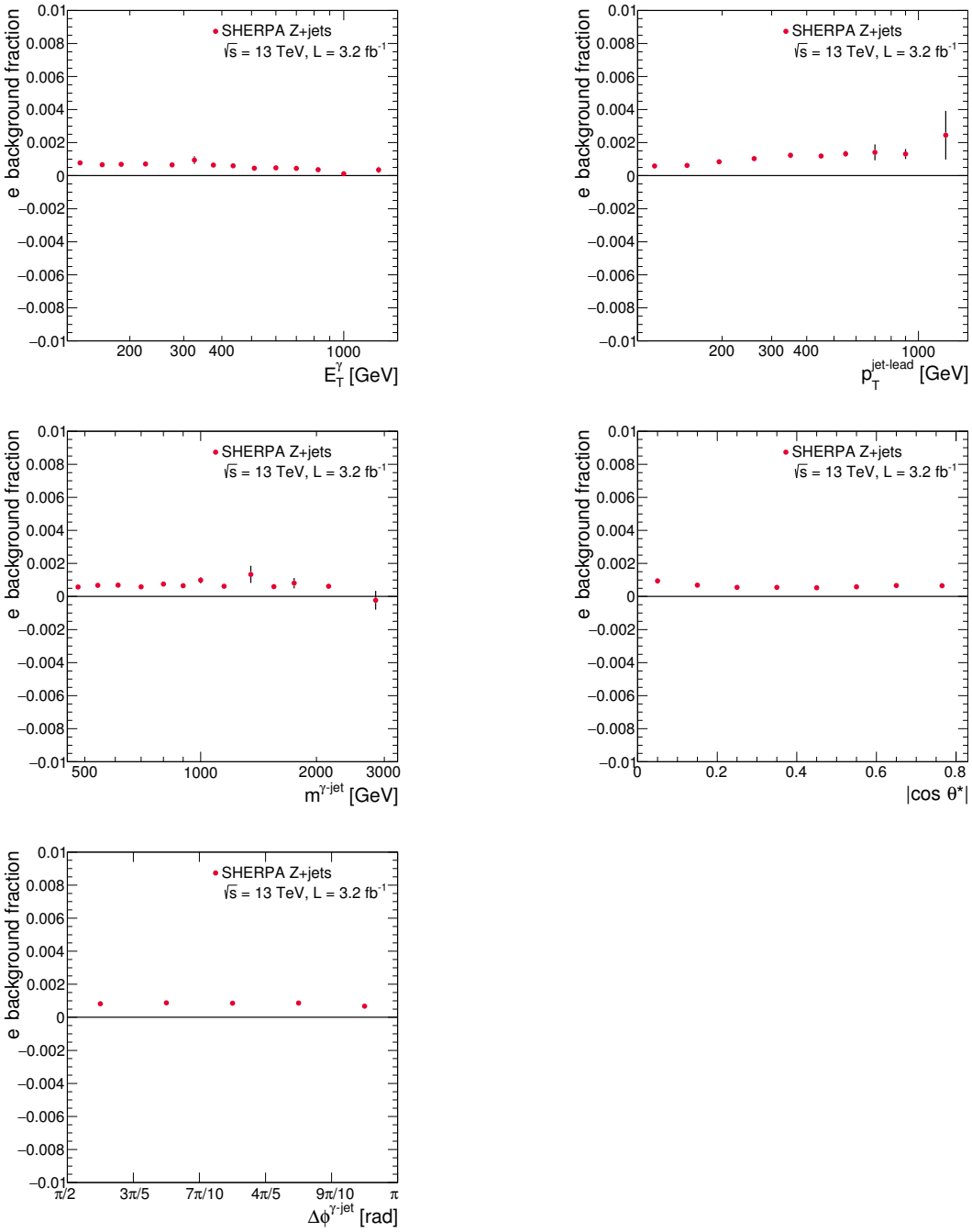

Figure 5.23: Fraction of Z+jet background to photon+jet production as a function of E_{T}^{γ}, $p_{\mathrm{T}}^{\mathrm{jet-lead}}$, $m^{\gamma-\mathrm{jet}}$ and $|\cos\theta^{*}|$ using the MC samples of SHERPA 2.2. Truth matching to $e^{\pm}$ is applied with $\Delta R < 0.2$. The error bars represent the statistical uncertainty of the MC samples.

5.8 Detector-level results

The estimated signal yields using the signal leakage fractions from PYTHIA or SHERPA are shown in Figures 5.24 and 5.25, in which the MC simulations are normalized to the data. Figure 5.24 show the measured E_{T}^{γ} distribution; both PYTHIA and SHERPA provide a good description of the data, except at high E_{T}^{γ}. The measured $p_{\mathrm{T}}^{\mathrm{jet-lead}}$ distribution is also shown in Figure 5.24; PYTHIA describes the data only at low $p_{\mathrm{T}}^{\mathrm{jet-lead}}$ values, whereas SHERPA gives a good description of the data in the full measured range. The measured $m^{\gamma-\mathrm{jet}}$, $|\cos\theta^{*}|$ and $\Delta\phi^{\gamma-\mathrm{jet}}$ distributions are shown in Figure 5.25. Both PYTHIA and SHERPA provide a good description of the data, except at high $m^{\gamma-\mathrm{jet}}$. The description by SHERPA of the measured $\Delta\phi^{\gamma-\mathrm{jet}}$ distribution is good, while that by PYTHIA is somewhat poorer.

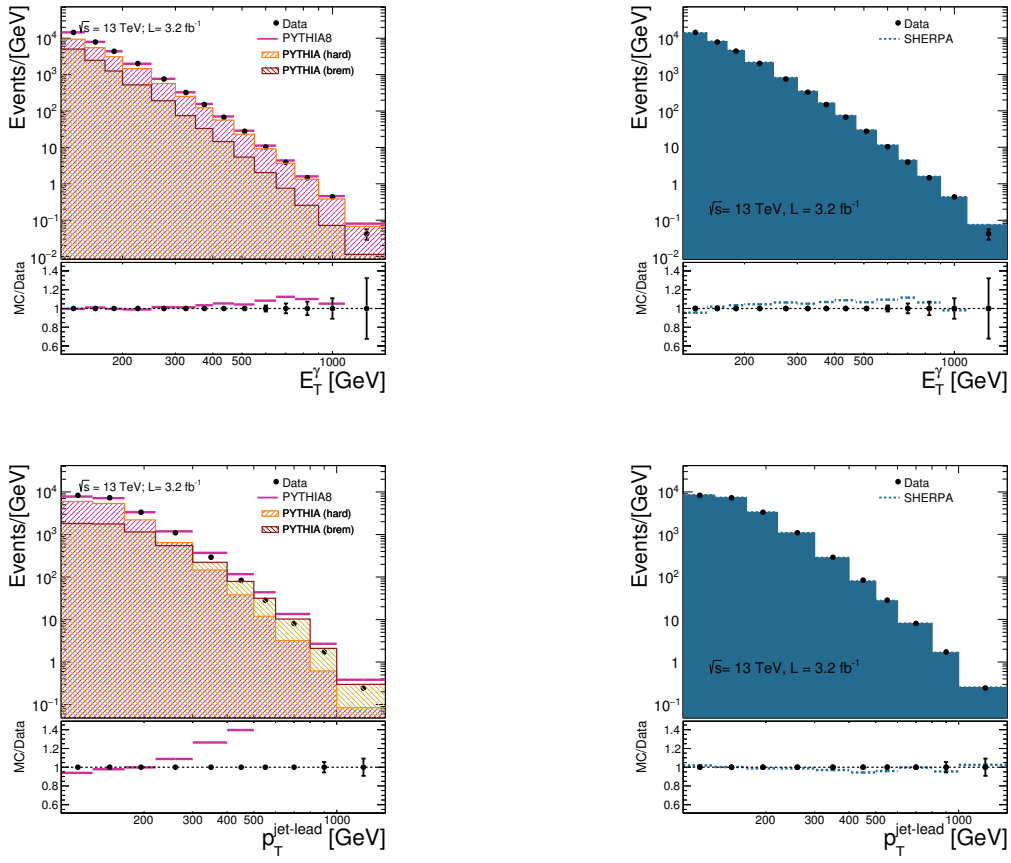

Figure 5.24: The estimated signal yields in data using signal leakage fraction from PYTHIA (left) or SHERPA (right) as a function of E_{T}^{γ} and $p_{\mathrm{T}}^{\mathrm{jet-lead}}$. For comparison, the MC simulations of the signal from PYTHIA and SHERPA are also included. The hard and brem component are also shown in the left figures. The ratio of the MC to the data is shown in the lower part of each figure.

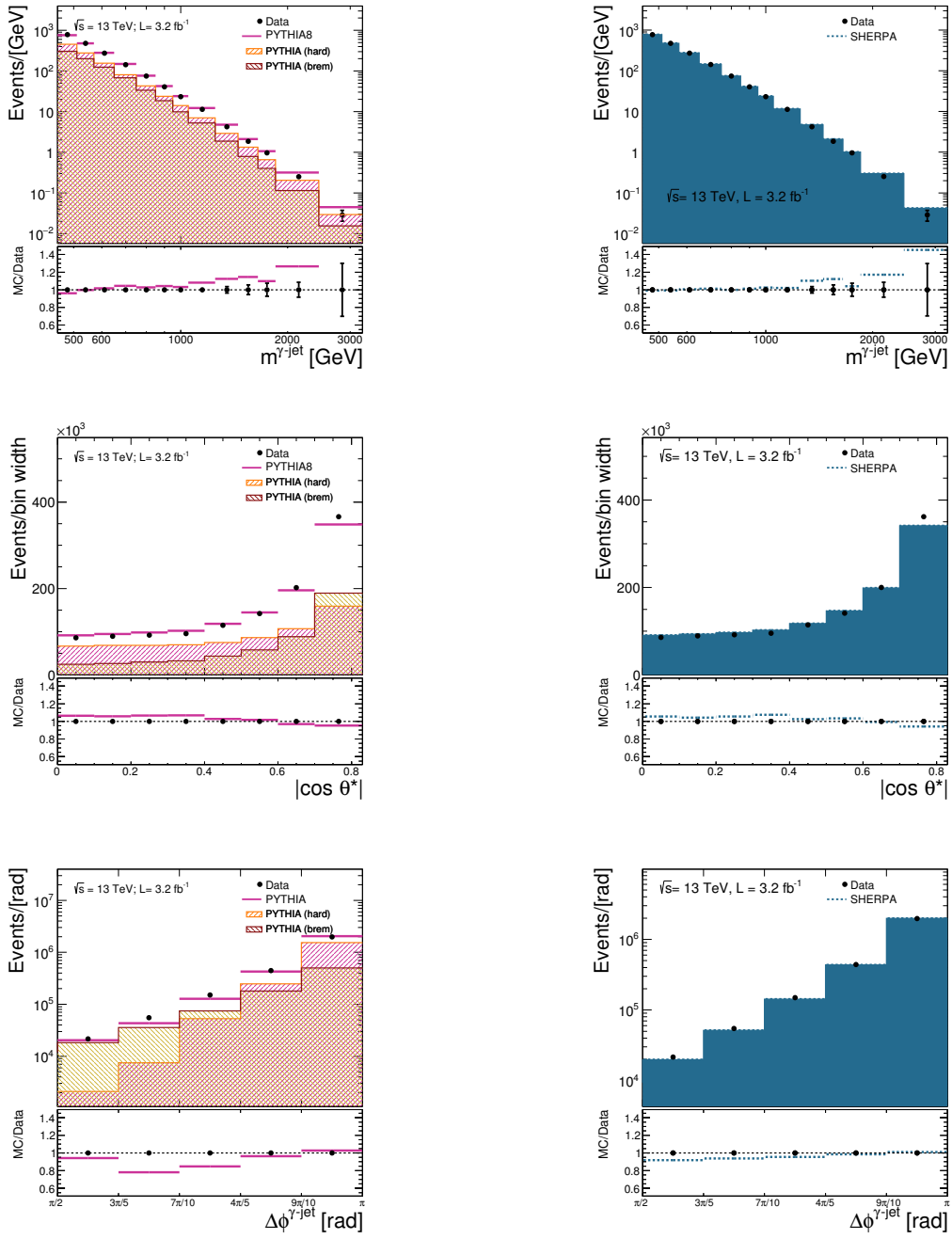

Figure 5.25: The estimated signal yields in data using signal leakage fraction from PYTHIA (left) or SHERPA (right) as a function of $m^{\gamma-\text{jet}}$, $|\cos\theta^*|$ and $\Delta\phi^{\gamma-\text{jet}}$. For comparison, the MC simulations of the signal from PYTHIA and SHERPA are also included. The hard and brem component are also shown in the left figures. The ratio of the MC to the data is shown in the lower part of each figure.

5.8.1 Optimization of the MC description

To study in more detail the success or failure of the PYTHIA MC simulations to describe the data distribution, the hard and brem contributions are shown in Figures 5.24 and 5.25. It is observed that the shape of the two components is quite different. Therefore, the shape of the MC distributions depends on the relative fraction of these two contributions. An improvement of the description of the data by the PYTHIA MC is achieved by performing a χ^2 fit to each data distribution of the relative fraction of the hard (α) and the brem (1 - α) contributions as the free parameter; α = 0.5 reproduces the original prediction of PYTHIA. The χ^2 function used is

$$\chi^2(\alpha) = \sum_i \Big(\frac{N_{\rm A}^{\rm sig}(i) - N_{\rm A}^{\rm MC}(i,\alpha)}{\Delta N_{\rm A}^{\rm sig}(i)} \Big)^2 \tag{5.4}$$

where the sum runs over the bins of a given distribution, $\Delta N_{\rm A}^{\rm sig}(i)$ is the statistical uncertainty in the data signal yield in bin i,

$$N_{\rm A}^{\rm MC}(i,\alpha) = \frac{N_{\rm A}^{\rm sig,TOT}}{\alpha N_{\rm A}^{\rm MC,H,TOT} + (1-\alpha) N_{\rm A}^{\rm MC,B,TOT}} (\alpha N_{\rm A}^{\rm MC,H}(i) + (1-\alpha) N_{\rm A}^{\rm MC,B}(i)) \tag{5.5}$$

and α is the free parameter in the fit. The other used symbols are defined as:

- $N_{\rm A}^{\rm MC,H}(i)$ ($N_{\rm A}^{\rm MC,B}(i)$) is the number of simulated events from the hard (brem) component in bin i;
- $N_{\rm A}^{\rm MC,H,TOT}$ ($N_{\rm A}^{\rm MC,B,TOT}$) is the total number of simulated events from the hard (brem) component;
- $N_{\rm A}^{\rm sig,TOT}$ is the total signal yield in data.

The optimisation is done in two steps. In the first one, the distributions of the signal yield in data using the leakage fractions from PYTHIA default are fitted. In the second step, the signal yields in data were re-evaluated using the leakage fractions from PYTHIA in which the hard and brem contributions were mixed according to the fitted value of α obtained in the first step; the resulting distributions of the signal yield in data were again fitted. The α values in the two steps are so similar so no further iteractions are performed. A systematic uncertainty on the background subtraction due to this admixture is included. Figure 5.26 shows the leakage fractions with PYTHIA optimised (best) and SHERPA. From this figures is evident that PYTHIA' s $\epsilon_{\rm B}$ are now more similar to the SHERPA equivalent fraction. In Figure 5.27 the signal

purities extracted using the signal leakage fractions of PYTHIA optimised and SHERPA are compared. After the optimisation, the variables that require an higher brem component are now closer to the SHERPA points.

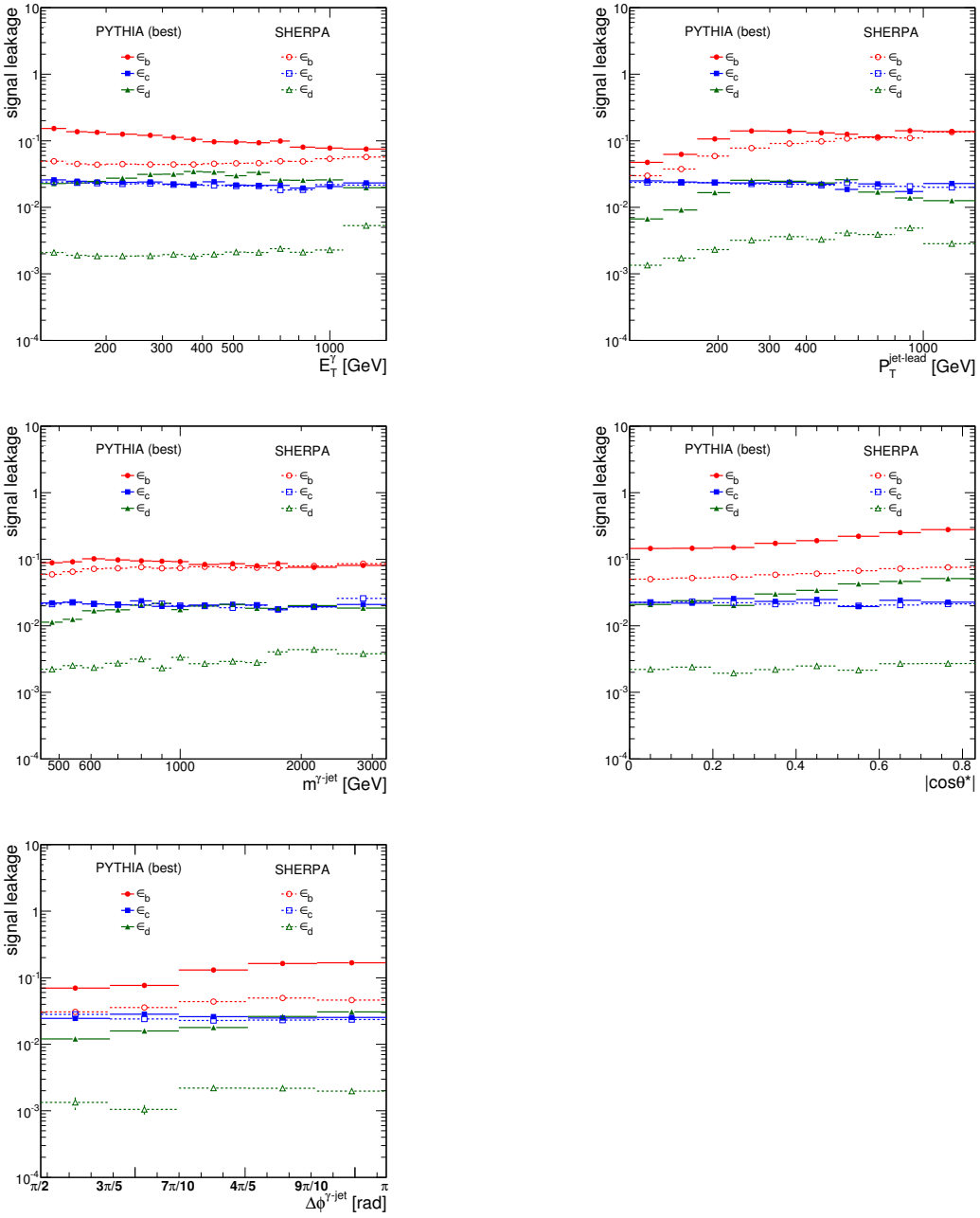

Figure 5.26: Signal leakage fractions from PYTHIA optimised and SHERPA for B (dots), C (squares) and D (triangles) control regions as functions of the studied variables.

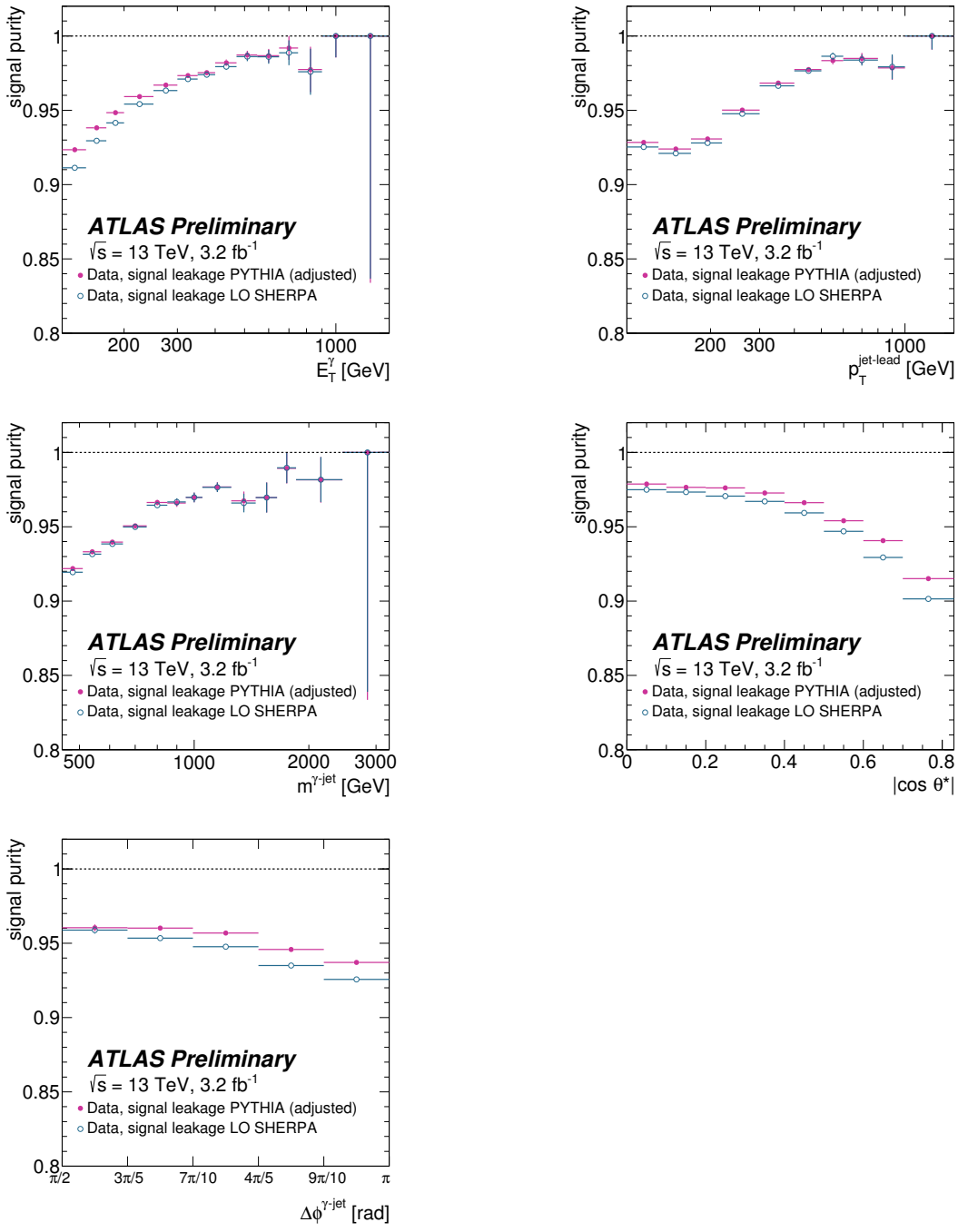

Figure 5.27: Estimated signal purities in data using PYTHIA (dots) and SHERPA (open circles) as a function of E_{T}^{γ}, $p_{\mathrm{T}}^{\mathrm{jet-lead}}$, $m^{\gamma-\mathrm{jet}}$ and $|\cos\theta^{*}|$.

Figure 5.28 shows the data distributions after the background subtraction (using the optimised admixture of hard and brem components in PYTHIA obtained in the second step) compared to the simulations of PYTHIA optimized and SHERPA. An improved description of the data by PYTHIA optimized is obtained. These data distributions are then used as the nominal signal yield in the cross section measurements. The resulting α fractions of the two components, together with the uncertainties in the fit are included in Table 5.1.

	α	$\Delta\alpha$
E_{T}^{γ}	0.4691	0.0070
$p_{\mathrm{T}}^{\mathrm{jet-lead}}$	0.6968	0.0030
$m^{\gamma-\mathrm{jet}}$	0.770	0.043
$\lvert\cos\theta^{*}\rvert$	0.3896	0.0067
$\Delta\phi^{\gamma-\mathrm{jet}}$	0.4023	0.0021

Table 5.1: Values of the fit free parameter α and its statistical uncertainty in the admixture of the hard and brem components in PYTHIA resulting from the fit to the data distributions. The fit is performed using MINUIT and the error treatment has been done using MIGRAD.

They are different for each observable. This is an expected feature since the two components are simulated to LO; the NLO QCD radiative corrections are expected to affect them differently and, furthermore, to entangle them, making any distinction physically impossible. In fact, variations between different observables are also observed in the application of the same procedure at parton level: the optimal value of α resulting from a fit of the parton-level predictions of the two components in PYTHIA to the NLO QCD calculations depends also on the variable. Thus, it is understood that the variation of the optimal value of α with the observable arises from higher-order effects; they can be mocked by mixing the LO descriptions of the two components in an observable-dependent way.

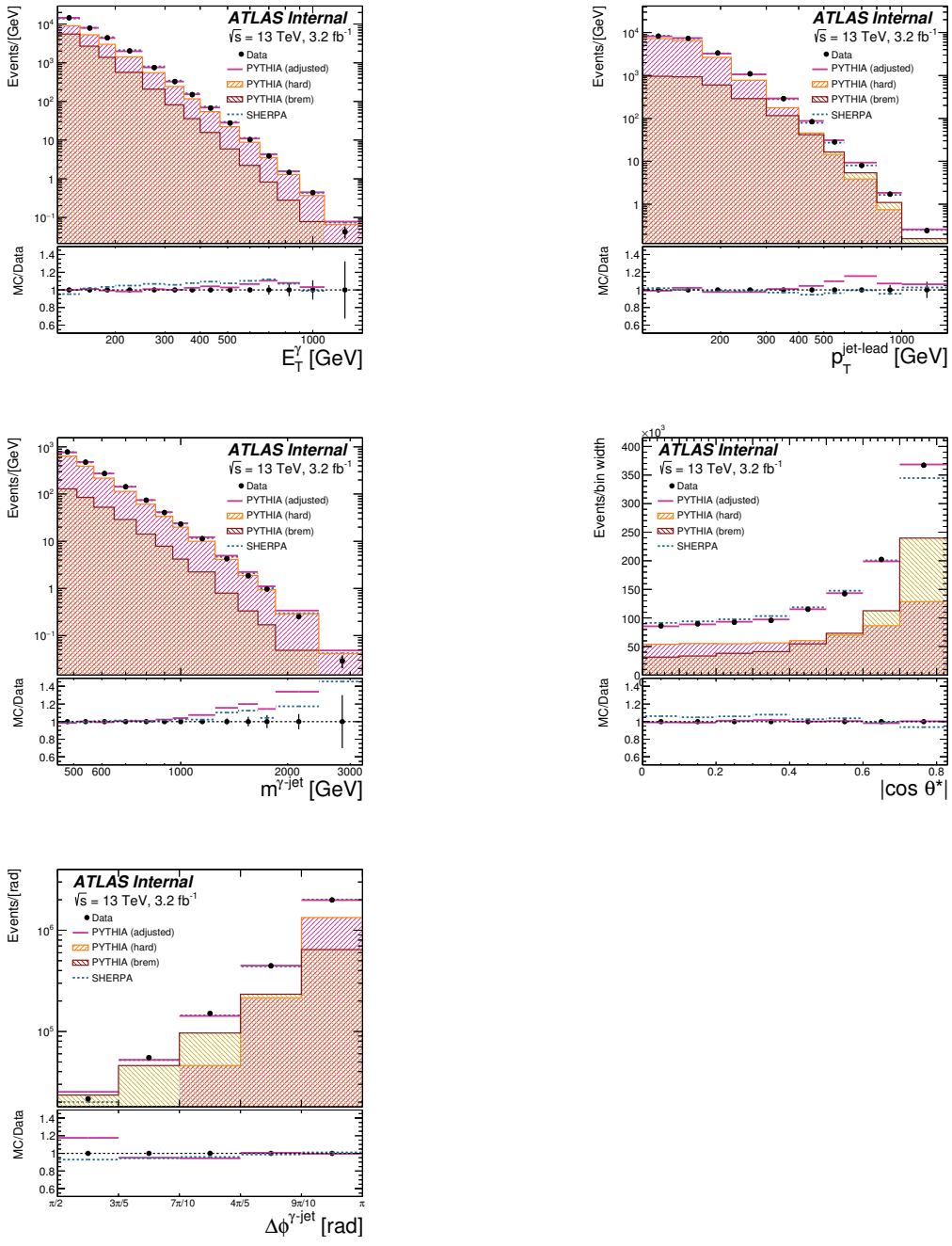

Figure 5.28: The estimated signal yields in data using signal leakage fraction from PYTHIA optimised as a function of E_{T}^{γ}, $p_{\mathrm{T}}^{\mathrm{jet-lead}}$, $m^{\gamma-\mathrm{jet}}$, $|\cos\theta^{*}|$ and $\Delta\phi^{\gamma-\mathrm{jet}}$. For comparison, the MC simulations of the signal from PYTHIA optimised and SHERPA are also included. The hard and brem component are also shown mixed according to the optimised value of α. The ratio of the MC to the data is shown in the lower part of each figure.

Chapter 6

Reconstruction quality and selection efficiency and purity

6.1 Reconstruction quality

The differential cross sections are obtained from the background-subtracted data distributions using a bin-by-bin method, as described in the previous section. To support the use of this method, the quality of the reconstruction has been studied. The signal reconstruction quality is evaluated using the MC samples. To assess the quality of the reconstruction, the variables at reconstructed and particle levels are compared in an event-by-event base. A MC event is required to fulfill both the requirements at the reconstruction and particle level; the particle and reconstructed level photons (jets) are required to be matched using the requirements $\Delta R < 0.2$ (0.4), where $\Delta R = \sqrt{(\Delta\eta)^2 + (\Delta\phi)^2}$.
Figures 6.1 and 6.2 show the correlation between the reconstruction and particle level for the variables studied for the PYTHIA optimized and SHERPA samples. The spread in $p_{\mathrm{T}}^{\mathrm{jet-lead}}$ and $m^{\gamma-\mathrm{jet}}$ is larger than in E_{T}^{γ}, $\Delta\phi^{\gamma-\mathrm{jet}}$ and $|\cos\theta^*|$ due to the better resolution in the photon transverse energy and angular variables. A good reconstruction quality is obtained for all the variables.

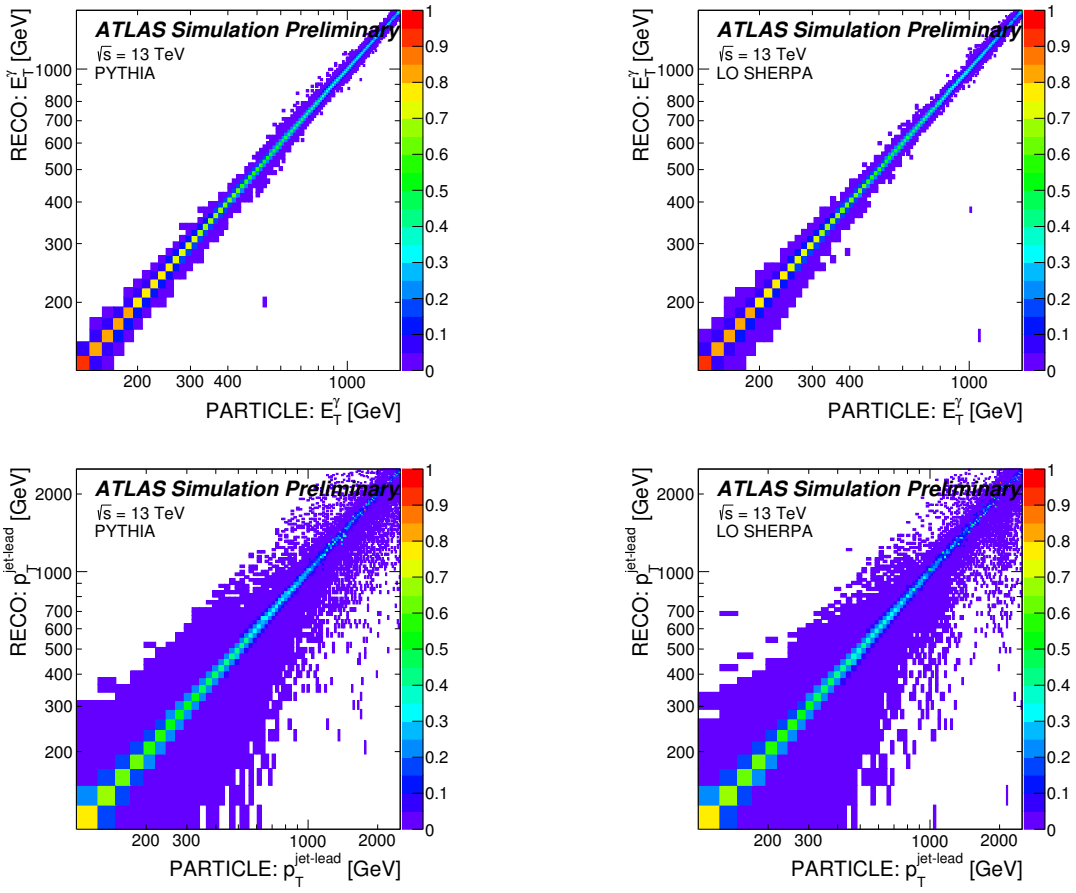

Figure 6.1: The correlation matrices between the reconstruction and particle level for E_{T}^{γ} and $p_{\mathrm{T}}^{\mathrm{jet-lead}}$ for PYTHIA optimised (left) and SHERPA (right).

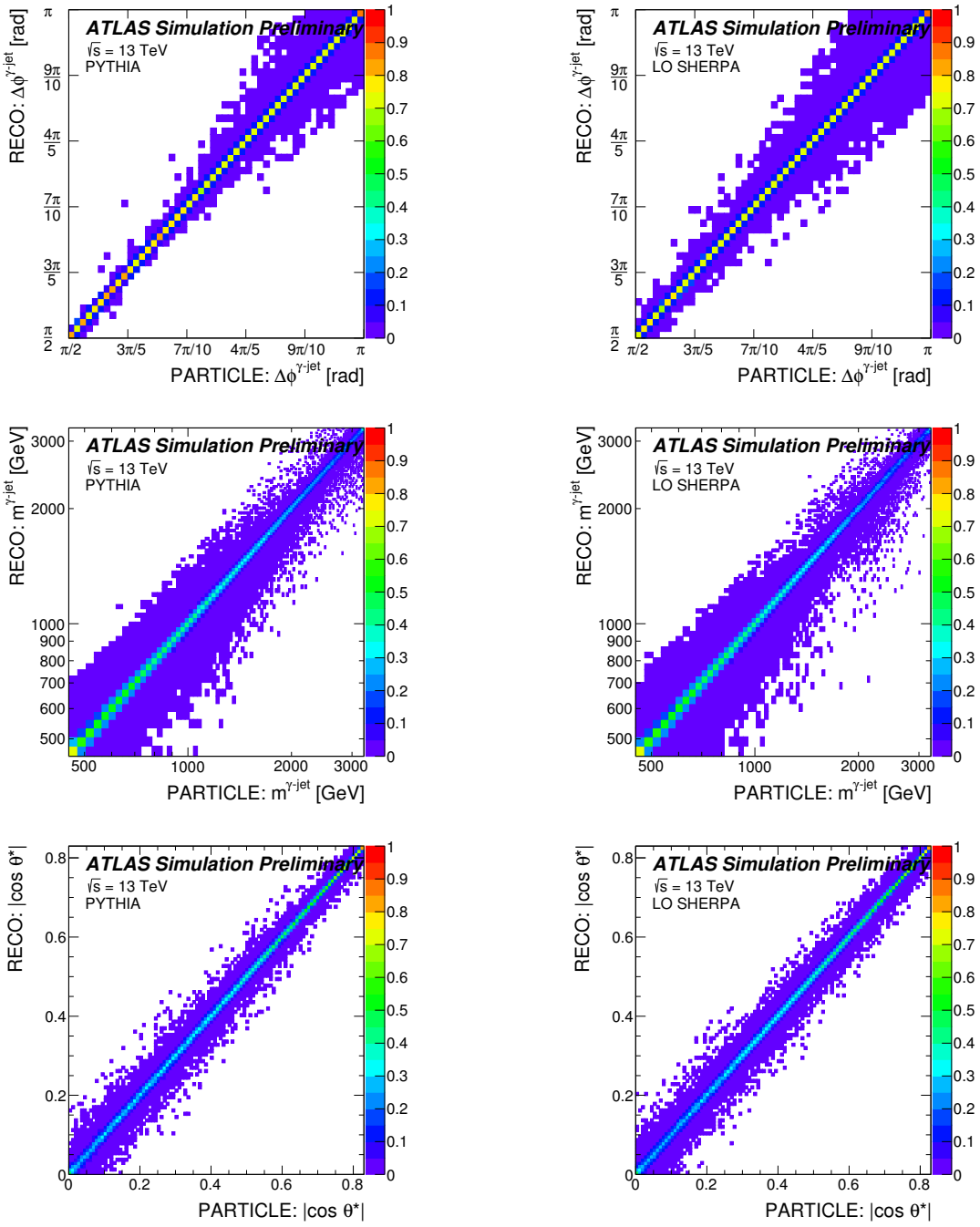

Figure 6.2: The correlation matrices between the reconstruction and particle level for $m^{\gamma-\text{jet}}$, $|\cos\theta^*|$ and $\Delta\phi^{\gamma-\text{jet}}$ for PYTHIA optimised (left) and SHERPA (right).

6.2 Selection efficiency and purity

The selection efficiency and purity are evaluated using the Pythia optimised and Sherpa samples.
The integrated selection efficiency is computed as

$$\epsilon = \frac{N^{reco,part}}{N^{part}} \tag{6.1}$$

where $N^{\text{reco,part}}$ is the number of MC events that pass all the selection requirements both at reconstruction and particle level and N^{part} is the number of MC events that pass the selection requirement at particle level. The integrated selection efficiency has been found to be 83 % for both PYTHIA and SHERPA samples.
The bin-by-bin selection efficiency is computed as

$$\epsilon_{\text{i}} = \frac{N_i^{\text{reco,part}}}{N_i^{\text{part}}} \tag{6.2}$$

where $N_i^{\text{reco,part}}$ is the number of MC events that pass all the selection requirements both at reconstruction and particle level and are generated and reconstructed in bin i and N_i^{part} is the number of MC events that pass the selection requirement at particle level, located in bin i. Figure 6.3 shows the bin-to-bin selection efficiency as function of the variables studied for PYTHIA and SHERPA. It is tipically above ≈ 60 % and it is very similar between the two MC simulations.
The integrated selection purity has been computed as:

$$P = \frac{N^{reco,part}}{N^{reco}} \tag{6.3}$$

where N^{reco} is the number of MC events that pass the selection requirement at reconstruction level. The integrated selection purity has been found to be 93 % (94 %) from the PYTHIA (SHERPA) samples.
The bin-by-bin selection purity is computed as

$$P_{\text{i}} = \frac{N_i^{\text{reco,part}}}{N_i^{\text{reco}}} \tag{6.4}$$

where $N_i^{\text{reco,part}}$ is the number of MC events that pass all the selection requirements both at reconstruction and particle level and are generated and reconstructed in bin i and N_i^{part} is the number of MC events that pass the selection requirement at particle level, located in bin i. Figure 6.4 shows the

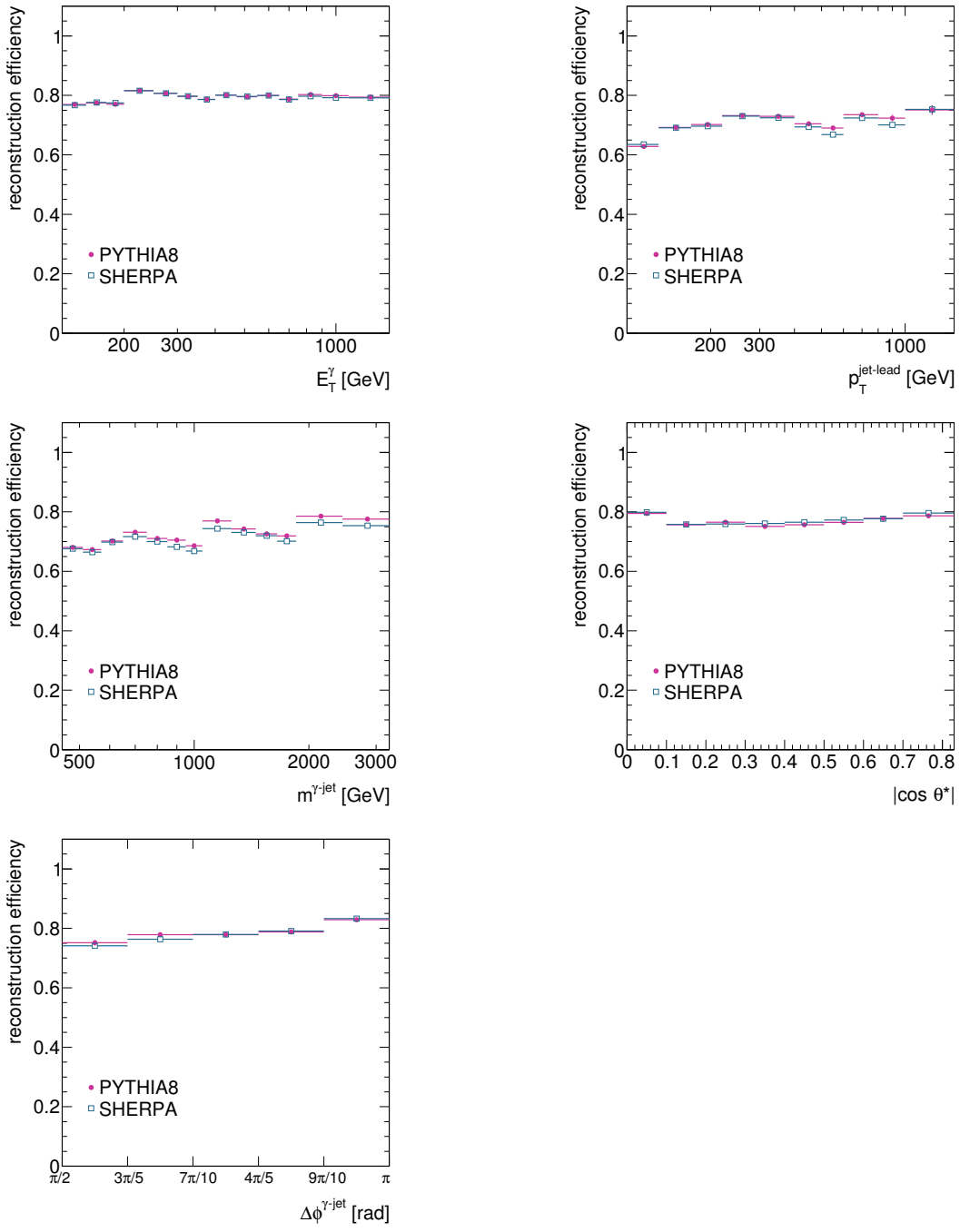

Figure 6.3: Selection efficiency for PYTHIA optimised (dots) and SHERPA (squares) as a function of E_{T}^{γ}, $p_{\mathrm{T}}^{\mathrm{jet-lead}}$, $m^{\gamma-\mathrm{jet}}$, $|\cos\theta^*|$ and $\Delta\phi^{\gamma-\mathrm{jet}}$.

bin-to-bin selection purities as functions of the studied variables for PYTHIA and SHERPA. It is typically very similar for both PYTHIA and SHERPA.
The bin-to-bin selection efficiencies and purities are not used in the unfolding procedure. The unfolding factors are going to be defined in the next chapter.

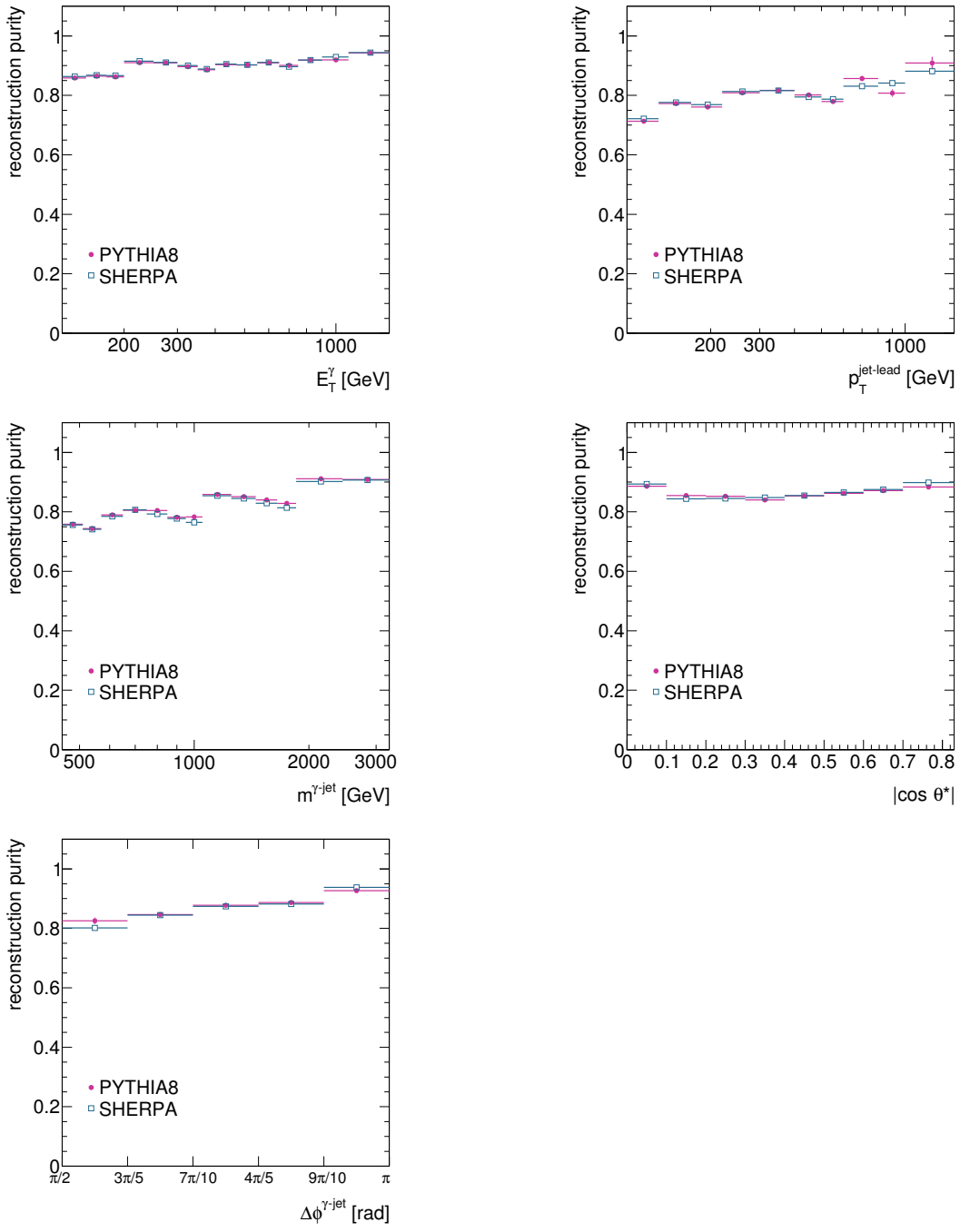

Figure 6.4: Selection purity for PYTHIA optimised (dots) and SHERPA (squares) as a function of E_{T}^{γ}, $p_{\mathrm{T}}^{\mathrm{jet-lead}}$, $m^{\gamma-\mathrm{jet}}$, $|\cos\theta^*|$ and $\Delta\phi^{\gamma-\mathrm{jet}}$.

Chapter 7

Cross-section measurement procedure

Isolated-photon plus jet cross sections are measured for photons with $E_{\mathrm{T}}^{\gamma} > 125$ GeV, $|\eta^{\gamma}| < 2.37$ (excluding the region $1.37 < |\eta^{\gamma}| < 1.56$). Isolation is ensured by requiring $E_{\mathrm{T}}^{\mathrm{iso}} < 4.2 \cdot 10^{-3} \cdot E_{\mathrm{T}}^{\gamma} + 10$ GeV. Differential cross sections are measured as functions of E_{T}^{γ}, $p_{\mathrm{T}}^{\mathrm{jet-lead}}$ and $\Delta\phi^{\gamma-\mathrm{jet}}$, for the leading jet with $p_{\mathrm{T}}^{\mathrm{jet-lead}} > 100$ GeV and $|y^{\mathrm{jet-lead}}| < 2.37$. Differential cross sections as functions of $m^{\gamma-\mathrm{jet}}$ and $|\cos\theta^{*}|$ are also measured with the additional requirements $|\eta^{\gamma} + y^{\mathrm{jet-lead}}| < 2.37$, $|\cos\theta^{*}| < 0.83$ and $m^{\gamma-\mathrm{jet}} > 450$ GeV.
The data distributions, after background subtraction, are corrected to the particle level using bin-by-bin correction factors determined using the MC samples. These correction factors take into account the efficiency of the selection criteria and the purity and efficiency of the photon and jet reconstruction. For this approach to be valid, the uncorrected distributions of the data must be adequately described by the MC simulations at the detector level. This condition is mostly satisfied by both the PYTHIA optimised and SHERPA MC samples as described in the previous chapter. PYTHIA optimised describes better than SHERPA the measured E_{T}^{γ} distribution, whereas the SHERPA simulation describes better than PYTHIA optimised the measured $p_{\mathrm{T}}^{\mathrm{jet-lead}}$, $m^{\gamma-\mathrm{jet}}$ and $\Delta\phi^{\gamma-\mathrm{jet}}$ distributions. Both simulations describe well the measured $|\cos\theta^{*}|$ distribution. The SHERPA samples are used to compute the nominal unfolding corrections to the data distributions. For the nominal signal leakage fractions, PYTHIA optimised is used since, as argued in Section 3.3 , it includes the contribution from photons radiated off quarks without any restrinction on the opening angle.
In summary:

- nominal signal leakage fraction obtained using PYTHIA optimised;

- nominal unfolding corrections obtained using SHERPA.

The data distributions are unfolded to the particle level via the formula

$$\frac{d\sigma}{dA}(i) = \frac{N_{\mathrm{A}}^{\mathrm{sig}}(i) \cdot C^{\mathrm{MC}}(i)}{\mathcal{L} \cdot \Delta A(i)}, \tag{7.1}$$

where $(d\sigma/dA)$ is the differential cross section as a function of the variable A, $N_{\mathrm{A}}^{\mathrm{sig}}(i)$ is the number of data background subtracted events in bin i, $C^{\mathrm{MC}}(i)$ is the correction factor in bin i, $\mathcal{L}$ is the integrated luminosity and $\Delta A(i)$ is the i bin width. As mentioned above, the nominal unfolding corrections are computed using the SHERPA samples as

$$C^{\mathrm{MC}}(i) = \frac{N_{\mathrm{part}}^{\textsc{Sherpa}}(i)}{N_{\mathrm{reco}}^{\textsc{Sherpa}}(i)}. \tag{7.2}$$

For the systematic uncertainties performed with the PYTHIA optimised samples, the unfolding corrections were computed as

$$C^{\mathrm{MC}}(i) = \frac{\alpha \cdot N_{\mathrm{part}}^{Pythia,H}(i) + (1-\alpha) \cdot N_{\mathrm{part}}^{\textsc{Pythia},B}}{\alpha \cdot N_{\mathrm{reco}}^{\textsc{Pythia},H}(i) + (1-\alpha) \cdot N_{\mathrm{reco}}^{\textsc{Pythia},B}} \tag{7.3}$$

where α is the value obtained from the fit to the data distribution of each observable. Both unfolding corrections are shown in Figure 7.1. The correction factors are very similar for PYTHIA and SHERPA.

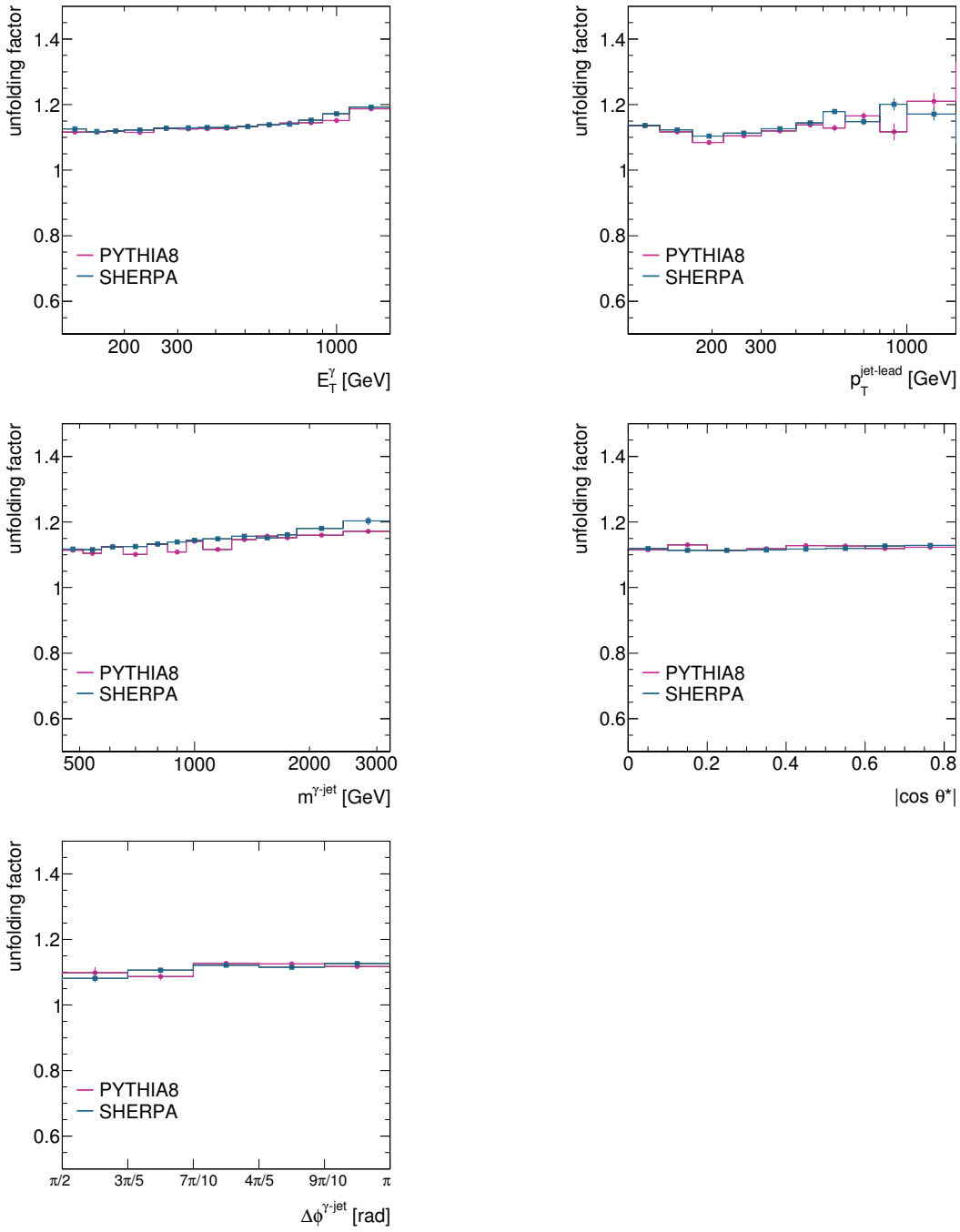

Figure 7.1: Unfolding factors for PYTHIA optimised (dots) and SHERPA (squares) as a function of E_{T}^{γ}, $p_{\mathrm{T}}^{\mathrm{jet-lead}}$, $m^{\gamma-\mathrm{jet}}$, $|\cos\theta^*|$ and $\Delta\phi^{\gamma-\mathrm{jet}}$.

7.1 Cross-check using reweighted MC

A cross-check of the bin-by-bin unfolding was performed by reweighting the MC distributions of SHERPA at reco level to the data. The ratio of the data to the MC distributions of SHERPA is shown in Figure 7.2 for each studied variable. A χ^2 fit to this ratio was performed; the function used in each case is shown in the same figure af the ratio. This function is then used to perform the reweight of the SHERPA sample at truth level.

The cross-check was performed by measuring the cross section using the reweighted SHERPA for the estimation of the bin-by-bin unfolding corrections. The relative difference with respect to the measurements obtained using SHERPA default for the unfolding is shown in Figure 7.3. It is observed that the use or not of the reweighted SHERPA does not change the measurements: the deviations are smaller than 0.15% except in the first bin of $\Delta\phi^{\gamma-\text{jet}}$, in which the difference is 0.4%.

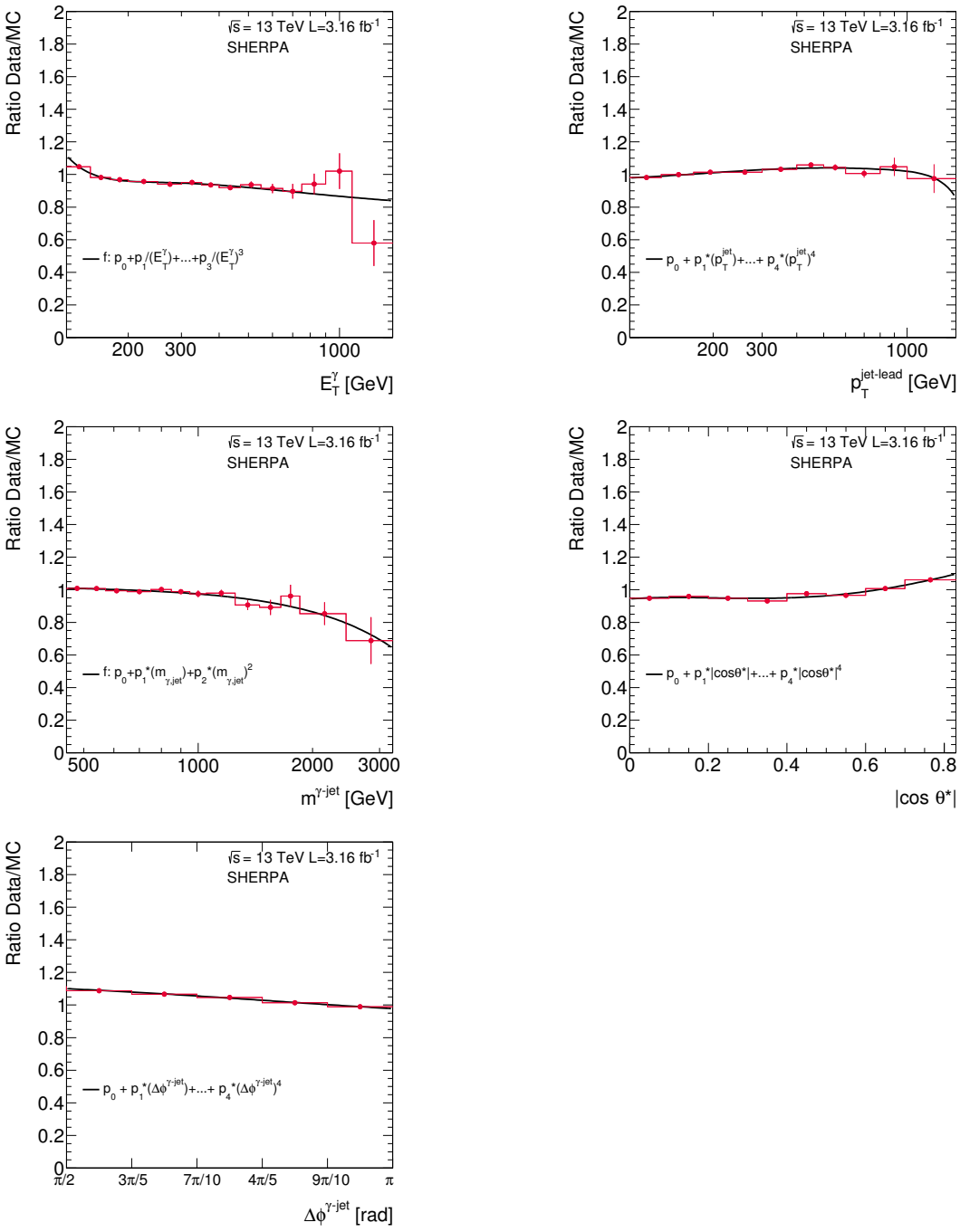

Figure 7.2: Ratio of the data and SHERPA distributions as a function of E_{T}^{γ}, $p_{\mathrm{T}}^{\mathrm{jet-lead}}$, $m^{\gamma-\mathrm{jet}}$, $|\cos\theta^{*}|$ and $\Delta\phi^{\gamma-\mathrm{jet}}$. The solid line represents the fit to the ratio. The error bars are statistical only.

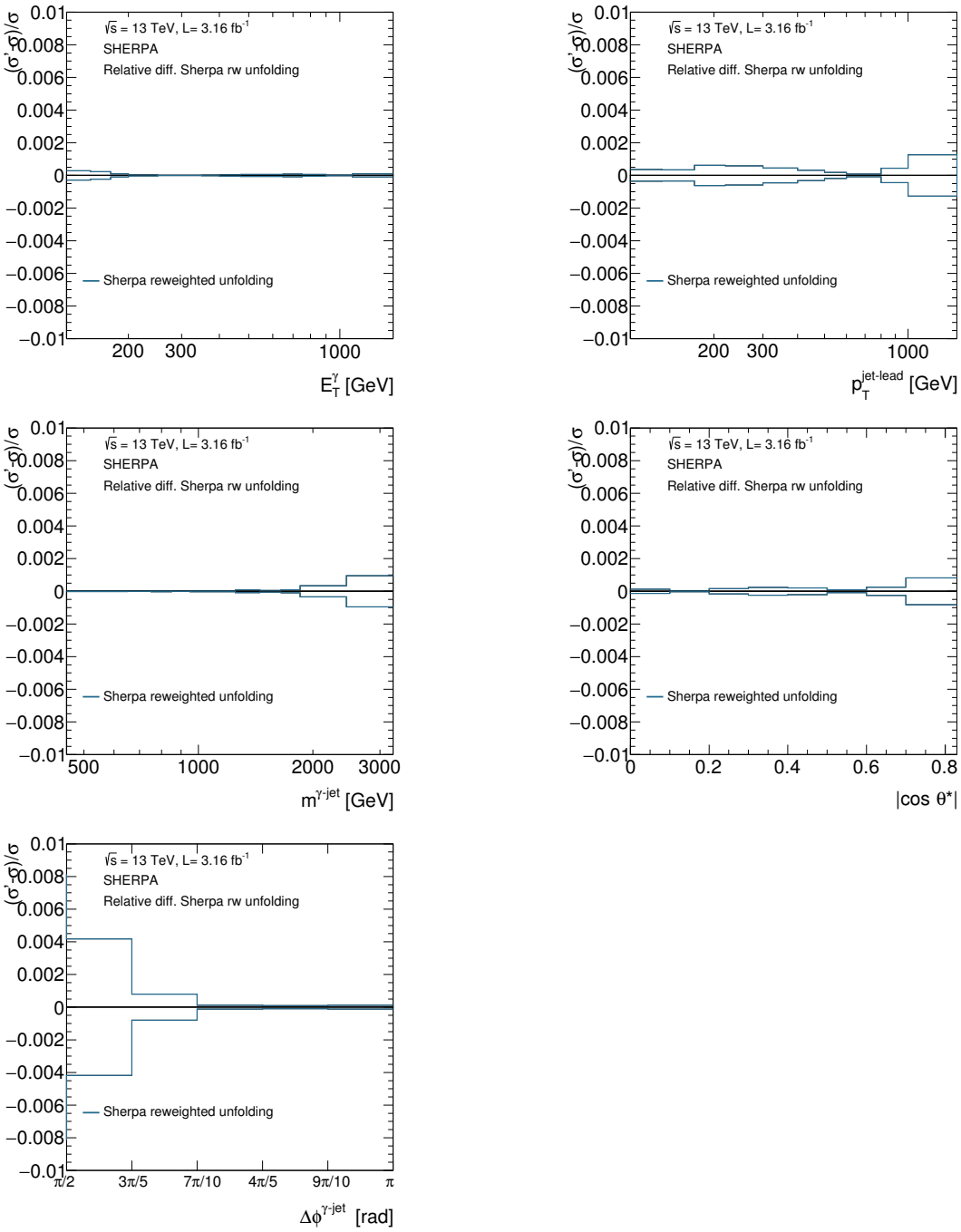

Figure 7.3: Relative difference between the measured cross section using the reweighted SHERPA for the estimation of the bin-by-bin unfolding corrections and those using SHERPA default as a function of E_{T}^{γ}, $p_{\mathrm{T}}^{\mathrm{jet-lead}}$, $m^{\gamma-\mathrm{jet}}$, $|\cos\theta^{*}|$ and $\Delta\phi^{\gamma-\mathrm{jet}}$.

7.2 Cross-check using Bayesian unfolding

A more sophisticated unfolding method, based on the iterative application of the Bayes' theorem [81], is investigated to cross-check and validate the results obtained using the bin-by-bin unfolding method. The Bayesian unfolding method takes properly into account the migrations between bins and the purity and selection criteria when the MC description of the data is not adequate. The main requirement of this method relies on having a sufficiently large MC sample to construct the reference matrices, otherwise the results are less reliable than those obtained from the bin-by-bin method, since they are more affected by such lack of statistics. Another problem which affects the unfolding based on the Bayes' theorem is the abnormal blow up of the statistical uncertainty of the resulting cross section, which appears when a large number of iterations to achieve convergence are used. To make a trustworthy comparison between the Bayesian and the bin-by-bin methods, these issues are investigated before attempting the cross-check. Figure 7.4 shows the relative difference between the results obtained using N iterations with respect to those obtained using 4 iterations. The oscillations for $N < 4$ are quite large, while they disappear for $N > 4$. For this reason, the nominal Bayes' unfolding is performed with 4 iterations. The comparison between the cross section unfolded via the bin-by-bin and the Bayesian methods is shown in Figure 7.5. The difference between the two unfolding approaches is smaller that 1% for each variable. In the regions of phase space where the MC statistics is poor, some deviations are observed. For comparison, the statistical uncertainty of the cross section is also included in the figures and shows that the size of this uncertainty is much bigger the the difference of the cross sections obtained with the two methods. The correlation matrices used in the Bayesian unfolding are shown in Figure 7.6.

These results are obtained using SHERPA for the unfolding corrections and PYTHIA optimised for the signal leakage fractions. All the shown results validate the use of the bin-by-bin unfolding method as the nominal unfolding technique to measure the cross sections.

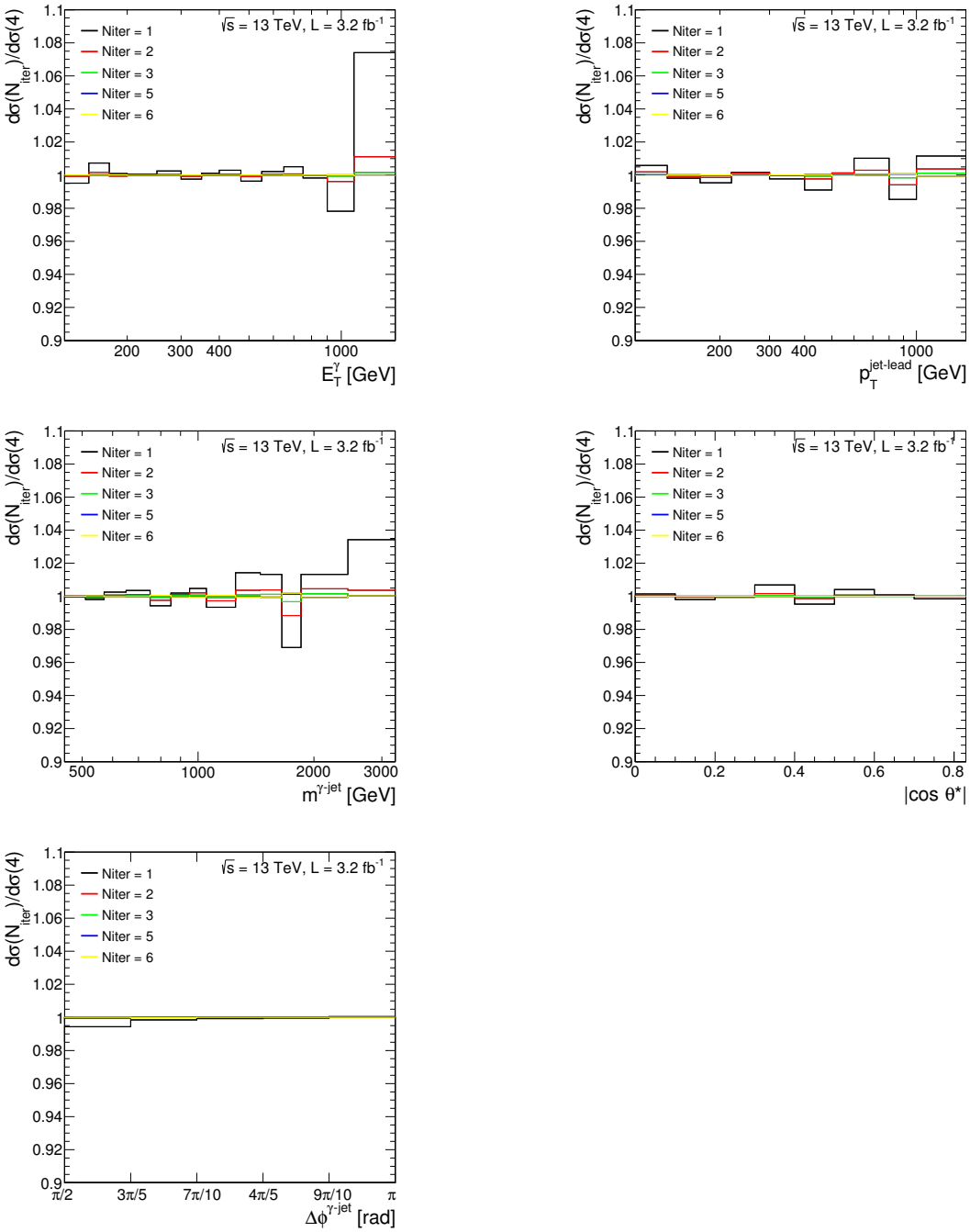

Figure 7.4: Ratios between the cross sections unfolded using the Bayesian method with N iterations and the results unfolded using 4 iterations as a function of E_{T}^{γ}, $p_{\mathrm{T}}^{\mathrm{jet-lead}}$, $m^{\gamma-\mathrm{jet}}$, $|\cos\theta^{*}|$ and $\Delta\phi^{\gamma-\mathrm{jet}}$.

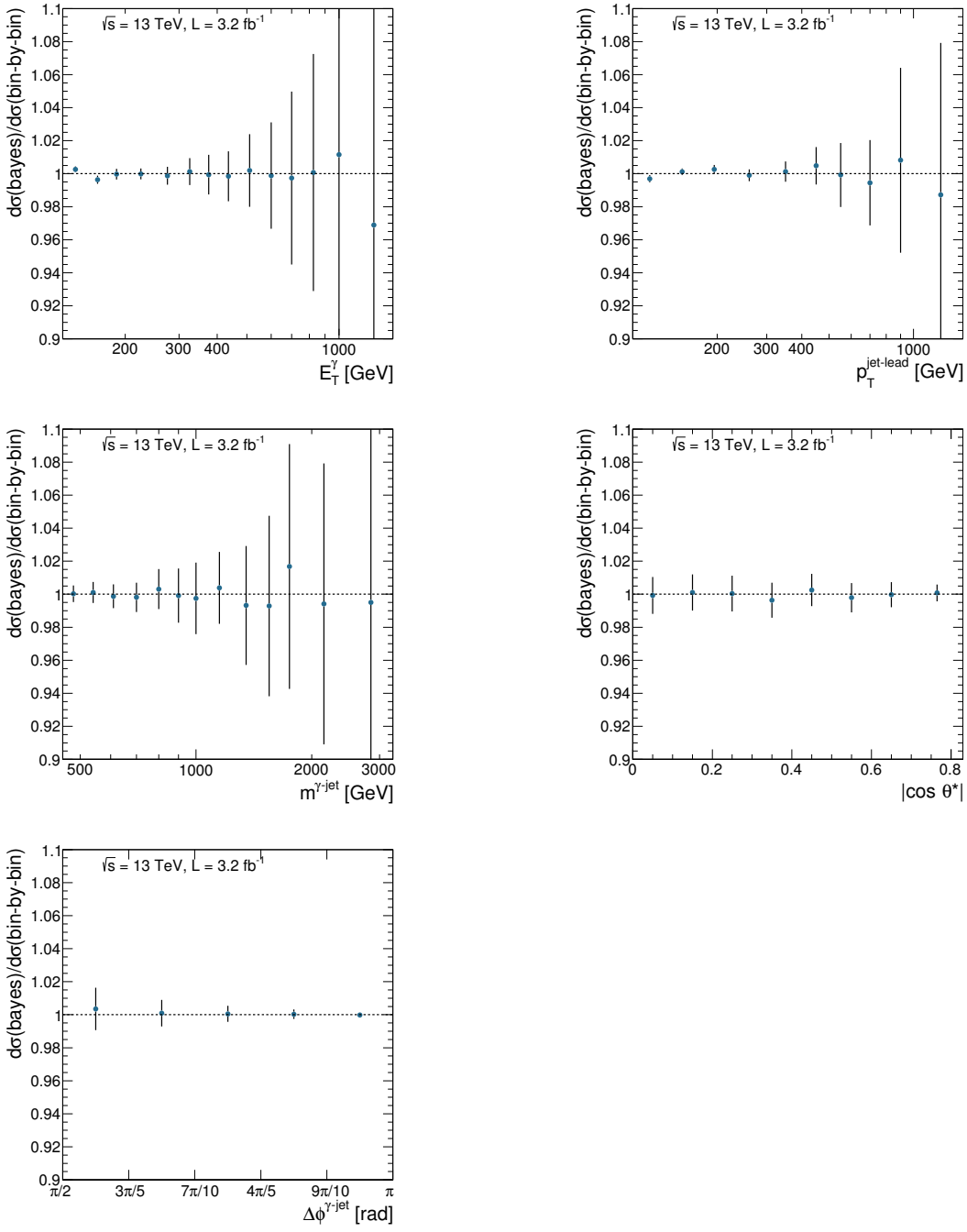

Figure 7.5: Ratio between the cross sections unfolded using the Bayesian method with four iterations and the nominal cross sections as a function of E_{T}^{γ}, $p_{\mathrm{T}}^{\mathrm{jet-lead}}$, $m^{\gamma-\mathrm{jet}}$, $|\cos\theta^{*}|$ and $\Delta\phi^{\gamma-\mathrm{jet}}$. For illustration, the relative statistical uncertainties of the nominal cross sections are shown as error bars.

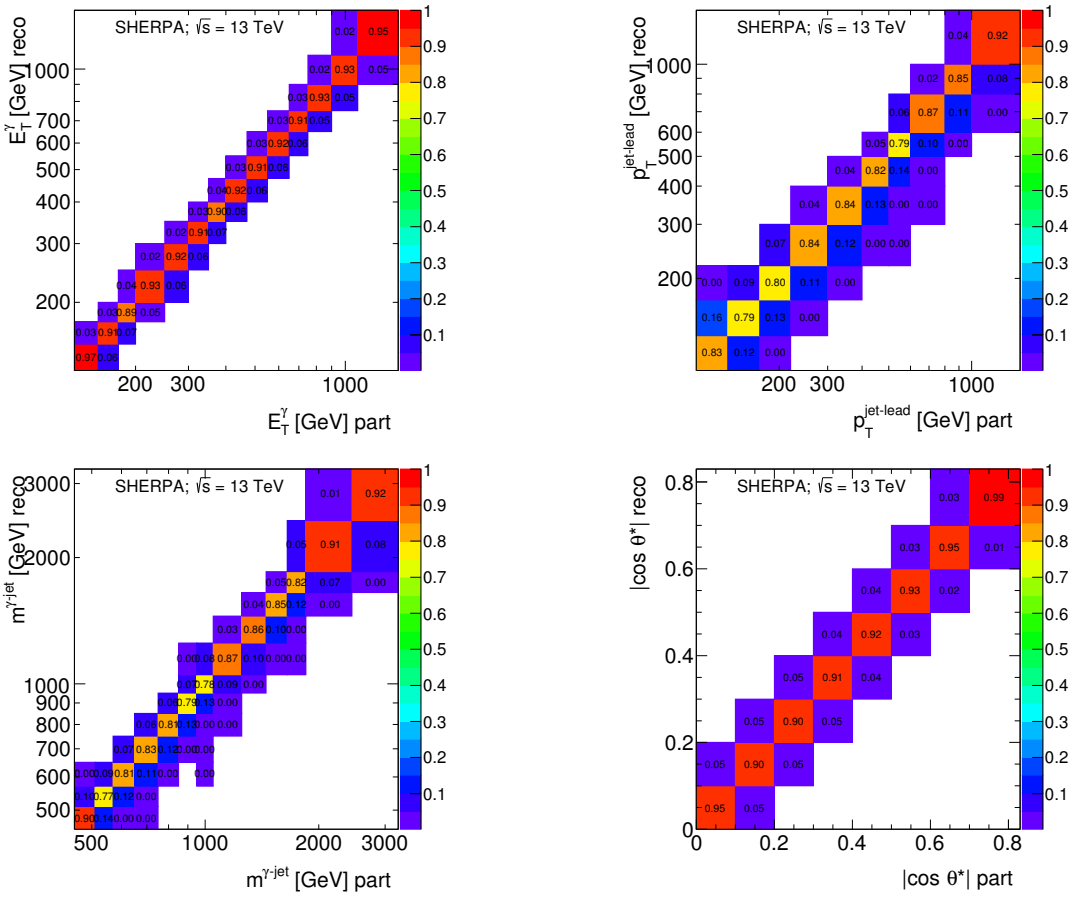

Figure 7.6: Correlation matrices in the Bayesian approach from SHERPA MC for E_{T}^{γ}, $p_{\mathrm{T}}^{\mathrm{jet-lead}}$, $m^{\gamma-\mathrm{jet}}$, $|\cos\theta^*|$ and $\Delta\phi^{\gamma-\mathrm{jet}}$.

Chapter 8

Systematic uncertainties

The sources of systematic uncertainties that affect the measurements are investigated. These sources include:

- the photon energy scale and resolution;
- the jet energy scale and resolution;
- the model dependence on the signal leakage fractions and unfolding corrections;
- the photon identification efficiency;
- the choice of background control regions;
- the isolation correction;
- the identification and isolation correlation in the background;
- the pile-up reweighting;
- the MC sample statistics;
- the luminosity.

Each source is analysed in detail below.

8.1 Photon energy scale and resolution

Differences in the energy scale and resolution in data and simulations lead to systematic uncertainties. The relative uncertainty in the photon energy scale (GES) and resolution (GER) is estimated according to the recommendations

of the ATLAS "e/γ" working group [82].
A total of 67 individual components influencing the energy measurement of the photon are varied within their uncertainties to assess the overall uncertainty on the energy measurements. The uncertainties are then propagated through the analysis separately, to maintain the full information on the correlations. Similarly to the energy scale uncertainty, the energy resolution is also influenced by different contributions (7 components), which were also propagated through the analysis separately to maintain the full information on the correlations.
The systematic uncertainties on the measured cross sections due to the effects mentioned above are estimated by varying each individual source of uncertainty separately in the MC simulations and then added in quadrature. Figure 8.1 show the resulting uncertainties. The large sensitivity to the photon energy scale comes from the fact that the cross-section decreases fast as a function of E_{T}^{γ}. The same uncertainties are also estimated using a bootstrap technique, to remove the effects of statistical fluctuations. The relative systematic uncertainty obtained adding in quadrature the results of the replicas is shown as the solid lines. In a subsequent step, the result of the replicas for each nuisance parameter as a function of the measured variables are fitted. The sum in quadrature of the fits are shown as dotted lines in Figure 8.2, which represents the smoothed relative systematic uncertainty due to the photon energy scale and resolution and are compared with those mentionated above. The photon energy resolution uncertainties have a much smaller impact than the GES uncertainties and are shown separately in Appendix B.1.

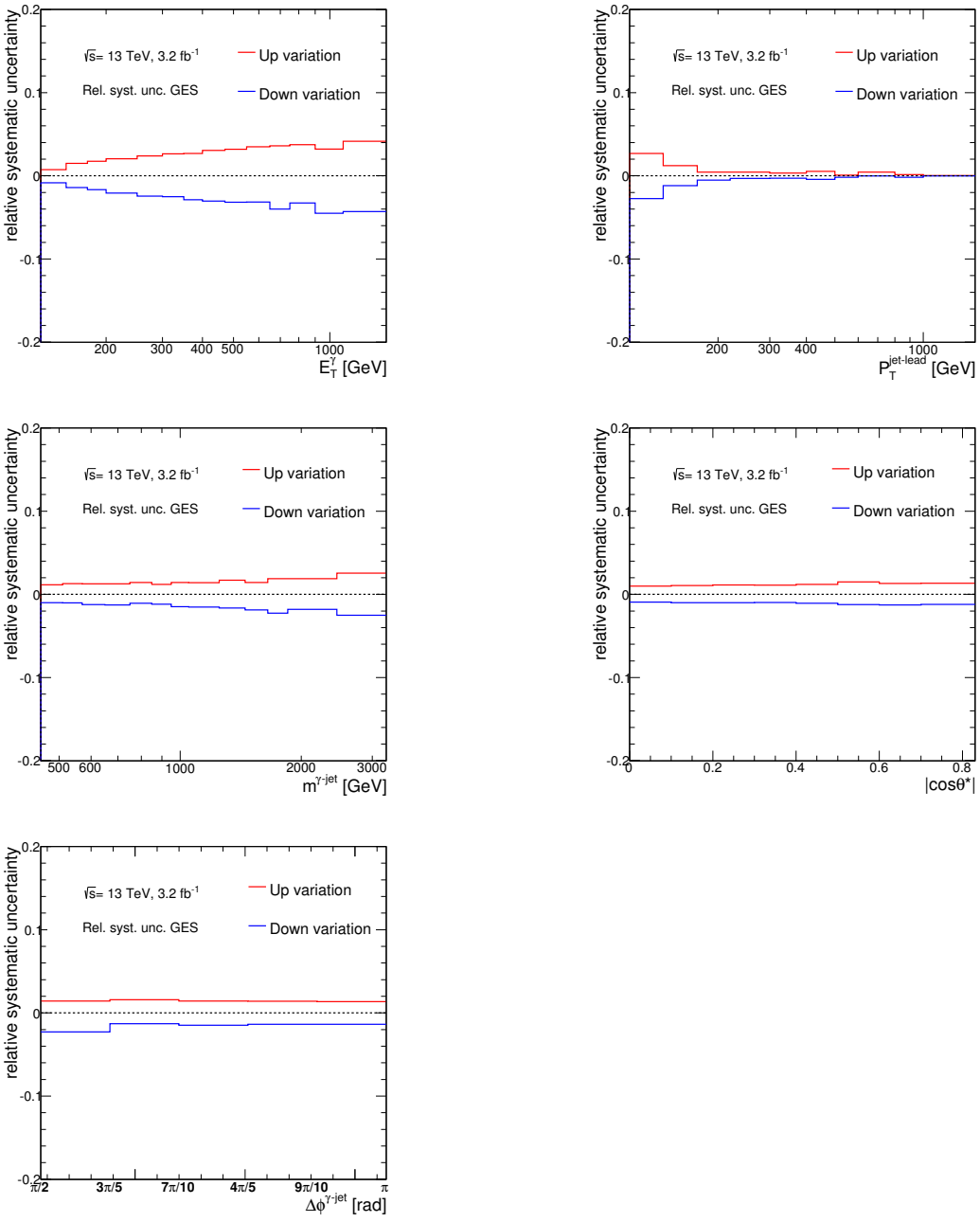

Figure 8.1: Systematic uncertainties on the measured cross sections due to the uncertainty in the photon energy scale and resolution as a function of E_{T}^{γ}, $p_{\mathrm{T}}^{\mathrm{jet-lead}}$, $m^{\gamma-\mathrm{jet}}$, $|\cos\theta^{*}|$ and $\Delta\phi^{\gamma-\mathrm{jet}}$. The red (blue) lines represent the upward (downward) variations.

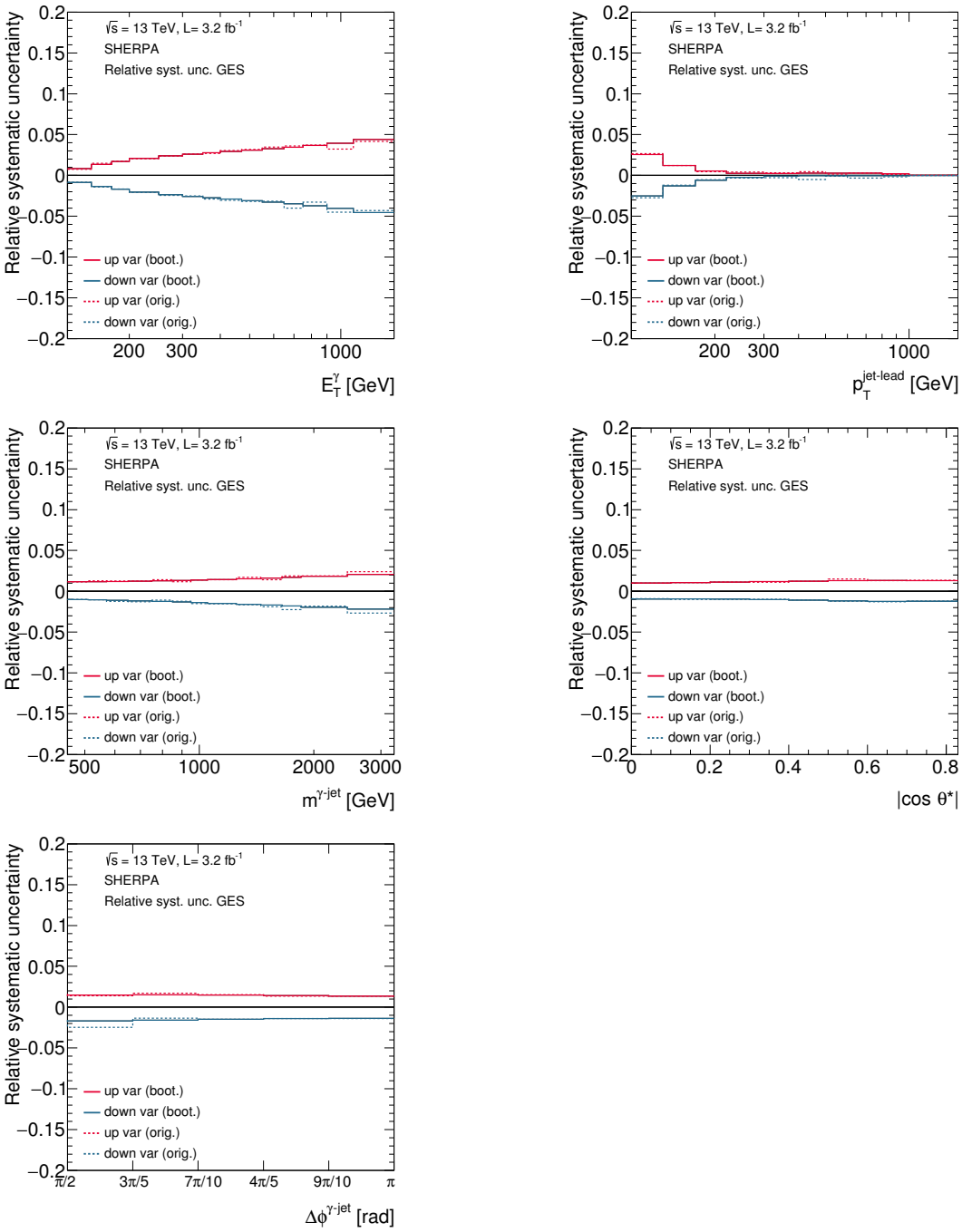

Figure 8.2: Systematic uncertainties on the measured cross sections due to the uncertainty in the photon energy scale and resolution as a function of E_{T}^{γ}, $p_{\mathrm{T}}^{\mathrm{jet-lead}}$, $m^{\gamma-\mathrm{jet}}$, $|\cos\theta^{*}|$ and $\Delta\phi^{\gamma-\mathrm{jet}}$. The solid (dashed) lines display the estimation with (without) the bootstrap method.

8.2 Jet energy scale

Differences in the jet energy scale in data and simulations lead to systematic uncertainties. The relative uncertainty in the jet energy scale (JES) is estimated according to the recommendations [73, 83] of the ATLAS "JetEtmiss" working group.
A total of 76 individual components influencing the energy measurement of the jets are studied and varied within their uncertainties to assess the overall uncertainty on the jet energy measurement. These uncertainties are then propagated through the analysis separately to maintain the full information on the correlations. These components include

- 65 nuisance parameters from the in situ analyses ($Z + jet$, $\gamma + jet$ and multi-jet balance);
- 3 nuisance parameters from the η intercalibration (modelling, statistic/method and calibration non-closure);
- 1 nuisance parameter from the behaviour of high-p_{T} jets in propagation of single hadron uncertainties to the jets;
- 4 nuisance parameters from pile-up (3 of which are μ/N_{PV} dependent);
- 1 nuisance parameter from the flavour composition of the sample;
- 1 nuisance parameter from the flavour response uncertainty;
- 1 nuisance parameter for punch-through jets.

Figure 8.3 shows the resulting uncertainties. The uncertainties are also estimated using a bootstrap technique and the estimations are shown in Figure 8.4 and compared to those mentioned above.

8.3 Jet energy resolution

The systematic uncertainty due to the jet energy resolution (JER) accounts for the fact that the simulated sample has a better energy resolution than the data. The impact of this difference is estimated by smearing the MC simulated distributions and comparing the smeared and non-smeared results according to the recommendations of the ATLAS "JetEtmiss" working group. Figure 8.5 shows the resulting uncertainties as functions of the studied observables. The uncertainty in $p_{\mathrm{T}}^{\mathrm{jet-lead}}$ is also estimated using a bootstrap technique and shown as a dashed line in the same figure.

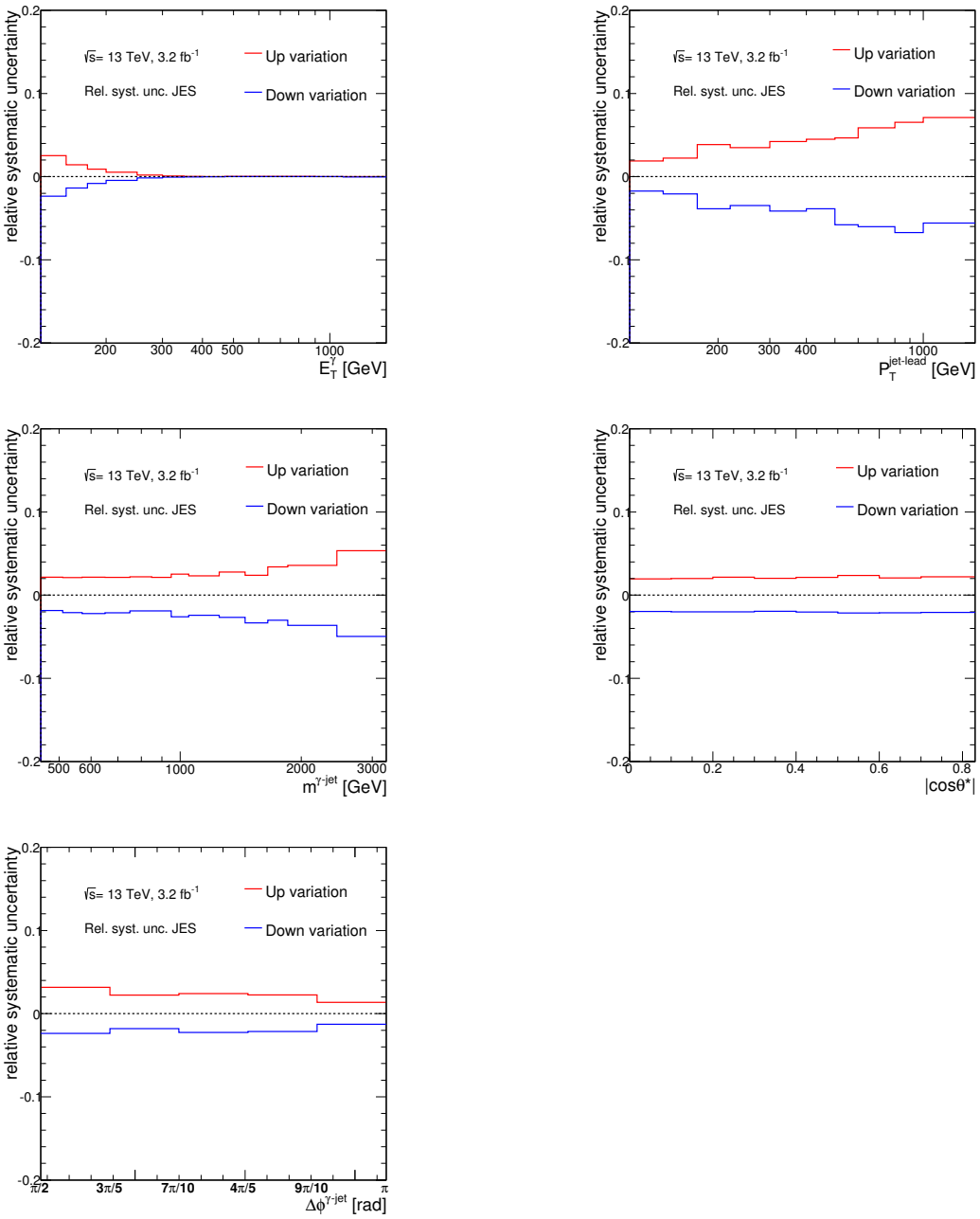

Figure 8.3: Systematic uncertainties on the measured cross sections due to the uncertainty in the jet energy scale as a function of E_{T}^{γ}, $p_{\mathrm{T}}^{\mathrm{jet-lead}}$, $m^{\gamma-\mathrm{jet}}$, $|\cos\theta^{*}|$ and $\Delta\phi^{\gamma-\mathrm{jet}}$. The red (blue) lines represent the upward (downward) variations.

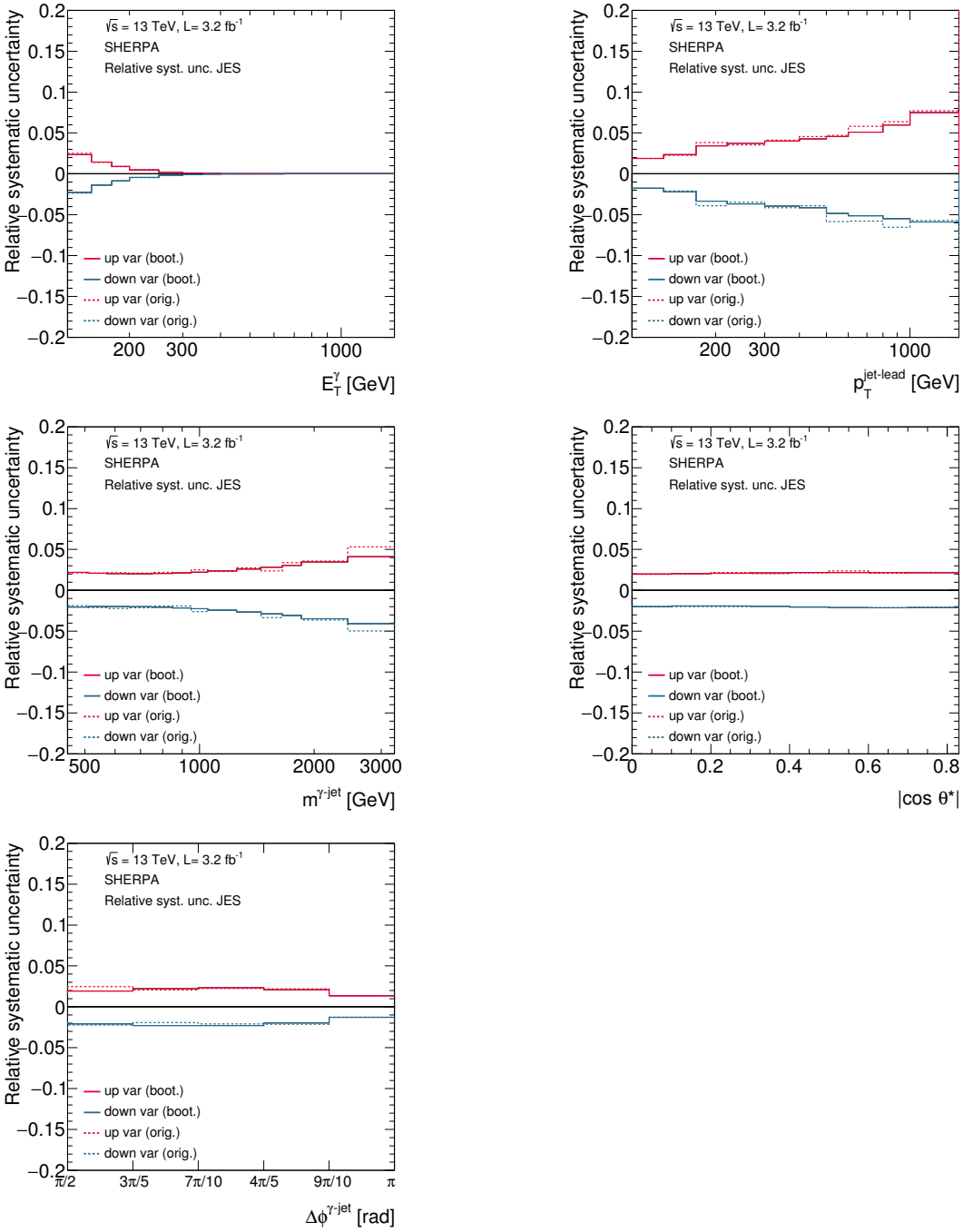

Figure 8.4: Systematic uncertainties on the measured cross sections due to the uncertainty in the jet energy scale as a function of E_{T}^{γ}, $p_{\mathrm{T}}^{\mathrm{jet-lead}}$, $m^{\gamma-\mathrm{jet}}$, $|\cos\theta^{*}|$ and $\Delta\phi^{\gamma-\mathrm{jet}}$. The solid (dashed) lines display the estimation with (without) the bootstrap method.

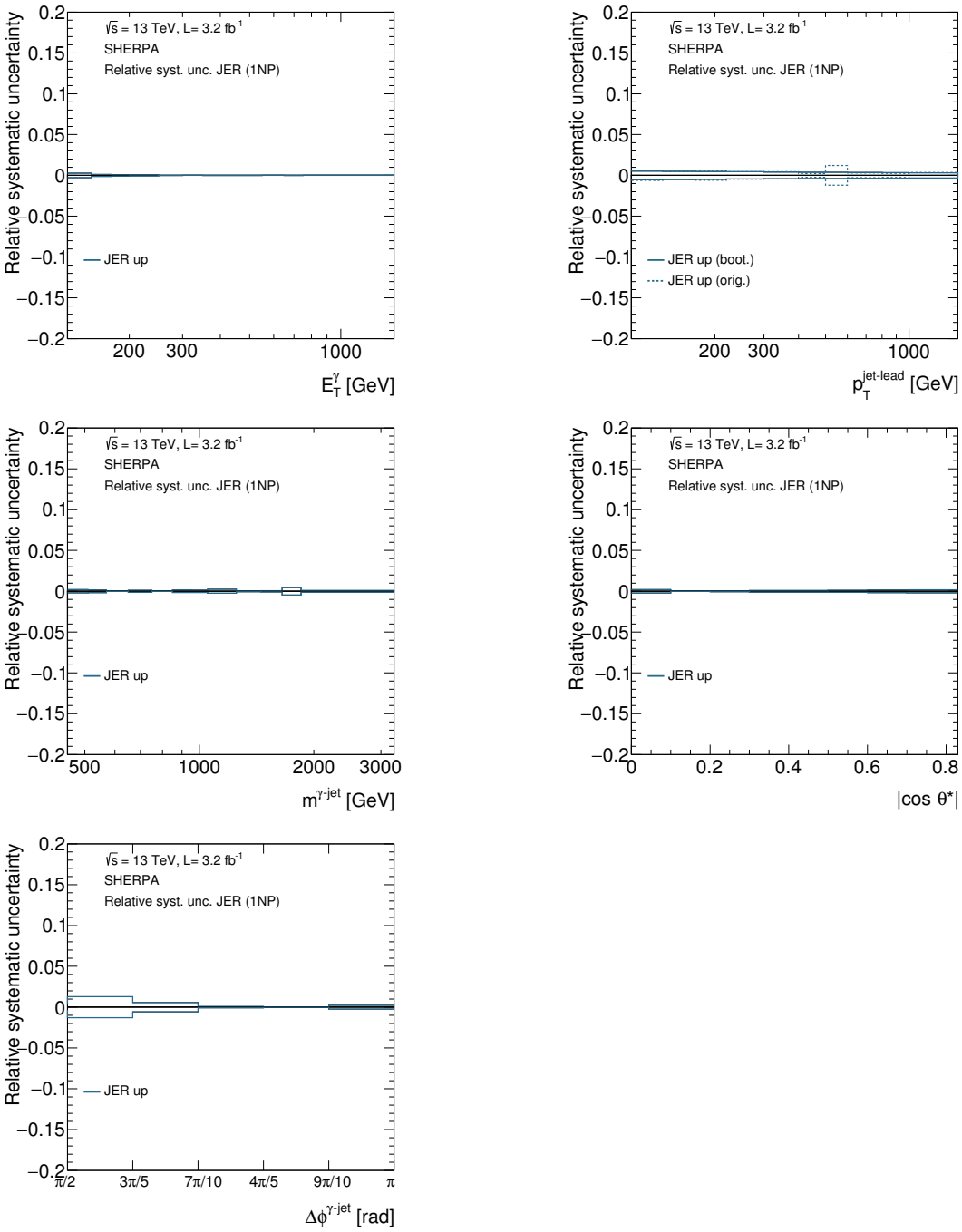

Figure 8.5: Systematic uncertainties on the measured cross sections due to the uncertainty in the jet energy resolution as a function of E_{T}^{γ}, $p_{\mathrm{T}}^{\mathrm{jet-lead}}$, $m^{\gamma-\mathrm{jet}}$, $|\cos\theta^{*}|$ and $\Delta\phi^{\gamma-\mathrm{jet}}$. The solid (dashed) lines display the estimation with (without) the bootstrap method.

8.4 Parton shower and hadronisation model dependence

The effect due to the parton shower and the hadronisation models in the signal leakage fractions and unfolding correction is estimated as the deviation observed from the nominal results by using alternate MC simulations of the signal. Figures 8.6 and 8.7 show the resulting uncertainties for:

- Signal leakage fractions: the signal leakage fractions of PYTHIA optimised are used to subtract the background via the data-driven method for the nominal results. The effects on the cross sections of using either PYTHIA default or SHERPA for the signal leakage fractions are shown in Figure 8.6. In each case the unfolding procedure is performed with SHERPA. From the deviations with respect to the nominal values, an envelope is built and in the cases where the changes in the cross section in a given bin go in the same direction, the largest absolute value of the change is taken and symmetrised.

- Unfolding corrections: SHERPA is used in the measurements of the nominal cross sections to unfold. The effects on the measured cross sections of using PYTHIA optimised for the unfolding are shown in Figure 8.7. The signal leakage fractions are evaluated with PYTHIA optimised.

Separated in this way, possible partial cancellations of the two effects are avoided. The resulting uncertainties from these two effects are added in quadrature when estimating the total systematic uncertainty.

8.5 Photon identification efficiency

The uncertainty on the photon identification efficiency has been estimated by propagating the uncertainties in the scale factors, estimated from the MC samples, which are applied to the MC events to match the tight identification efficiency between data and simulation, to the cross section. Figure 8.8 shows the resulting uncertainties.

8.6 Choice of background control regions

The 2D-sideband method has been used to subtract the background in the signal region. The estimation of the background contamination in the signal

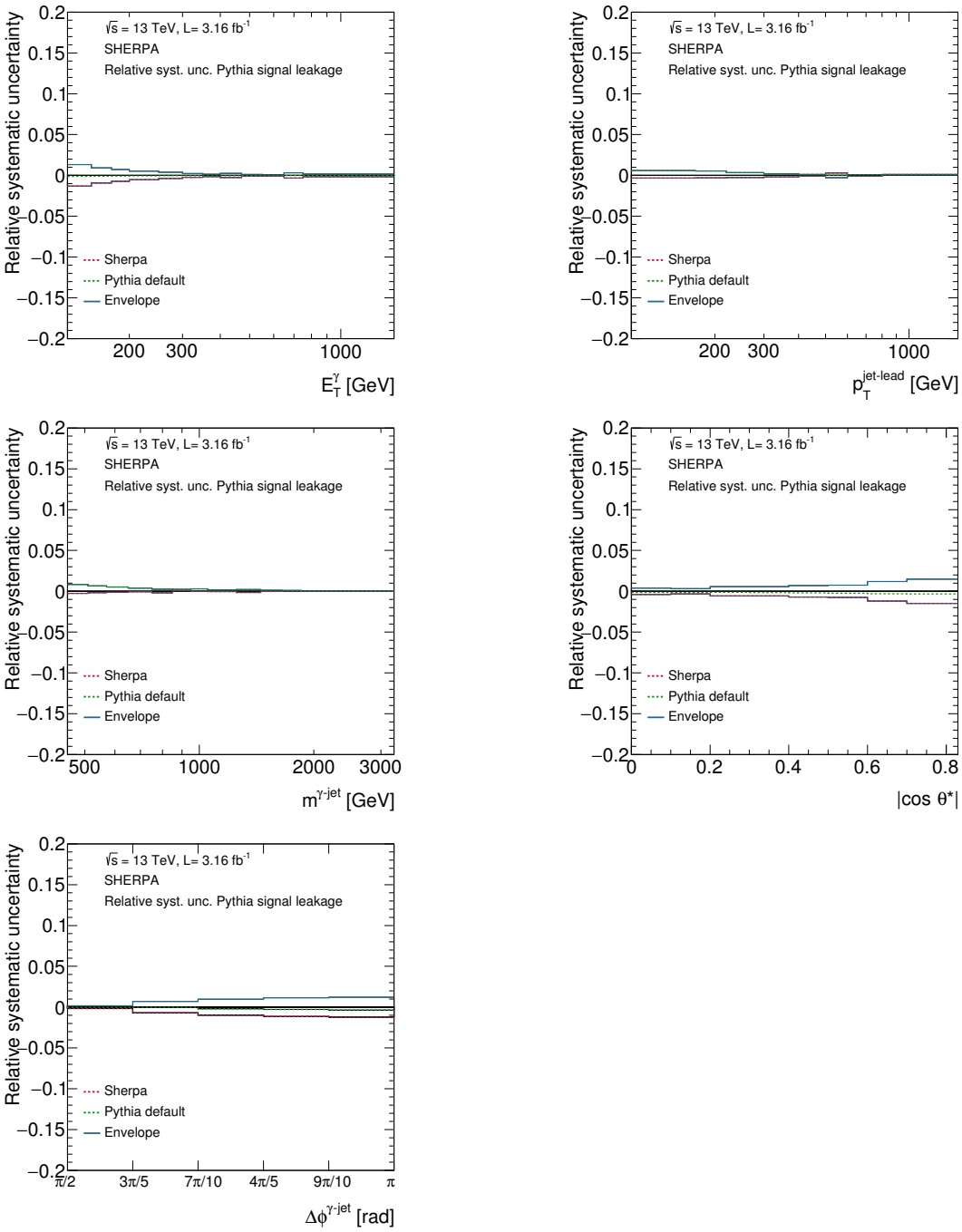

Figure 8.6: Systematic uncertainties on the measured cross sections due to the parton shower and hadronisation models as a function of E_{T}^{γ}, $p_{\mathrm{T}}^{\mathrm{jet-lead}}$, $m^{\gamma-\mathrm{jet}}$, $|\cos\theta^{*}|$ and $\Delta\phi^{\gamma-\mathrm{jet}}$ using either PYTHIA default or SHERPA to estimate the signal purity. The envelope is shown as the blue solid line.

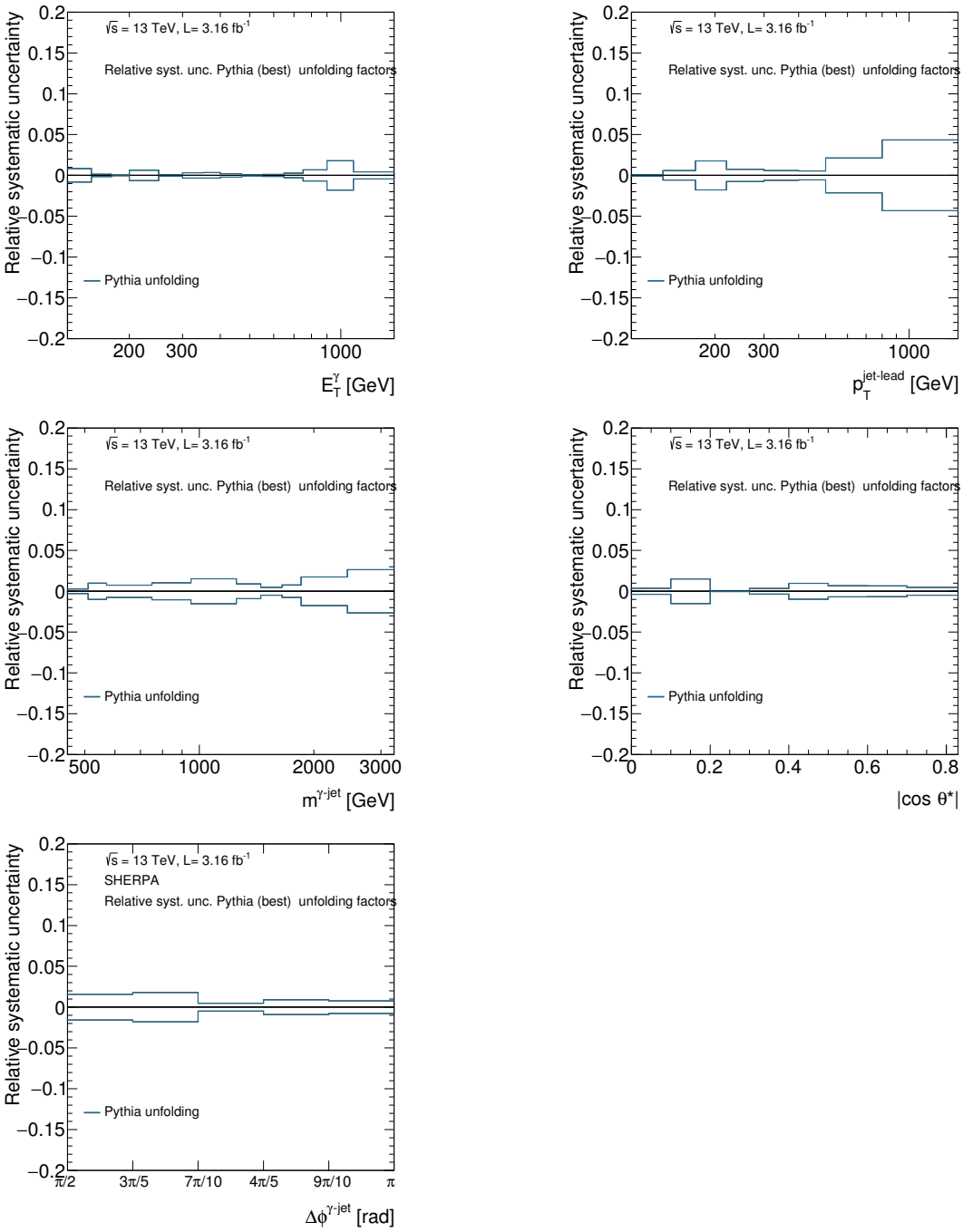

Figure 8.7: Systematic uncertainties on the measured cross sections due to the parton shower and hadronisation models as a function of E_{T}^{γ}, $p_{\mathrm{T}}^{\mathrm{jet-lead}}$, $m^{\gamma-\mathrm{jet}}$, $|\cos\theta^{*}|$ and $\Delta\phi^{\gamma-\mathrm{jet}}$ using PYTHIA optimised to estimate the unfolding corrections.

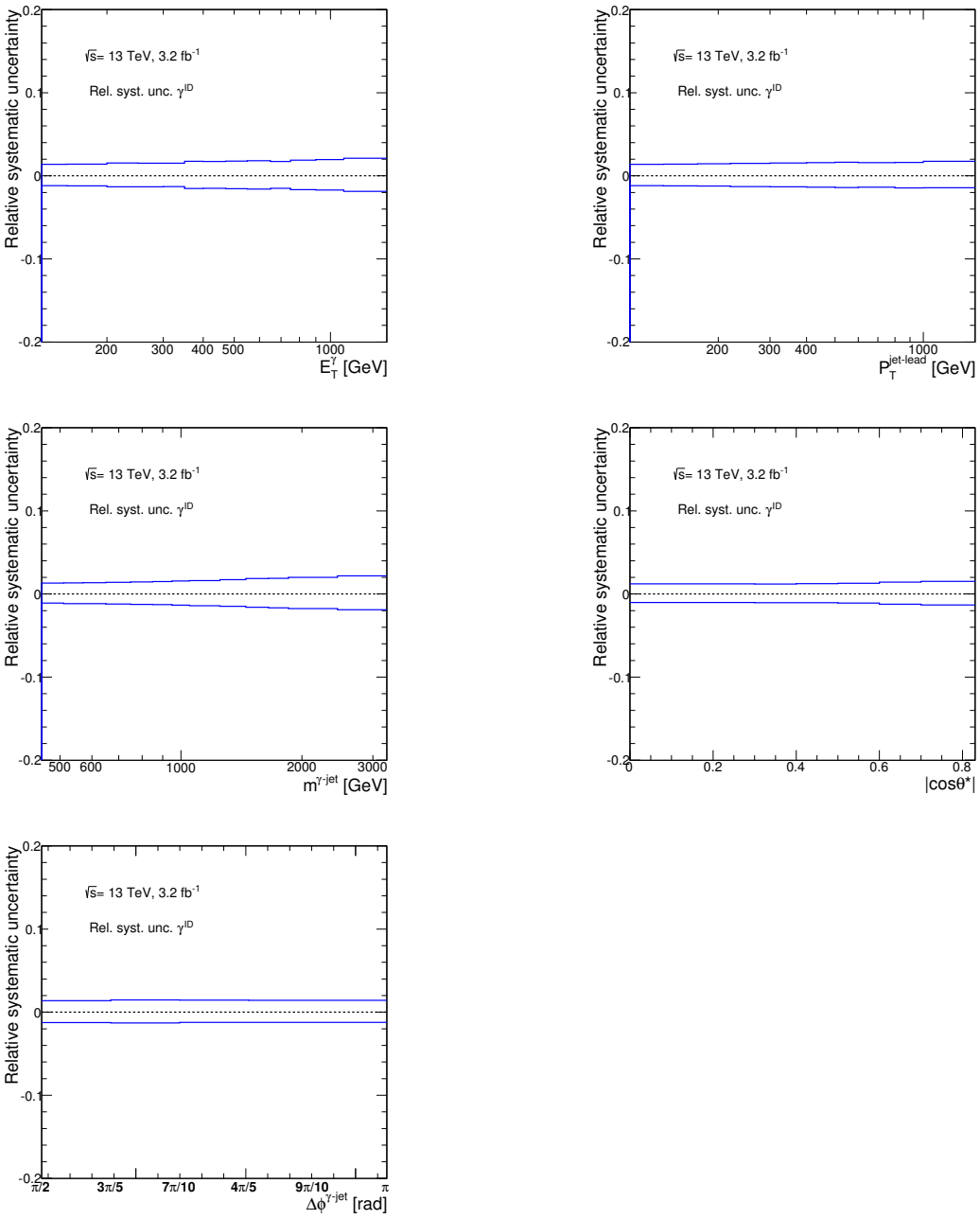

Figure 8.8: Systematic uncertainty on the measured cross sections due to the uncertainty in the photon identification efficiency as a function of E_{T}^{γ}, $p_{\mathrm{T}}^{\mathrm{jet-lead}}$, $m^{\gamma-\mathrm{jet}}$, $|\cos\theta^{*}|$ and $\Delta\phi^{\gamma-\mathrm{jet}}$.

region is affected by the choice of the background control regions.
The uncertainty associated to this choice is evaluated by studing three sources:

- varying the E_{T}^{γ}-dependent isolation requirement for the regions B and D from the nominal cut ($E_{\mathrm{T}}^{iso} > 4.2 \cdot 10^{-3} \cdot E_{\mathrm{T}}^{\gamma} + (4.8 + 2)$ GeV) by 1 GeV up and down. Figure 8.9 shows the resulting uncertainties.

- varying the definition of the photon identification variable. The nominal non-tight photon control region is defined by photons with pass the loose' requirement, but fail the tight identification criteria. The loose' identification criteria are defined by applying tight cuts on the R_{had}, R_{η}, R_{ϕ}, $w_{\eta 2}$ and w_{stot} shower-shape variables. The uncertainty due to this choice is estimated by repeating the analysis with different loose' definitions: *LoosePrime2*, *LoosePrime3* and *LoosePrime5* [84]. A bootstrap technique is applied to the relative differences to the nominal cross section values to estimate the statistical uncertainties on the relative differences. Figure 8.10 shows the resulting uncertainties on the cross sections, estimated as the envelopes of the observed variations.

- investigating the dependence of the results on the upper cut on E_{T}^{iso} for regions B and D. For this purpose, the 50 GeV cut was removed. The relative differences in the cross sections induced by such a variation, shown in Figure 8.11, are typically smaller than 0.2%.

The resulting uncertainties from these effects are added in quadrature when extimating the total systematic uncertainty.

8.7 Isolation correction

Data-driven corrections to $E_{\mathrm{T}}^{\mathrm{iso}}$ are included in the MC samples, which lead to an improved description of the $E_{\mathrm{T}}^{\mathrm{iso}}$ distributions in data by the MC simulations. A systematic uncertainty is assigned to the modelling of the $E_{\mathrm{T}}^{\mathrm{iso}}$ distribution in MC comparing the nominal results (with the data-driven corrections applied to MC) with those obtained without the application of the data-driven corrections to the simulated events; the resulting uncertainties on the cross sections are shown in Figure 8.12.

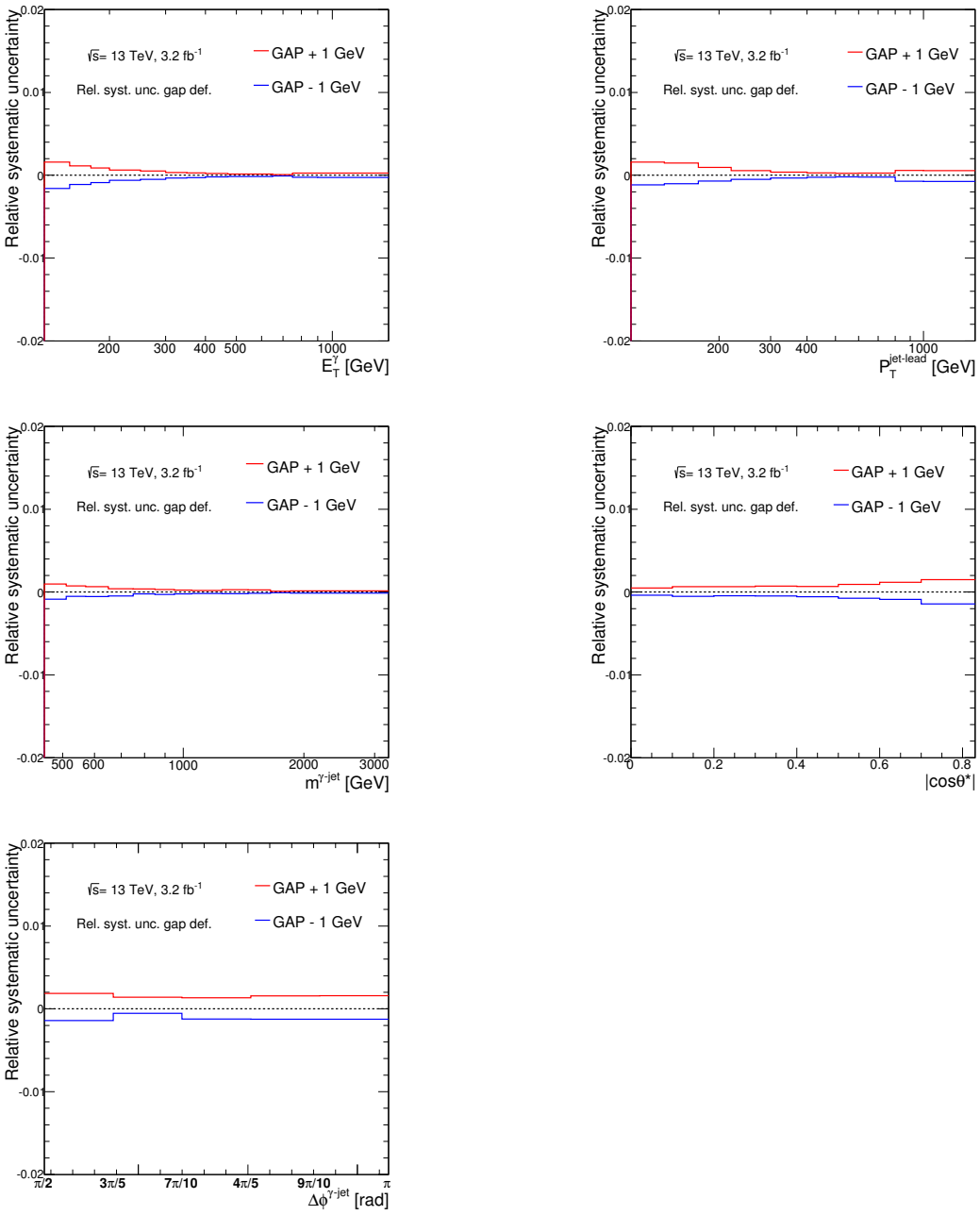

Figure 8.9: Systematic uncertainty on the measured cross sections due to the uncertainty in the choice of the background control regions (different $E_{\mathrm{T}}^{\mathrm{iso}}$ requirements) as a function of E_{T}^{γ}, $p_{\mathrm{T}}^{\mathrm{jet-lead}}$, $m^{\gamma-\mathrm{jet}}$, $|\cos\theta^{*}|$ and $\Delta\phi^{\gamma-\mathrm{jet}}$.

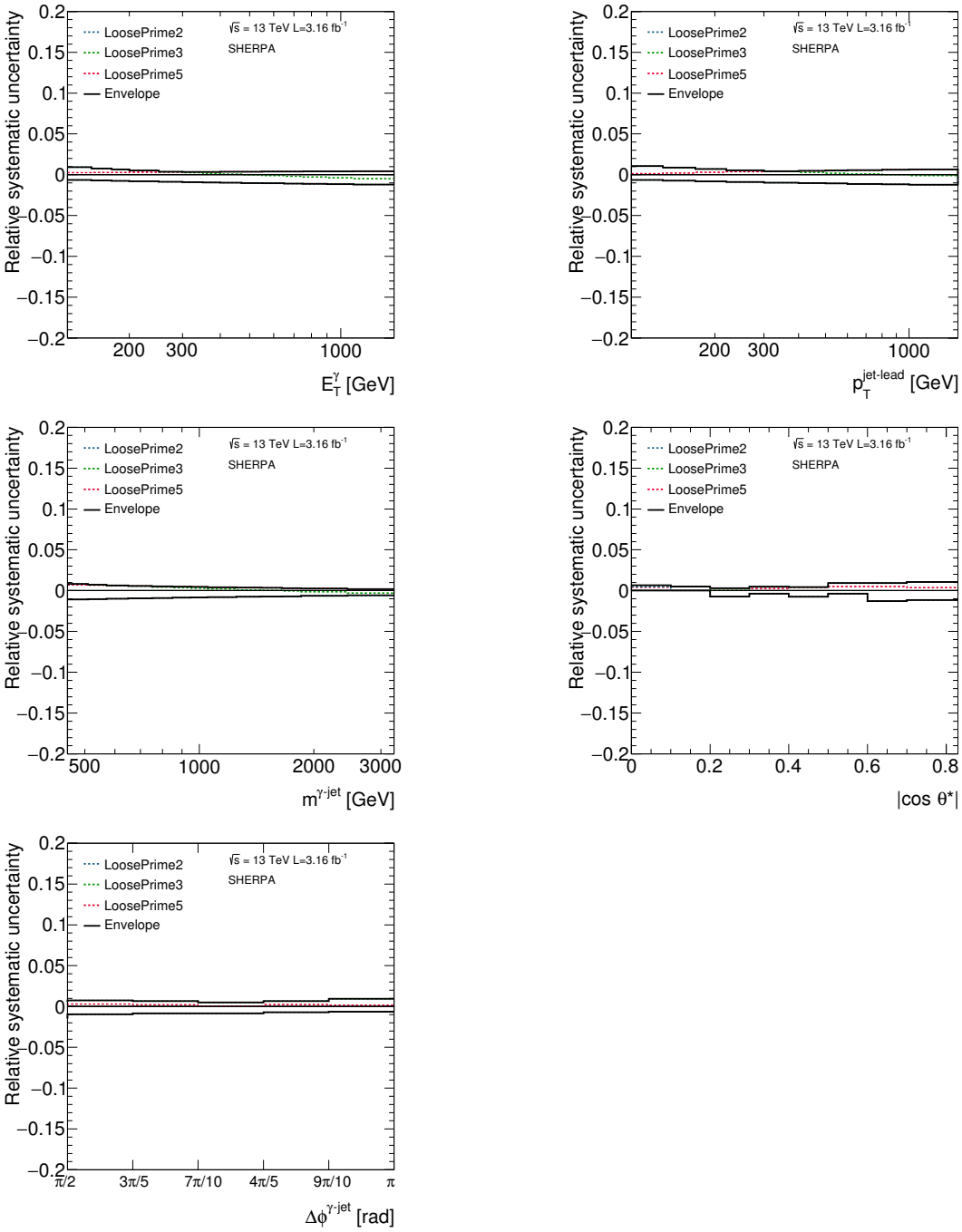

Figure 8.10: Systematic uncertainty on the measured cross sections due to the uncertainty in the choice of the background control regions (*loose'* definitions) as a function of E_{T}^{γ}, $p_{\mathrm{T}}^{\mathrm{jet-lead}}$, $m^{\gamma-\mathrm{jet}}$, $|\cos\theta^{*}|$ and $\Delta\phi^{\gamma-\mathrm{jet}}$.

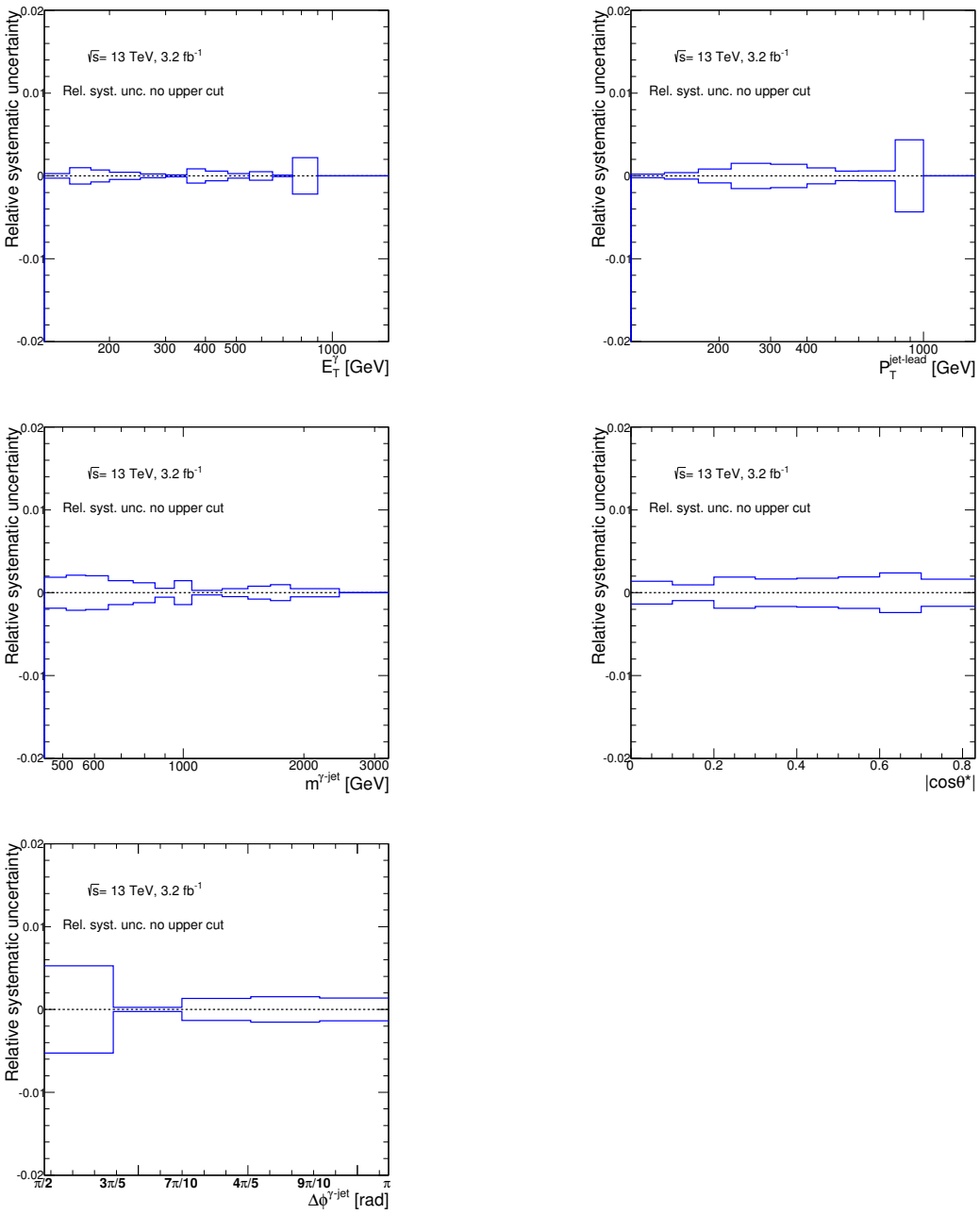

Figure 8.11: Systematic uncertainty on the measured cross sections due to the uncertainty in the choice of the background control regions (removing the 50 GeV upper cut for regions B and D) as a function of E_{T}^{γ}, $p_{\mathrm{T}}^{\mathrm{jet-lead}}$, $m^{\gamma-\mathrm{jet}}$, $|\cos\theta^{*}|$ and $\Delta\phi^{\gamma-\mathrm{jet}}$.

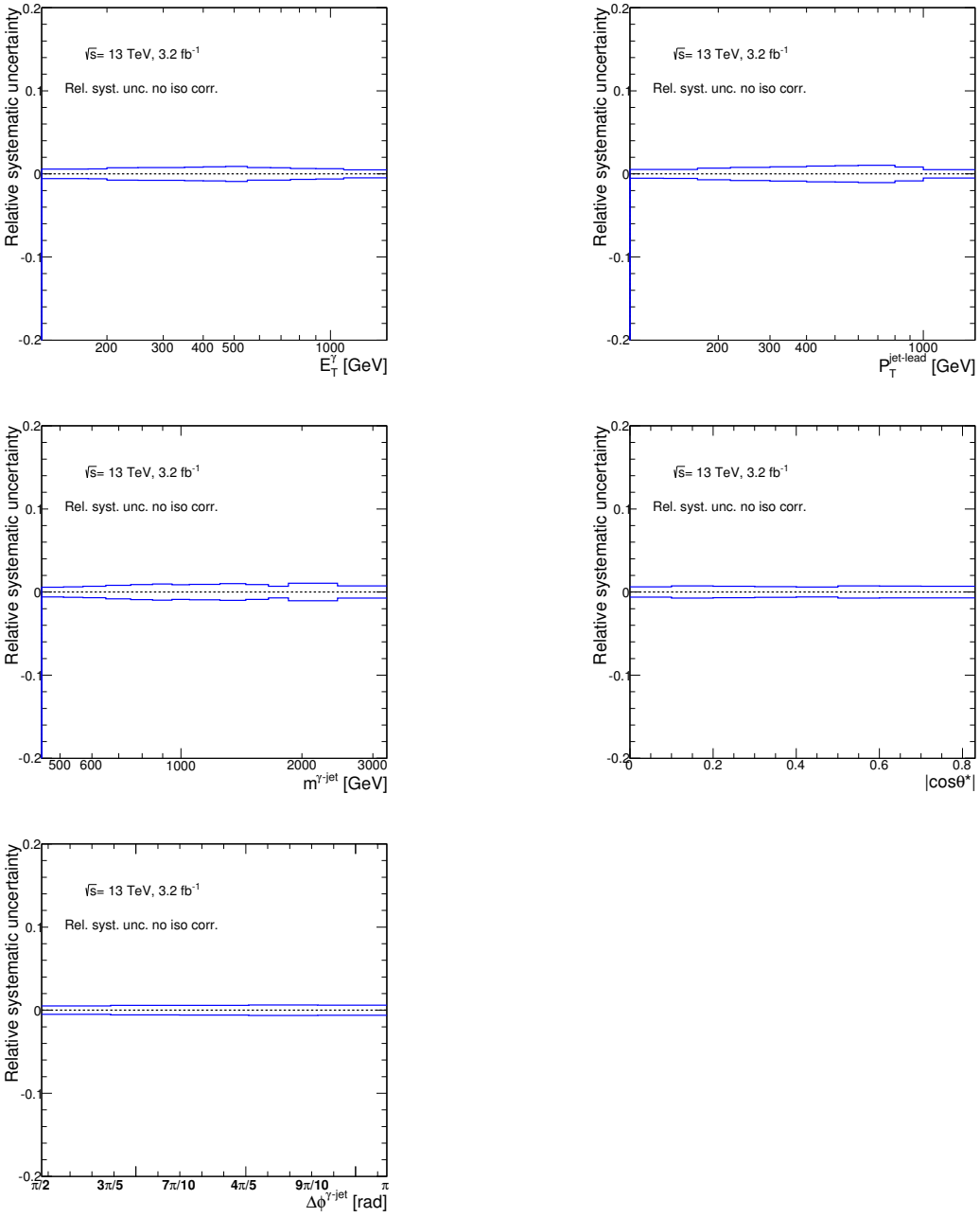

Figure 8.12: Systematic uncertainty on the measured cross sections due to the effects of the isolation corrections as a function of E_{T}^{γ}, $p_{\mathrm{T}}^{\mathrm{jet-lead}}$, $m^{\gamma-\mathrm{jet}}$, $|\cos\theta^{*}|$ and $\Delta\phi^{\gamma-\mathrm{jet}}$.

8.8 Identification and isolation correlation in the background

The isolation and identification photon variables used to define the plane in the 2D-sideband method to subtract the background are assumed to be uncorrelated for background events ($R_{\text{bckg}} = 1$). Any correlation between these variables would affect the estimation of the purity of the signal yield and would lead to systematic uncertainties in the background-subtraction procedure. For this study, the non-isolated regions B and D are further subdivided into two regions each [77]: B', B'', D' and D''. These regions are defined as follows:

- Region B': tight photons in the range $4.2 \cdot 10^{-3}$ E_{T}^{γ} + threshold < E_{T}^{iso} < $4.2 \cdot 10^{-3}$ E_{T}^{γ} + threshold + 8 GeV;
- Region B'': tight photons in the range $4.2 \cdot 10^{-3}$ E_{T}^{γ} + threshold +8 GeV < E_{T}^{iso} < 50 GeV;
- Region D': non-tight photons in the range $4.2 \cdot 10^{-3}$ E_{T}^{γ} + threshold < E_{T}^{iso} < $4.2 \cdot 10^{-3}$ E_{T}^{γ} + threshold + 8 GeV;
- Region D'': non-tight photons in the range $4.2 \cdot 10^{-3}$ E_{T}^{γ} + threshold +8 GeV < E_{T}^{iso} < 50 GeV;

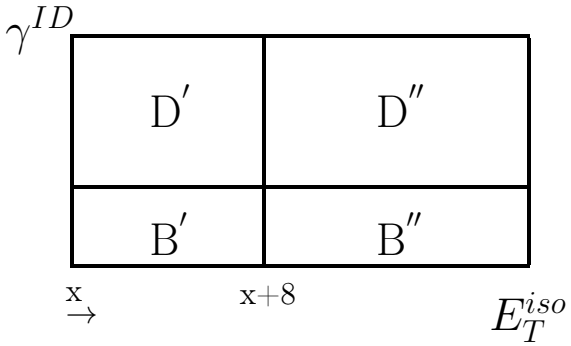

Figure 8.13: An illustration of the definition of regions B', B'', D' and D'' from regions B and D described in Section 5.7. In the lower part of the figure, x represents the "threshold", varied in the range [6.8 - 11.8] GeV in steps of 1 GeV. x+8 GeV is used to define the upper limit of regions B' and D'.

The lower limit of regions B' and D' is varied: the starting value is denoted as "threshold", so as to study the dependence on the initial value within the region of highly non-isolated photons, which could be affected by the brem component. The "threshold" value is variated between 6.8 and 11.8 GeV in steps of 1 GeV. The extent of the regions B' and D' is always 8 GeV. The lower limit of regions B'' and D'' is varied accordingly so as to match the upper limits of regions B' and D'. The upper limit of regions B'' and D'' is always 50 GeV. An illustration of the definition of these 4 sub-regions can be find in Figure 8.13. These regions are used to compute $R^{'}_{bckg} = (N_{B'} \cdot N_{D''})/(N_{B''} \cdot N_{D'})$ and there is an extrapolation when used as R_{bckg}, which is defined using regions A, B, C and D. As a result of this study, a range in R_{bckg} is set so as to cover the deviations from unity observed for the estimations based on subtracting the signal leakage with SHERPA or PYTHIA optimised. The range in R_{bckg}, which is taken as the uncertainty, is indicated in Figures 8.14 by the dotted lines. Figure 8.15 shows the resulting uncertainties on the measured cross sections.

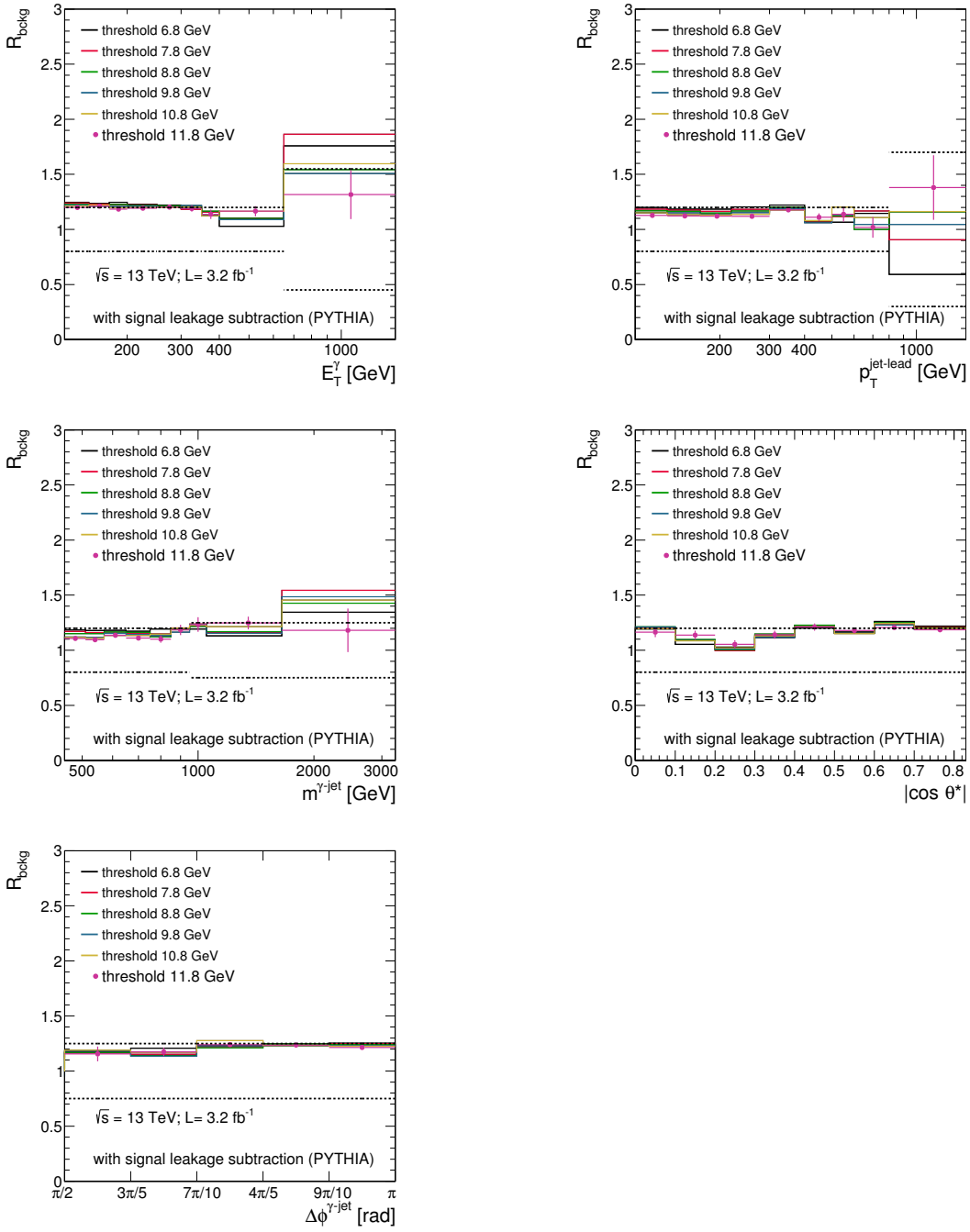

Figure 8.14: R_{bckg} as a function of E_{T}^{γ}, $p_{\mathrm{T}}^{\mathrm{jet-lead}}$, $m^{\gamma-\mathrm{jet}}$, $|\cos\theta^{*}|$ and $\Delta\phi^{\gamma-\mathrm{jet}}$. The signal leakage contributions in the control regions are removed using PYTHIA optimised. The range in R_{bckg}, which is taken as uncertainty, is indicated by the dotted lines.

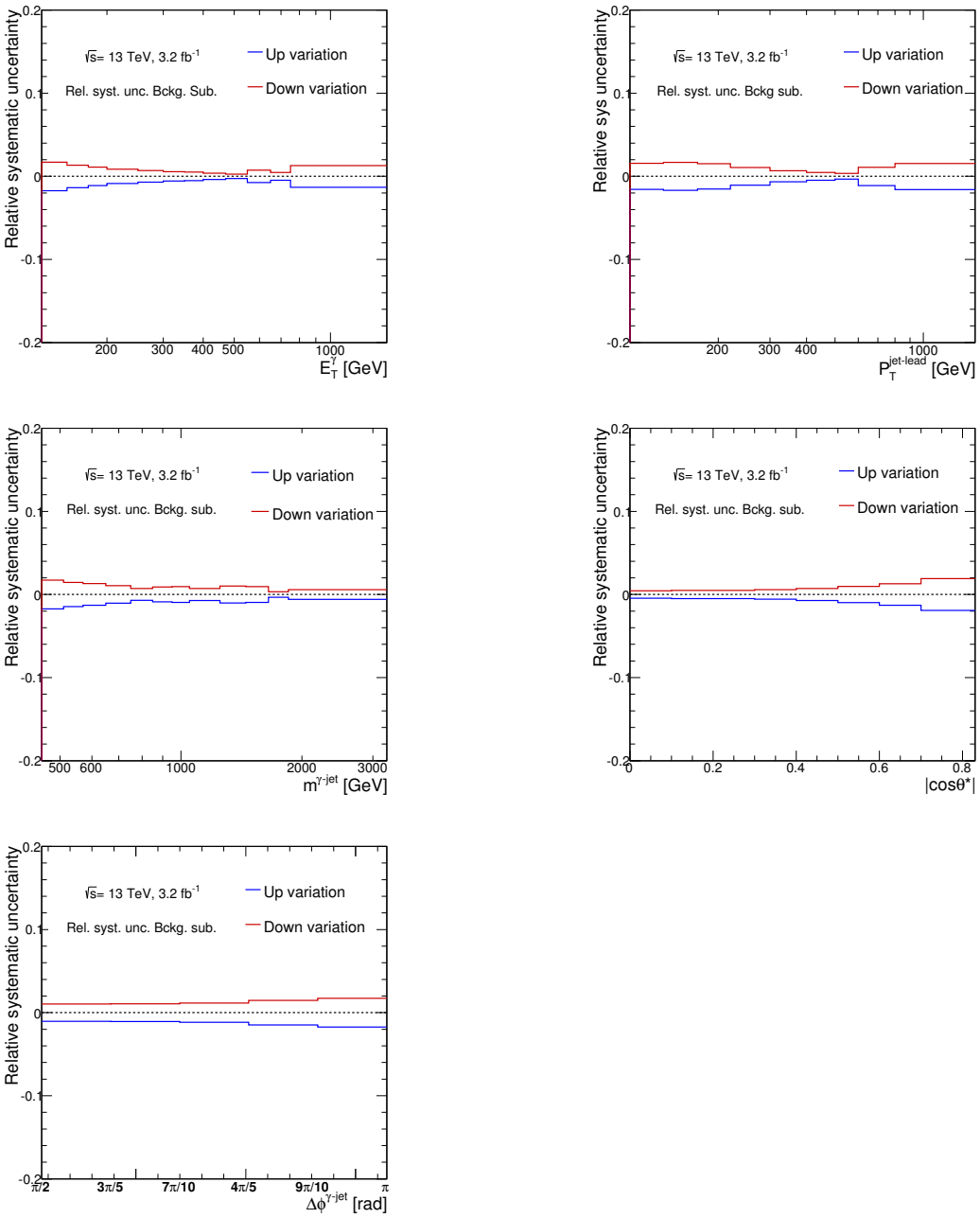

Figure 8.15: Systematic uncertainty on the measured cross sections due to the photon ID and $E_{\mathrm{T}}^{\mathrm{iso}}$ correlations in background events (R_{bckg}) as a function of E_{T}^{γ}, $p_{\mathrm{T}}^{\mathrm{jet-lead}}$, $m^{\gamma-\mathrm{jet}}$, $|\cos\theta^{*}|$ and $\Delta\phi^{\gamma-\mathrm{jet}}$.

8.9 Pile-up reweighting

To match the in-time and out-of-time pileup conditions in the data, the distribution of $< \mu >$ in simulated events is reweighted to that of the data after applying a factor 1/1.16[1]. An uncertainty due to this reweighting is estimated by changing this factor applied to the data to 1/1.09 or 1/1.23. Figure 8.16 shows the resulting uncertainties on the cross sections.

8.10 MC sample statistics

The limited MC statistics affects mainly the bin-by-bin correction factors. Figure 8.17 shows the statistical uncertainty of the MC samples (light-blue shaded area) together with the main systematic uncertainties.

8.11 Uncertainty on the measurement of the integrated luminosity

The uncertainty on the integrated luminosity is ± 2.1 % [85]. This uncertainty is fully correlated in all bins of all the measured cross sections and it was not added in quadrature to the other uncertainties.

8.12 Total systematic uncertainty

The total systematic uncertainty is computed by adding in quadrature the sources of uncertainty listed in the previous sections, except that on the integrated luminosity. Figure 8.17 shows the resulting total systematic uncertainty, which takes into account the statistical uncertainties in the data for the signal region A as well as for the control regions B, C and D. For $E_{\mathrm{T}}^{\gamma} <$ 600 GeV, the systematic uncertainty dominates while for higher values, the statistical uncertainty of the data limits the precision of the measurements. The same happens for $m^{\gamma-\mathrm{jet}} < 1600$ GeV and $p_{\mathrm{T}}^{\mathrm{jet}} < 1000$ GeV. For $|\cos\theta^{*}|$, the systematic uncertainty dominates in the whole measured range.

[1] https://twiki.cern.ch/twiki/bin/viewauth/Atlas/DataPreparationCheckListForPhysicsAnalysis

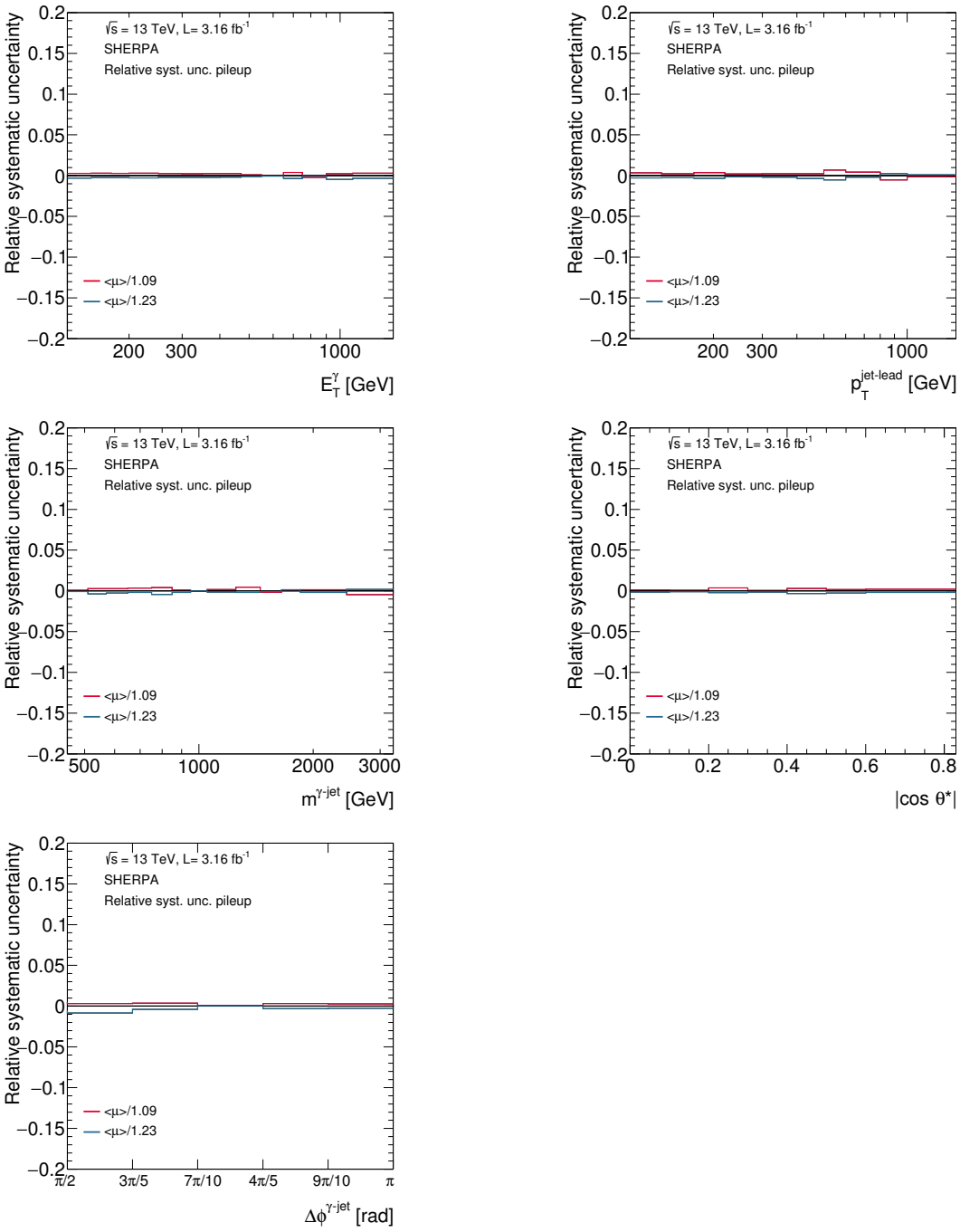

Figure 8.16: Systematic uncertainty on the measured cross sections due to the pileup reweighting as a function of E_{T}^{γ}, $p_{\mathrm{T}}^{\mathrm{jet-lead}}$, $m^{\gamma-\mathrm{jet}}$, $|\cos\theta^{*}|$ and $\Delta\phi^{\gamma-\mathrm{jet}}$.

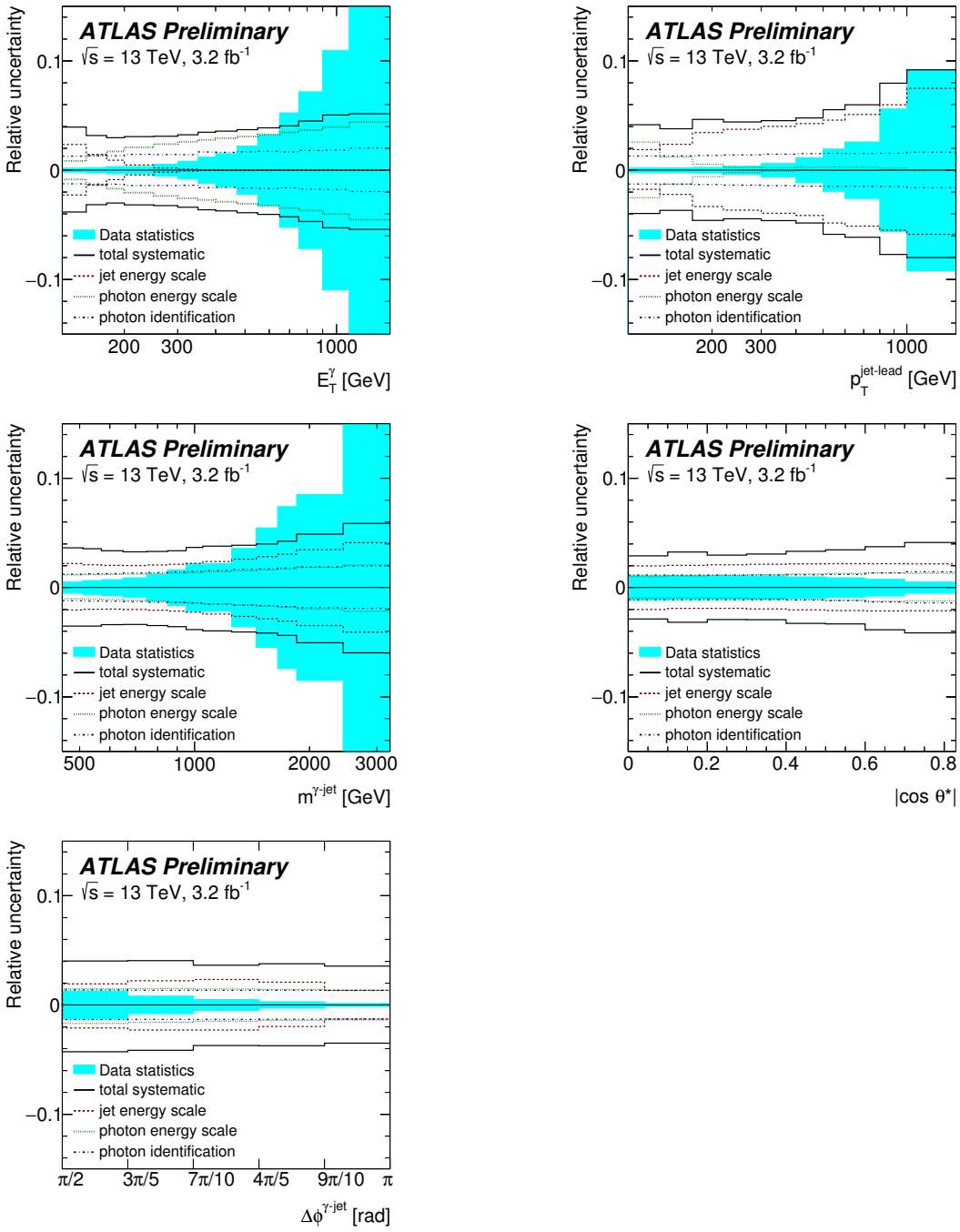

Figure 8.17: Total systematic and statistical uncertainties from the data as a function of E_{T}^{γ}, $p_{\mathrm{T}}^{\mathrm{jet-lead}}$, $m^{\gamma-\mathrm{jet}}$, $|\cos\theta^{*}|$ and $\Delta\phi^{\gamma-\mathrm{jet}}$.

Chapter 9

Next-to-leading-order QCD calculations

The NLO pQCD predictions that are compared to the measurements have been made calculated using the programs JETPHOX or SHERPA 2.2.2. The details are given below.

9.1 Predictions using JETPHOX

One set of the NLO QCD predictions used in the analysis presented here is computed using the JETPHOX 1.3.1_2 program [86] [87]. It includes the full NLO QCD calculation of both the direct-photon and fragmentation contributions to the cross section.
The number of flavours was set to five. The renormalisation (μ_{R}), factorisation (μ_{F}) and fragmentation (μ_{f}) scales were chosen to be $\mu_{\mathrm{R}} = \mu_{\mathrm{F}} = \mu_{\mathrm{f}} = E_{\mathrm{T}}^{\gamma}$. The calculations were performed using the MMHT2014 [88] parametrisations of the proton PDFs and the NLO BFG set II photon fragmentation function [89]. The strong coupling constant was calculated at two loops with $\alpha_s(m_{\mathrm{Z}}) = 0.120$. Predictions based on the CT14 [90] and NNPDF3.0 [91] proton PDF sets were also computed; in these cases, the strong coupling constant was calculated at two loops with $\alpha_s(m_{\mathrm{Z}}) = 0.118$. The calculations were performed using a parton-level isolation cut, which required a total transverse energy below $4.2 \cdot 10^{-3} \cdot E_{\mathrm{T}}^{\gamma} + 10$ GeV from the partons inside a cone of radius $R = 0.4$ around the photon direction. The anti-$\mathrm{k_t}$ algorithm with radius $R = 0.4$ was applied to the partons in the events generated by this program to compute the cross-section predictions.
Figure 9.1 shows the predicted cross sections for the studied variables and obtained with the MMHT2014, CT14 and NNPDF3.0 PDFs.

The parton-level predictions of PYTHIA nominal and PYTHIA fitted are

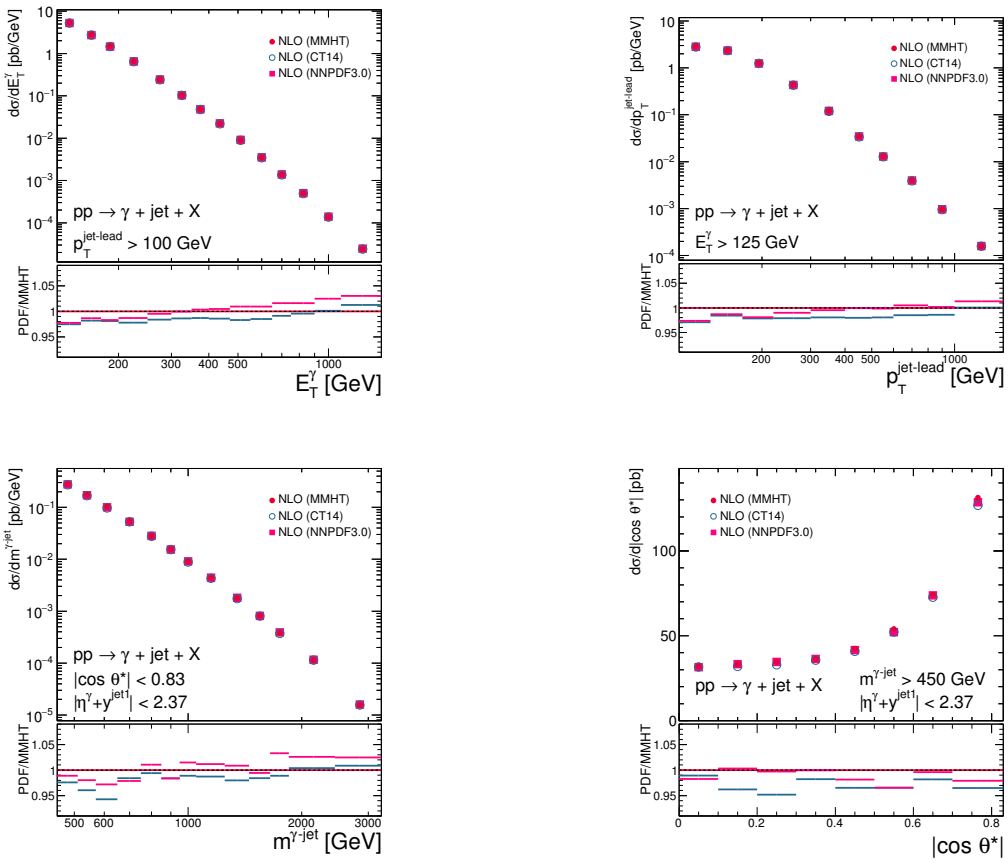

Figure 9.1: Predicted NLO QCD cross sections based on the MMHT2014 (dots),CT14 (open circles) and NNPDF3.0 (squares) proton PDFs as a function of E_{T}^{γ}, $p_{\mathrm{T}}^{\mathrm{jet-lead}}$, $m^{\gamma-\mathrm{jet}}$ and $|\cos\theta^{*}|$. The lower part of the figures shows the ratio of the NLO calculations to that based on MMHT2014, which is taken as the nominal one.

compared to the NLO QCD calculations based on the MMHT2014 in Figure 9.2. The PYTHIA fitted parton-level calculations were obtained by using the same method for the optimisation described in the previous section, adjusting in this case the hard and brem PYTHIA components at parton level to describe best the NLO predictions. After this procedure, the parton-level cross sections of PYTHIA give an adequate description of the NLO QCD predictions to be used for the estimation of the hadronisation corrections.

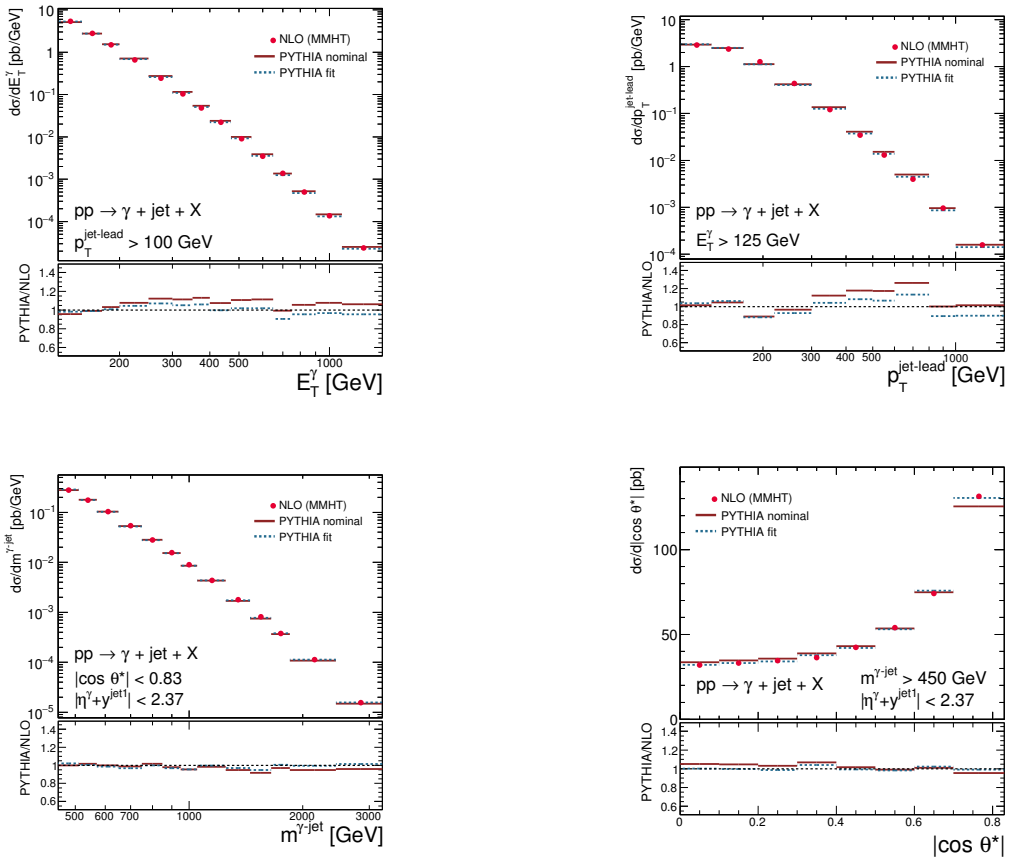

Figure 9.2: Predicted NLO QCD cross sections based on the MMHT2014 calculations(dots) as functions of E_{T}^{γ}, $p_{\mathrm{T}}^{\mathrm{jet-lead}}$, $m^{\gamma-\mathrm{jet}}$ and $|\cos\theta^*|$. The predictions at parton level of PYTHIA nominal (solid lines) and PYTHIA fitted (dashed lines) are also shown. The MC predictions are normalised to the integrated NLO QCD calculations. The lower part of the figures shows the ratio of the parton-level MC to the NLO QCD calculations.

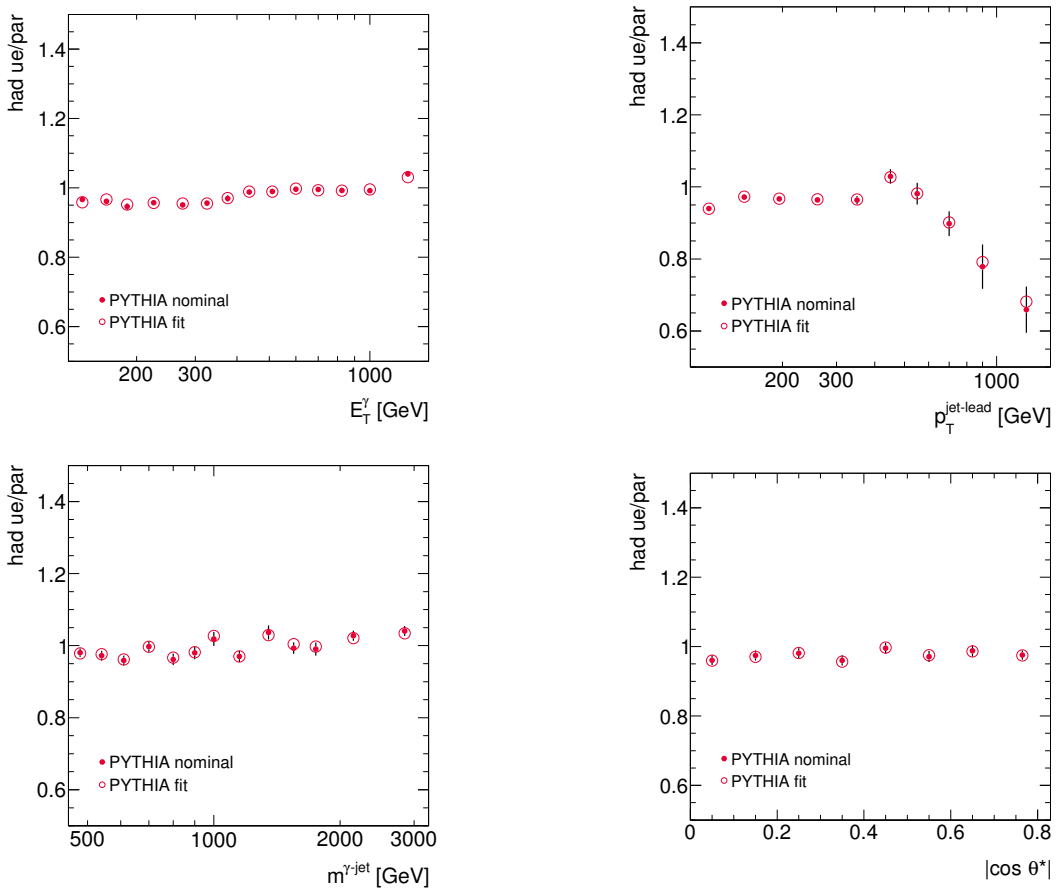

Figure 9.3: C_{NLO} correction factors from PYTHIA nominal (dots) and PYTHIA fitted (open circles) as functions of E_{T}^{γ}, $p_{\mathrm{T}}^{\mathrm{jet-lead}}$, $m^{\gamma-\mathrm{jet}}$ and $|\cos\theta^*|$.

9.2 Hadronisation and underlying-event corrections to the JETPHOX predictions

Since the measurements refer to jets of hadrons and include underlying-event (UE) effects, whereas the NLO QCD calculations refer to jets of partons without such effect, the JETPHOX predictions are corrected to particle level with UE using MC models. The correction factor, C_{NLO}, is defined as the ratio of the cross section for jets of hadrons with UE and that for jets of partons and is estimated by using PYTHIA 8.165 and the AU2 CTEQ6L1 tune [92].

For this method to be valid, the parton level of the MC simulations must be

close in shape to the NLO QCD predictions of JETPHOX. The comparison of the MC simulations and the NLO QCD calculations is shown in Figure 9.2. The parton-level predictions of PYTHIA fitted give an adequate description of the NLO QCD calculations. Figure 9.3 shows the C_{NLO} correction factors for each cross section. The dependence of C_{NLO} with $p_{\mathrm{T}}^{\mathrm{jet-lead}}$ is due to the photon isolation requirement in the brem component, as can be seen in Figure 9.4. Figure 9.4(a) shows C_{NLO} separately for the brem and hard components in PYTHIA. Figure 9.4(b) shows C_{NLO} with and without the application of the photon isolation requirement.

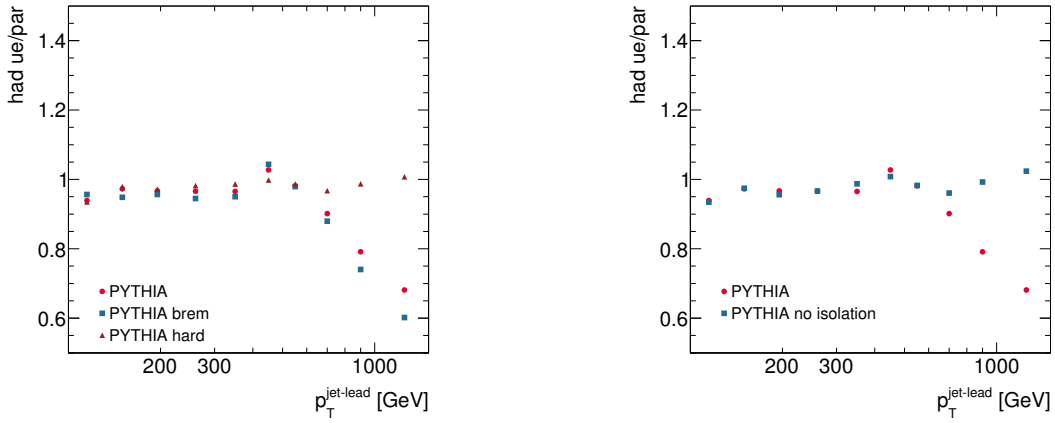

Figure 9.4: (Left) C_{NLO} correction factor from PYTHIA fitted (dots), as well as for the hard (triangles) and brem (squares) components, as a function of $p_{\mathrm{T}}^{\mathrm{jet-lead}}$. (Right) C_{NLO} correction factor from PYTHIA fitted with (dots) and without (squares) the photon isolation requirement as a function of $p_{\mathrm{T}}^{\mathrm{jet-lead}}$.

9.2.1 Uncertainties on the non-perturbative corrections

To estimate the uncertainties on the non-perturbative corrections, samples of events are generated with PYTHIA 8.186 using the LO NNPDF2.3 A14 tune as well as two variations around it, namely Var1Up and Var1Down. The rationale for such an approach is that for the LO NNPDF2.3 A14 tune variations are available to explore the dependence of the non-perturbative corrections with e.g. the modelling of the underlying event. The generation of the events arising from photon bremsstrahlung in QCD dijet events is extremely CPU intensive. It took approximately two months to generate 3×10^9 events to have enough statistics so that the estimations of the non-perturbative corrections in the tails of the distributions were sufficiently accurate. The non-perturbative corrections thus obtained are shown in Figure 9.5 and compared to those described above, which were performed using PYTHIA 8.165 and the AU2 CTEQ6L1 tune. It turned out that the LO NNPDF2.3 A14 tune and its variations yield corrections closer to unity than those of the AU2 CTEQ6L1 tune. Furthermore, the differences in the corrections between the LO NNPDF2.3 A14 tune and the AU2 CTEQ6L1 tune are much larger than the differences between the LO NNPDF2.3 A14 tune and its variations. The former differences are particulary significant in the tail of the distribution of $p_{\mathrm{T}}^{\mathrm{jet-lead}}$. In addition to the PDFs, many parameter settings are different between the LO NNPDF2.3 A14 tune and the AU2 CTEQ6L1 tune, for example the parameters governing the space and time showers;

in particular, the parameter "SpaceShower:rapidityOrder" was switched off (on) in the AU2 CTEQ6L1 (LO NNPDF2.3 A14) tune. Given this scenario, a revision of the choice for the nominal values of the non-perturbative corrections was mandatory and its described in the next section, together with an estimation of the uncertainties.

9.2.2 Revision of the nominal non-perturbative corrections and their uncertainties

The following approach was followed regarding the nominal values of the non-perturbative corrections and the estimation of the uncertainties:

- the average of the corrections obtained using the AU2 CTEQ6L1 and LO NNPDF2.3 A14 tunes is taken as the nominal correction.
- half of the difference between the corrections obtained using the AU2 CTEQ6L1 and LO NNPDF2.3 A14 tunes is taken as the uncertainty.

This approach is the less-biased compromise and the estimated uncertainty envelops the estimations obtained with the AU2 CTEQ6L1 and LO NNPDF2.3 A14 tunes. In order to suppress the influence of the statistical fluctuation, in the regions of the observables where the corrections are approximately flat, the result of a fit to constant function is used. The results are shown in Figure 9.5. The uncertainties in the non-perturbative corrections thus obtained are as follows: below 2.2% for the E_{T}^{γ}; approximately 1% for the $m^{\gamma-\mathrm{jet}}$ distribution; approximately 1.5% for the $|\cos\theta^{*}|$ distribution; and for the $p_{\mathrm{T}}^{\mathrm{jet-lead}}$ distribution the uncertainty is below 3.2% for $p_{\mathrm{T}}^{\mathrm{jet-lead}} < 600$ GeV and increases up to 21% for $p_{\mathrm{T}}^{\mathrm{jet-lead}} \approx 1.5$ TeV. More details about the revision of the nominal non-perturbative corrections and their uncertainties are given in [93].

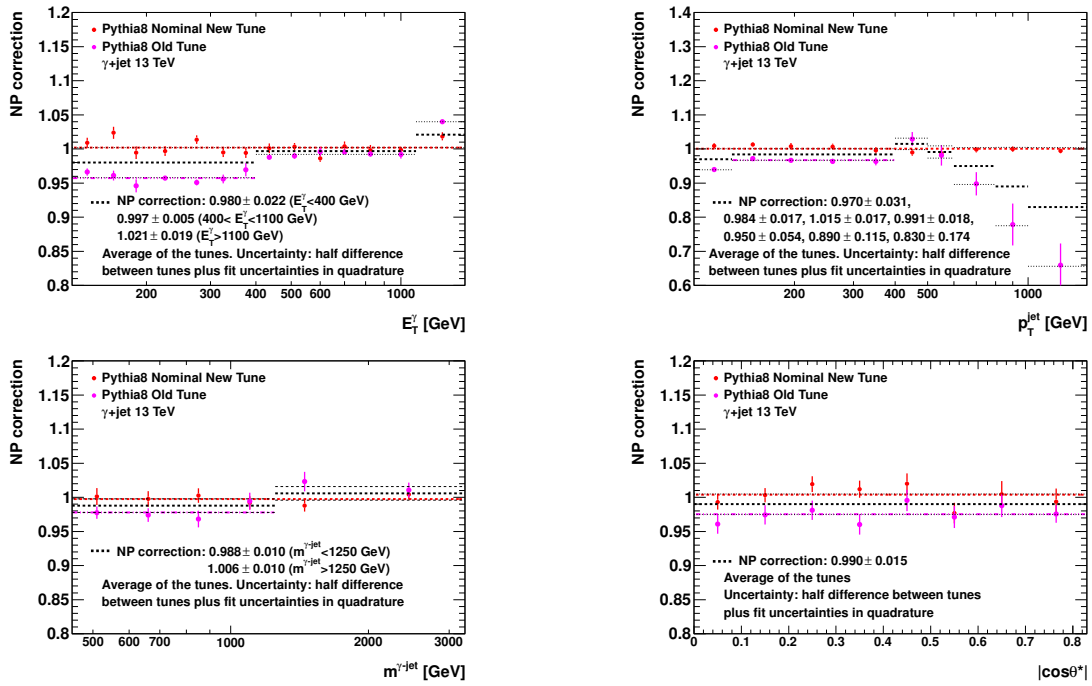

Figure 9.5: Non-perturbative corrections from PYTHIA as functions of E_{T}^{γ}, $p_{\mathrm{T}}^{\mathrm{jet-lead}}$, $m^{\gamma-\mathrm{jet}}$ and $|\cos\theta^{*}|$ for different tunes: the AU2 CTEQ6L1 tune ("Old tune", magenta dots) and the LO NNPDF2.3 A14 tune ("Nominal New tune", red dots). The new non-perturbative corrections are shown as the dashed black lines and the uncertainty on the corrections is shown by the dotted black lines.

9.3 Theoretical uncertainties of JETPHOX predictions

The following sources of uncertainty in the theoretical predictions were considered:

- the uncertainty on the NLO QCD calculations due to terms beyond NLO was estimated by repeating the calculations using values of μ_{R}, μ_{F} and μ_{f} scaled by factors 0.5 and 2. The three scales were either varied simultaneously, individually or by fixing one and varying the other two. In all cases, the condition $0.5 \leq \mu_{\mathrm{A}}/\mu_{\mathrm{B}} \leq 2$ was imposed, where A, $B = R$, F, f and $A \neq B$. The final uncertainty was taken as the largest deviation from the nominal value among the 14 possible variations;

- the uncertainty on the NLO QCD calculations due to those on the proton PDFs was estimated by repeating the calculations using the 50 additional sets from the MMHT2014 error analysis and applying the Hessian method [94] for the evaluation of the PDF uncertainties;

- the uncertainty on the NLO QCD calculations due to the variation of the value of $\alpha_{\mathrm{s}}(m_{\mathrm{Z}})$ was estimated by repeating the calculations using two additional sets of proton PDFs from the MMHT2014 analysis, for which different values of $\alpha_{\mathrm{s}}(m_{\mathrm{Z}})$ were assumed in the fits, namely $\alpha_{\mathrm{s}}(m_{\mathrm{Z}}) = 0.118$ and 0.122;

- the uncertainty due to the non-perturbative effects of hadronisation and underlying event was estimated as described in the previous subsection.

The dominat theoretical uncertainty is that arising from the terms beyond NLO. Figures 9.6 to 9.11 show an overview of the relative theoretical uncertainties in the kinematic region of the measurements except for that due to the non-perturbative corrections. Figure 9.12 shows the total theoretical uncertainty (excluding that due to the non-perturbative corrections) for each cross section. The theoretical uncertainty was obtained by adding in quadrature the individual uncertainties listed above.
The theoretical uncertainties were also computed for the calculations based on the CT14 PDFs and are compared to those based on the (baseline) MMHT2014 PDFs in Figures 9.6 to 9.9.

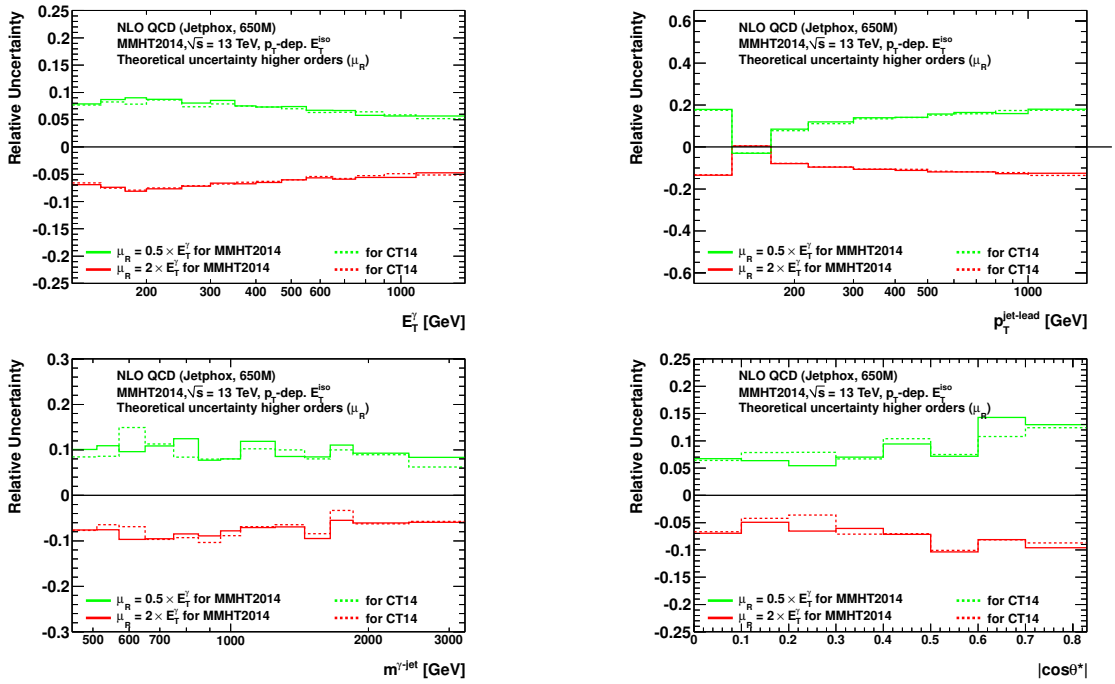

Figure 9.6: Theoretical uncertainty arising from terms beyond NLO (variating μ_{R}) using MMHT2014 (solid lines) and CT14 (dotted lines) as a function of E_{T}^{γ}, $p_{\mathrm{T}}^{\mathrm{jet-lead}}$, $m^{\gamma-\mathrm{jet}}$ and $|\cos\theta^{*}|$.

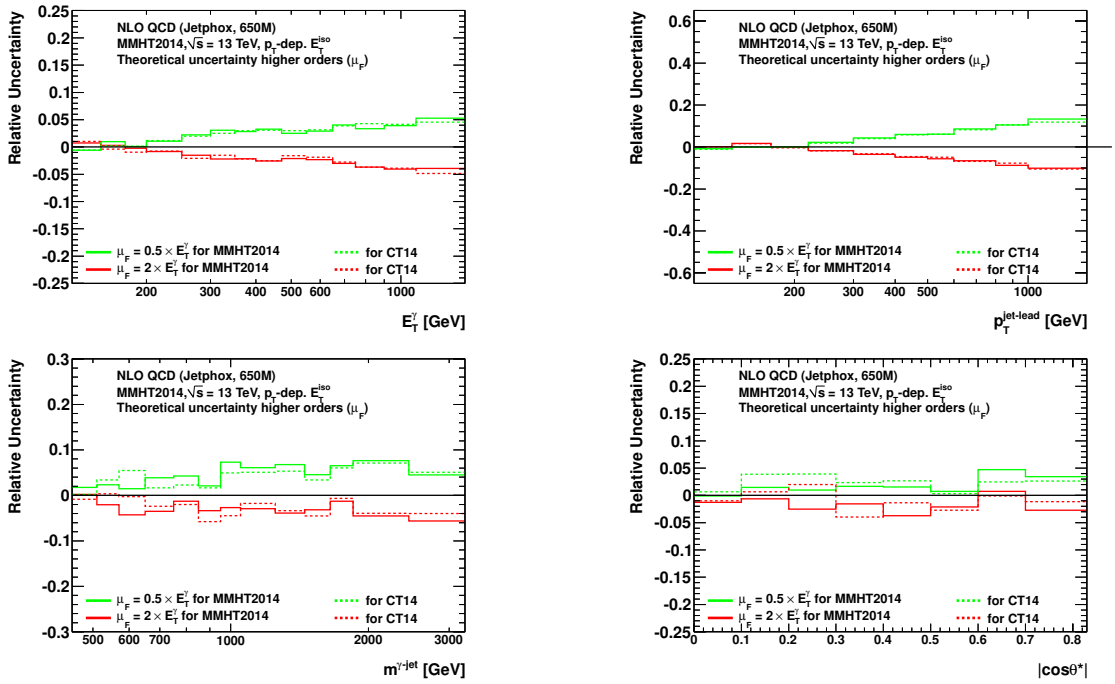

Figure 9.7: Theoretical uncertainty arising from terms beyond NLO (variating μ_{F}) using MMHT2014 (solid lines) and CT14 (dotted lines) as a function of E_{T}^{γ}, $p_{\mathrm{T}}^{\mathrm{jet-lead}}$, $m^{\gamma-\mathrm{jet}}$ and $|\cos\theta^{*}|$.

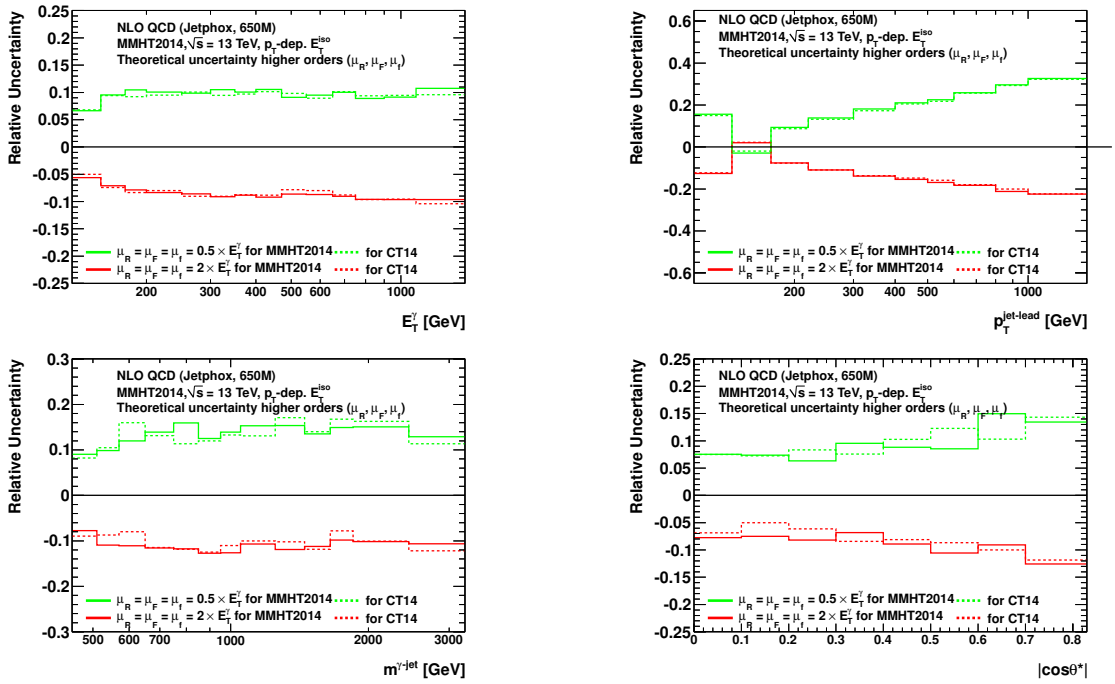

Figure 9.8: Theoretical uncertainty arising from terms beyond NLO (simultaneous variation of μ_{R}, μ_{F} and μ_{f}) using MMHT2014 (solid lines) and CT14 (dotted lines) as a function of E_{T}^{γ}, $p_{\mathrm{T}}^{\mathrm{jet-lead}}$, $m^{\gamma-\mathrm{jet}}$ and $|\cos\theta^{*}|$.

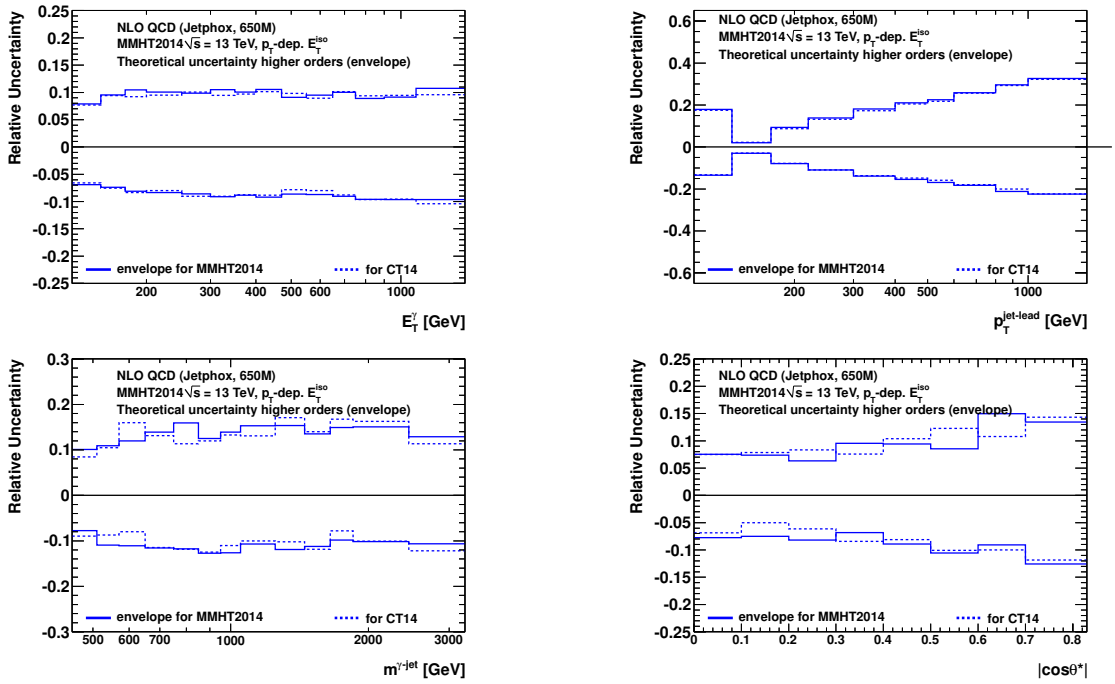

Figure 9.9: Theoretical uncertainty arising from terms beyond NLO (envelope of all 14 variations) using MMHT2014 (solid lines) and CT14 (dotted lines) as functions E_{T}^{γ}, $p_{\mathrm{T}}^{\mathrm{jet-lead}}$, $m^{\gamma-\mathrm{jet}}$ and $|\cos\theta^{*}|$.

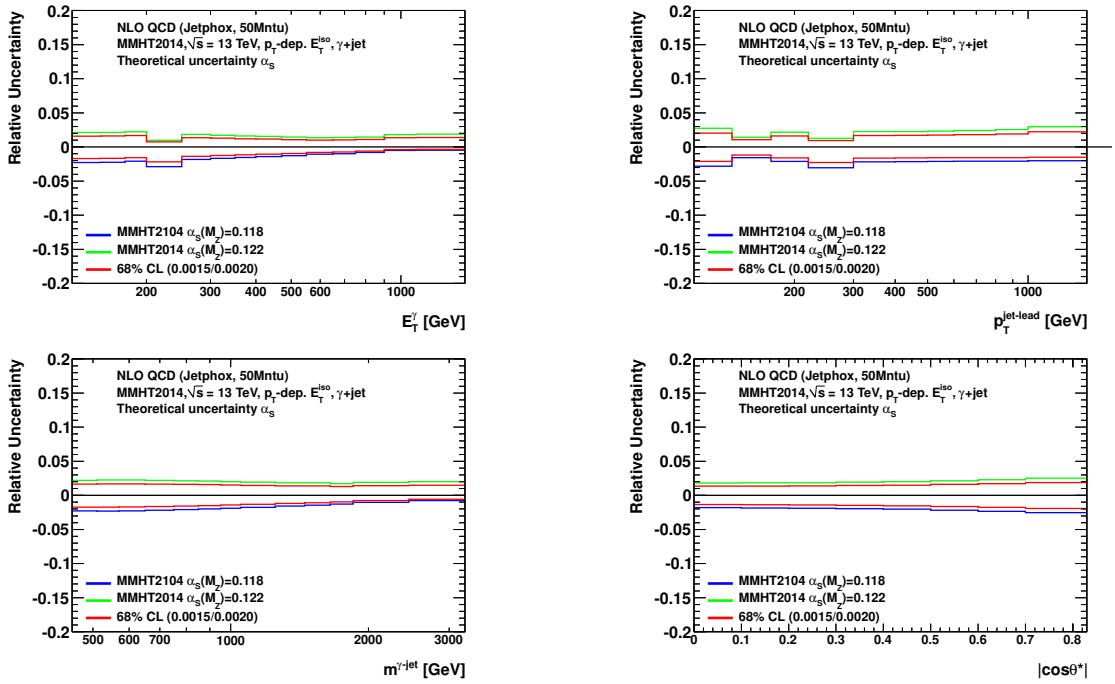

Figure 9.10: Theoretical uncertainty arising from the uncertainty in α_{s} as a function of E_{T}^{γ}, $p_{\mathrm{T}}^{\mathrm{jet-lead}}$, $m^{\gamma-\mathrm{jet}}$ and $|\cos\theta^{*}|$.

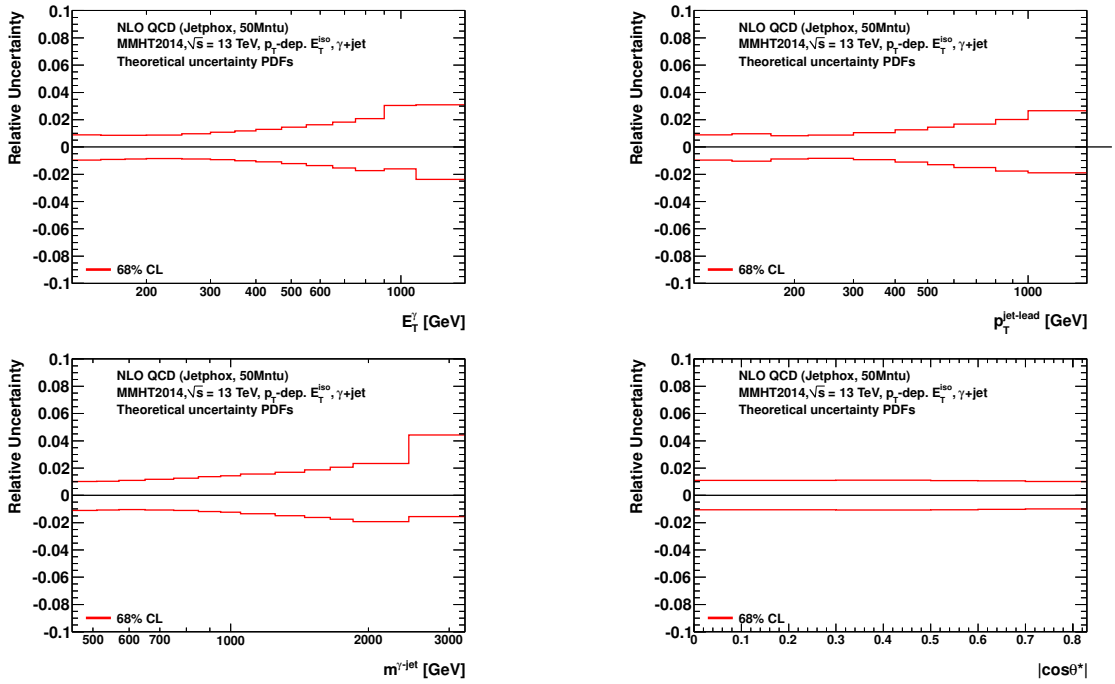

Figure 9.11: Theoretical uncertainty arising from the uncertainty in the PDFs as a function of E_{T}^{γ}, $p_{\mathrm{T}}^{\mathrm{jet-lead}}$, $m^{\gamma-\mathrm{jet}}$ and $|\cos\theta^{*}|$.

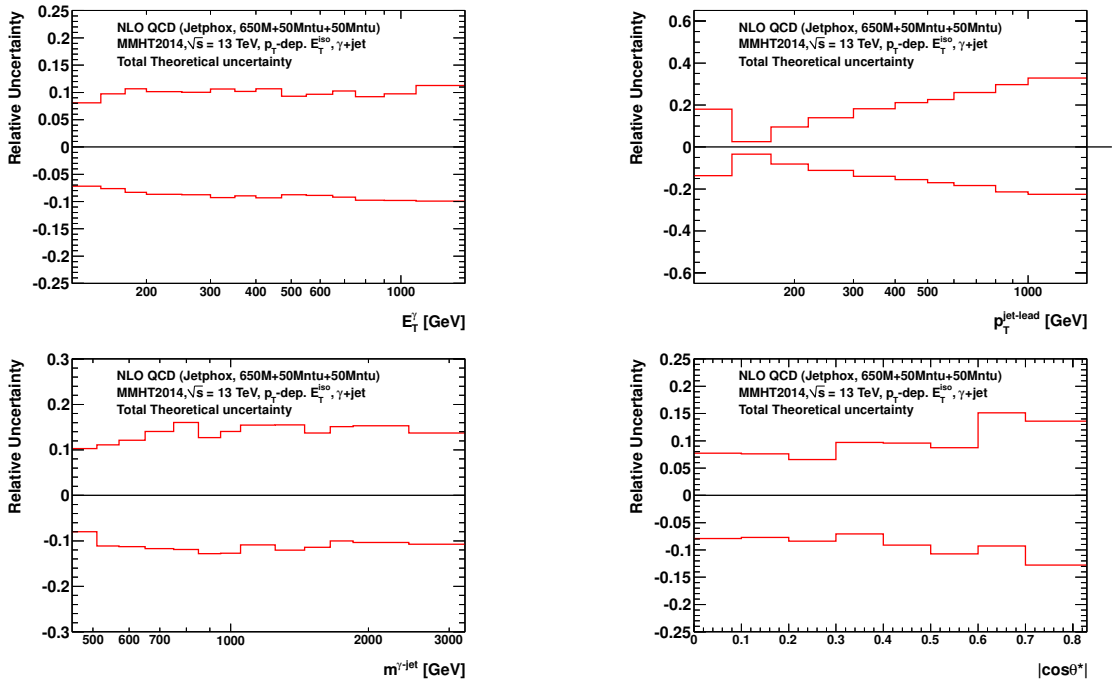

Figure 9.12: Total theoretical uncertainty excluding that due to the non-perturbative corrections as a function of E_{T}^{γ}, $p_{\mathrm{T}}^{\mathrm{jet-lead}}$, $m^{\gamma-\mathrm{jet}}$ and $|\cos\theta^{*}|$.

9.4 Predictions using SHERPA 2.2.2

A second set of predictions was obtained with SHERPA 2.2.2 program. It consistently combines parton-level calculations of γ + 1, 2 jets at NLO and γ + 3,4 jets at LO [95] [96] supplemented with a parton shower [97] while avoiding double-counting effects [98]. A requirement on the photon isolation at the matrix-element level is imposed using Frixione's criterion with R= 0.1, n=2 and $\epsilon = 0.1$. Dynamic factorisation and renormalisation scales are adopted as well as a dynamical merging scale with $\bar{Q}_{\mathrm{cut}} = 20$ GeV [99]. The strong coupling constant is set to $\alpha_{\mathrm{s}}(m_{\mathrm{Z}}) = 0.118$. Fragmentation into hadrons is performed using the same model as for the LO SHERPA samples. The NNPDF3.0NNLO PDFs are used in conjuction with the corresponding SHERPA default tuning. All the NLO SHERPA predictions are based on the particle-level variables from this computation after applying the requirements for the selected phase-space region.
The samples of events generated with SHERPA 2.2.2 were made in a such way that for each event the weights necessary to obtain the predictions for other PDF sets were available. Figure 9.13 shows the predicted cross sections for the variables studied. Shown are also the calculations based on the NNPDF3.0NNLO, MMHT2014 and CT14 PDFs. The differences between the predictions based on different proton PDFs are smaller than 3%.

9.5 Uncertainties of the predictions using SHERPA 2.2.2

The following sources of uncertainty in the theoretical predictions were considered:

- the uncertainty on the NLO SHERPA calculations due to terms beyond NLO was estimated by repeating the calculations using values of μ_{R} and μ_{F} scaled by factors 0.5 and 2. The two scales were either varied simultaneously, individually or by fixing one and varying the other two. In all cases, the condition $0.5 \leq \mu_{\mathrm{A}}/\mu_{\mathrm{B}} \leq 2$ was imposed, where A, B = R, F and $A \neq B$. The final uncertainty was taken as the largest deviation from the nominal value among the 6 possible variations;

- the uncertainty on the NLO SHERPA calculations due to those on the proton PDFs was estimated by repeating the calculations using 100 replicas from the NNPDF3.0 error analysis;

- the uncertainty on the NLO SHERPA calculations due to that on the value of $\alpha_{\mathrm{s}}(m_{\mathrm{Z}})$ was estimated by repeating the calculations using two additional sets of proton PDFs from the NNPDF3.0 analysis, for which different values of $\alpha_{\mathrm{s}}(m_{\mathrm{Z}})$ were assumed in the fits, namely $\alpha_{\mathrm{s}}(m_{\mathrm{Z}})$ = 0.117 and 0.119.

The dominat theoretical uncertainty is that arising from the terms beyond NLO. Figures 9.14 to 9.16 show an overview of the relative theoretical uncertainties in the kinematic region of the measurements. The total theoretical uncertainty was obtained by adding in quadrature the individual uncertainties listed above.
For the NLO SHERPA predictions there is no need to apply non-perturbative corrections since the predictions contain the effects of hadronisation and underlying event. Nevertheless, an uncertainty should be assigned for this effect, but no tune other than the default one is available. It is expected that the uncertainty should be of similar size as that evaluated using PYTHIA.

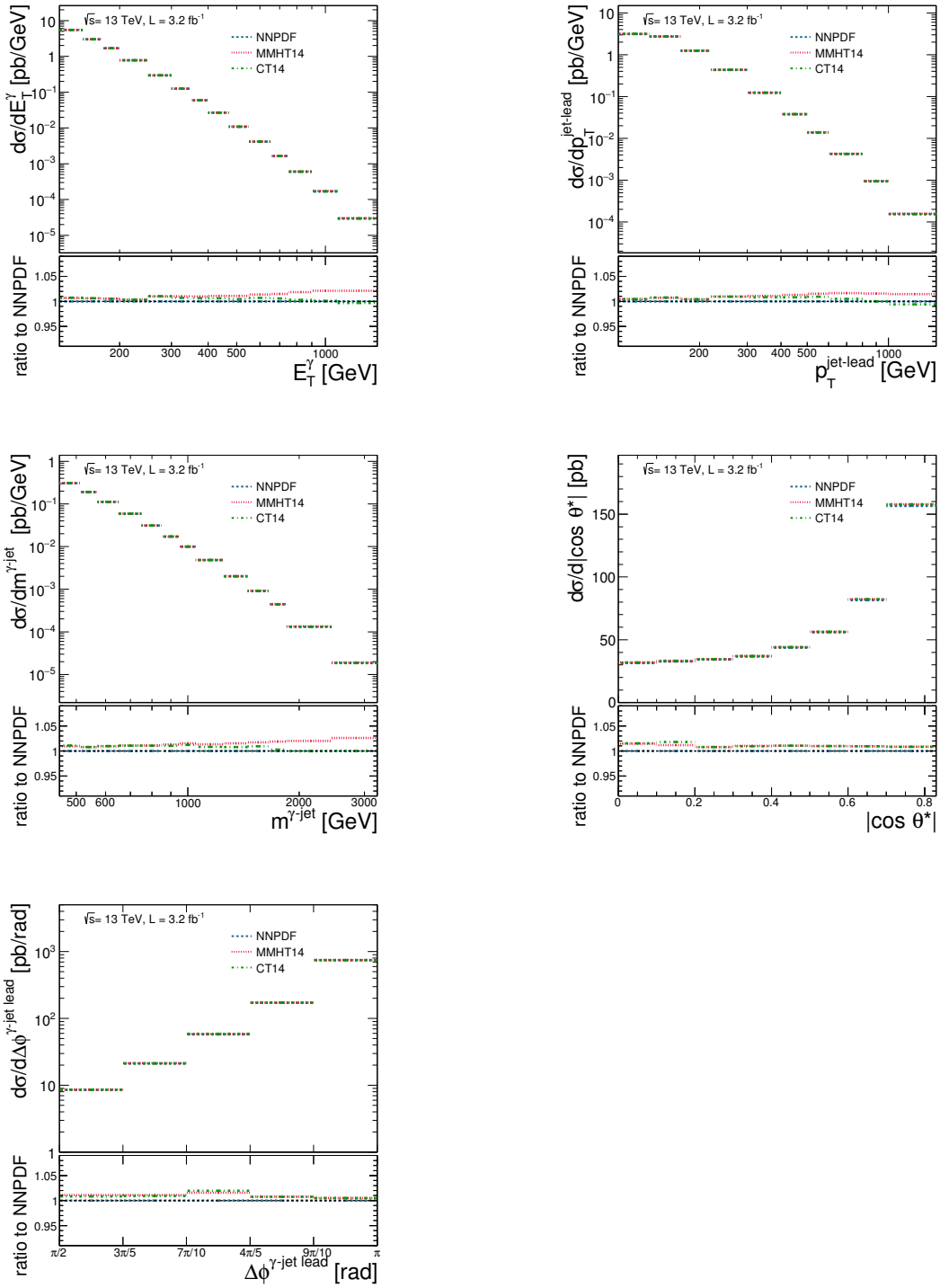

Figure 9.13: Predictions of NLO SHERPA based on the NNPDF3.0NNLO (blue dashed lines), MMHT2014 (red dotted lines) and CT14 (green dot-dashed lines) proton PDFs for the cross sections for isolated photon plus one jet production as functions of the studied variables. The lower part of each figure shows the ratio of the predictions to that based on NNPDF3.0NNLO PDFs.

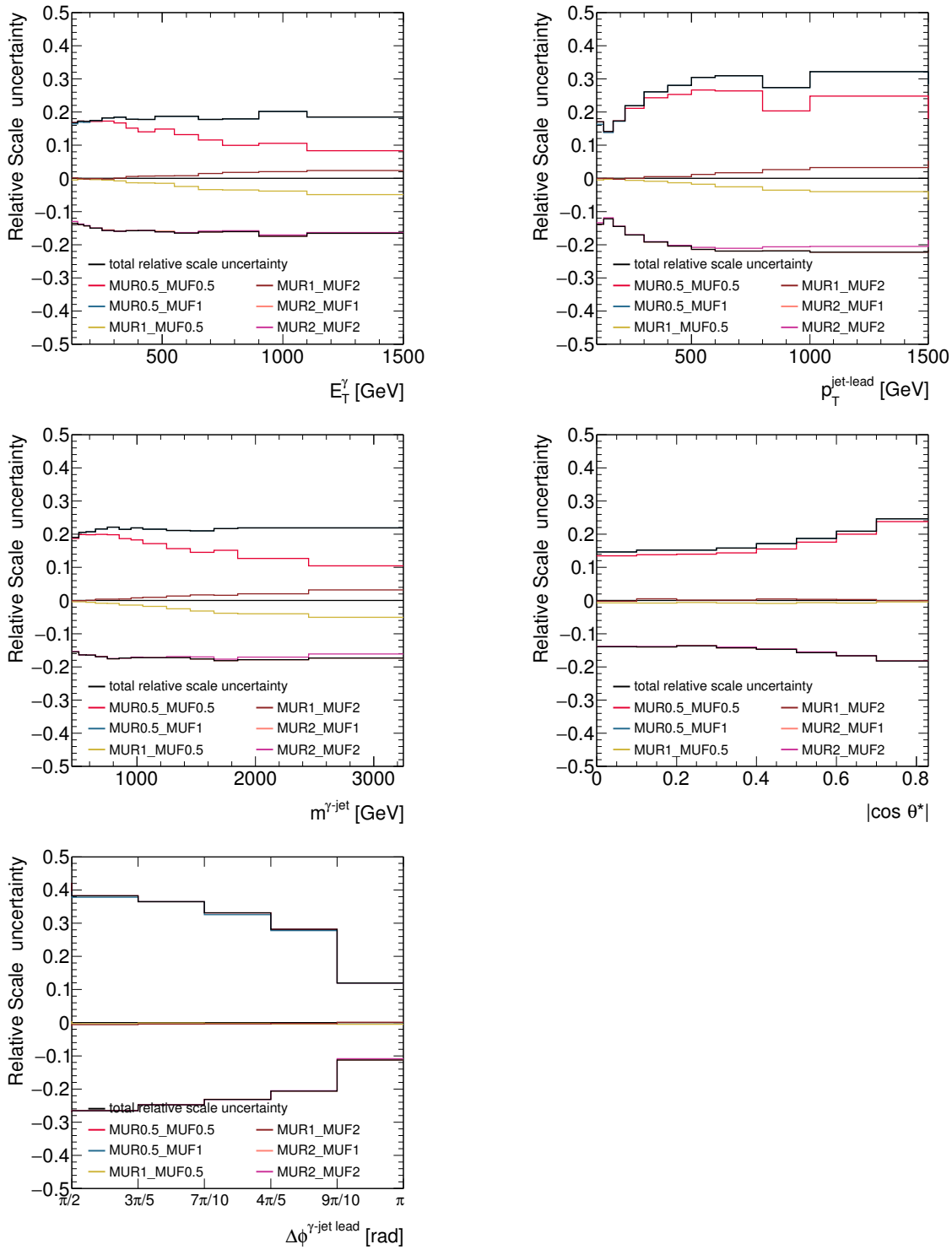

Figure 9.14: Relative uncertainties of the NLO SHERPA predictions as functions of the different variables, arising from the variation of the scales: $\mu_R = \mu_F = 0.5 \cdot E_T^\gamma$ (red histograms); $\mu_R = 0.5 \cdot E_T^\gamma$ and $\mu_F = E_T^\gamma$ (blue histograms); $\mu_R = E_T^\gamma$ and $\mu_F = 0.5 \cdot E_T^\gamma$ (yellow histograms); $\mu_R = E_T^\gamma$ and $\mu_F = 2 \cdot E_T^\gamma$ (brown histograms); $\mu_R = 2 \cdot E_T^\gamma$ and $\mu_F = E_T^\gamma$ (pink histograms); $\mu_R = \mu_F = 2 \cdot E_T^\gamma$ (magenta histograms). The envelope of the six variations is represented by the black histogram.

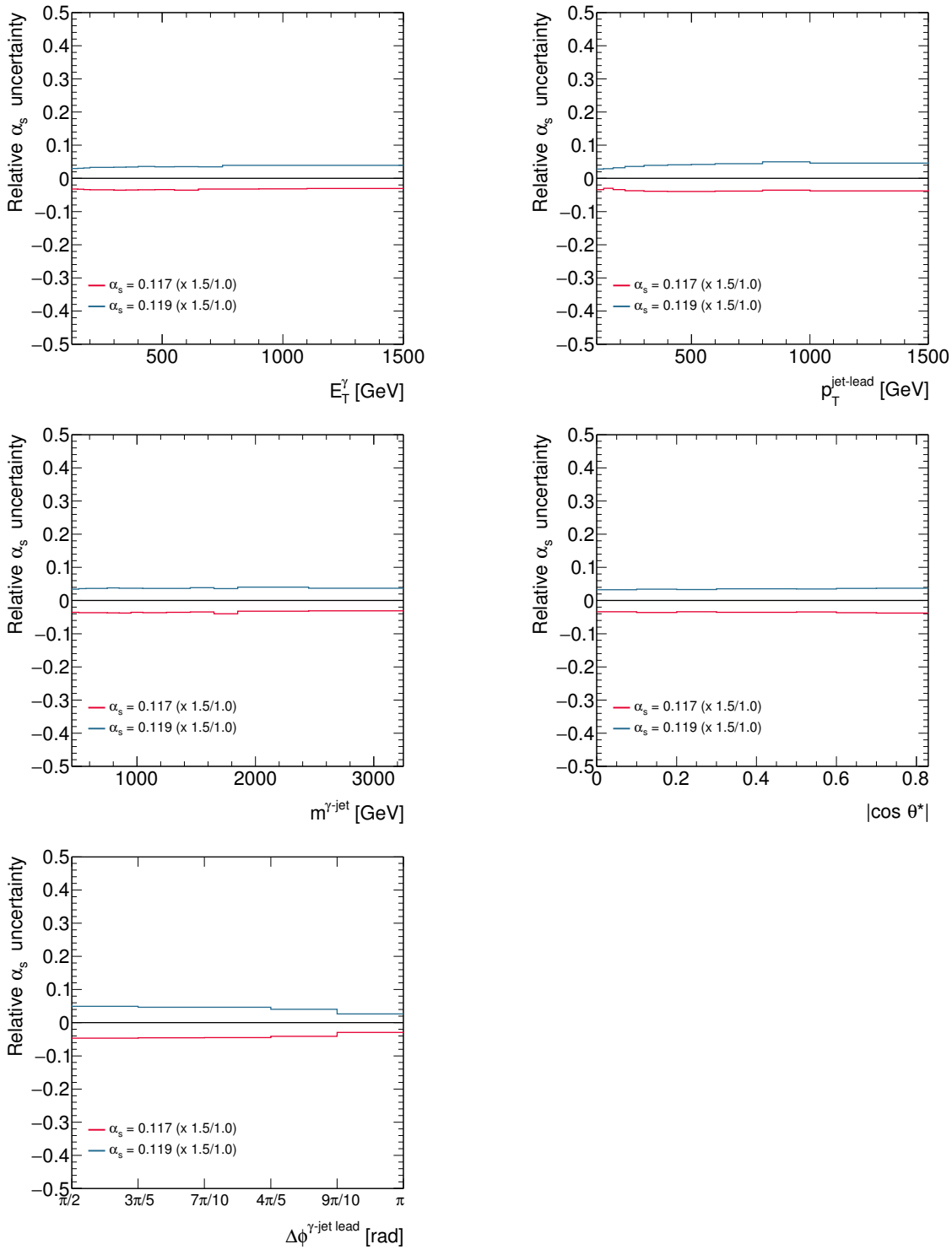

Figure 9.15: Relative uncertainties of the NLO SHERPA as functions of the different variables, arising from the uncertainty in α_s.

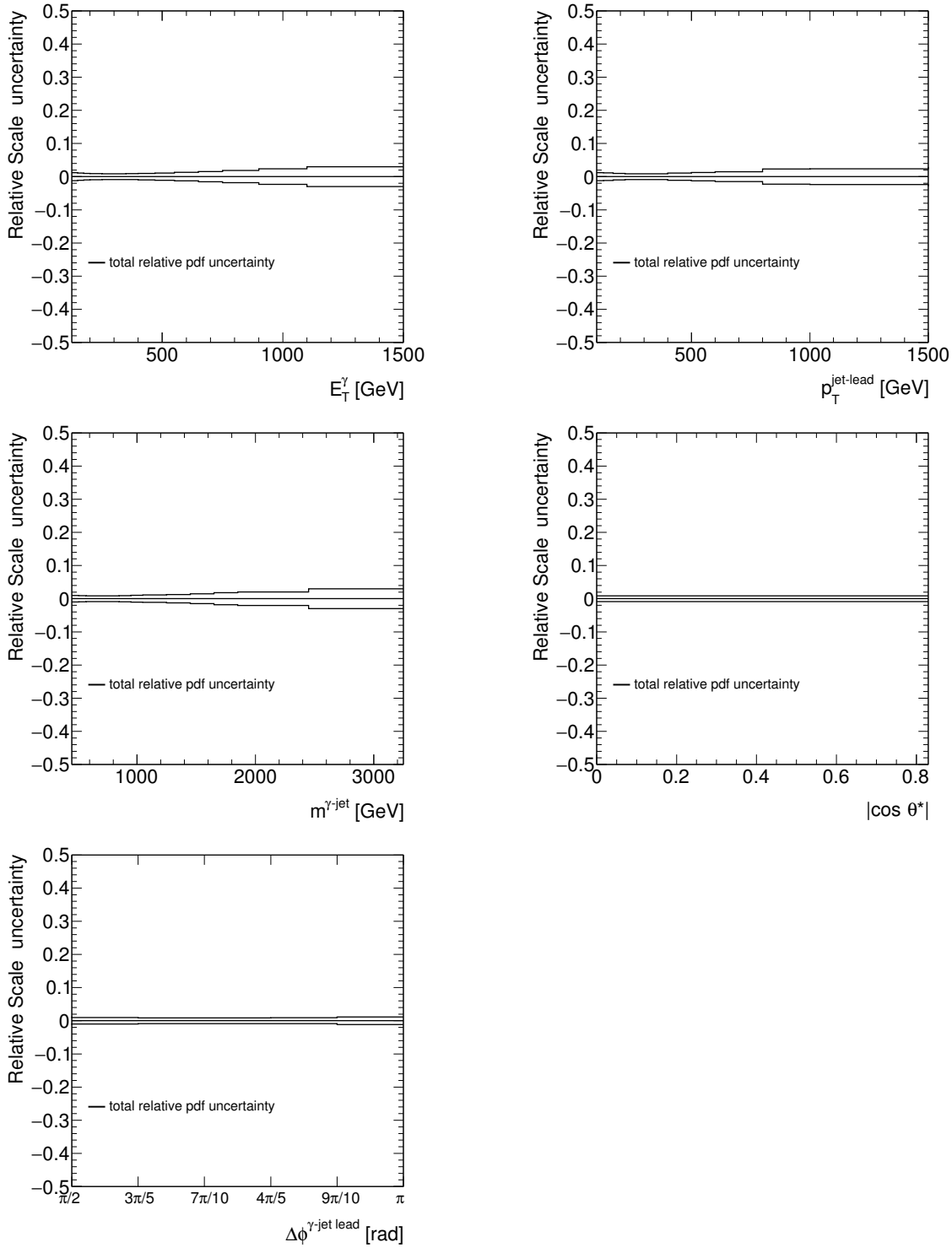

Figure 9.16: Relative uncertainties of the NLO SHERPA as functions of the different variables, arising from the uncertainty in the PDFs.

Chapter 10

Results

The measured differential cross sections presented in this chapter, refer to isolated prompt photons with $E_{\mathrm{T}}^{\mathrm{iso}} < 4.2 \cdot 10^{-3} \cdot E_{\mathrm{T}}^{\gamma} + 10$ GeV and jets of hadrons. The measured fiducial cross section for the isolated-photon plus jet production is:

$$\sigma_{\mathrm{meas}} = 300 \pm 10(\mathrm{exp.}) \pm 6(\mathrm{lumi.})\ \mathrm{pb}$$

where "exp." is referred to the sum in quadrature of the statistical and systematic uncertainties and "lumi." denotes the uncertainty on the integrated luminosity. The fiducial cross sections predicted by NLO QCD JETPHOX (multi-leg NLO QCD plus parton shower SHERPA) using the MMHT2014 (NNPDF3.0NNLO) PDF sets are

$$\sigma_{\mathrm{JETPHOX}} = 291^{+25}_{-21}(\mathrm{scale})^{+2}_{-3}(\mathrm{PDF})^{+4}_{-5}(\alpha_{\mathrm{s}}) \pm 6(\mathrm{non-perturb.})\ \mathrm{pb}$$

and

$$\sigma_{\mathrm{NLOSHERPA}} = 319^{+54}_{-45}(\mathrm{scale}) \pm 3(\mathrm{PDF})^{+10}_{-11}(\alpha_{\mathrm{s}})\ \mathrm{pb}$$

which are consistent with the measured value within the theoretical uncertainties. Figure 10.1 shows the isolated-photon plus jet cross sections as functions of E_{T}^{γ}, $p_{\mathrm{T}}^{\mathrm{jet-lead}}$, $\Delta\phi^{\gamma-\mathrm{jet}}$, $m^{\gamma-\mathrm{jet}}$ and $|\cos\theta^{*}|$. The measured $d\sigma/dE_{\mathrm{T}}^{\gamma}$ decreased by six orders of magnitude over the range between 125 GeV and 1.5 TeV. The experimental uncertainty, excluding the one on the luminosity, is less than 5% over the whole range. It is dominated by the photon energy scale for $E_{\mathrm{T}}^{\gamma} \leq 700$ GeV, and it increases to 33% at $E_{\mathrm{T}}^{\gamma} \sim 1.5$ TeV due to the statistical uncertainty in this region. The measured $d\sigma/dp_{\mathrm{T}}^{\mathrm{jet-lead}}$ decreases by 4 orders of magnitude from $p_{\mathrm{T}}^{\mathrm{jet-lead}} \sim 100$ GeV to 1.5 TeV. The experimental uncertainty is below 5% for $p_{\mathrm{T}}^{\mathrm{jet-lead}} < 500$ GeV, excluding that on the luminosity, and is dominated by the jet energy scale uncertainty. The measured $d\sigma/d\Delta\phi^{\gamma-\mathrm{jet}}$ is restricted to the range $\Delta\phi^{\gamma-\mathrm{jet}} > \pi/2$ to avoid the phase space region dominated by the photon production in association

with multi jet events. It increases when $\Delta\phi^{\gamma-\text{jet}}$ tends to π. The experimental uncertainty is $\sim 4\%$, excluding that in the luminosity. The measured $d\sigma/dm^{\gamma-\text{jet}}$ decreases more than 4 orders of magnitude up to highest measured value of 3.25 TeV. The experimental uncertainty is $\sim 4\%$ up to $m^{\gamma-\text{jet}} \leq$ 1.5 TeV, dominated by the photon and jet energy scales, excluding that on the luminosity, while for $m^{\gamma-\text{jet}} > 1.5$ TeV the statistical uncertainty becomes dominant. The measured $d\sigma/d|\cos\theta^*|$ increases as $|\cos\theta^*|$ increases. Excluding the uncertainty on the luminosity, the experimental one is 3%-4%; the only significant contributions arise from the photon and jet energy scales and the photon identification efficiency.
The predictions of the PYTHIA (default) and LO SHERPA MC models are compared to the measured cross sections in Figure 10.1. The two predictions are normalised to the measured integrated fiducial cross section. The difference in the normalisation between data and PYTHIA (LO SHERPA) is $\sim +10\%$ ($+40\%$) and it is due to the tree-level matrix elements on which the predictions are based and are affected by a large normalisation uncertainty because of missing higher-order terms. For this reason the theoretical uncertainties are not included in Figure 10.1. Both PYTHIA and SHERPA give an adequate description of the shape of the measured $d\sigma/dE_{\text{T}}^{\gamma}$, PYTHIA is slightly better than SHERPA for $E_{\text{T}}^{\gamma} \leq 600$ GeV. For $d\sigma/dp_{\text{T}}^{\text{jet}-\text{lead}}$, the prediction of LO SHERPA gives an adequate description of the data in the whole measured range, while PYTHIA overestimates the data for $p_{\text{T}}^{\text{jet}-\text{lead}} \geq$ 200 GeV; this behavior is attributed to a large contribution of the photon bremsstrahlung predicted by the used tune of PYTHIA. LO SHERPA gives a good description of the measured $d\sigma/d\Delta\phi^{\gamma-\text{jet}}$, whereas PYTHIA underestimates the data in the range $3\pi/5 < \Delta\phi^{\gamma-\text{jet}} < 4\pi/5$ rad. Moreover, both predictions are in a fair agreement for $m^{\gamma-\text{jet}} < 1.25$ TeV and for the whole $|\cos\theta^*|$ range.
The predictions of the fixed-order NLO QCD calculations of JETPHOX based on the MMHT2014 PDF set and corrected for hadronisation and underlying effects, as explained in Chapter 9, are compared to the measurements in Figure 10.2 . The predictions of the multi-leg NLO QCD plus parton shower calculations of SHERPA based on the NNPDF3.0NNLO PDF set are compared to the measurements in Figure 10.3. The two different kind of predictions describe the data within the experimental and theoretical uncertainties. For the cross section as a function of $\Delta\phi^{\gamma-\text{jet}}$, only the prediction of NLO SHERPA is compared to the measured cross section, due to the unability of JETPHOX to reproduce the data down to $\Delta\phi^{\gamma-\text{jet}} = \pi/2$, due to its limitation in the number of final-state partons. For most of the points, the theoretical uncertainties are larger than those of experimental origin. The predictions of JETPHOX (NLO SHERPA) are also obtained with other

parametrisations of the proton PDFs, namely CT14 and NNPDF3.0NLO (CT14 and MMHT2014), and differ by less than 5%. This means that the description of the data achieved by the predictions does not depend on the choice of a specific PDF set. Thus, the NLO pQCD predictions provide an adequate description of the measurements within the uncertainties.
The measured increase of the differential cross section as a function of $|\cos\theta^*|$ is well reproduced by both predictions. To show the sensitivity to the t-channel quark or gluon exchange, the predicted cross section $d\sigma/d|\cos\theta^*|$ for LO direct and fragmentation processes are compared to the measurements in Figure 10.4. Although the two contributions are no longer distinguishable at NLO, the LO calculations are useful in illustrating the dynamics of the two processes. The contribution from the fragmentation, dominated by gluon exchange, shows a steeper increase when $|\cos\theta^*| \to 1$ respect to the direct process, dominated by the quark exchange. The shape of the measured cross section $d\sigma/d|\cos\theta^*|$ is closer to that of the direct process than to that of the fragmentation contribution. This is consistent with the dominance of the processes in which the exchanged particle is a quark.
The measured differential cross sections as a function of the studied variables, with their experimental uncertainties are reported in Tab C.1-C.5 in Appendix C.

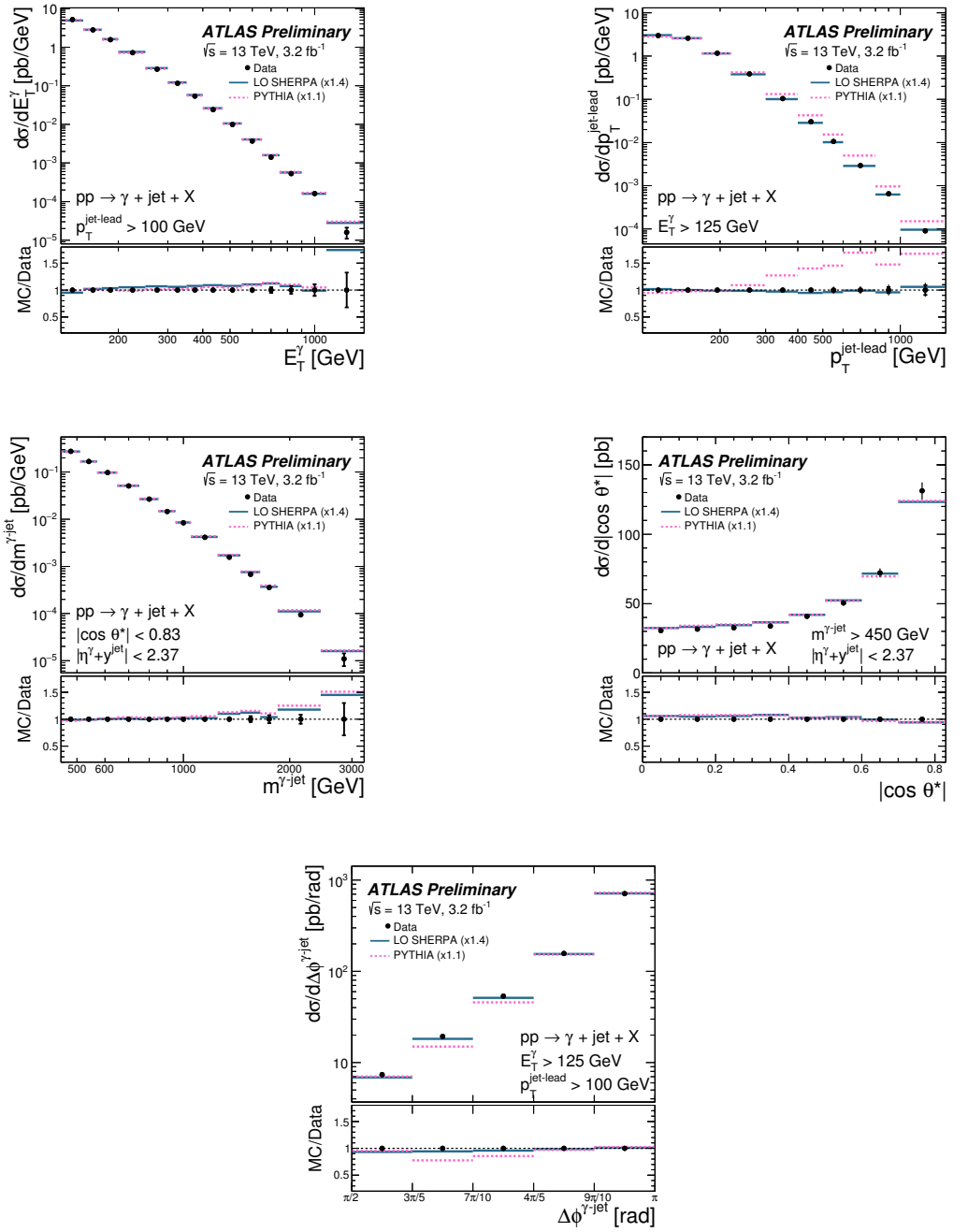

Figure 10.1: Measured cross sections for isolated-photon plus one jet production (dots) as functions of E_{T}^{γ}, $p_{\mathrm{T}}^{\mathrm{jet-lead}}$, $\Delta\phi^{\gamma-\mathrm{jet}}$, $m^{\gamma-\mathrm{jet}}$ and $|\cos\theta^{*}|$. For comparison, the tree-level plus parton-shower predictions from LO SHERPA (solid lines) and PYTHIA default (dashed lines) normalised to the integrated measured cross sections (using the factors in parantheses) are also shown. The bottom part of each figure shows the ratios of the ;C predictions to the measured cross section. The inner (outer) error bars represent the statistical uncertainties (the sum in quadrature of the statistical and systematic uncertainties).

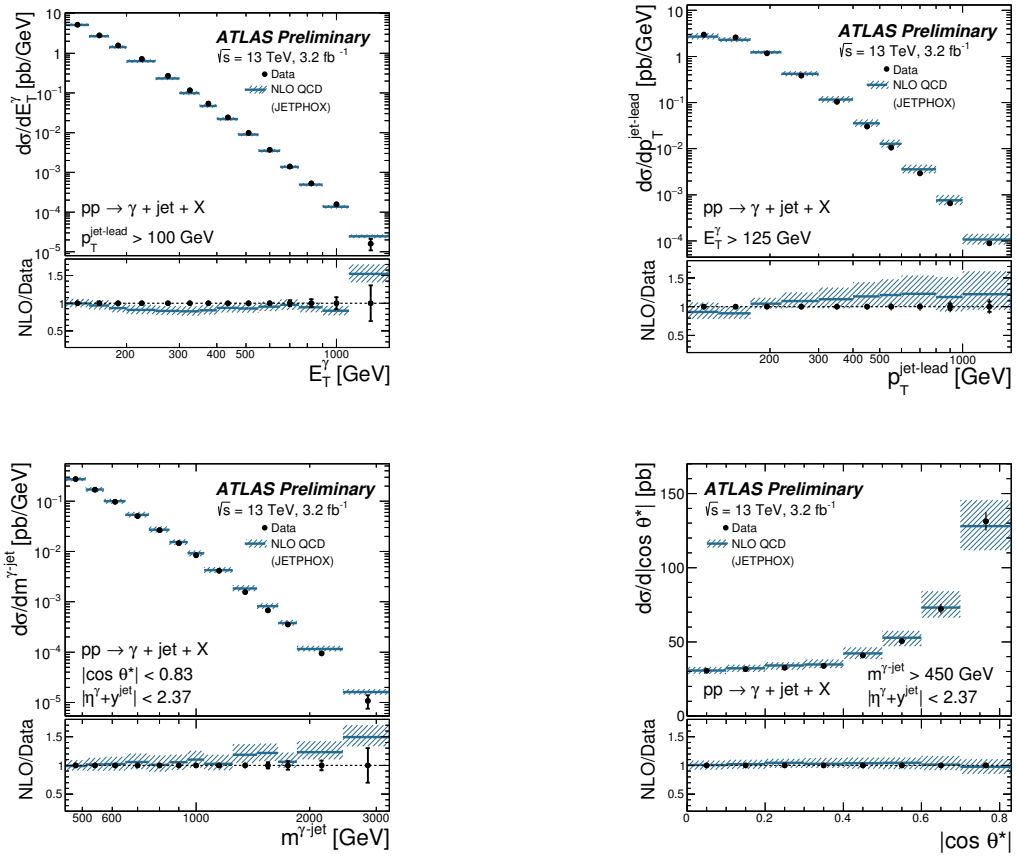

Figure 10.2: Measured cross sections for isolated-photon plus one jet production (dots) as functions of E_{T}^{γ}, $p_{\mathrm{T}}^{\mathrm{jet-lead}}$, $m^{\gamma-\mathrm{jet}}$ and $|\cos\theta^{*}|$. For comparison, the NLO QCD predictions from JETPHOX corrected for hadronisation and underlying-event effects (solid lines) are also shown. The bottom part of each figure shows the ratios of the NLO QCD predictions to the measured cross section. The inner (outer) error bars represent the statistical uncertainties (the statistical and systematic uncertainties added in quadrature) and the hatched band displays the theoretical uncertainty. For most of the points, the inner error bars are smaller than the marker size and, thus, not visible.

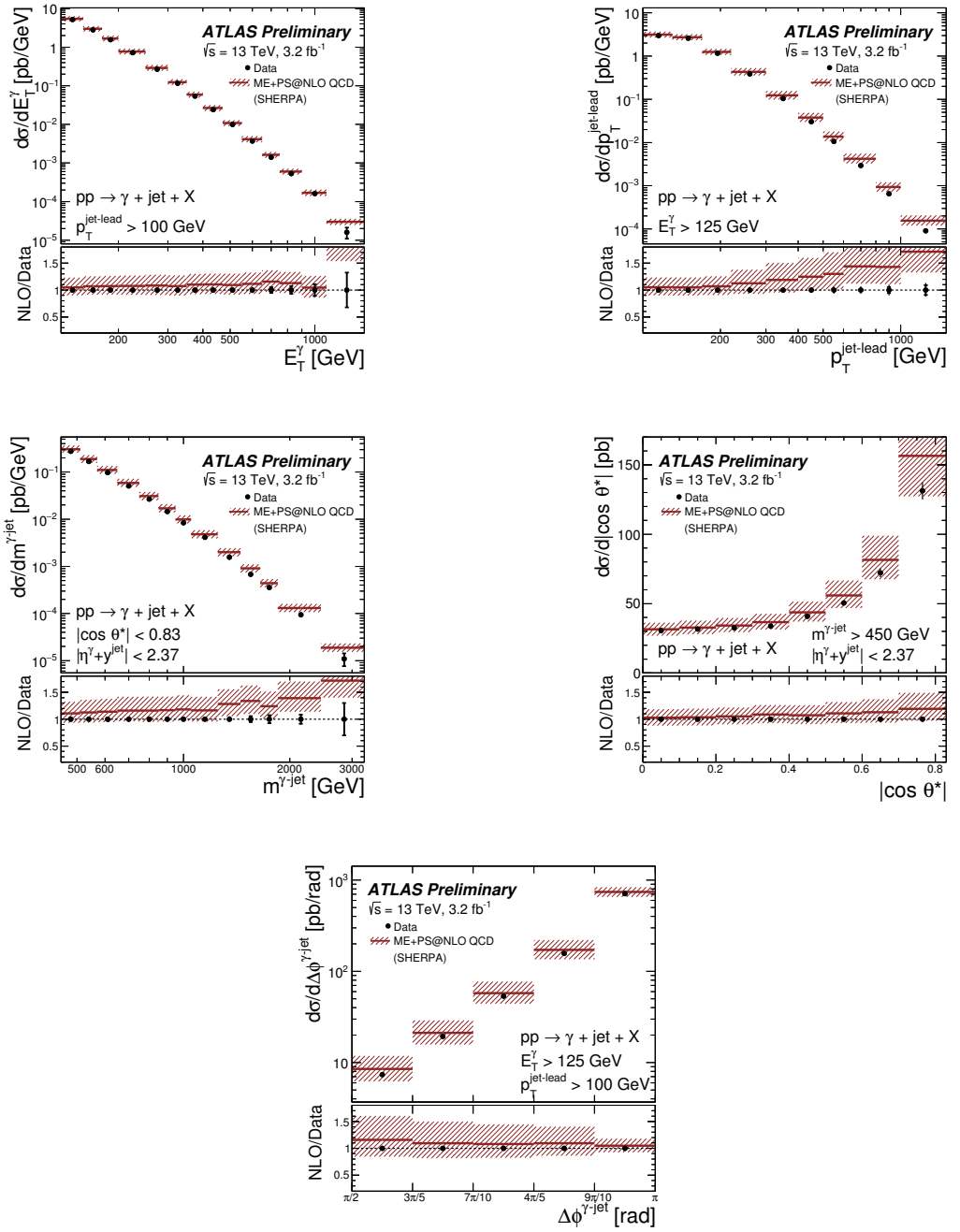

Figure 10.3: Measured cross sections for isolated-photon plus one jet production (dots) as functions of E_{T}^{γ}, $p_{\mathrm{T}}^{\mathrm{jet-lead}}$, $\Delta\phi^{\gamma-\mathrm{jet}}$, $m^{\gamma-\mathrm{jet}}$ and $|\cos\theta^{*}|$. For comparison, the multi-leg NLO QCD plus parton shower predictions from SHERPA (solid lines) are also shown. The bottom part of each figure shows the ratios of the predictions to the measured cross section. The inner (outer) error bars represent the statistical uncertainties (the statistical and systematic uncertainties added in quadrature) and the hatched band displays the theoretical uncertainty. For most of the points, the inner error bars are smaller than the marker size and, thus, not visible.

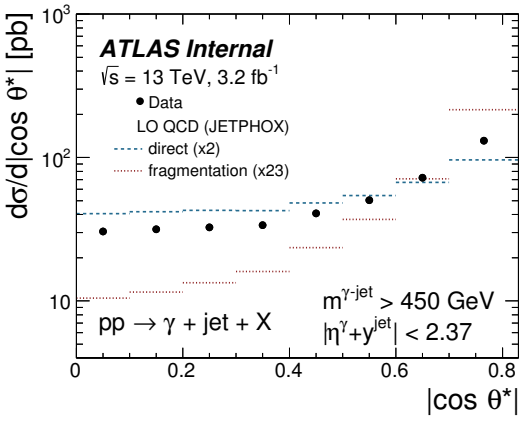

Figure 10.4: Measured cross section for isolated-photon plus one jet production (dots) as a functions of $|\cos\theta^*|$. For comparison, the LO QCD predictions from JETPHOX for the direct (dashed line) and fragmentation (dotted line) processes, normalised to the integrated measured cross section by the factors shown in parentheses, are shown.

Summary and Conclusions

Measurements of the cross sections for the production of one isolated photon in association with one jet in pp collisions at $\sqrt{s} = 13$ TeV are presented in this thesis. These measurements are based on an integrated luminosity of 3.2 fb^{-1} of ATLAS data recorded at the LHC in 2015. The photon is required to have $E_{\mathrm{T}}^{\gamma} > 125$ GeV and $|\eta^{\gamma}| < 2.37$, excluding the region $1.37 < |\eta^{\gamma}| < 1.56$. The jets are reconstructed using the anti-k$_{\mathrm{t}}$ algorithm with radius parameter $R = 0.4$. The cross sections are measured as functions of E_{T}^{γ}, $p_{\mathrm{T}}^{\mathrm{jet-lead}}$ and $\Delta\phi^{\gamma-\mathrm{jet}}$ with $p_{\mathrm{T}}^{\mathrm{jet-lead}} > 100$ GeV; the measurements extended up to values of 1.5 TeV in E_{T}^{γ} and $p_{\mathrm{T}}^{\mathrm{jet-lead}}$.
The dependence on $m^{\gamma-\mathrm{jet}}$ and $|\cos\theta^{*}|$ is measured in an unbiased phase space requiring: $|\eta^{\gamma} + y^{\mathrm{jet-lead}}| < 2.37$, $|\cos\theta| < 0.83$ and $m^{\gamma-\mathrm{jet}} > 450$ GeV.

The predictions of the tree-level plus parton shower MC models by Pythia and LO Sherpa give a satisfactory description of the shape of the data distributions, except for $p_{\mathrm{T}}^{\mathrm{jet-lead}}$ in the case of Pythia. The fixed-order NLO QCD calculatios of Jetphox, corrected for hadronisation and UE effects, and the multi-leg NLO QCD plus parton shower calculations of Sherpa describe the measured cross sections within the experimental and theoretical uncertainties. The comparison of predictions based on different parametrisation of the proton PDFs, shows thet the description of the data achieved does not depend significantly on the specific PDF set used. The only well founded prediction for $d\sigma/d\Delta\phi^{\gamma-\mathrm{jet}}$ is that of NLO Sherpa, which is able to reproduce the data down to $\Delta\phi^{\gamma-\mathrm{jet}} = \pi/2$ due to the inclusion of the matrix element for $2 \rightarrow\ n$ processed with $n = 4$ and 5. The measured dependence on $|\cos\theta^{*}|$ is consistent with the dominance of processes in which a quark is exchanged; excluding the uncertainty in the luminosity, the experimental (theoretical) uncertainty in $d\sigma/d|\cos\theta^{*}|$ is 3-4% (10% for Jetphox and 15-25% for NLO Sherpa), as shown in Figure 10.5. All these studies provide tests of the pQCD description of the dynamics of isolated-photon plus jet production in pp collisions at $\sqrt{s} = 13$ TeV [100]. The experimental uncertainties are in general much smaller than the uncertainties in the predictions

and, thus, calculations with higher precision will allow stringent tests of the theory.

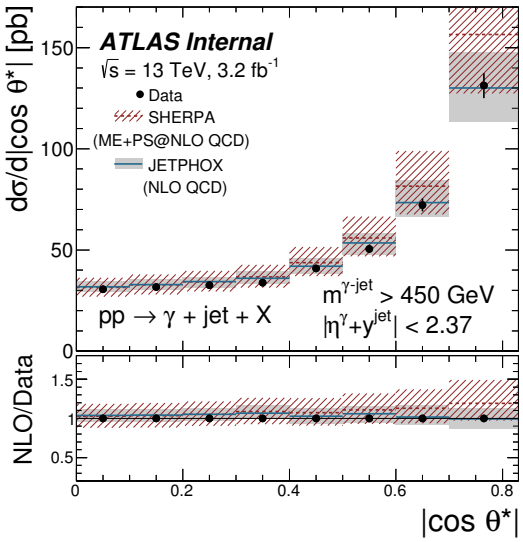

Figure 10.5: Measured cross section for isolated-photon plus one jet production as a function of $|\cos\theta^*|$. For comparison, the multi-leg NLO QCD plus parton shower predictions from SHERPA (dashed line) and the NLO QCD predictions from JETPHOX corrected for hadronisation and underlying-event effects (solid line) are also shown. The inner (outer) error bars represent the statistical uncertainties (the statistical and systematic uncertainties added in quadrature) and the bands display the theoretical uncertainty.

Bibliography

[1] D. d'Enterria and J. Rojo, *Quantitative constraints on the gluon distribution function in the proton from collider isolated-photon data*, , Nucl. Phys. B 860 (2012) 311, arXiv:1202.1762.

[2] L. Carminati et al., *Sensitivity of the LHC isolated-gamma+jet data to the parton distribution functions of the proton*, Europhys. Lett. 101 (2013) 61002, arXiv:1212.5511.

[3] J. Campbell et al. *Direct photon production and PDF fits reloaded*, FERMILAB-PUB-18-018-T, Nikhef/2017-068, arXiv:1802.03021.

[4] ATLAS Collaboration, *Dynamics of isolated-photon plus jet production in pp collisions at* $\sqrt{s} = 7$ *TeV with the ATLAS detector*, Nucl. Phys. B 875, 2013, 483-535, arXiv:1307.6795.

[5] ATLAS Collaboration, *Measurement of the production cross section of an isolated photon associated with jets in proton-proton collisions at* $\sqrt{s} = 7$ *TeV with the ATLAS detector*, Phys. Rev. D85, 2012, 092014, arXiv:1203.316.

[6] ATLAS Collaboration, *High-*E_{T} *isolated-photon plus jets production in pp collisions at* $\sqrt{s} = 8$ *TeV with the ATLAS detector*, Nucl.Phys. B 918, 2017, 257-316, arXiv:1611.06586.

[7] CMS Collaboration, *Rapidity distributions in exclusive Z +jets and* γ *+ jet events in pp collisions at* $\sqrt{s} = 7$ *TeV*, Phys. Rev. D 88, 2013, 112009, arXiv:1310.3082.

[8] CMS Collaboration, *Measurement of the triple-differential cross section for photon + jets production in proton-proton collisions at* $\sqrt{s} = 7$ *TeV*, JHEP 1406, 2014, 009, arXiv:1311.6141.

[9] CMS Collaboration, *Comparison of the* Z/γ^* *+ jets to* γ *+ jets cross section in pp collisions at* $\sqrt{s} = 8$ *TeV*, JHEP 1510, 2015, 128, arXiv:1505.06520.

[10] S.L. Glashow, *Partial Symmetries of Weak Interactions*, Nucl. Phys. 22, 1961, pp. 579-588. DOI:10.1016/0029-5582(61)90469-2.

[11] S. Weinberg, *A Model of Leptons*, Phys. Rev. Lett. 19, 1967, pp. 1264-1266. DOI:10.1103/PhysRevLett.19.1264.

[12] A. Salam and J. C. Ward, *Weak and electromagnetic interactions*, Nuovo Cimento 11.4, 1959, pp 568-577. DOI:10.1007/BF02726525.

[13] P. W. Higgs, *Spontaneous Symmetry Breakdown without Massless Boson*, Phys. Rev. 145, 1966, pp. 1156-1163. DOI:10.1103/PhysRevLett.145.1156.

[14] F. Englert and R. Brout, *Broken Symmetry and the Mass of Gauge Vector Mesons*, Phys. Rev. Lett. 13, 1964, pp. 321-323. DOI:10.1103/PhysRevLett.13.321.

[15] ATLAS Collaboration, *Observation of a new particle in the search for the Standard Model Higgs boson with the ATLAS detetor at the LHC*, Phys. Lett. B 176, 2012, pp. 1-29. DOI:10.1016/j.physletb.2012.08.020.

[16] CMS Collaboration, *Observation of a new boson at a mass of 125 GeV with the CMS experiment at the LHC*, Phys. Lett. B 176, 2012, pp. 30-61. DOI:10.1016/j.physletb.2012.08.021.

[17] ATLAS and CMS Collaborations, *Combined Measurement of the Higgs Boson Mass in pp collisions at* $\sqrt{s} = 7$ *and 8 TeV with the ATLAS and CMS experiments*, Phys. Rev. Lett. 114, 2015, 191803. arXiv:1503.07589.

[18] ATLAS and CMS Collaborations, *Measurements of the Higgs boson production and decay rates and constraints on its couplings from a combined ATLAS and CMS analysis of the LHC in pp collision data at* $\sqrt{s} = 7$ *and 8 TeV*, JHEP 08, 2016, 045. arXiv:1606.02266.

[19] The Royal Swedish Academy of Sciences, October 2013, https://www.nobelprize.org/nobel_prizes/physics/laureates/2013/.

[20] T. Muta, *Foundation of Quantum Chromodynamics*, World Scientific Lectures Notes in Physics, Vol.57, 1998. Reference therein.

[21] D.J. Gross and F. Wilczek, *Ultraviolet behavior of non-abelian gauge theories*, Phys. Rev. Lett. 30, 1973, pp. 1343-1346, DOI:10.1103/PhysRevLett.30.1343.

[22] H.D. Politzer, *Reliable perturbative results for strong interactions*, Phys. Rev. Lett. 30, 1973, pp. 1346-1349, DOI:10.1103/PhysRevLett.30.1346.

[23] A.H. Mueller, *Perturbative QCD*, Adv. Ser. Direct. High Energy Phys. 5, 1988, 1.

[24] C.G. Callan Jr., *Broken scale invariance in scalar field theory. Phys. Rev. D 2 (1970) 1541; K. Symanzik, Small distance behavior in field theory and power counting*, Comm. Math. Phys. 18, 1970, 227.

[25] V.N. Gribov and L. N. Lipatov, *Deep inelastic ep scattering in perturbation theory*, Sov. J. Nucl. Phys. 15, 1972, 438.

[26] L. N. Lipatov, *The parton model and perturbation theory*, Sov. J. Nucl. Phys. 20, 1975, 94.

[27] Y. L. Dokshitzer, *Calculation of structure functions of deep-inelastic scattering and e^+e^- annihilation by perturbation theory in quantum chromodynamics*, Sov. Phys. JETP 46, 1977, 641.

[28] G. Altarelli and G. Parisi, *Asymptotic Freedom in Parton Language*, Nucl. Phys. B 126 (1997) 298.

[29] R.K. Ellis, W.J. Stirling and B.R. Webber , *QCD and collider physics*, Cambridge University Press, 1996.

[30] P. Aurenche, R.Baier, M. Fontannaz and D. Schiff, *Prompt Photon Production at Large pT Scheme Invariant QCD Predictions and Comparison with Experiment.*, Nucl. Phys. B 297, 1988, pp 661-696.

[31] S. Catani, Y.L. Dokshitzer, M.H. Seymour and B.R. Webber, *Longitudinally invariant Kt clustering algorithms for hadron hadron collisions*, Nucl. Phys. B 406,1993, 187 and references therein .

[32] Evans, Lyndon, and Bryant, Philip, (eds.), *LHC Machine*, JINST, 3:S08001, 2008.

[33] The ATLAS Collaboration, *The ATLAS Experiment at the CERN Large Hadron Collider*, JINST, 3:S08003, 2008 .

[34] The CMS Collaboration, *The CMS Experiment at the CERN Large Hadron Collider*, JINST, 3:S08004, 2008.

[35] The LHCb Collaboration, *The LHCb Experiment at the CERN Large Hadron Collider*, JINST, 3:S08005, 2008.

[36] The ALICE Collaboration, *The ALICE Experiment at the CERN Large Hadron Collider*, JINST, 3:S08002, 2008.

[37] ATLAS Collaboration, *The ATLAS Experiment at the CERN Large Hadron Collider*, JINST, 3:S08003, 2008, pp. 53-110.

[38] ATLAS Collaboration, *ATLAS pixel detector: Technical Design Report*, CERN- LHCC-98-013. Geneva, 1998. https://cds.cern.ch/record/381263.

[39] ATLAS Collaboration, *ATLAS Insertable B-Layer Technical Design Report*, CERN-LHCC-2010-013, ATLAS-TDR-19.

[40] ATLAS Collaboration, *The ATLAS Experiment at the CERN Large Hadron*, JINST, 3:S08003, 2008, pp. 110-164.

[41] ATLAS Collaboration, *ATLAS liquid argon calorimeter: Technical design report*, CERN-LHCC-96-41, 1996.

[42] ATLAS Collaboration, *ATLAS tile calorimeter: Technical design report*, CERN-LHCC-96-42, 1996.

[43] ATLAS Collaboration, *ATLAS magnet system: Technical design report*, CERN- LHCC-97-18, 1997.

[44] ATLAS Collaboration, *ATLAS central solenoid: Technical design report*, CERN- LHCC-97-21, 1997.

[45] ATLAS Collaboration, *ATLAS barrel toroid: Technical Design Report*, CERN-LHCC-97-019, 1997.

[46] ATLAS Collaboration, *The ATLAS Experiment at the CERN Large Hadron*, JINST, 3:S08003, 2008, pp. 164-210.

[47] ATLAS Collaboration, *The ATLAS Experiment at the CERN Large Hadron*, JINST, 3:S08003, 2008, pp. 218-256.

[48] ATLAS Collaboration, *Performance of the ATLAS Trigger system in 2015*, Eur. Phys. J. C (2017) 77: 317.

[49] ATLAS Collaboration, *ATLAS Computing Technical Design Report*, CERN-LHCC-2013-022, ATLAS-TDR-017.

[50] I. Bird, *Computing for the Large Hadron Collider*, Annual Review of Nuclear and Particle Science 61 (2011), pp. 99–118.

[51] *Worldwide LHC Computing GRID*. http://wlcg.web.cern.ch/.

[52] T. Sjostrand, S. Mrenna and P. Z. Skands, *PYTHIA 6.4 Physics and Manual*, JHEP 0605 (2006), p. 26. DOI:10.1088/1126-6708/2006/05/026.

[53] T. Gleisberg et al., *Event generation with SHERPA 1.1*, JHEP 02 (2009), p. 7. DOI:10.1088/1126-6708/2009/02/007.

[54] B. Andersson et al., *Parton Fragmentation and String Dynamics*, Phys. Rept. 97 (1983), pp. 31-145. DOI:10.1016/0370-1573(83)90080-7.

[55] B. R. Webber, *A QCD Model for Jet Fragmentation Including Soft Gluon Interference*, Nucl. Phys. B 238 (1984), pp. 492. DOI:10.1016/0550-3213(84)90333-X.

[56] T. Sjostrand, S. Mrenna and P. Z. Skands, *A Brief Introduction to PYTHIA 8.1*, Commun. 178 (2008) 852, arXiv:0710.3820.

[57] R. D. Ball et al., *Parton distributions with LHC data*, Nucl. Phys. B 867 (2013) 244, arXiv:1207.1303.

[58] H.-L. Lai et al., *New parton distributions for collider physics*, Phys. Rev. D 82 (2010) 074024, arXiv:1007.2241.

[59] S. Agostinelli et al., *GEANT4 - a simulation toolkit*, Nucl. Instrum. Meth. A 506 (2003) 250.

[60] ATLAS Collaboration, *The ATLAS simulation infrastructure*, Eur. Phys. J. C 70 (2010) 823, arXiv:1005.4568.

[61] S. Frixione, *Isolated photons in perturbative QCD*, Phys. Lett. B 429 (1998) 369, arXiv:hep-ph/9801442.

[62] ATLAS Collaboration, *Measurement of the photon identification efficiencies with the ATLAS detector using LHC Run-1 data*, Eur. Phys. J. C 76 (2016) 666.

[63] W. Lampl et al., *Calorimeter Clustering Algorithms: Description and Performance*, ATL-LARG-PUB-2008-002 (2008), http://cds.cern.ch/record/1099735.

[64] T. Cornelissen et al., *Concepts, Design and Implementation of the ATLAS New Tracking (NEWT)*, ATL-SOFT-PUB-2007-007 (2007), http://cds.cern.ch/record/1020106.

[65] T. Cornelissen, *The global χ^2 track fitter in ATLAS*, J. Phys. Conf. Ser. 119 (2008).

[66] ATLAS Collaboration, *Improved electron reconstruction in ATLAS using the Gaussian Sum Filter-based model for bremsstrahlung*, ATL-CONF-2012-047 (2012), http://cds.cern.ch/record/1449796.

[67] ATLAS Collaboration, *Electron efficiency measurements with the ATLAS detector using 2012 LHC proton-proton collision data*, Eur. Phys. J. C (2017) 77.

[68] ATLAS Collaboration, *Electron and photon energy calibration with the ATLAS detector using data collected in 2015 at* $\sqrt{s} = 13$ *TeV*, ATLAS-PHYS-PUB-2016-015.

[69] M. Tanemura et al., *A new algorithm for three-dimentional voronoi tessellation*, Journal of Computational Physics 51, pp. 191-207, 1983.

[70] ATLAS Collaboration, *Expected photon performance in the ATLAS experiment*, ATL-PUB-2011-007 (2011).

[71] ATLAS Collaboration, *Photon identification in 2015 ATLAS data*, ATL-PHYS-PUB-2016-014 (2016). https://cds.cern.ch/record/2203125.

[72] ATLAS Collaboration, *Jet calibration and systematic uncertainties for jets reconstructed in the atlas detector at* $\sqrt{s} = 13$ *TeV*, ATLAS-PHYS-PUB-2015-015, https://cds.cern.ch/record/2037613.

[73] ATLAS Collaboration, *Jet energy scale measurements and their systematic uncertainties in proton-proton collisions at* $\sqrt{s} = 13$ *TeV with the ATLAS detector*, Phys.Rev. D96 (2017) 7, arXiv:1703.09665.

[74] M. Cacciari, G.P. Salam and G. Soyez, *The Catchment Area of Jets*, JHEP 0804 (2008) 005, arXiv:0802.1188.

[75] ATLAS Collaboration, *Selection of jets produced in 13 TeV proton-proton collisions with the ATLAS detector*, ATLAS-CONF-2015-029, https://atlas.web.cern.ch/Atlas/GROUPS/PHYSICS/CONFNOTES/ATLAS-CONF-2015-029/.

[76] ATLAS Collaboration, *2015 start-up trigger menu and initial performance assessment of the ATLAS trigger using Run-2 data*, ATL-DAQ-PUB-2016-001, https://cds.cern.ch/record/2136007.

[77] ATLAS Collaboration, *Measurement of the cross section for inclusive isolated-photon production in pp collisions at* $\sqrt{s} = 13$ *TeV using the ATLAS detector*, Physics Letters B 770, 2017, pp 473-493, arXiv:1701.06882.

[78] ATLAS Collaboration, *High-E_{T} isolated-photon plus jet production in pp collisions at $\sqrt{s}$ = 8 TeV with the ATLAS detector*, Nucl.Phys. B 918, 2017, pp 257-316, arXiv:1611.06586.

[79] D.D. Boos, *Introduction to the bootstrap world*, Statist. Sci. 18, 2003, 168.

[80] ATLAS Collaboration, *Search for new phenomena with the atlas detector in monophoton events from proton-proton collisions at $\sqrt{s}$ = 13 TeV*, ATL-COM-PHYS-2015-291.

[81] G. D'Agostini, *A multidimensional unfolding method based on Bayes' theorem*, Nucl. Instrum. Meth. A 362 (1995) 487.

[82] L. Fayard et al., *Energy calibration prerecommendation for Run 2*, ATL-COM-PHYS-2015-1300.

[83] ATLAS Collaboration, *Monte Carlo Calibration and Combination of In-situ Measurements of Jet Energy Scale, Jet Energy Resolution and Jet Mass in ATLAS*.

[84] H. Abreu et al., *Measurement of the inclusive isolated prompt photon cross section in pp collisions at $\sqrt{s}$ = 7 TeV with the ATLAS detector using 35 pb^{-1}.*, ATL-COM-PHYS-2011-645.

[85] "Website of ATLAS Public Luminosity Results", https://twiki.cern.ch/twiki/bin/view/AtlasPublic/LuminosityPublicResultsRun2.

[86] S. Catani, M. Fontannaz, J. Ph. Guillet and E. Pilon, *Cross section of isolated prompt photons in hadron-hadron collisions*, JHEP 0205, 2002, 028, arXiv:hep-ph/0204023.

[87] P. Aurenche, M. Fontannaz, J. Ph. Guillet, E. Pilon and M. Werlen, *A new critical study of photon production in hadronic collisions*, Phys. Rev. D 73, 2006, 094007, arXiv:hep-ph/0602133.

[88] L.A. Harland-Lang, A.D. Martin, P. Motylinski and R.S. Thorne, *Parton distributions in the LHC era: MMHT 2014 PDFs*, Eur. Phys. J. C 75, 2015, 204, https://arxiv.org/abs/1412.3989.

[89] L. Bourhis, M. Fontannaz and J.Ph. Guillet, *Quark and gluon fragmentation functions into photons*, Eur. Phys. J. C2, 1998, 529, arXiv:hep-ph/9704447.

[90] S. Dulat et al., *New parton distribution functions from a global analysis of quantum chromodynamics*, Phys. Rev. D 93, 2016, 033006, arXiv:1506.07443.

[91] NNPDF Collaboration, R.D. Ball et al., *Parton distributions for the LHC Run II*, JHEP 1504, 2015, 040, arXiv:1410.8849.

[92] J. Pumplin et al., *New generation of parton distributions with uncertainties from global QCD analysis*, JHEP 0207 (2002) 012, arXiv: hep-ph/0201195.

[93] G. Callea et al., *First measurement of the isolated-photon plus jet production in pp collisions at $\sqrt{s}$ = 13 TeV with the ATLAS detector*, ATL-COM-PHYS-2017-104, https://cds.cern.ch/record/2244858.

[94] J. Pumplin et al., *Uncertainties of predictions from parton distribution functions. II. The Hessian method*, Phys. Rev. D 65 (2001) 014013, arXiv: hep-ph/0101032.

[95] F. Krauss, R. Kuhn and G. Soff, *AMEGIC++ 1.0: A Matrix element generator in C++*, JHEP 0202, 2002, 044, arXiv:hep-ph/0109036.

[96] F. Cascioli, P. Maierhofer and S. Pozzorini, *Scattering Amplitudes with Open Loops*, Phys. Rev. Lett. 108, 2012, 111601, arXiv:1111.5206.

[97] S. Schumann and F. Krauss, *A Parton shower algorithm based on Catani-Seymour dipole factorisation*, JHEP 0803, 2008, 038, arXiv:0709.1027.

[98] S. Hoche, F. Krauss, M. Schonherr and F. Siegert, *QCD matrix elements + parton showers: The NLO case*, JHEP 1304, 2013, 027, arXiv:1207.5030.

[99] F. Siegert, *A practical guide to event generation for prompt photon production with Sherpa*, J. Phys. G 44, 2017, 044007, arXiv:1611.07226.

[100] ATLAS Collaboration, *First measurement of the isolated-photon plus jet production in pp collisions at $\sqrt{s}$ = 13 TeV with the ATLAS detector*, ATLAS-CONF-2017-059.

[101] A. Valassi, *Combining correlated measurements of several different physical quantities*, Nucl. Instrum. Meth. A 500 (2003) 391.

Appendix A

Data-driven methods used in the Photon identification

As already described in Section 4.1.4, a careful identification of photon candidates is necessary to reject backgrond events, coming from photon originated from hadronic decays, or to hadrons wrongly identified as photons. The precise measurement of the photon identification efficiency is performed using data-driven methods, as the description of the photon interaction with the material is not precise enough to accurately determine the photon ID efficiency from simulation alone. In ATLAS there are currently three data-driven methods to estimate the photon ID efficiency, that cover different ranges of photon transverse energy with partial overlaps. This Appendix describes in detail the measured tight identification criteria efficiency mesured with the dataset colleted by the ATLAS detector in 2015. Events were recorded in 3.2 fb^{-1} of proton-proton collisions at a center-of-mass energy of $\sqrt{s} = 13$ TeV during the 2015 data taking period.

A.1 Collision data and simulated samples

Events are considered only if recorded when the entire ATLAS detector was fully operational. Events containing at least one photon must pass at least one of several single photon triggers, with requirements on the DVs weaker than those used for the loose ID, and with E_{T} thresholds varying from 10 to 140 GeV[1]. In this way, a good coverage with high statistics is ensured over a wide E_{T} range. Events containing leptons must satisfy the lowest unprescaled single-lepton triggers, with an E_{T} threshold of 24 GeV, or di-

[1]Triggers with lower thresholds were pre-scaled as soon as the instantaneous luminosity increased, to maintain the trigger rate at an sustainable level.

electron (di-muon) triggers with an E_{T} threshold of 15 GeV (14 GeV). The isolation requirements imposed to the photon candidates in the three data-driven methods are $E_{\mathrm{T}}^{iso} < 0.065 \cdot E_{\mathrm{T}}$ and $p_{\mathrm{T}}^{iso} < 0.05 \cdot p_{\mathrm{T}}$, in a cone with an opening $\Delta R < 0.2$, where E_{T}^{iso} and p_{T}^{iso} are the calorimetric and track isolation variables respectively. The analyses also use simulated Monte Carlo samples:

- photon+jet events (γ-jet) generated by PYTHIA8, with photon E_{T} in the range [17; 1500] GeV: used to model the photon properties;
- dijet-like events, containing both photon+jet and dijet events in realistic proportions, generated by PYTHIA8, with jet filter thresholds between 17 and 55 GeV: used to model the hadronic background;
- $Z \to \ell^+\ell^-\gamma$ decays (where $\ell = e, \mu$) generated by SHERPA: used to model the signal in the "radiative Z" method;
- $Z \to \ell^+\ell^-$ decays generated by POWHEG+PYTHIA: used for the "electron extrapolation" method and for cross-checks in the "radiative Z" method;
- $Z(\to \ell^+\ell^-)$ + jet generated by SHERPA: used to model the hadronic background in the "radiative Z" method.

All samples needed to model the signal are generated with high statistics. Photon+jet simulations are performed in bins of the photon E_{T}: up to $E_{\mathrm{T}} = 800$ GeV each simulation contains 2 million or 1 million events, while for larger E_{T}, up to 3 TeV, each slice contains 100 000 events. Simulated samples for $Z \to \ell^+\ell^-$ and $Z \to \ell^+\ell^-\gamma$ contain respectively 20 million and 5 million events, for each lepton flavour. Signal samples have also been simulated with a different description of the detector geometry, to assess the systematic effects due to a mismodelling of the materials. These samples include additional material, compared to the nominal one, both in the tracking detector and directly in front of the calorimeter. All samples are generated with underlying event and pile-up. The interaction of the particles in the final state with the detector material is simulated with GEANT4, the detector response is simulated, and the events are processed through the full ATLAS reconstruction. In order to improve the description of the photon DVs, corrections are applied to the simulated values, by applying a shift to each of them, whose value is optimised separately for unconverted and converted photons, and as a function of the pseudorapidity. The general procedure is to select photons from data and compare their DVs distributions to those from the simulation. Photons with $E_{\mathrm{T}} < 25$ GeV are selected from radiative

$Z \to \ell^+\ell^-\gamma$ decays, while those with $E_{\mathrm{T}} \geq 25$ GeV are obtained from reconstructed photons passing the tight ID and the isolation requirements, in events selected by a single-photon trigger. An example of such procedure is displayed in Figure A.1.

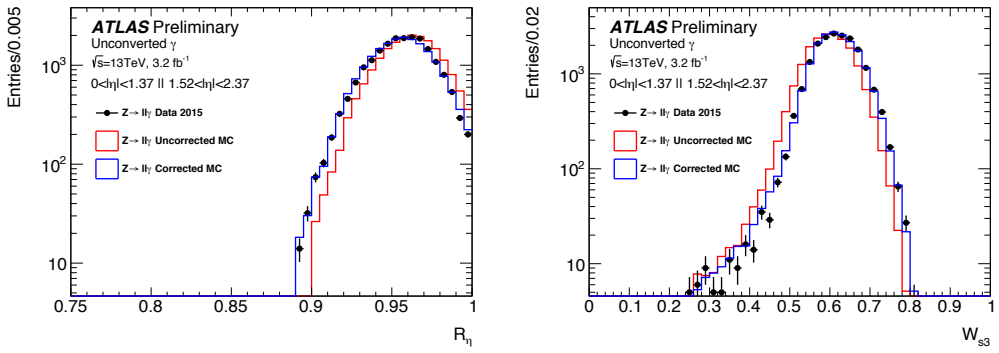

Figure A.1: Two examples of shower-shape variables for unconverted photons: the black points are for the photons from $Z \to \ell^+\ell^-\gamma$ events from data, the red histogram for the photons from $Z \to \ell^+\ell^-\gamma$ event from simulation before applying the shift, and the blue histogram after applying the shift [71].

A.2 Data-driven efficiency measurements

A.2.1 Radiative photons from $Z \to \ell^+\ell^-\gamma$ decays

Radiative $Z \to \ell\ell\gamma$ decays are selected by placing kinematic requirements on the dilepton pair, on the invariant mass of the three particles in the final state, and on the quality requirements on the two leptons. Muon candidates are formed from tracks reconstructed both in the Inner Detector and in the muon spectrometer, with transverse momentum larger than 10 GeV and absolute pseudorapidity less than 2.4. For the electrons, stronger selection criteria are applied, to avoid the possibility of an electron to be misidentified as a photon. Electrons are required to have $p_{\mathrm{T}} \geq 10$ GeV and $|\eta| \leq 1.37$ or $1.52 \leq |\eta| \leq 2.47$, and to satisfy the identification criteria based on tracking and transition radiation information from the Inner Detector, shower shape variables computed from the lateral and longitudinal profiles of the energy deposited in the EM calorimeter, and track-cluster matching quality. For both electron and muon candidates, the longitudinal impact parameter, $|z_{\mathrm{PV}}|$, with respect to primary vertex and transverse impact parameter significance, $|d_0|/\sigma_{d_0}$, are required to satisfy $|z_{\mathrm{PV}}| \leq 10$ mm and $|d_0|/\sigma_{d_0} \leq 10$.

The photon selection is performed separately for converted and unconverted candidates, which are required to be in the ECAL fiducial acceptance and to have transverse energy larger than 10 GeV. The photon candidates have to satisfy the object quality and photon cleaning requirements in order to reject misidentified electrons as photons and clusters affected by cells with read-out problems. The same isolation criteria are also applied to electron and muon candidates. The $Z \to \ell\ell\gamma$ candidates are selected by requiring two opposite-sign charged leptons of the same flavour satisfying the previous criteria. An angular separation $\Delta R \geq 0.2$ between the photon and each of the two leptons is required to avoid contamination on the photon cluster. The two-dimensional distribution of $\ell\ell$ vs $\ell\ell\gamma$ invariant masses is shown in Figure A.2, for the selected events in data passing the previous criteria. The sample is dominated by Z+jet background events in which the jet

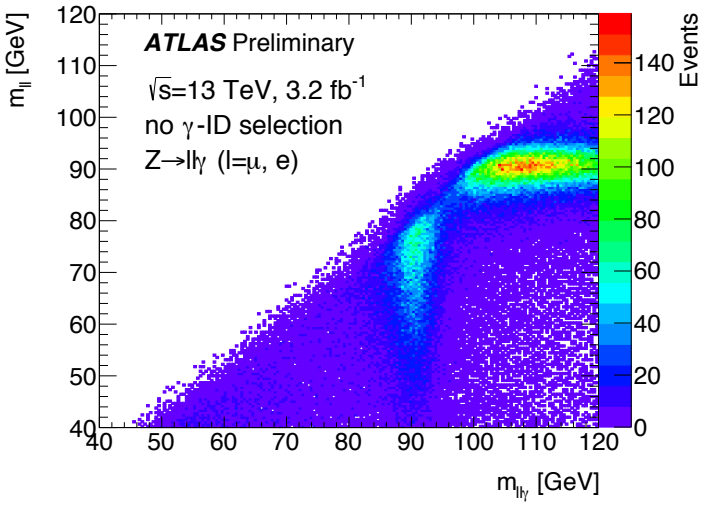

Figure A.2: Two-dimentional distribution of $m_{\ell\ell\gamma}$ and $m_{\ell\ell}$ for all reconstructed $Z \to \ell\ell\gamma$ candidates [71].

is misreconstructed as a photon. These events, which have a cross section about three orders of magnitude higher than $\ell\ell\gamma$ events, have $m_{\ell\ell} \approx m_Z$ and $m_{\ell\ell\gamma} \geq m_Z$, while final-state radiation $Z \to \ell\ell\gamma$ events have $m_{\ell\ell} \leq m_Z$ and $m_{\ell\ell\gamma} \approx m_Z$. In order to reduce the Z+jet background, the requirements of 40 GeV $\leq m_{\ell\ell} \leq$ 83 GeV and 83 GeV $\leq m_{\ell\ell\gamma} \leq$ 100 GeV are applied. The efficiency of photon tight identification is evaluated from the selected photon sample and measured as the fraction of selected photons (probes) that pass the tight identification criteria:

$$\varepsilon_{\mathrm{ID}} = \frac{N_{probes,tight}}{N_{probes}} \tag{A.1}$$

The residual background contamination from Z+jet events is estimated through a maximum-likelihood (template) fit to $m_{\ell\ell\gamma}$ after the cut on it. The data are fit to a sum of the photon and the background contributions. The photon and background distributions ("templates") are extracted from the $Z \to \ell\ell\gamma$ and Z+jet simulations, corrected to take into account data-MC differences in the lepton efficiencies, and in the photon and lepton energy scales and resolutions. The signal and background yields are determined from the data by maximizing the likelihood. The photon purity for 10 GeV $\leq E_{\mathrm{T}} \leq$ 20 GeV is estimated from the template fit using $Z + \gamma$ and Z+jet SHERPA samples. In the signal region (83 GeV $\leq m_{\ell\ell\gamma} \leq$ 100 GeV) the purity is about 91.6% in the $\mu\mu\gamma$ channel and 92.7% in the $ee\gamma$ channel. The sample purity is accounted for, when computing the identification efficiency.
A closure test has been performed, applying the analysis to a simulated sample, containing $Z \to \ell\ell\gamma$ and Z+jet events in realistic proportions: the difference between the ID efficiency computed by the analysis, and that computed directly on genuine photons from the simulation, is about 4.5% (5.5%), for converted (unconverted) photons and it has been taken into account as a systematic uncertainty. Additional uncertainties, arising from material modeling and alternative MC event generators, have been considered. In the first case distorted geometry MC sample has been used, where the detector geometry is simulated with more material in front of the ECAL. Subtraction of background events with templated fit method has been obtained with the use of templates extracted from the distorted geometry MC instead of the nominal one. One more MC-related uncertainty, due to the choice of event generator, arises from deviation in the MC predictions of the background. Uncertainty estimation is similar to the one described earlier: background subtraction in data with template fit method is redone with extraction of templates from alternative MC event generator POWHEG+PYTHIA instead of nominal one (SHERPA). The differences with respect to the nominal results are treated as additional systematic uncertainties.

A.2.2 $e \to \gamma$ extrapolation

The similarity between the electromagnetic showers induced by isolated electrons and photons in the ECAL is exploited to extrapolate the expected photon distributions of the DVs. The photon identification efficiency is thus estimated from the distributions of the same variables in a pure and large sample of electrons with E_{T} between 30 GeV and 100 GeV obtained from $Z \to ee$ decays, using a "tag-and-probe" method. Events are selected if they contain two opposite-sign electrons in the ECAL fiducial acceptance, with $p_{\mathrm{T}} \geq$ 25 GeV, at least seven hits in the silicon detectors, one hit in

the pixel detector, and the invariant mass 70 GeV $\leq m_{ee} \leq$ 110 GeV. The "tag" electron is required to match the trigger object within a cone with $\Delta R \leq 0.15$ and to pass the tight electron identification requirement. The background contamination of the electron "probes" is determined from the m_{ee} spectrum of the selected events, using a template whose normalization is extracted from events with $m_{ee} \geq 120$ GeV, and whose shape is obtained from events in which the probe electron candidate fails both isolation and loose identification requirements. The differences between the photon and electron distributions of the DVs are studied using simulated samples of prompt photons and electrons from $Z \rightarrow ee$ decays, separately for converted and unconverted photons. For most DVs, the difference between showers is more sizable between electrons and unconverted photons, than for converted photons, because the latter are actually two electron showers overlapped. An exception is the azimuthal width (R_ϕ) of the shower, that is affected more for converted photons, due to the opposite bendings of the two tracks in the magnetic field. To reduce such differences, a mapping technique based on the Smirnov transform is used for both converted and unconverted photons. For each shower shape variable x, the cumulative distribution functions (CDF) of simulated electrons ($\mathrm{CDF}_e(x)$) and photons ($\mathrm{CDF}_\gamma(x)$) are calculated. The transform $f(x)$ is defined such that $\mathrm{CDF}_e(x) = \mathrm{CDF}_\gamma(f(x))$. By applying the appropriate transform for each DV, the electron sample can be transformed into a sample of objects with photon-like shower shapes. In Figure A.3 this process is illustrated for the shower shape R_ϕ. However, as the process is applied to each DV independently, the correlations between shower shapes are preserved from the source sample, which introduces some intrinsic uncertainty to the method. These effects are assessed by comparing the efficiency measured from a pure sample of simulated photons to the efficiency measured from a simulated electron sample after applying the Smirnov transforms. The difference between the efficiencies extracted from the two samples is treated as a systematic uncertainty. For both converted and unconverted photons, it is about 1%. An additional source of systematic uncertainty may come from the modelling of the shower shape distributions and correlations in the photon and electron simulations used to extract the mappings. The largest uncertainties in the distributions of the discriminating variables originate from limited knowledge of the material in front of the calorimeter. The extraction of the mappings is repeated using MC with distorted geometry. The difference between the efficiencies obtained using the nominal and the distorted is about 2% (4%) for converted (unconverted) photons. Also the effect of a possible background contamination in the selected electron probes in data is taken into account as an additional systematic uncertainty.

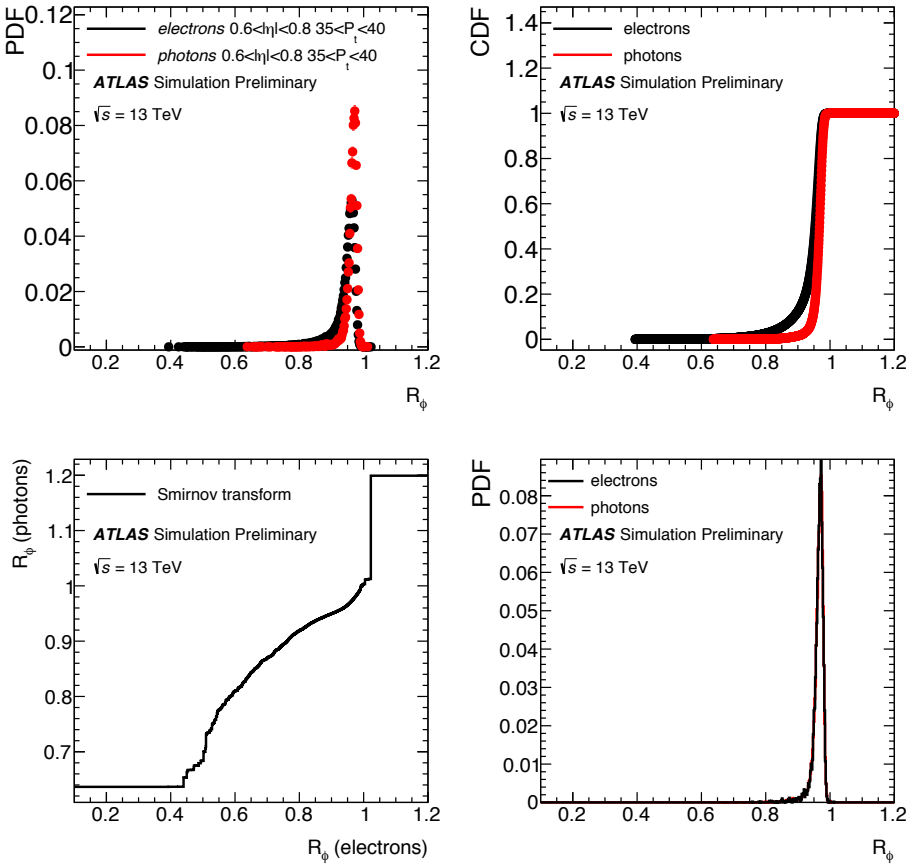

Figure A.3: Diagram illustrating the process of Smirnov transform for R_ϕ. This discriminating variable was chosen due to its distribution, particulary different between electrons and unconverted photons. The pdf in each sample (top-left plot) is used to calculate the respective CDF (top-right plot). From the two CDFs, the Smirnov transform can be derived (bottom-left plot). Applying the transform leads to an R_ϕ distribution of the transformed electrons, which well reproduces the photon distribution (bottom-right plot) [71].

A.2.3 Matrix method

An inclusive sample of photon candidates is selected using single photon triggers by requiring at least one photon candidate in the ECAL fiducial acceptance and with 20 GeV $\leq E_{\mathrm{T}} \leq$ 1500 GeV. The distribution of the track isolation of selected candidates, computed in a cone $\Delta R < 0.4$ (as opposed to $\Delta R < 0.2$ used in the isolation requirement on the photon candidates), is used to discriminate between prompt and background photon candidates, before and after applying the tight identification criteria. In the following, N_{all} and N_{pass} are the total number of photon candidates in the selected sample ("all" sample) and in the sample of candidates passing the tight identification criteria ("pass" sample), respectively, while $N_{\mathrm{all}}^{\mathrm{iso}}$ and $N_{\mathrm{pass}}^{\mathrm{iso}}$ are the number of candidates in the "all" and "pass" samples that pass the track isolation requirement. The quantities $\varepsilon_{\mathrm{all}}^{\mathrm{S(B)}}$ and $\varepsilon_{\mathrm{pass}}^{\mathrm{S(B)}}$ are the track isolation efficiencies for prompt (background) photons in the "all" and "pass" samples. The yields of prompt (S) and background (B) photons in the "all" and "pass" samples, respectively $N_{\mathrm{all}}^{\mathrm{S}}$, $N_{\mathrm{all}}^{\mathrm{B}}$, $N_{\mathrm{pass}}^{\mathrm{S}}$, $N_{\mathrm{pass}}^{\mathrm{B}}$, are obtained by solving a system of four equations:

$$N_{\mathrm{all}} = N_{\mathrm{all}}^{\mathrm{S}} + N_{\mathrm{all}}^{\mathrm{B}} \tag{A.2}$$

$$N_{\mathrm{pass}} = N_{\mathrm{pass}}^{\mathrm{S}} + N_{\mathrm{pass}}^{\mathrm{B}} \tag{A.3}$$

$$N_{\mathrm{all}}^{\mathrm{iso}} = \varepsilon_{\mathrm{all}}^{\mathrm{S}} \cdot N_{\mathrm{all}}^{\mathrm{S}} + \varepsilon_{\mathrm{all}}^{\mathrm{B}} \cdot N_{\mathrm{all}}^{\mathrm{B}} \tag{A.4}$$

$$N_{\mathrm{pass}}^{\mathrm{iso}} = \varepsilon_{\mathrm{pass}}^{\mathrm{S}} \cdot N_{\mathrm{pass}}^{\mathrm{S}} + \varepsilon_{\mathrm{pass}}^{\mathrm{B}} \cdot N_{\mathrm{pass}}^{\mathrm{B}} \tag{A.5}$$

The identification efficiency $\varepsilon^{\mathrm{ID}} = N_{\mathrm{pass}}^{\mathrm{S}}/N_{\mathrm{all}}^{\mathrm{S}}$ is thus:

$$\varepsilon_{\mathrm{ID}} = \frac{\frac{\varepsilon_{\mathrm{pass}} - \varepsilon_{\mathrm{pass}}^{\mathrm{B}}}{\varepsilon_{\mathrm{pass}}^{\mathrm{S}} - \varepsilon_{\mathrm{pass}}^{\mathrm{B}}} \cdot N_{\mathrm{pass}}}{\frac{\varepsilon_{\mathrm{all}} - \varepsilon_{\mathrm{all}}^{\mathrm{B}}}{\varepsilon_{\mathrm{all}}^{\mathrm{S}} - \varepsilon_{\mathrm{all}}^{\mathrm{B}}} \cdot N_{\mathrm{all}}} \,. \tag{A.6}$$

where $\varepsilon_{\mathrm{pass(all)}} = N_{\mathrm{pass(all)}}^{\mathrm{iso}}/N_{\mathrm{pass(all)}}$ is the fraction of tight (all) photon candidates in data that satisfy the track isolation criteria.

The prompt-photon track isolation efficiencies ($\varepsilon_{\mathrm{all}}^{\mathrm{S}}$ and $\varepsilon_{\mathrm{pass}}^{\mathrm{S}}$) are estimated from simulated prompt-photon samples. The differences between the prompt track isolation efficiencies calculated with these samples and those with additional material are treated as systematic uncertainties.

The background-photon track isolation efficiencies ($\varepsilon_{\mathrm{all}}^{\mathrm{B}}$ and $\varepsilon_{\mathrm{pass}}^{\mathrm{B}}$) are estimated from control samples enriched with background photons, selected by reversing the tight selection on the variables computed from the energy in

the cells of the first ECAL layer, also called "narrow strip variables": F_{side}, $\omega_{s,3}$, ΔE, E_{ratio}. Since in such samples no candidates pass the tight cuts by construction, in order to obtain $\varepsilon^{\text{B}}_{\text{pass}}$, a "relaxed tight" criterion is defined, consisting of the candidates which fail at least one of the requirements on the narrow strip variables, but pass the rest of the selection in the tight identification definition. Due to the very small correlation (few %) between the track isolation and the narrow strip variables, the background-photon track isolation efficiency is similar for photons satisfying tight or relaxed tight criteria. The differences between the track isolation efficiencies for background photons passing the tight or the relaxed tight criteria are estimated from simulations and included in the systematic uncertainties. The contamination from prompt photons in the background enriched samples is accounted for in this procedure by using as an additional input the fraction of signal events passing or failing the relaxed tight requirements, as determined from the prompt-photon simulation. The fraction of prompt photons in the background control samples decreases from about 20% to 0.1%, with increasing photon transverse momentum. The whole procedure is tested on a simulated sample of γ+jet and dijet events, and the difference between the true track isolation efficiency for background photons and the one estimated with this procedure is taken as a systematic uncertainty. The typical relative uncertainty in the background-photon track isolation efficiency is 3–5%. An additional systematic uncertainty, due to the use of the prompt-photon simulation to estimate the fraction of signal photons in the background control regions, is estimated by calculating these fractions using alternative MC samples based on a detector simulation with a conservative estimate of additional material in front of the calorimeter. The distorted material relative uncertainty is about 1% below 30 GeV and less than 0.1% at higher E_{T} . The total systematic uncertainty decreases with the transverse energy. It reaches 5–6% below 40 GeV, and 1% at higher E_{T}, where the contribution of this method is the most important.

As an example, Figure A.4 shows the track isolation efficiencies for prompt and background unconverted photons, with $|\eta| \leq 0.6$, in the "all" and "pass" samples, together with the corresponding efficiencies measured in data, for photons passing or failing the tight ID criteria. The track isolation criteria for background photons decreases with E_{T}, since the candidates with larger transverse energy are produced from more energetic jets, which are characterized by a large number of tracks near the photon candidates.

The final result is obtained by multiplying the measured efficiency by a correction factor to take into account the preselection of the sample using different photon triggers, which already apply some loose requirements to the photon discriminating variables. The correction factor is computed, using

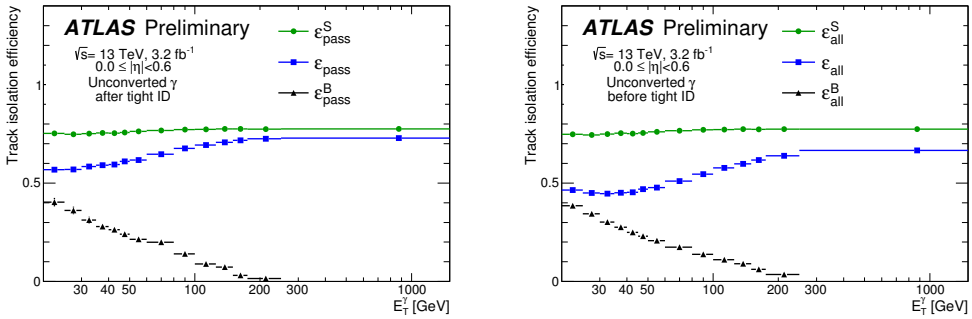

Figure A.4: Track isolation efficiencies for unconverted photon candidates. Errors include statistical and systematic uncertainties. Left: candidates passing the tight identification criteria. Right: candidates in the inclusive sample [71].

the γ+jet simulated sample, as the ratio between the tight identification efficiency for all reconstructed photons and that for photons that were used to trigger the event[2].

A.2.4 Efficiencies measured in data

The identification efficiency measurements obtained from the three data-driven methods, discussed in the previous sections, are compared in Figures A.5-A.6. In the overlapping E_{T} regions, the $\varepsilon_{\mathrm{ID}}$ values are consistent with each other within the uncertainties. Relatively large fluctuations of the radiative Z decay measurements are observed, due to their large statistical uncertainties.

The photon identification efficiency increases from 53–64%(47–61%) for unconverted (converted) photons at $E_{\mathrm{T}} \approx 10$ GeV to 88–92% (96–98%) for $E_{\mathrm{T}} \geq 100$ GeV.

A.2.5 Comparison with the simulation

In this section the results of the data-driven efficiency measurements are compared to the identification efficiencies predicted in the simulation. Prompt photons produced in photon+jet events have different kinematic distributions inside each eta region, with respect to photons originating in radiative Z boson decays. Moreover, the latter are always well isolated, while the former

[2]The effect of this factor on the ID efficiency ranges from -2% to -0.1%, decreasing towards high E_{T}.

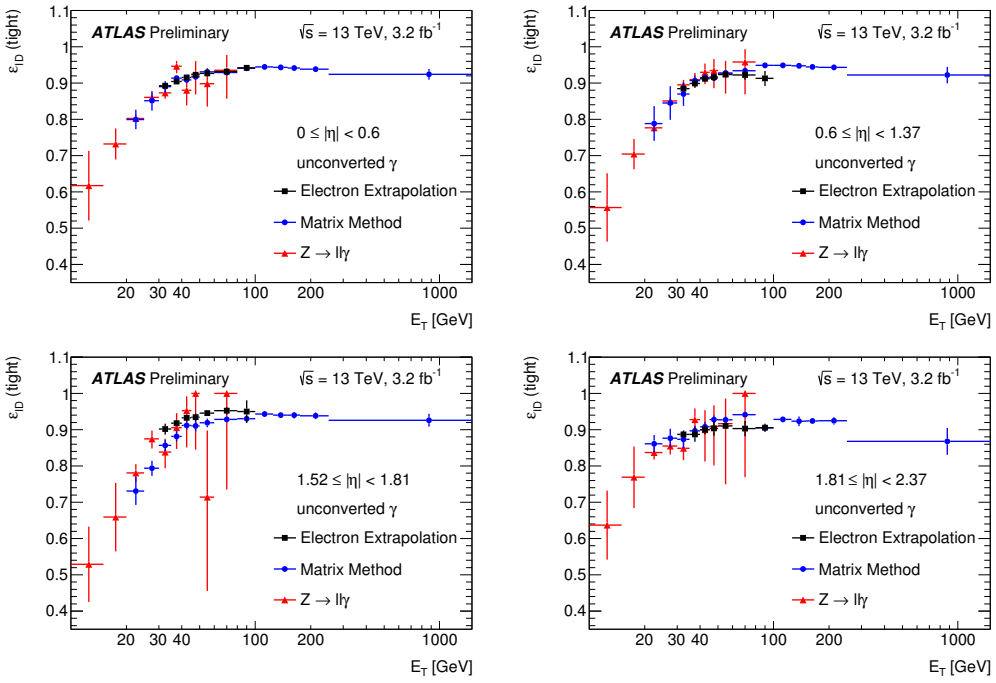

Figure A.5: Comparison of the data-driven mesurements of the identification efficiency for unconverted photons as function of E_{T} in the region 10 GeV $\leq E_{\mathrm{T}} \leq$ 1500 GeV, for the four pseudorapidity intervals. The uncertainty bars represent the sum in quadrature of the statistical and systematic uncertainties estimated in each method [71].

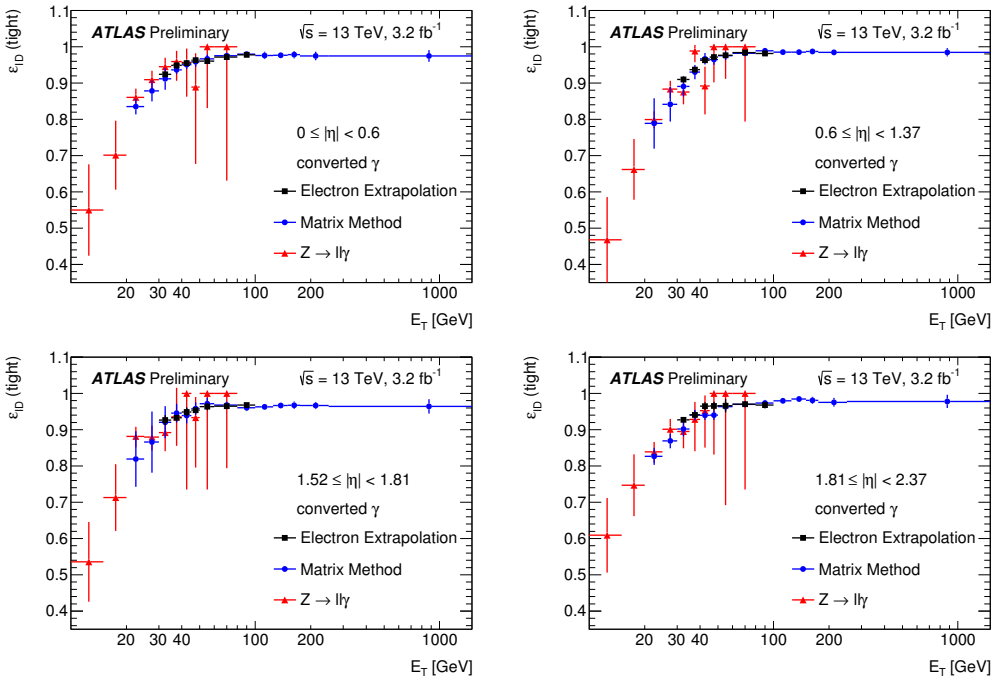

Figure A.6: Comparison of the data-driven mesurements of the identification efficiency for converted photons as function of E_{T} in the region 10 GeV $\leq E_{\mathrm{T}} \leq$ 1500 GeV, for the four pseudorapidity intervals. The uncertainty bars represent the sum in quadrature of the statistical and systematic uncertainties estimated in each method [71].

have a significant contribution from fragmentation. After the isolation requirement, the difference in identification efficiency between the two cases is small. Nonetheless, to account for such a difference, the efficiency measured in data with radiative Z boson decays is compared to the prediction from simulated $Z \to \ell\ell\gamma$ events (Figures A.7–A.8), while the efficiencies measured in data with the electron extrapolation and the matrix method are compared to the predictions from simulated photon+jet events (Figures A.9–A.10).

		E_{T} range [GeV]		
		10–30	30–100	100–1500
Unconverted γ	Total	1.4%–18.5%	0.3%–1.4%	0.4%–4.2%
	Total	1.4%–18.5%	0.3%–1.4%	0.4%–4.2%
	Statistics	1.2%– 2.4%	0.1%–0.8%	0.4%–1.9%
	Systematics	0.6%–18.5%	0.2%–1.3%	0.1%–3.9%
	Background	0.4%– 6.7%	0.0%–1.2%	0.0%–0.4%
	Material	0.3%– 8.5%	0.0%–1.0%	0.1%–3.9%
	Non-closure	0.0%–12.3%	0.0%–0.3%	-
	Conversion	-	0.0%–0.1%	-
	Generator	0.0%– 9.8%	-	-
Converted γ	Total	1.9%–30.8%	0.1%–1.2%	0.5%–2.0%
	Total	1.9%–30.8%	0.1%–1.2%	0.5%–2.0%
	Statistics	1.1%– 5.8%	0.1%–0.8%	0.4%–1.9%
	Systematics	1.6%–30.5%	0.1%–1.2%	0.1%–0.8%
	Background	0.6%–16.3%	0.0%–0.8%	0.0%–0.1%
	Material	0.5%–16.5%	0.0%–0.9%	0.1%–0.8%
	Non-closure	0.0%–15.6%	0.0%–0.3%	0.0%–0.0%
	Conversion	-	0.0%–0.0%	-
	Generator	0.0%–15.0%	-	-

Table A.1: Ranges of total uncertainty on the data-to-MC photon identification efficiency ratios and breakdown of the different sources of uncertainty for unconverted and converted photons, in three bins of transverse energy, giving the minimum and maximum values in the four pseudorapidity regions. A dash indicates that a particular systematic uncertainty is not applied in that E_{T} range.

No significant differences are observed between data-driven measurements and the simulations. The difference between the simulation and the data-driven measurements is taken into account by computing data-to-MC efficiency ratios, also referred to as scale factors (SF).

The SF are computed independently for each method and then combined. The data-to-MC efficiency ratios are shown in the bottom plots of Figures A.7 to A.10. Because of their good agreement and of the independence of the data samples, the SF as function of E_{T} are combined into a single result

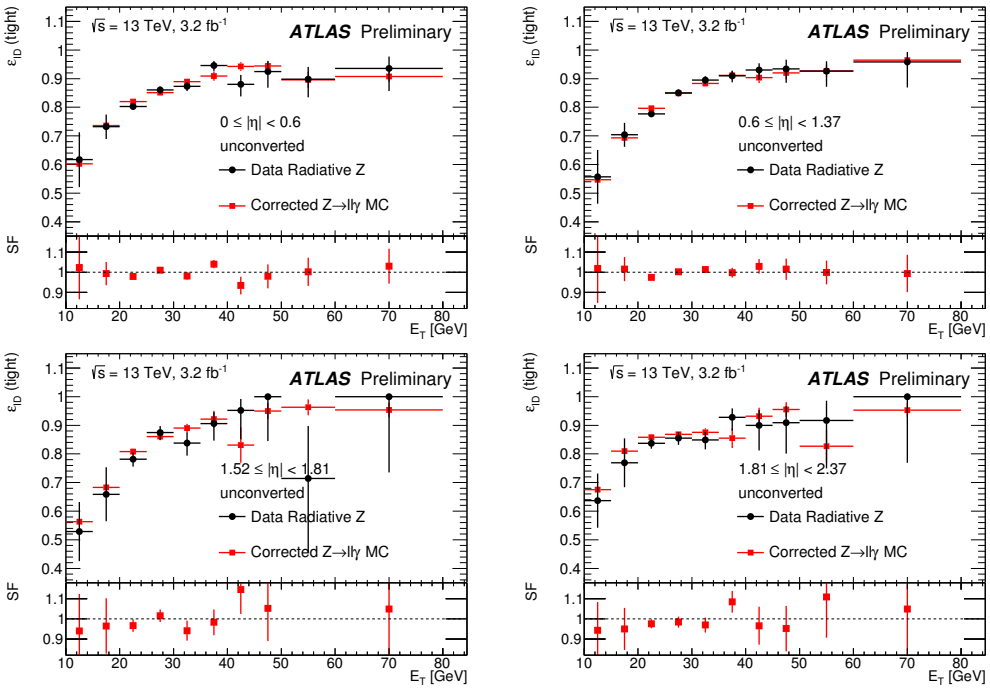

Figure A.7: Comparison of the radiative Z boson data-driven efficiency measurements of unconverted photons to the $Z \to \ell\ell\gamma$ simulation as function of E_{T} in the region $10 \leq E_{\mathrm{T}} \leq 80$ GeV, in the four pseudorapidity intervals. The bottom panels show the ratio of the data-driven results to the MC predictions ("scale factor", SF). The uncertainty bars represent the sum in quadrature of the statistical and systematic uncertainties [71].

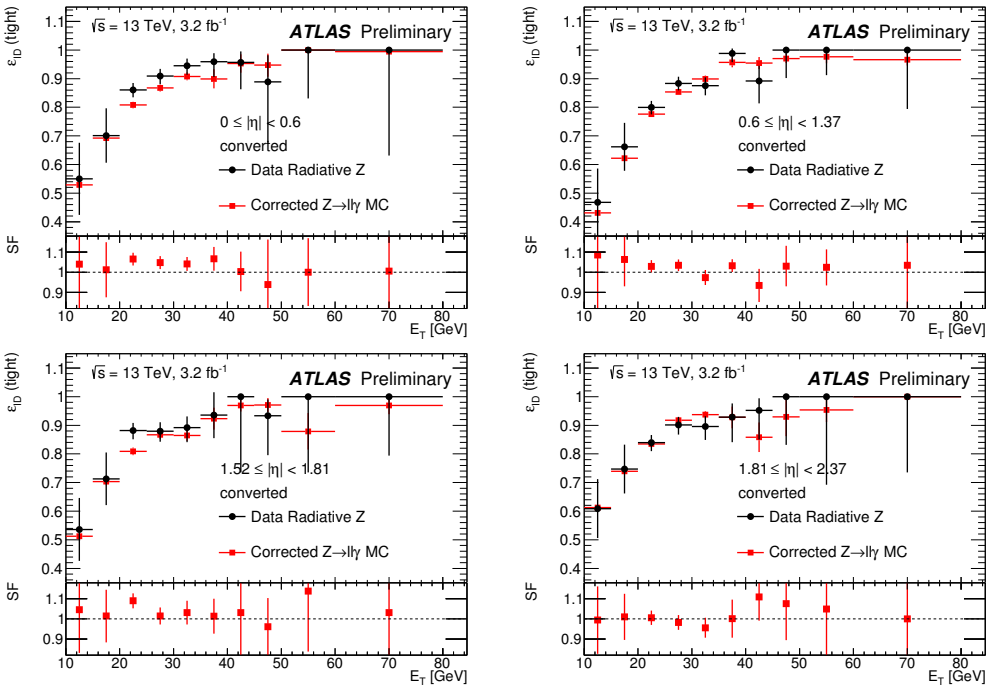

Figure A.8: Comparison of the radiative Z boson data-driven efficiency measurements of converted photons to the $Z \to \ell\ell\gamma$ simulation as function of E_{T} in the region $10 \leq E_{\mathrm{T}} \leq 80$ GeV, in the four pseudorapidity intervals. The bottom panels show the ratio of the data-driven results to the MC predictions ("scale factor", SF). The uncertainty bars represent the sum in quadrature of the statistical and systematic uncertainties [71].

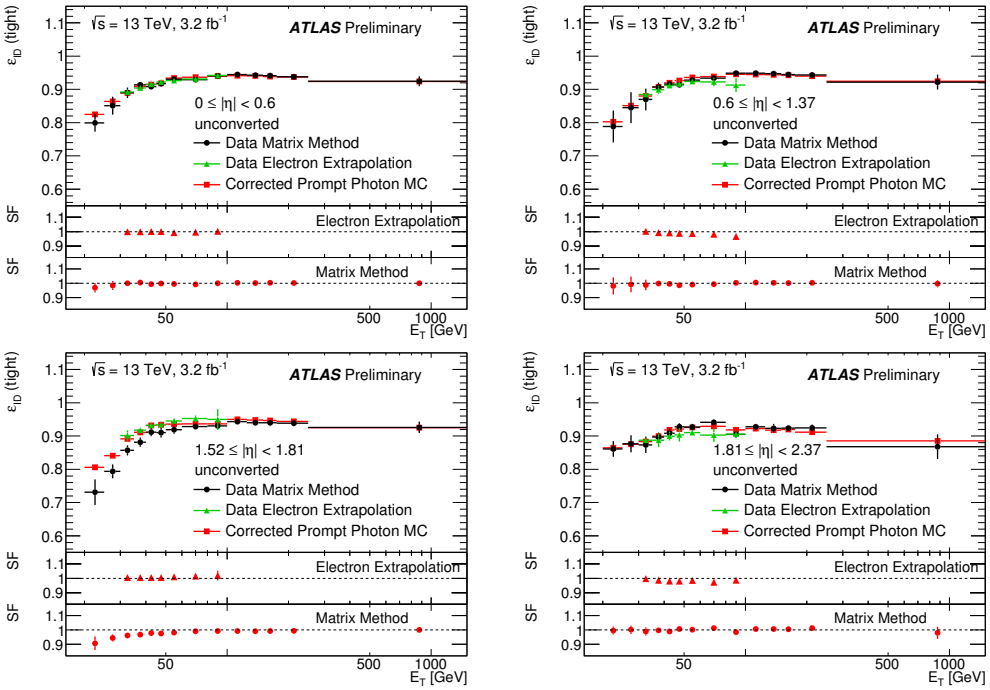

Figure A.9: Comparison of the electron extrapolation and matrix method data-driven efficiency measurements of unconverted photons to the respectively prompt-photon MC predictions as function of E_{T} in the region 20 $\leq E_{\mathrm{T}} \leq$ 1500 GeV, in the four pseudorapidity intervals. The bottom panels show the ratio of the data-driven results to the MC predictions ("scale factor", SF). The uncertainty bars represent the sum in quadrature of the statistical and systematic uncertainties [71].

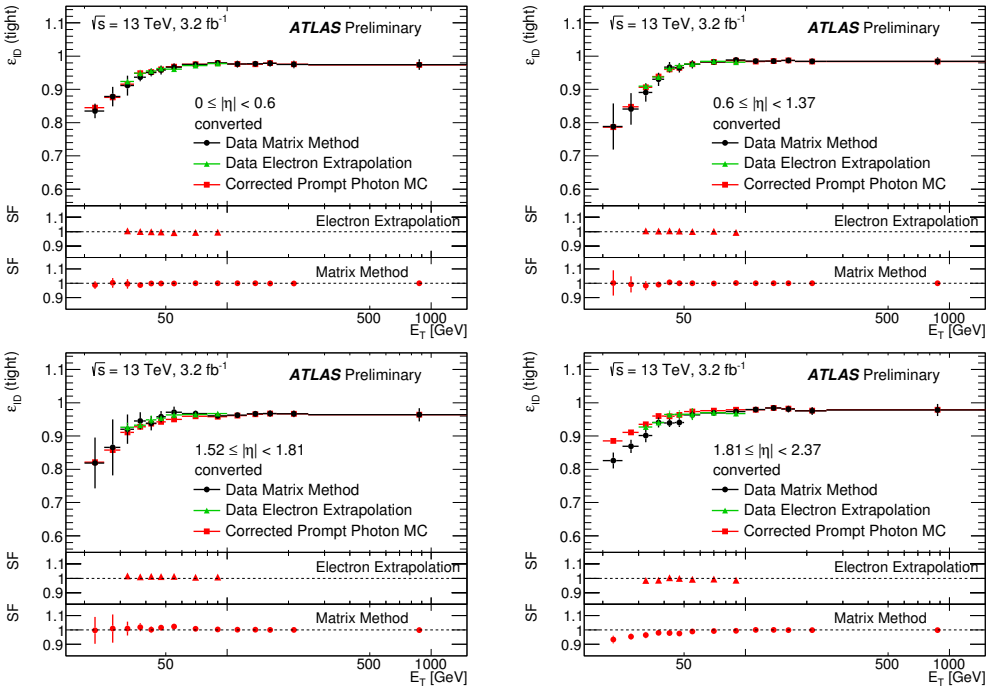

Figure A.10: Comparison of the electron extrapolation and matrix method data-driven efficiency measurements of converted photons to the respectively prompt-photon MC predictions as function of E_{T} in the region $20 \leq E_{\mathrm{T}} \leq 1500$ GeV, in the four pseudorapidity intervals. The bottom panels show the ratio of the data-driven results to the MC predictions ("scale factor", SF). The uncertainty bars represent the sum in quadrature of the statistical and systematic uncertainties [71].

in the overlapping regions. The combination is performed indipendently in each E_{T} bin, in each pseudorapidity region, and separately for unconverted and converted photons, using the Best Linear Unbiased Estimate (BLUE) technique [101]. The combined values are displayed in Figure A.11, as a function of E_{T}, separately for unconverted and converted photons, and in different η regions.

Most SF values are close to unity. This confirms that the simulation, with the applied corrections, provides a good description of the photon shower shapes in the collision data. In analyses with photons in final state, the combined scale factors are then applied to simulated photons as weights to provide an even better description of the identification efficiency.

Table A.1 lists the statistical uncertainties and all the sources of systematic uncertainties, arising from: the background modelling/subtraction; the description of the detector material/geometry in the simulation; the residual discrepancies in closure tests; the identification of conversions; the usage of a different generator for photon simulation.

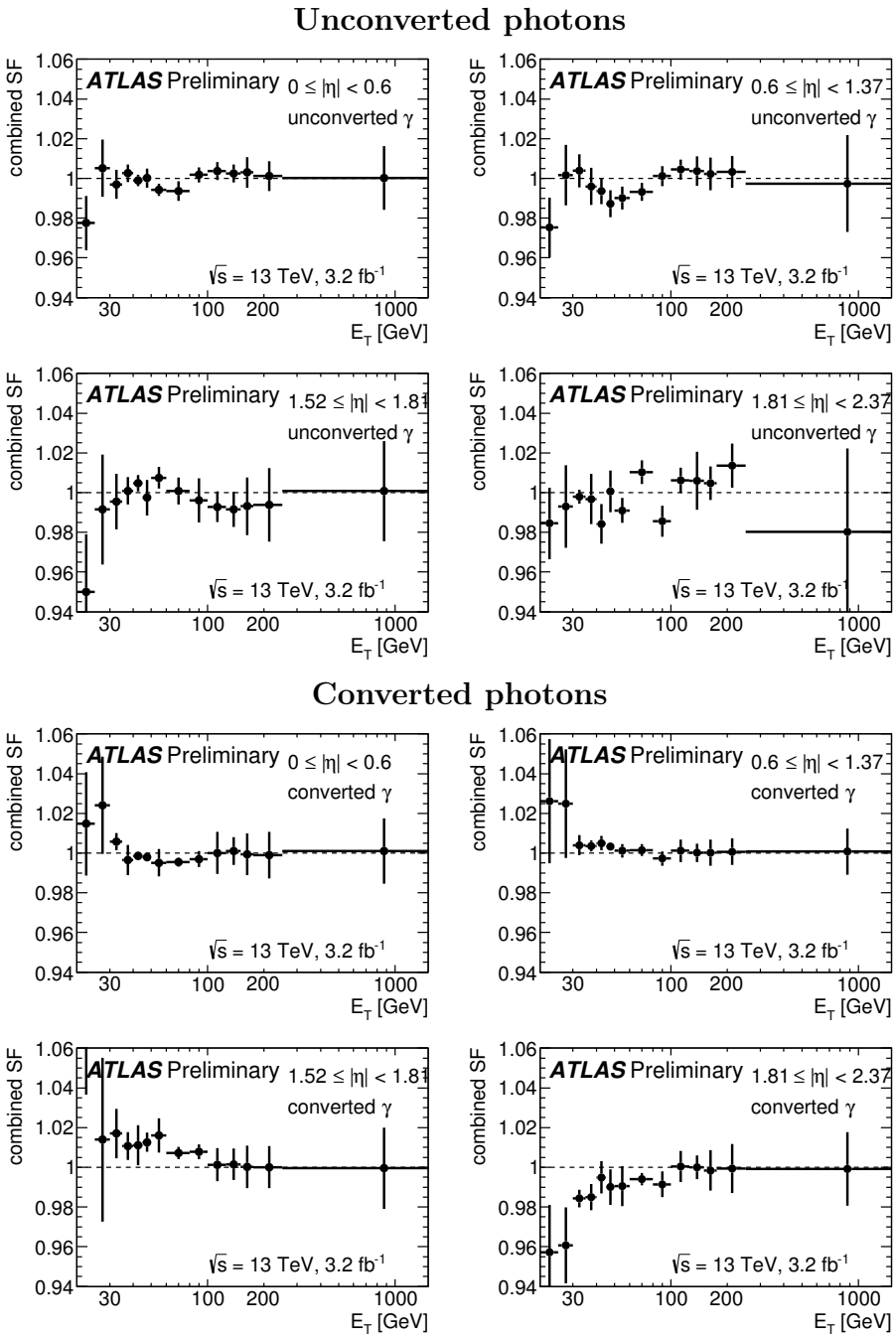

Figure A.11: Data-to-MC efficiency ratios (SF) from the combination of the three measurements described in the text, for unconverted (top) and converted (bottom) photons, in the four pseudorapidity intervals. The uncertainty bars represent the sum in quadrature of the statistical and systematic uncertainties [71].

Appendix B

Additional studies

B.1 Photon energy resolution uncertainty

The systematic uncertainties due to the photon energy scale and resolution were added in quadrature and are shown in Section 8.1. In this appendix, the systematic uncertainty due to the photon energy resolution is shown separately. The estimated uncertainties, shown in Figure B.1, are much smaller than those of the photon energy scale.

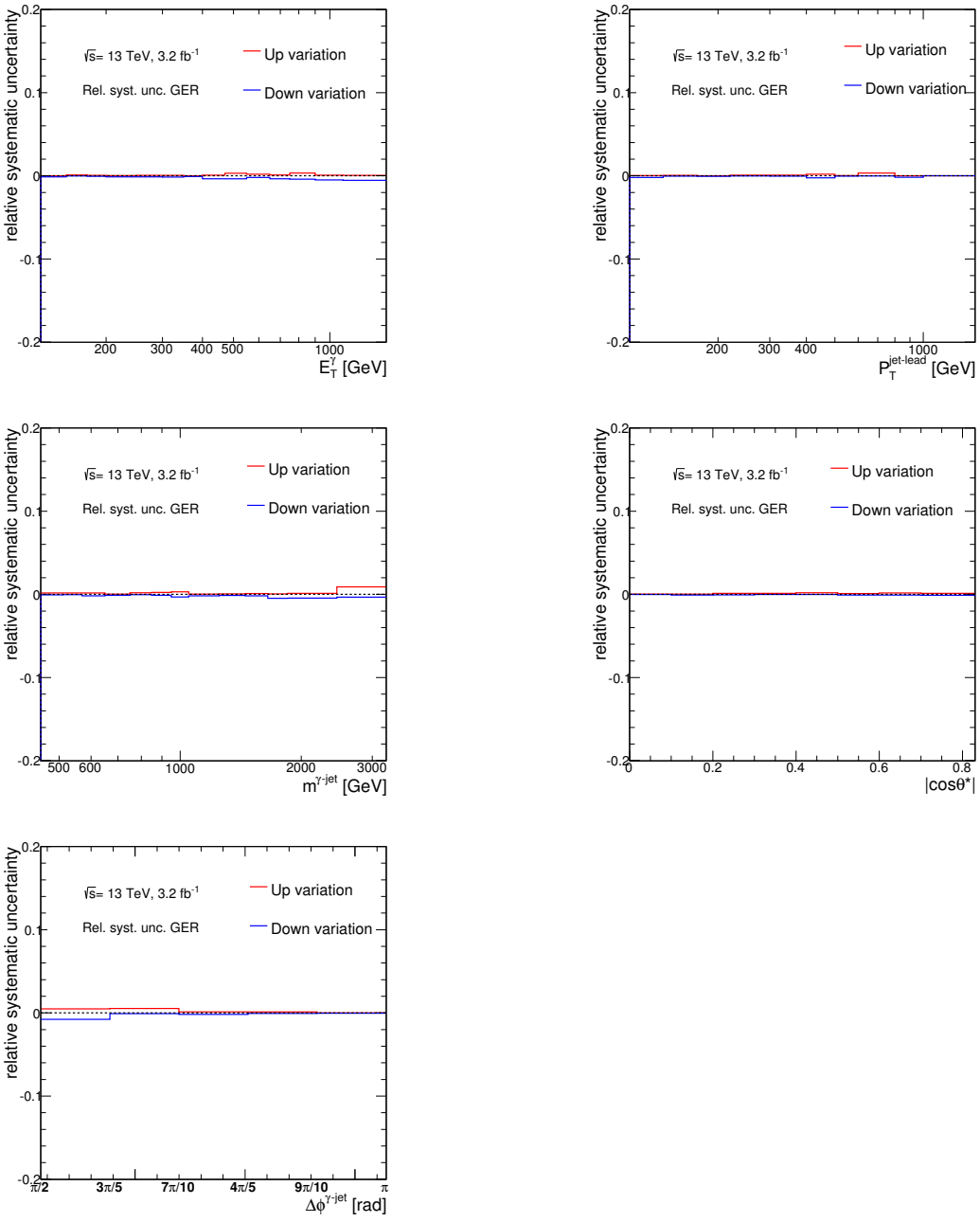

Figure B.1: Systematic uncertainties on the measured cross sections due to the uncertainty in the photon energy resolution as a function of E_{T}^{γ}, $p_{\mathrm{T}}^{\mathrm{jet-lead}}$, $m^{\gamma-\mathrm{jet}}$, $|\cos\theta^{*}|$ and $\Delta\phi^{\gamma-\mathrm{jet}}$.

B.2 Use of MC samples with a distorted geometry

The cross section $d\sigma/dE_{\mathrm{T}}^{\gamma}$ for inclusive photon production, as a function of E_{T}^{γ}, has been evaluated using the MC simulations of the signal with PYTHIA default (both for the signal leakage fractions and for the unfolding) either with the nominal or a distorted detector geometry, which includes additional material in the inner detector and in front of the calorimeter system. The reason of this additional study, only for the inclusive photon production and not for the photon plus jet final states, is explained in the following. The goal is to quantify the effect on the photon reconstruction efficiency only; the additional material would also have an effect also in the jet energy scale, which is already accounted in the in situ measurements used in the jet calibration method. The relative difference between the two cross sections is shown in Figure B.2; the uncertainty is tipically smaller than 0.5 %.

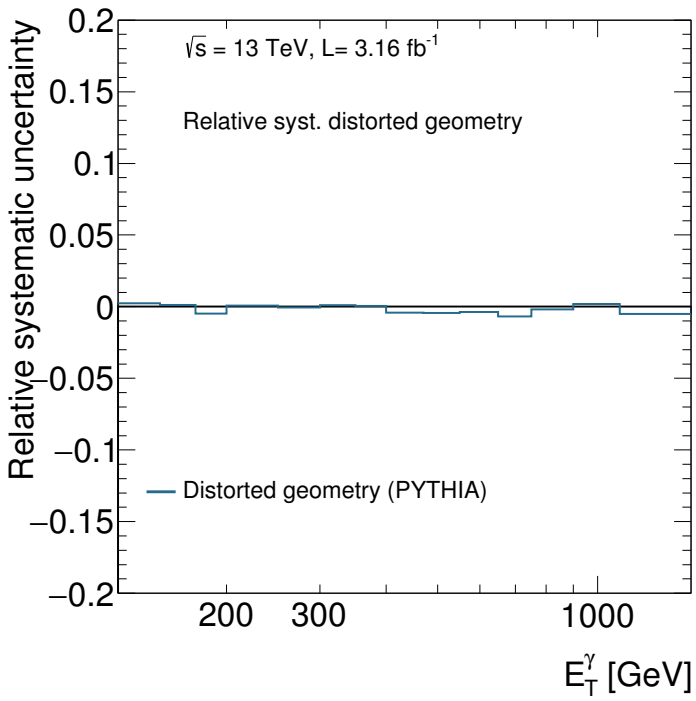

Figure B.2: The relative difference in the cross section $d\sigma/dE_{\mathrm{T}}^{\gamma}$ for inclusive photon production using the MC simulations with a distorted and the nominal geometry as a function of E_{T}^{γ}.

B.3 Additional studies on converted and unconverted photons

B.3.1 Converted photon fraction

A detailed study of the fraction of converted photons has been performed to ensure the level of agreement between data and Monte Carlo. The fraction of converted photons for a sample of tight and isolated events is shown in Figure B.3. After background subtraction (Figure B.4), the fraction of converted photons in data is constant ($\sim 30\%$) as a function of E_{T}^{γ}, $p_{\mathrm{T}}^{\mathrm{jet-lead}}$, $\Delta\phi^{\gamma-\mathrm{jet}}$, $m^{\gamma-\mathrm{jet}}$. It increases from 25% up to 35% as a function of $|\cos\theta^{*}|$; this behaviour is explained by the fact that low $|\cos\theta^{*}|$ values correspond to central values of η^{γ}, in which the fraction of converted photons is smaller than in other regions. The MC simulations of the signal from SHERPA are also included in Figure B.4 and well describe the data. Figure B.5 shows the ratios of data and PYTHIA optimised for these fractions. The differences between data and MC are typically below 4%. To study the effect of the simulated fraction of true converted photons on the cross sections, its contribution in the MC was changed by $\pm$ 10%. The ratios of the fractions between the data and the modified MC samples are also shown in Figure B.5. The effect on the cross section is shown in Figure B.6 and is very small. No systematic uncertainty was retained for this effect.

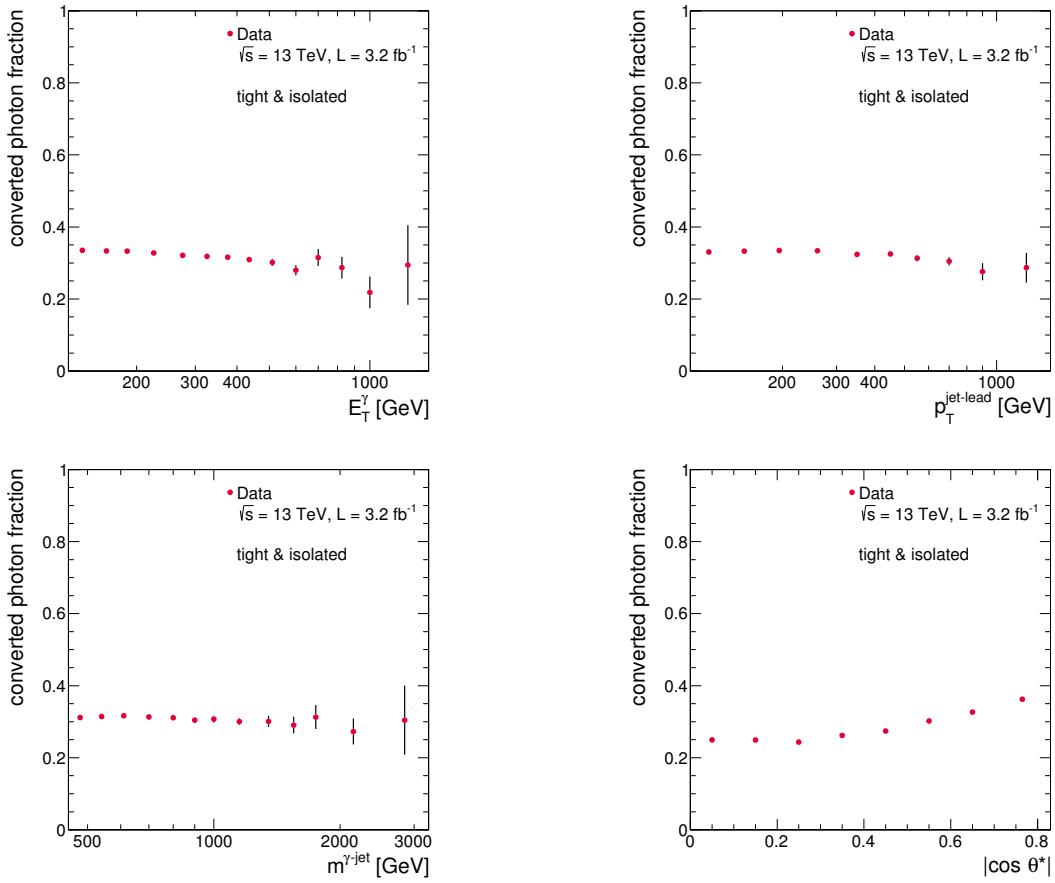

Figure B.3: Measured fraction of converted photons as a function of E_{T}^{γ}, $p_{\mathrm{T}}^{\mathrm{jet-lead}}$, $m^{\gamma-\mathrm{jet}}$ and $|\cos\theta^{*}|$ in the signal region.

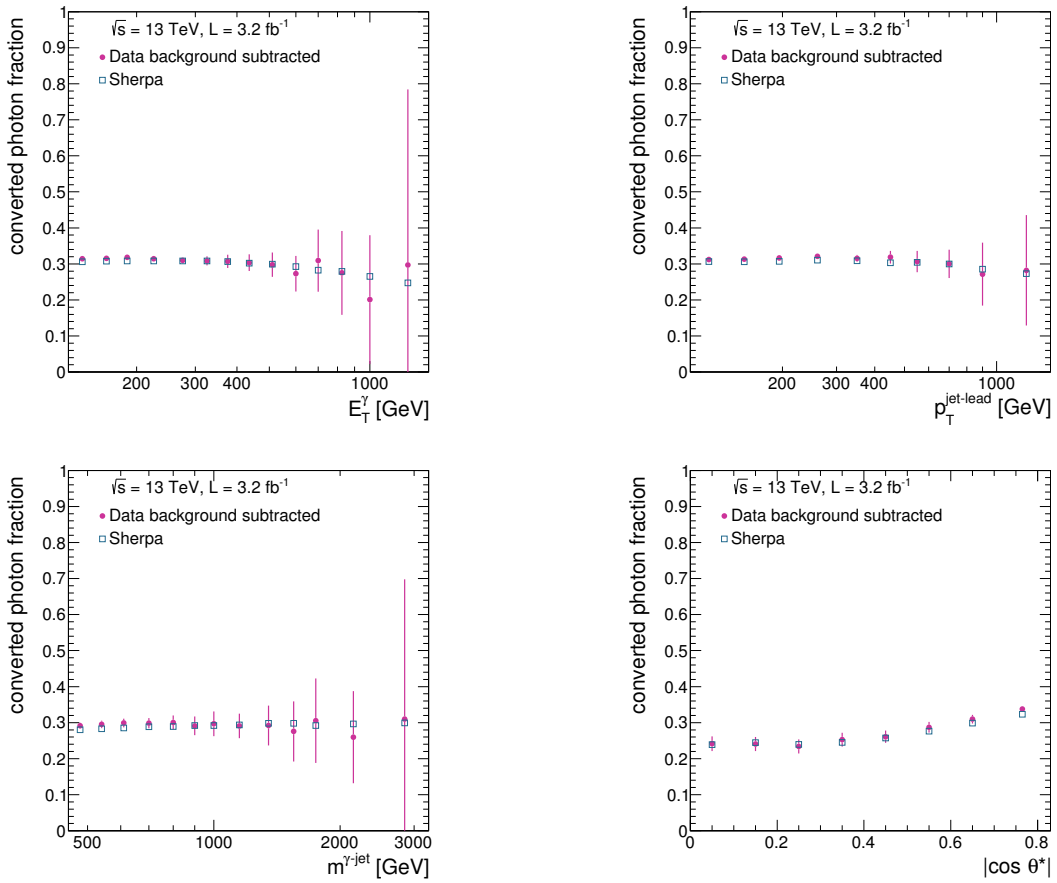

Figure B.4: Measured fraction of converted photons as a function of E_{T}^{γ}, $p_{\mathrm{T}}^{\mathrm{jet-lead}}$, $m^{\gamma-\mathrm{jet}}$ and $|\cos\theta^{*}|$ after the background subtraction. For comparison, the fractions computed with SHERPA (squares) MC samples are also included.

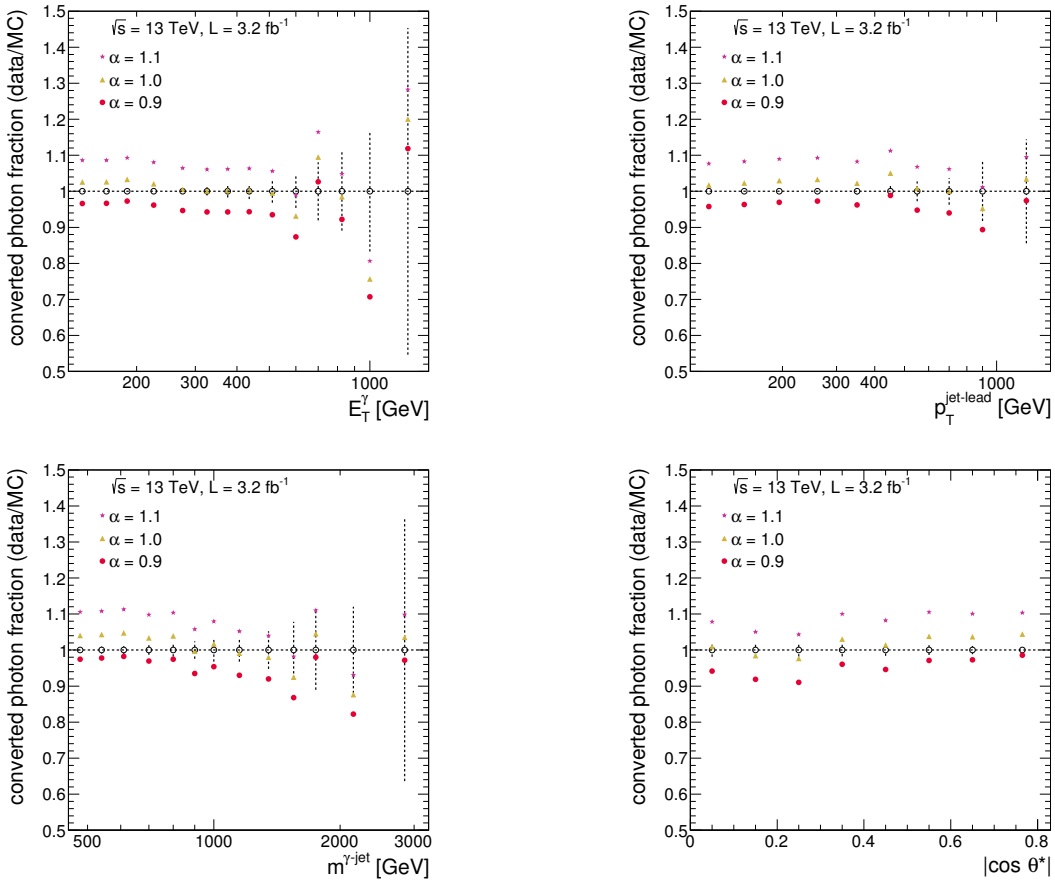

Figure B.5: Ratio of the fraction of converted photons in data and PYTHIA optimised as a function of E_{T}^{γ}, $p_{\mathrm{T}}^{\mathrm{jet-lead}}$, $m^{\gamma-\mathrm{jet}}$ and $|\cos\theta^{*}|$. The ratios of the fractions in data and MC, when the amount of true converted photons in the MC was increased or decreased by the α value shown in the legend, are also included. The vertical dashed lines display the relative statistical uncertainty in the data.

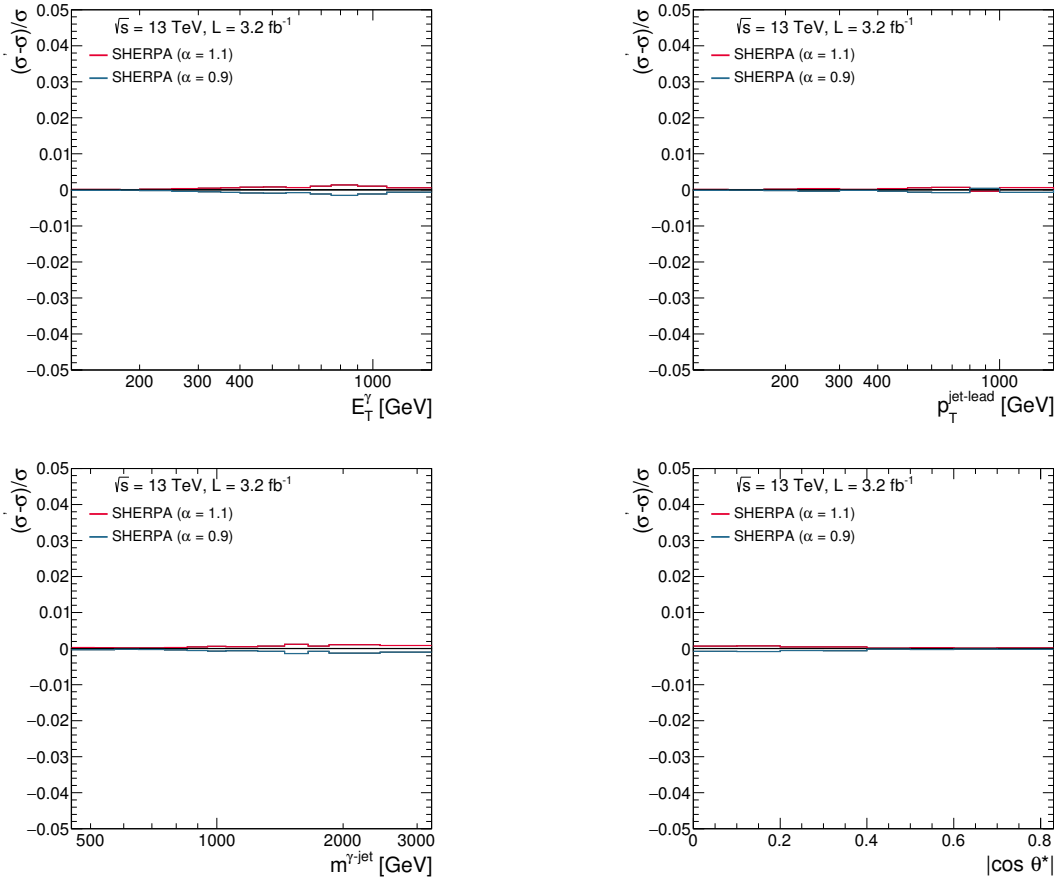

Figure B.6: Relative differences between the cross sections measured using MC samples with the contribution of true converted photons increased or decreased by 10% and the nominal cross section as a function of E_{T}^{γ}, $p_{\mathrm{T}}^{\mathrm{jet-lead}}$, $m^{\gamma-\mathrm{jet}}$ and $|\cos\theta^{*}|$.

B.3.2 Converted and unconverted cross sections

The nominal cross sections were obtained using both converted and unconverted photons. In this section, the cross sections are evaluated using either converted or unconverted photons. The signal yields in data have been obtained using the two dimensional sideband method with the signal leakage fractions determined from the MC simulations of PYTHIA optimised using either converted or unconverted photons. The distributions for converted (unconverted) photons after background subtraction have been unfolded using the MC simulations of SHERPA to the particle level consisting of true leading photons that are tagged at particle level as converted (unconverted) photons. The resulting cross sections are added up and the sum is compared to the nominal cross section in Figure B.7, a good agreement is found. In the previous section the effect of changing by $\pm$ 10% the relative contribution of true leading photons that are tagged at particle level as converted photons was studied by comparing the nominal cross sections with the cross section obtained after the variations. That study accounts for the effects on both the signal leakage fractions and the unfolding. The results are presented in Figures B.8 and B.9 respectively. In addition, cross sections were evaluated using either converted or unconverted photons only and unfolding to the same phase space as for the nominal cross sections; these are different measurements than those mentioned above, where the cross sections were unfolded to the particle level consisting of true leading photons that are tagged at particle level as converted (unconverted) photons. The resulting cross sections and their ratios are shown in Figure B.10. It is expected that the major source of systematic uncertainty on the ratio arises from the variation of the contribution of true converted photons. The systematic uncertainty of varying the contribution of true converted photons by $\pm$ 10% was evaluated and is shown as a shaded band in Figure B.10: the ratio is consistent with unity within the uncertainties.

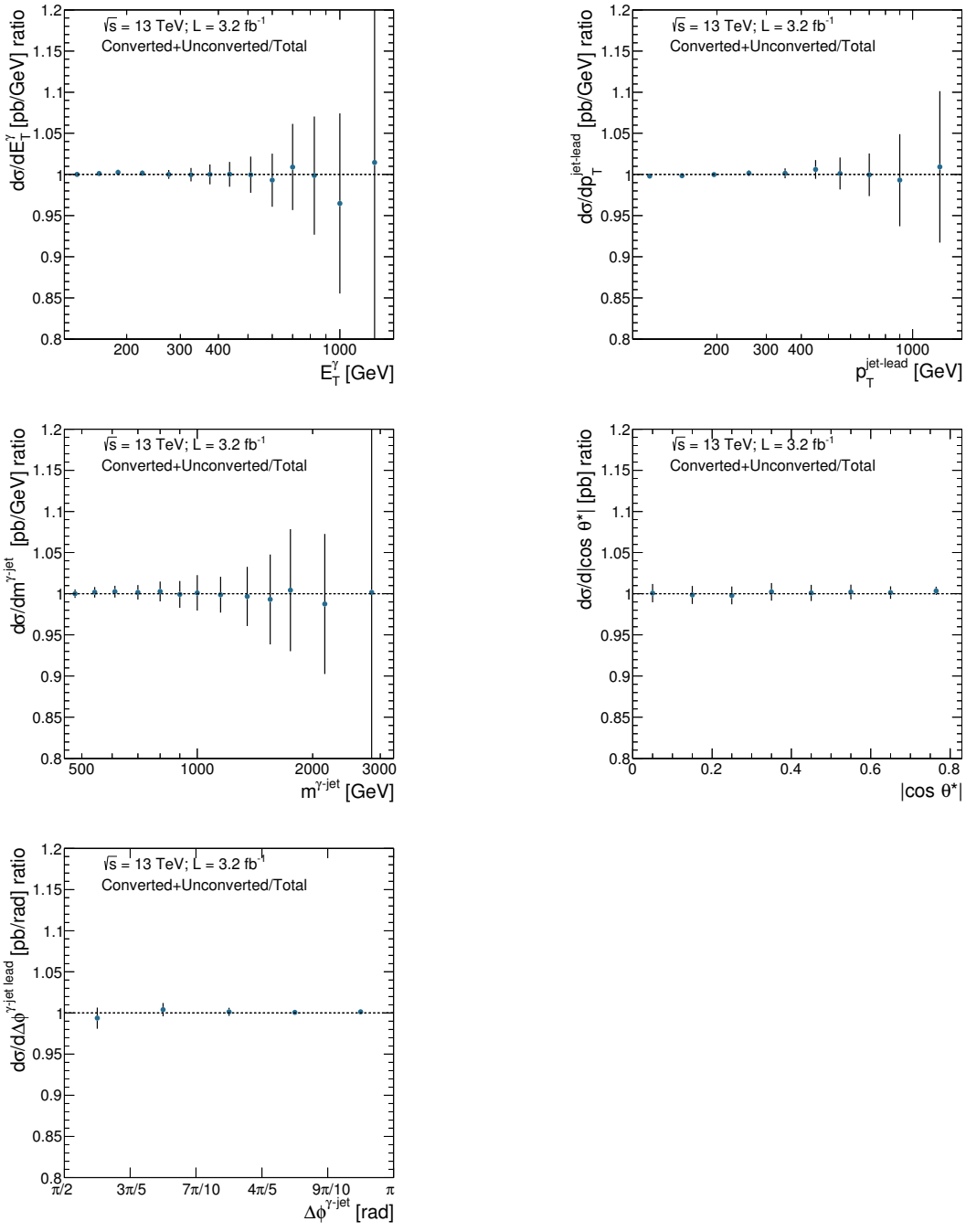

Figure B.7: Relative difference between the measured cross sections obtained from the sum of the converted and unconverted photon cross sections and the nominal cross section as a function of E_{T}^{γ}, $p_{\mathrm{T}}^{\mathrm{jet-lead}}$, $m^{\gamma-\mathrm{jet}}$, $|\cos\theta^{*}|$ and $\Delta\phi^{\gamma-\mathrm{jet}}$. The error bars represent the relative statistical uncertainties of the nominal cross sections.

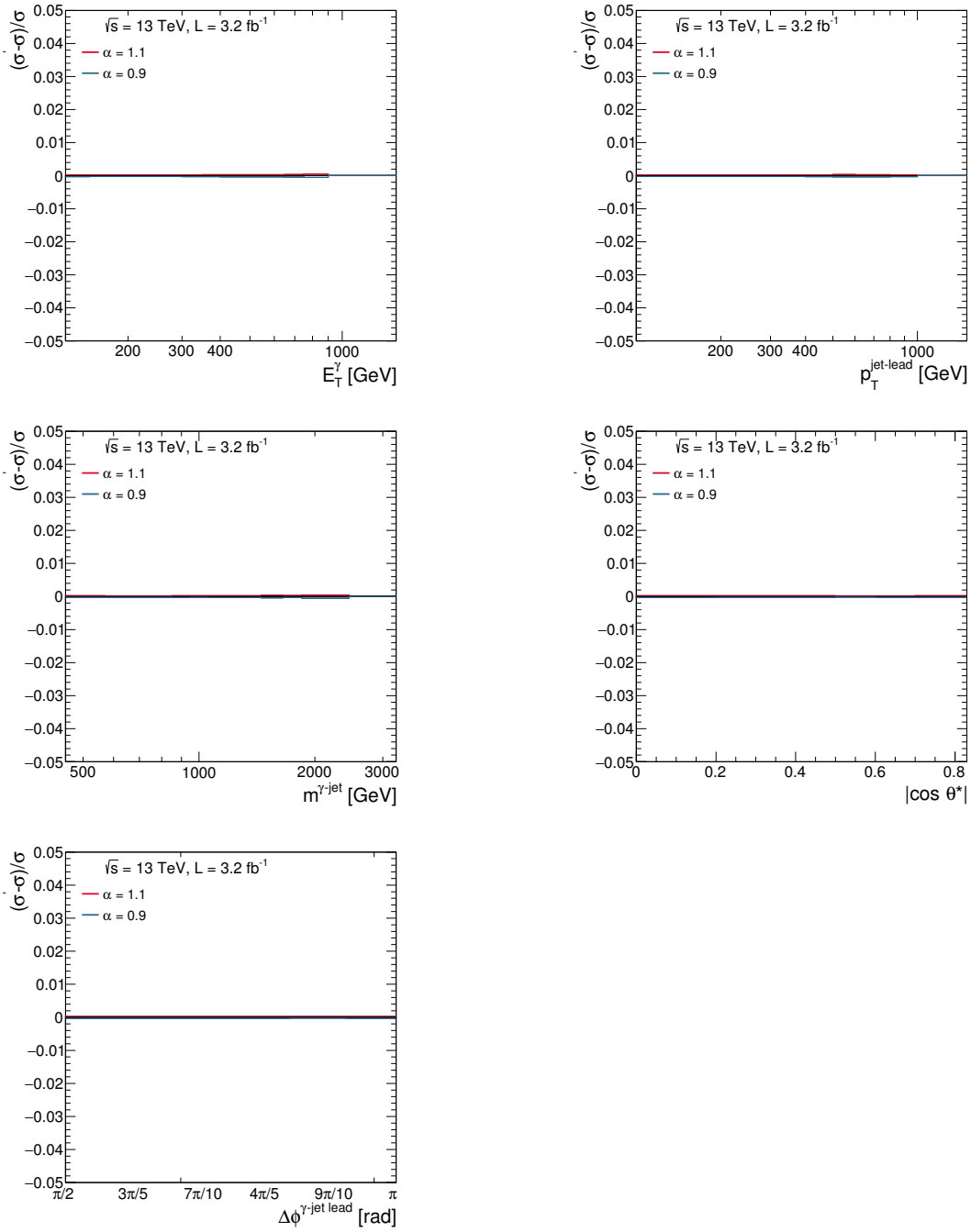

Figure B.8: Relative difference between the measured cross sections measured using MC samples (for the signal leakage fractions) with the contribution of true converted photons increased or decreased by 10% and the nominal cross sections as a function of E_{T}^{γ}, $p_{\mathrm{T}}^{\mathrm{jet-lead}}$, $m^{\gamma-\mathrm{jet}}$, $|\cos\theta^{*}|$ and $\Delta\phi^{\gamma-\mathrm{jet}}$.

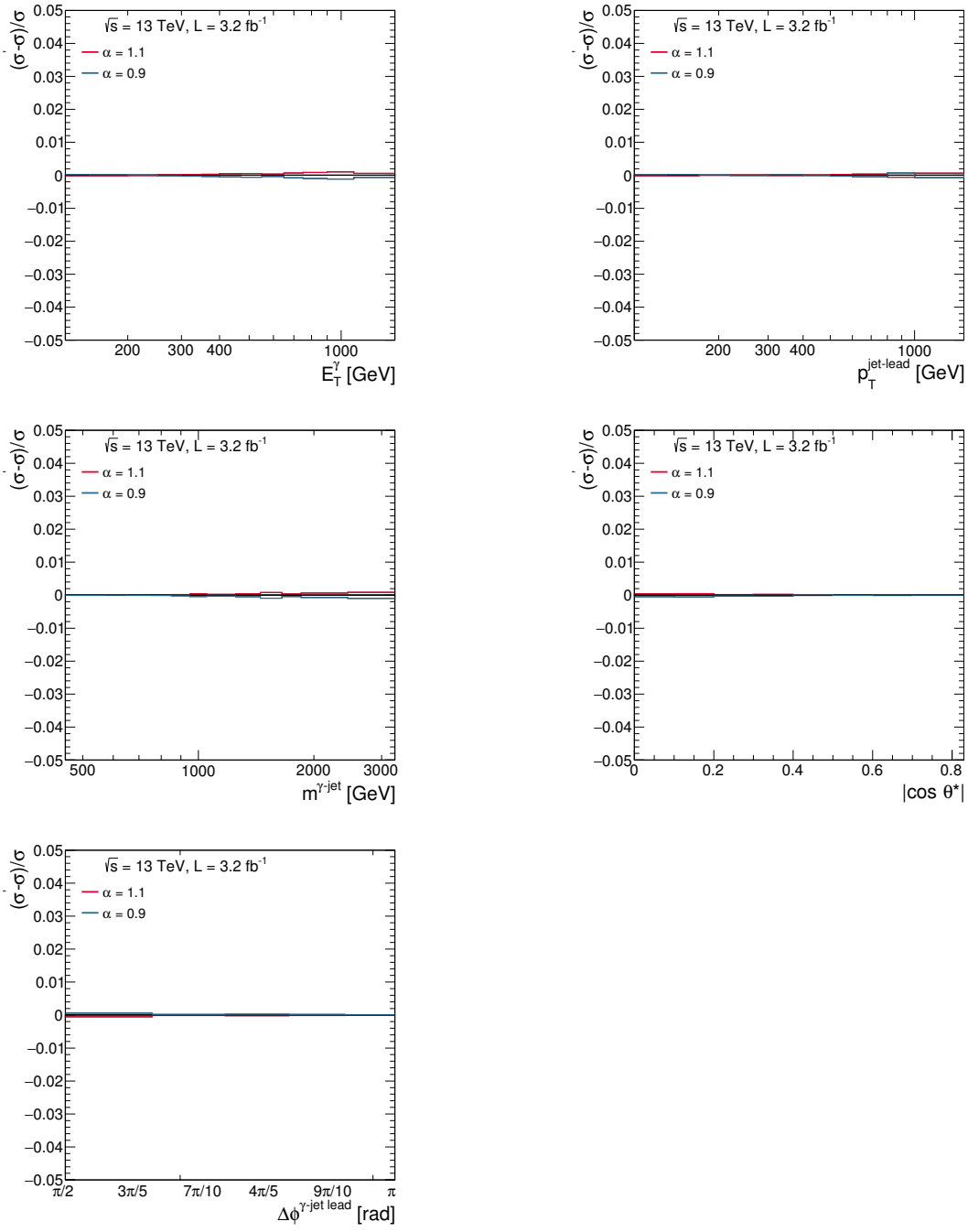

Figure B.9: Relative difference between the measured cross sections measured using MC samples (for the unfolding) with the contribution of true converted photons increased or decreased by 10% and the nominal cross sections as a function of E_{T}^{γ}, $p_{\mathrm{T}}^{\mathrm{jet-lead}}$, $m^{\gamma-\mathrm{jet}}$, $|\cos\theta^{*}|$ and $\Delta\phi^{\gamma-\mathrm{jet}}$.

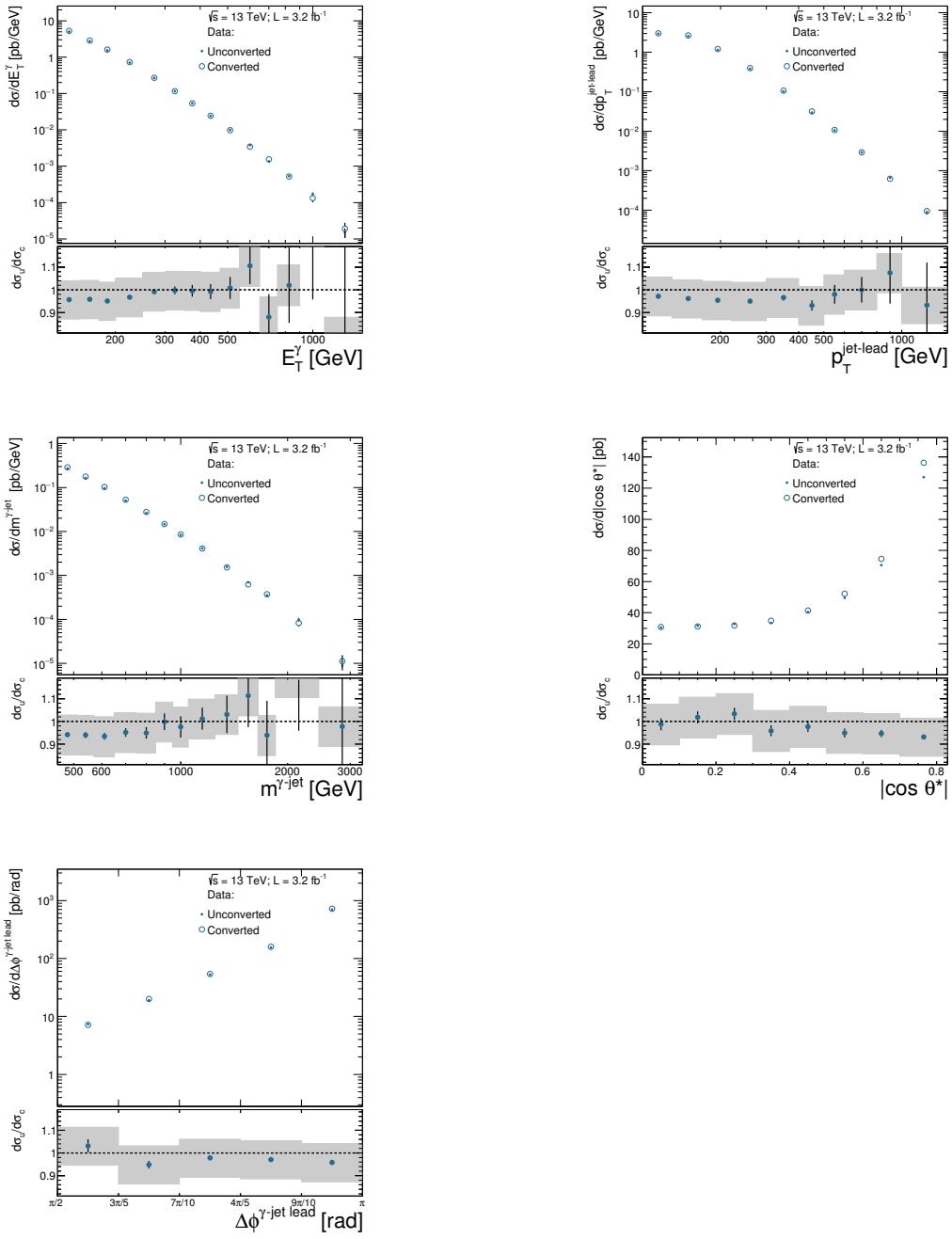

Figure B.10: Measured cross sections using unconverted (dots) or converted (open circles) photons only as functions of E_{T}^{γ}, $p_{\mathrm{T}}^{\mathrm{jet-lead}}$, $m^{\gamma-\mathrm{jet}}$, $|\cos\theta^{*}|$ and $\Delta\phi^{\gamma-\mathrm{jet}}$. The lower part of the figures shows the ratio unconverted ans converted (dots); the error bars in the ratio display the statistical uncertainty in the ratio and the shaded bands represent the systematic uncertainty arising from the variation of the contribution of true converted photons increased or decreased by 10%.

B.4 Study with a different isolation cut

An additional study using a different isolation requirement has been performed. Another E_{T}^{γ} dependent cut was used:

$$E_{\mathrm{T}}^{\mathrm{iso,cut}} = 2.2 \cdot 10^{-2} \cdot E_{\mathrm{T}}^{\gamma} + 2.45 \text{ GeV}$$

This is the requirement that is recommended by the ATLAS "Isolation forum" and "Egamma Combined Performance group". Despite this is an "official working point" (WP) cut, a different requirement was used in the analysis ($E_{\mathrm{T}}^{\mathrm{iso,cut}} = 4.2 \cdot 10^{-3} \cdot E_{\mathrm{T}}^{\gamma} + 4.8$ GeV) for several reasons that are briefly described in the following.

Figure B.11 shows the efficiency of both requirements as a function of E_{T}^{γ}, based on the estimations of both Pythia and Sherpa. It is observed that the efficiency of the WP coincides with that of the analysis requirement for $E_{\mathrm{T}}^{\gamma} = 125$ GeV. The behaviour of the analysis requirement is approximately constant as a function of E_{T}^{γ}, whereas that of the WP increases with the increasing of E_{T}^{γ}.

A study of the signal purity provided by both requirements was performed and the results are presented in Figure B.12 as a function of the studied variables. It is observed that the signal purity obtained with the analysis requirement is higher than that of the WP for all the bins in all distributions.

The size of the systematic uncertainties obtained by both requirements was also compared. As an example, the uncertainty due to the photon identification and isolation correlation in the background is shown in Figure B.13 and in Figure 8.15 for the analysis requirement. As in this case, many other uncertainties are larger for the WP than for the analysis requirement. Therefore, the measurements presented here would have lower precision if the WP had been used for the isolation requirement than the one chosen.

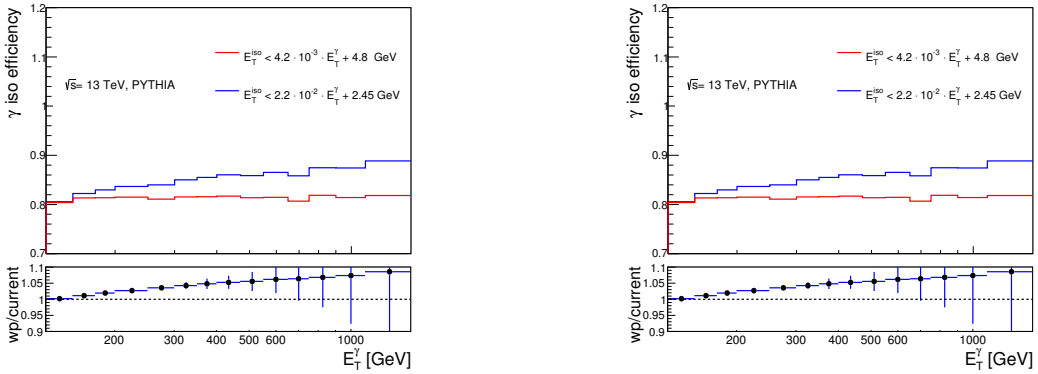

Figure B.11: Estimated efficiencies from PYTHIA default and SHERPA for this analysis (red) and the WP (blue) $E_{\mathrm{T}}^{\mathrm{iso}}$ requirements as a function of E_{T}^{γ}. The lower part of the figures shows the ratio between the WP and this analysis efficiencies (dots).

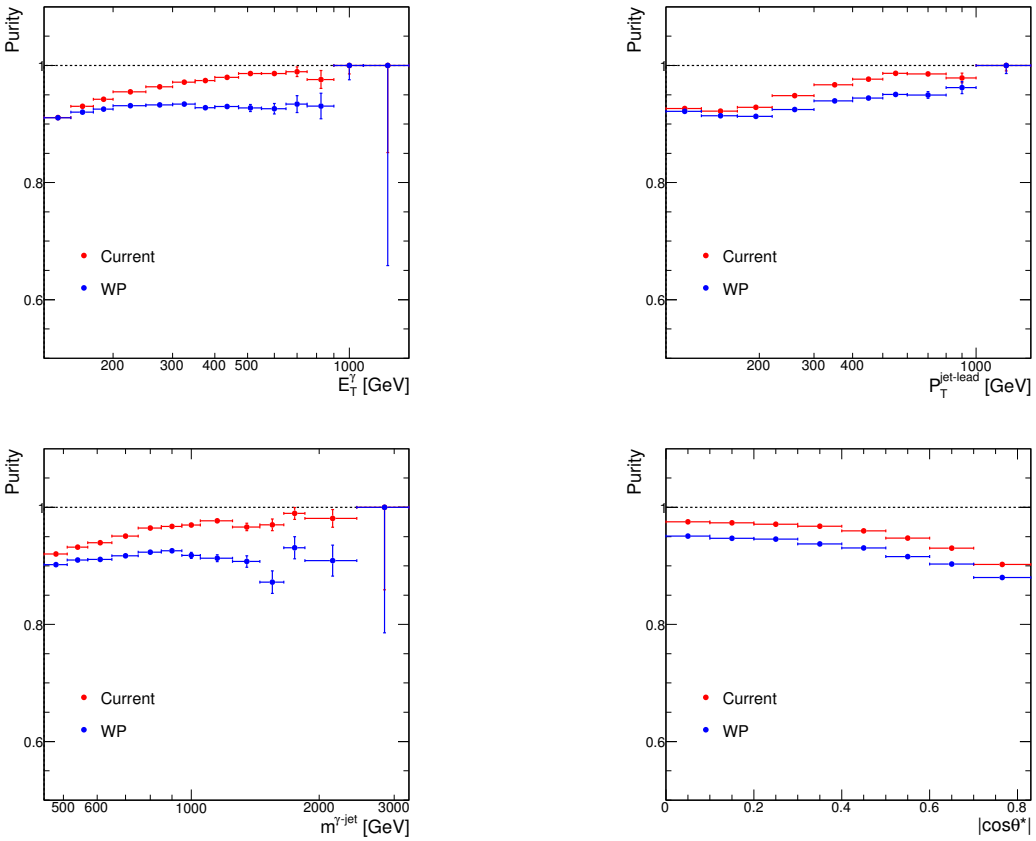

Figure B.12: Estimated signal purities in data using signal leakage fractions from SHERPA and this analysis (red) and the WP (blue) $E_{\mathrm{T}}^{\mathrm{iso}}$ requirements as a function of E_{T}^{γ}, $p_{\mathrm{T}}^{\mathrm{jet-lead}}$, $m^{\gamma-\mathrm{jet}}$ and $|\cos\theta^*|$.

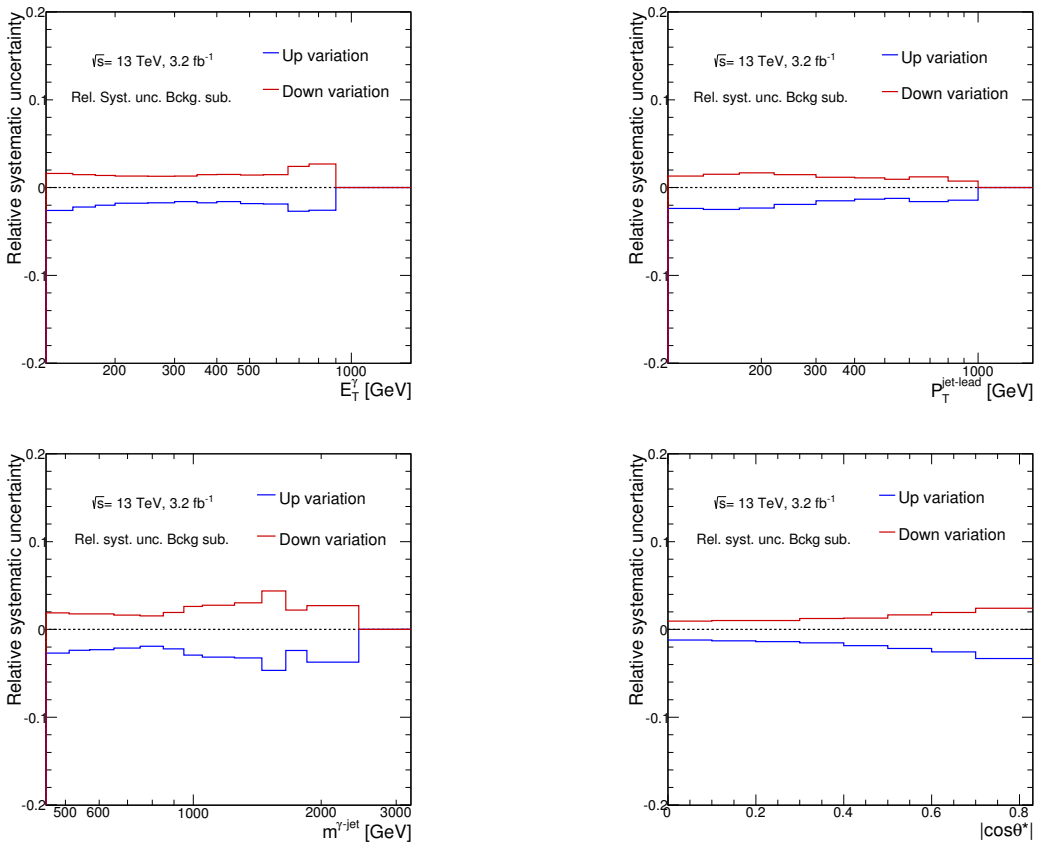

Figure B.13: Systematic uncertainties on the measured cross sections due to the correlation between the photon identification and isolation for background events as functions of E_{T}^{γ}, $p_{\mathrm{T}}^{\mathrm{jet-lead}}$, $m^{\gamma-\mathrm{jet}}$ and $|\cos\theta^{*}|$.

Appendix C

Tables of cross-section measurements

In this appendix the tables that include the measured differential cross section measurements as a function of the studied variables, are shown in Table C.1 to C.5. They are reported together with the statistical uncertainty in the data (in %), the total systematic uncertainty excluding that on the luminosity (in %) and the contribution from different sources of systematic uncertainty in (%), listed in Chapter 8.

E_{T}^{γ} [GeV]	$d\sigma/dE_{\mathrm{T}}^{\gamma}$ [pb/GeV]	Stat. (%)	Total syst. (%)		GES (%)		GER (%)		JES (%)		JER (%)		Leak. (%)		γ ID (%)	
			Up	Down	Up	Down	Up	Down	Up	Down	Up	Down	Up	Down	Up	Down
125 - 150	5.191	± 0.2	3.9	-3.8	0.8	-0.9	< 0.1	< 0.1	2.4	-2.3	0.3	-0.3	1.3	-1.3	1.3	-1.2
150 - 175	2.796	± 0.2	3.2	-3.2	1.4	-1.3	< 0.1	< 0.1	1.4	-1.4	0.1	-0.1	0.9	-0.9	1.3	-1.3
175 - 200	1.561	± 0.3	3.0	-3.0	1.7	-1.7	< 0.1	-0.1	0.9	-0.9	0.1	-0.1	0.7	-0.7	1.3	-1.3
200 - 250	0.7184	± 0.3	3.1	-3.2	2.1	-2.0	< 0.1	-0.1	0.5	-0.4	0.1	-0.1	0.5	-0.5	1.4	-1.4
250 - 300	0.2696	± 0.5	3.1	-3.2	2.4	-2.4	< 0.1	-0.1	0.2	-0.2	< 0.1	< 0.1	0.4	-0.4	1.4	-1.4
300 - 350	0.1161	± 0.8	3.2	-3.4	2.6	-2.6	< 0.1	-0.2	0.1	-0.1	< 0.1	< 0.1	0.2	-0.2	1.4	-1.4
350 - 400	0.05370	± 1.2	3.5	-3.6	2.8	-2.7	< 0.1	-0.2	< 0.1	< 0.1	< 0.1	< 0.1	0.1	-0.1	1.7	-1.6
400 - 470	0.02408	± 1.5	3.6	-3.7	2.9	-2.9	< 0.1	-0.2	< 0.1	< 0.1	< 0.1	< 0.1	0.3	-0.3	1.6	-1.6
470 - 550	0.009892	± 2.2	3.7	-3.9	3.1	-3.1	< 0.1	-0.3	< 0.1	< 0.1	< 0.1	< 0.1	0.1	-0.1	1.7	-1.6
550 - 650	0.003711	± 3.2	3.9	-4.0	3.3	-3.3	< 0.1	-0.3	< 0.1	< 0.1	< 0.1	< 0.1	0.1	-0.1	1.7	-1.7
650 - 750	0.001411	± 5.2	4.1	-4.3	3.4	-3.5	< 0.1	-0.4	< 0.1	< 0.1	< 0.1	< 0.1	0.3	-0.3	1.7	-1.6
750 - 900	0.0005304	± 7.2	4.5	-4.7	3.7	-3.7	< 0.1	-0.4	< 0.1	< 0.1	< 0.1	< 0.1	0.2	-0.2	1.8	-1.7
900 - 1100	0.0001615	± 10.9	5.1	-5.3	3.9	-4.0	< 0.1	-0.4	< 0.1	< 0.1	< 0.1	< 0.1	0.2	-0.2	1.8	-1.8
1100 - 1500	0.00001605	± 32.4	5.2	-5.4	4.4	-4.5	< 0.1	-0.5	< 0.1	< 0.1	< 0.1	< 0.1	0.2	-0.2	2.0	-1.9

E_{T}^{γ} [GeV]	$E_{\mathrm{T}}^{\mathrm{iso}}$ gap (%)		γ invert. var. (%)		$E_{\mathrm{T}}^{\mathrm{iso}}$ upp. lim. (%)	$E_{\mathrm{T}}^{\mathrm{iso}}$ MC (%)	R_{bckg} (%)		Pile-up (%)		Unf. (%)	MC stat. (%)	Trigger (%)	Lumi. (%)
	Up	Down	Up	Down			Up	Down	Up	Down				
125 - 150	0.1	-0.1	0.9	-0.6	± 0.2	± 0.6	1.7	-1.7	0.3	-0.3	± 0.8	± 0.2	± 1.0	± 2.1
150 - 175	0.1	-0.1	0.8	-0.7	± 0.2	± 0.6	1.3	-1.4	0.3	-0.2	± 0.2	± 0.1	± 1.0	± 2.1
175 - 200	0.1	< 0.1	0.7	-0.7	± 0.2	± 0.6	1.1	-1.1	0.3	-0.2	< 0.1	± 0.1	± 1.0	± 2.1
200 - 250	< 0.1	< 0.1	0.5	-0.8	± 0.2	± 0.7	0.9	-0.9	0.3	-0.3	± 0.6	± 0.1	± 1.0	± 2.1
250 - 300	< 0.1	< 0.1	0.4	-0.9	± 0.1	± 0.8	0.7	-0.7	0.3	-0.2	± 0.1	± 0.1	± 1.0	± 2.1
300 - 350	< 0.1	< 0.1	0.3	-0.9	± 0.1	± 0.8	0.6	-0.6	0.2	-0.2	± 0.3	± 0.1	± 1.0	± 2.1
350 - 400	< 0.1	< 0.1	0.3	-0.9	± 0.2	± 0.8	0.5	-0.5	0.3	-0.2	± 0.3	± 0.2	± 1.0	± 2.1
400 - 470	< 0.1	< 0.1	0.4	-1.0	± 0.1	± 0.8	0.4	-0.4	0.2	-0.2	± 0.2	± 0.2	± 1.0	± 2.1
470 - 550	< 0.1	< 0.1	0.4	-1.0	± 0.1	± 0.9	0.3	-0.3	0.1	-0.1	± 0.1	± 0.2	± 1.0	± 2.1
550 - 650	< 0.1	< 0.1	0.4	-1.0	< 0.1	± 0.8	0.3	-0.3	< 0.1	-0.1	± 0.1	± 0.2	± 1.0	± 2.1
650 - 750	< 0.1	< 0.1	0.4	-1.1	< 0.1	± 0.8	0.5	-0.5	0.4	-0.3	± 0.3	± 0.4	± 1.0	± 2.1
750 - 900	< 0.1	< 0.1	0.4	-1.1	± 0.3	± 0.7	1.3	-1.3	< 0.1	< 0.1	± 0.7	± 0.5	± 1.0	± 2.1
900 - 1100	< 0.1	< 0.1	0.4	-1.1	< 0.1	± 0.6	1.3	-1.3	0.2	-0.5	± 1.8	± 0.7	± 1.0	± 2.1
1100 - 1500	< 0.1	< 0.1	0.4	-1.2	< 0.1	± 0.5	1.3	-1.3	0.3	-0.3	± 0.4	± 0.3	± 1.0	± 2.1

Table C.1: The measured cross section for isolated-photon plus jet production as a function of E_{T}^{γ} (in pb/GeV) together with the statistical uncertainty in the data (in %), the total systematic uncertainty excluding that in the luminosity (in %) and the contributions from the different sources of systematic uncertainty (in %).

$p_{\mathrm{T}}^{\mathrm{jet-lead}}$ [GeV]	$d\sigma/dp_{\mathrm{T}}^{\mathrm{jet-lead}}$ [pb/GeV]	Stat. (%)	Total syst. (%)		GES (%)		GER (%)		JES (%)		JER (%)		Leak. (%)		γ ID (%)	
			Up	Down	Up	Down	Up	Down	Up	Down	Up	Down	Up	Down	Up	Down
100 - 130	2.979	$\pm$ 0.2	4.1	-4.0	2.6	-2.5	$<$ 0.1	-0.1	1.9	-1.8	0.5	-0.5	0.6	-0.3	1.3	-1.3
130 - 170	2.597	$\pm$ 0.2	3.8	-3.7	1.2	-1.3	$<$ 0.1	$<$ 0.1	2.4	-2.2	0.5	-0.5	0.6	-0.3	1.3	-1.3
170 - 220	1.166	$\pm$ 0.3	4.6	-4.6	0.5	-0.6	$<$ 0.1	$<$ 0.1	3.4	-3.3	0.5	-0.5	0.5	-0.3	1.3	-1.3
220 - 300	0.3849	$\pm$ 0.4	4.4	-4.5	0.3	-0.2	$<$ 0.1	$<$ 0.1	3.7	-3.7	0.5	-0.5	0.3	-0.3	1.4	-1.4
300 - 400	0.1037	$\pm$ 0.6	4.5	-4.6	0.2	-0.1	$<$ 0.1	$<$ 0.1	4.0	-3.9	0.4	-0.4	0.2	-0.2	1.5	-1.4
400 - 500	0.03028	$\pm$ 1.1	4.8	-4.8	0.3	$<$ 0.1	$<$ 0.1	$<$ 0.1	4.3	-4.1	0.4	-0.4	0.1	-0.1	1.5	-1.5
500 - 600	0.01057	$\pm$ 1.9	5.5	-5.9	0.3	$<$ 0.1	$<$ 0.1	$<$ 0.1	4.6	-4.8	0.4	-0.4	0.3	-0.3	1.5	-1.5
600 - 800	0.002926	$\pm$ 2.6	6.0	-6.1	0.3	$<$ 0.1	$<$ 0.1	$<$ 0.1	5.1	-5.1	0.4	-0.4	0.1	-0.1	1.5	-1.5
800 - 1000	0.0006549	$\pm$ 5.6	8.0	-7.7	0.2	$<$ 0.1	$<$ 0.1	$<$ 0.1	6.0	-5.5	0.3	-0.3	0.1	-0.1	1.5	-1.5
1000 - 1500	0.00009047	$\pm$ 9.2	9.2	-8.0	$<$ 0.1	$<$ 0.1	$<$ 0.1	$<$ 0.1	7.5	-5.9	0.3	-0.3	0.1	-0.1	1.6	-1.6

$p_{\mathrm{T}}^{\mathrm{jet-lead}}$ [GeV]	$E_{\mathrm{T}}^{\mathrm{iso}}$ gap (%)		γ invert. var. (%)		$E_{\mathrm{T}}^{\mathrm{iso}}$ upp. lim. (%)	$E_{\mathrm{T}}^{\mathrm{iso}}$ MC (%)	R_{bckg} (%)		Pile-up (%)		Unf. (%)	MC stat. (%)	Trigger (%)	Lumi. (%)
	Up	Down	Up	Down			Up	Down	Up	Down				
100 - 130	0.1	-0.1	1.1	-0.6	$<$ 0.1	$\pm$ 0.5	1.6	-1.6	0.3	-0.3	$\pm$ 0.1	$\pm$ 0.2	$\pm$ 1.0	$\pm$ 2.1
130 - 170	0.1	-0.1	0.9	-0.7	$<$ 0.1	$\pm$ 0.5	1.7	-1.7	0.2	-0.3	$\pm$ 0.6	$\pm$ 0.2	$\pm$ 1.0	$\pm$ 2.1
170 - 220	0.1	-0.1	0.7	-0.8	$<$ 0.1	$\pm$ 0.7	1.5	-1.5	0.4	-0.3	$\pm$ 1.8	$\pm$ 0.1	$\pm$ 1.0	$\pm$ 2.1
220 - 300	$<$ 0.1	$<$ 0.1	0.5	-0.9	$<$ 0.1	$\pm$ 0.8	1.1	-1.1	0.2	-0.1	$\pm$ 0.8	$\pm$ 0.2	$\pm$ 1.0	$\pm$ 2.1
300 - 400	$<$ 0.1	$<$ 0.1	0.4	-1.0	$<$ 0.1	$\pm$ 0.9	0.7	-0.7	0.2	-0.2	$\pm$ 0.6	$\pm$ 0.3	$\pm$ 1.0	$\pm$ 2.1
400 - 500	$<$ 0.1	$<$ 0.1	0.5	-1.0	$<$ 0.1	$\pm$ 0.9	0.5	-0.5	0.2	-0.3	$\pm$ 0.6	$\pm$ 0.5	$\pm$ 1.0	$\pm$ 2.1
500 - 600	$<$ 0.1	$<$ 0.1	0.5	-1.1	$<$ 0.1	$\pm$ 1.0	0.3	-0.3	0.7	-0.5	$\pm$ 2.1	$\pm$ 0.7	$\pm$ 1.0	$\pm$ 2.1
600 - 800	$<$ 0.1	$<$ 0.1	0.6	-1.1	$<$ 0.1	$\pm$ 1.0	0.3	-0.3	0.4	-0.2	$\pm$ 2.1	$\pm$ 1.0	$\pm$ 1.0	$\pm$ 2.1
800 - 1000	$<$ 0.1	$<$ 0.1	0.6	-1.2	$\pm$ 0.2	$\pm$ 0.8	1.5	-1.6	0.2	-0.5	$\pm$ 4.3	$\pm$ 1.5	$\pm$ 1.0	$\pm$ 2.1
1000 - 1500	$<$ 0.1	$<$ 0.1	0.7	-1.2	$<$ 0.1	$\pm$ 0.5	1.5	-1.6	0.1	-0.2	$\pm$ 4.3	$\pm$ 1.6	$\pm$ 1.0	$\pm$ 2.1

Table C.2: The measured cross section for isolated-photon plus jet production as a function of $p_{\mathrm{T}}^{jet-lead}$ (in pb/GeV) together with the statistical uncertainty in the data (in %), the total systematic uncertainty excluding that in the luminosity (in %) and the contributions from the different sources of systematic uncertainty (in %).

$\Delta\phi^{\gamma-\text{jet}}$ [rad]	$d\sigma/d\Delta\phi^{\gamma-\text{jet}}$ [pb/rad]	Stat. (%)	Total syst. (%)		GES (%)		GER (%)		JES (%)		JER (%)		Leak. (%)		γ ID (%)	
			Up	Down	Up	Down	Up	Down	Up	Down	Up	Down	Up	Down	Up	Down
$\pi/2-3\pi/5$	7.377	± 1.3	4.0	-4.3	1.5	-1.7	0.1	-0.2	1.9	-2.1	1.3	-1.3	0.2	-0.2	1.4	-1.3
$3\pi/5-7\pi/10$	19.34	± 0.8	4.0	-4.2	1.5	-1.6	0.1	< 0.1	2.2	-2.3	0.6	-0.6	0.7	-0.7	1.4	-1.3
$7\pi/10-4\pi/5$	53.49	± 0.5	3.6	-3.7	1.5	-1.5	0.1	< 0.1	2.3	-2.3	0.1	-0.1	1.0	-1.0	1.3	-1.3
$4\pi/5-9\pi/10$	157.2	± 0.3	3.8	-3.7	1.4	-1.4	< 0.1	< 0.1	2.1	-2.0	< 0.1	< 0.1	1.1	-1.1	1.3	-1.3
$9\pi/10-\pi$	710.3	± 0.1	3.5	-3.5	1.3	-1.4	< 0.1	-0.1	1.4	-1.3	0.2	-0.2	1.2	-1.2	1.3	-1.3

$\Delta\phi^{\gamma-\text{jet}}$ [rad]	$E_{\text{T}}^{\text{iso}}$ gap (%)		γ invert. var. (%)		$E_{\text{T}}^{\text{iso}}$ upp. lim. (%)	$E_{\text{T}}^{\text{iso}}$ MC (%)	R_{bckg} (%)		Pile-up (%)		Unf. (%)	MC stat. (%)	Trigger (%)	Lumi. (%)
	Up	Down	Up	Down			Up	Down	Up	Down				
$\pi/2-3\pi/5$	0.1	< 0.1	0.8	-0.9	± 0.4	± 0.5	1.0	-1.1	0.3	-0.8	± 1.6	± 1.1	± 1.0	± 2.1
$3\pi/5-7\pi/10$	0.1	< 0.1	0.7	-0.8	± 0.1	± 0.7	1.1	-1.1	0.4	-0.4	± 1.8	± 0.6	± 1.0	± 2.1
$7\pi/10-4\pi/5$	< 0.1	< 0.1	0.5	-0.8	± 0.2	± 0.6	1.1	-1.2	0.1	< 0.1	± 0.5	± 0.3	± 1.0	± 2.1
$4\pi/5-9\pi/10$	0.1	< 0.1	0.7	-0.7	± 0.3	± 0.6	1.5	-1.5	0.3	-0.3	± 0.9	± 0.2	± 1.0	± 2.1
$9\pi/10-\pi$	0.1	-0.1	0.9	-0.6	± 0.3	± 0.6	1.7	-1.7	0.3	-0.3	± 0.8	± 0.1	± 1.0	± 2.1

Table C.3: The measured cross section for isolated-photon plus jet production as a function of $\Delta\phi^{\gamma-\text{jet}}$ (in pb/rad) together with the statistical uncertainty in the data (in %), the total systematic uncertainty excluding that in the luminosity (in %) and the contributions from the different sources of systematic uncertainty (in %).

$m^{\gamma-\text{jet}}$ [GeV]	$d\sigma/dm^{\gamma-\text{jet}}$ [pb/GeV]	Stat. (%)	Total syst. (%)		GES (%)		GER (%)		JES (%)		JER (%)		Leak. (%)		γ ID (%)	
			Up	Down	Up	Down	Up	Down	Up	Down	Up	Down	Up	Down	Up	Down
450 - 510	0.2760	± 0.5	3.6	-3.5	1.2	-1.0	0.1	< 0.1	2.2	-2.0	0.2	-0.2	0.8	-0.3	1.2	-1.2
510 - 570	0.1682	± 0.6	3.6	-3.5	1.2	-1.0	0.1	< 0.1	2.1	-2.0	0.2	-0.2	0.7	-0.2	1.3	-1.2
570 - 650	0.09722	± 0.7	3.4	-3.4	1.2	-1.1	0.1	< 0.1	2.0	-2.0	< 0.1	< 0.1	0.5	-0.1	1.3	-1.3
650 - 750	0.05070	± 0.9	3.3	-3.4	1.2	-1.2	< 0.1	< 0.1	2.0	-2.0	0.1	-0.1	0.4	-0.1	1.3	-1.3
750 - 850	0.02667	± 1.2	3.3	-3.5	1.3	-1.2	< 0.1	< 0.1	2.1	-2.1	< 0.1	< 0.1	0.3	-0.2	1.4	-1.3
850 - 950	0.01461	± 1.6	3.4	-3.6	1.3	-1.3	< 0.1	< 0.1	2.1	-2.2	0.2	-0.2	0.2	-0.2	1.4	-1.4
950 - 1050	0.008384	± 2.2	3.6	-3.8	1.4	-1.4	< 0.1	-0.1	2.2	-2.3	0.2	-0.2	0.3	-0.3	1.5	-1.4
1050 - 1250	0.004129	± 2.2	3.8	-4.0	1.4	-1.5	< 0.1	-0.1	2.4	-2.4	0.3	-0.2	0.2	< 0.1	1.6	-1.5
1250 - 1450	0.001555	± 3.6	3.9	-4.1	1.5	-1.6	< 0.1	-0.1	2.6	-2.6	0.1	-0.1	0.2	-0.2	1.7	-1.6
1450 - 1650	0.0006754	± 5.5	4.0	-4.2	1.6	-1.7	< 0.1	-0.1	2.8	-2.9	0.1	-0.1	0.1	< 0.1	1.7	-1.7
1650 - 1850	0.0003545	± 7.4	4.3	-4.4	1.7	-1.8	< 0.1	-0.1	3.1	-3.1	0.4	-0.4	0.1	-0.1	1.8	-1.7
1850 - 2450	0.00009419	± 8.5	4.9	-5.1	1.8	-1.9	< 0.1	-0.2	3.5	-3.5	0.1	-0.1	0.1	-0.1	1.9	-1.8
2450 - 3250	0.00001096	± 30.0	5.9	-6.0	2.1	-2.2	0.1	-0.2	4.1	-4.1	0.1	-0.1	0.1	-0.1	2.0	-1.9

$m^{\gamma-\text{jet}}$ [GeV]	$E_{\text{T}}^{\text{iso}}$ gap (%)		γ invert. var. (%)		$E_{\text{T}}^{\text{iso}}$ upp. lim. (%)	$E_{\text{T}}^{\text{iso}}$ MC (%)	R_{bckg} (%)		Pile-up (%)		Unf. (%)	MC stat. (%)	Trigger (%)	Lumi. (%)
	Up	Down	Up	Down			Up	Down	Up	Down				
450 - 510	0.1	-0.1	0.8	-1.1	± 0.1	± 0.6	1.7	-1.7	0.1	-0.1	± 0.3	± 0.3	± 1.0	± 2.1
510 - 570	0.1	-0.1	0.7	-1.0	± 0.1	± 0.6	1.5	-1.5	0.3	-0.4	± 1.0	± 0.3	± 1.0	± 2.1
570 - 650	0.1	< 0.1	0.6	-1.0	± 0.1	± 0.7	1.3	-1.3	0.3	-0.2	± 0.8	± 0.3	± 1.0	± 2.1
650 - 750	< 0.1	< 0.1	0.6	-1.0	< 0.1	± 0.8	1.1	-1.1	0.3	-0.2	± 0.8	± 0.3	± 1.0	± 2.1
750 - 850	< 0.1	< 0.1	0.5	-0.9	± 0.1	± 0.9	0.7	-0.7	0.4	-0.4	± 1.0	± 0.3	± 1.0	± 2.1
850 - 950	< 0.1	< 0.1	0.5	-0.9	< 0.1	± 1.0	0.7	-0.7	0.1	-0.2	± 1.0	± 0.4	± 1.0	± 2.1
950 - 1050	< 0.1	< 0.1	0.5	-0.8	± 0.1	± 0.9	0.6	-0.6	< 0.1	< 0.1	± 1.5	± 0.4	± 1.0	± 2.1
1050 - 1250	< 0.1	< 0.1	0.4	-0.8	± 0.1	± 0.9	0.6	-0.6	0.2	-0.1	± 1.5	± 0.4	± 1.0	± 2.1
1250 - 1450	0.1	< 0.1	0.4	-0.8	± 0.1	± 1.0	0.9	-0.9	0.5	-0.2	± 0.9	± 0.4	± 1.0	± 2.1
1450 - 1650	< 0.1	< 0.1	0.3	-0.7	± 0.1	± 0.9	0.8	-0.8	< 0.1	-0.1	± 0.5	± 0.6	± 1.0	± 2.1
1650 - 1850	< 0.1	< 0.1	0.3	-0.7	± 0.1	± 0.7	0.3	-0.3	< 0.1	< 0.1	± 0.8	± 0.8	± 1.0	± 2.1
1850 - 2450	< 0.1	< 0.1	0.3	-0.6	< 0.1	± 1.1	0.5	-0.5	0.2	-0.2	± 1.8	± 0.6	± 1.0	± 2.1
2450 - 3250	< 0.1	< 0.1	0.2	-0.6	< 0.1	± 0.7	0.5	-0.5	0.2	-0.5	± 2.6	± 1.1	± 1.0	± 2.1

Table C.4: The measured cross section for isolated-photon plus jet production as a function of $m^{\gamma-\text{jet}}$ (in pb/GeV) together with the statistical uncertainty in the data (in %), the total systematic uncertainty excluding that in the luminosity (in %) and the contributions from the different sources of systematic uncertainty (in %).

$\lvert\cos\theta^*\rvert$	$d\sigma/d\lvert\cos\theta^*\rvert$ [pb]	Stat. (%)	Total syst. (%)		GES (%)		GER (%)		JES (%)		JER (%)		Leak. (%)		γ ID (%)	
			Up	Down	Up	Down	Up	Down	Up	Down	Up	Down	Up	Down	Up	Down
0.0 - 0.10	30.56	± 1.1	2.9	-2.9	1.0	-1.0	< 0.1	< 0.1	2.0	-2.0	0.2	-0.2	0.4	-0.4	1.1	-1.1
0.10 - 0.20	31.61	± 1.1	3.3	-3.2	1.1	-0.9	< 0.1	< 0.1	2.0	-1.9	< 0.1	< 0.1	0.3	-0.3	1.1	-1.1
0.20 - 0.30	32.57	± 1.1	3.0	-2.9	1.1	-1.0	< 0.1	< 0.1	2.1	-1.9	0.1	-0.1	0.6	-0.6	1.1	-1.1
0.30 - 0.40	33.79	± 1.1	3.1	-2.9	1.2	-1.0	0.1	< 0.1	2.1	-2.0	0.1	-0.1	0.6	-0.6	1.1	-1.1
0.40 - 0.50	40.79	± 1.0	3.3	-3.3	1.2	-1.1	0.1	< 0.1	2.2	-2.0	0.1	-0.1	0.7	-0.7	1.2	-1.1
0.50 - 0.60	50.47	± 0.9	3.5	-3.3	1.3	-1.2	0.1	< 0.1	2.2	-2.1	0.1	-0.1	0.7	-0.7	1.2	-1.2
0.60 - 0.70	72.22	± 0.8	3.7	-3.9	1.3	-1.2	0.1	< 0.1	2.2	-2.1	0.2	-0.2	1.2	-1.2	1.3	-1.3
0.70 - 0.83	131.2	± 0.5	4.1	-4.1	1.3	-1.2	0.1	-0.1	2.2	-2.1	0.2	-0.2	1.5	-1.5	1.4	-1.4

$\lvert\cos\theta^*\rvert$	$E_{\mathrm{T}}^{\mathrm{iso}}$ gap (%)		γ invert. var. (%)		$E_{\mathrm{T}}^{\mathrm{iso}}$ upp. lim. (%)	$E_{\mathrm{T}}^{\mathrm{iso}}$ MC (%)	R_{bckg} (%)		Pile-up (%)		Unf. (%)	MC stat. (%)	Trigger (%)	Lumi. (%)
	Up	Down	Up	Down			Up	Down	Up	Down				
0.0 - 0.10	< 0.1	< 0.1	0.7	< 0.1	± 0.2	± 0.6	0.4	-0.4	0.1	-0.1	± 0.4	± 0.2	± 1.0	± 2.1
0.10 - 0.20	< 0.1	< 0.1	0.5	< 0.1	± 0.3	± 0.7	0.5	-0.5	0.1	-0.1	± 1.5	± 0.3	± 1.0	± 2.1
0.20 - 0.30	< 0.1	< 0.1	0.3	-0.7	± 0.2	± 0.7	0.5	-0.5	0.4	-0.2	< 0.1	± 0.3	± 1.0	± 2.1
0.30 - 0.40	< 0.1	< 0.1	0.5	-0.4	± 0.2	± 0.6	0.6	-0.6	< 0.1	-0.2	± 0.4	± 0.3	± 1.0	± 2.1
0.40 - 0.50	< 0.1	< 0.1	0.4	-0.8	± 0.3	± 0.6	0.7	-0.7	0.3	-0.3	± 1.0	± 0.3	± 1.0	± 2.1
0.50 - 0.60	< 0.1	< 0.1	0.9	-0.4	± 0.3	± 0.7	1.0	-1.0	0.2	-0.3	± 0.7	± 0.3	± 1.0	± 2.1
0.60 - 0.70	0.1	< 0.1	0.9	-1.3	± 0.4	± 0.7	1.3	-1.3	0.2	-0.2	± 0.7	± 0.3	± 1.0	± 2.1
0.70 - 0.83	0.1	-0.1	1.1	-1.1	± 0.4	± 0.7	1.9	-1.9	0.2	-0.2	± 0.5	± 0.2	± 1.0	± 2.1

Table C.5: The measured cross section for isolated-photon plus jet production as a function of $\lvert\cos\theta^*\rvert$ (in pb) together with the statistical uncertainty in the data (in %), the total systematic uncertainty excluding that in the luminosity (in %) and the contributions from the different sources of systematic uncertainty (in %).